



HAL
open science

Multicaloric effect in ferroic materials

Yang Liu

► **To cite this version:**

Yang Liu. Multicaloric effect in ferroic materials. Other. Université Paris Saclay (COMUE), 2016. English. NNT: 2016SACLCO41 . tel-01527891

HAL Id: tel-01527891

<https://theses.hal.science/tel-01527891>

Submitted on 26 May 2017

HAL is a multi-disciplinary open access archive for the deposit and dissemination of scientific research documents, whether they are published or not. The documents may come from teaching and research institutions in France or abroad, or from public or private research centers.

L'archive ouverte pluridisciplinaire **HAL**, est destinée au dépôt et à la diffusion de documents scientifiques de niveau recherche, publiés ou non, émanant des établissements d'enseignement et de recherche français ou étrangers, des laboratoires publics ou privés.

NNT : 2016SACL041

THESE DE DOCTORAT
DE
L'UNIVERSITE PARIS-SACLAY
PREPAREE A
"CENTRALESUPÉLEC"

ECOLE DOCTORALE N°573
Interfaces : approches interdisciplinaires / fondements, applications et innovation
Sciences et technologies industrielles

Spécialité de Doctorat: Physique de la Matière Condensée

Par

M Yang LIU

Multicaloric effect in ferroic materials

Thèse présentée et soutenue à «Campus de Châtenay-Malabry», «le 23 mai 2016» :

Composition du Jury :

| | | |
|-----------------|--|--------------------|
| M. B. Dkhil | Maître de Conférences, CentraleSupélec | Directeur de thèse |
| M. M. El Marssi | Professeur, Université de Picardie Jules Verne | Examineur |
| M. J.-M. Kiat | DR CNRS, CentraleSupélec | Examineur |
| M. Z. Kutnjak | Professeur, Jozef Stefan Institute | Rapporteur |
| M. X. Moya | Maître de Conférences, University of Cambridge | Rapporteur |

Titre : Effet Multicaloric dans matériaux ferroïques

Mots clés : effet électrocalorique, ferroélectrique, à l'état solide réfrigération, effet mechanocalorique, effet multicaloric, multiferroïque

Résumé : Les matériaux caloriques à l'état solide, qui subissent un changement de température adiabatique ou un changement d'entropie isothermale lors de certains stimuli externes (champ électrique, champ magnétique, contrainte ou pression mécanique) est appliquée ou retirée, sont prometteurs pour la réfrigération à l'état solide, comme alternative aux dispositifs de refroidissement conventionnels inventés il y a cent ans qui utilisent des gaz dangereux. Compte tenu des améliorations des systèmes de réfrigération à compression de vapeur approchant très vite de leur limite d'efficacité théorique, en plus des préoccupations environnementales accrues, il y a eu récemment une recrudescence de la recherche mondiale pour de nouvelles solutions de réfrigération plus économiques et respectueuses de l'environnement. Les caloriques les plus importants sont les matériaux "ferroïquement" ordonnés (ferroélectriques, ferroélastiques et ferromagnétique/antiferromagnétique) qui présentent souvent des effets caloriques géants près de leurs transitions ferroïques. Dans cette thèse, nous présentons nos résultats théoriques et expérimentaux sur l'effet électrocalorique, élastocalorique, barocalorique et magnétocalorique dans différents matériaux ferroïques. Nos résultats montrent que tous ces effets caloriques peuvent donner des solutions de réfrigération prometteuses avec un faible impact environnemental. Nous abordons les ferroélectriques qui apparaissent comme matériaux idéaux permettant à la fois des réponses électrocaloriques, élastocaloriques et barocaloriques géantes près de

la température ambiante. Pour la première fois, nous mettons en évidence un effet électrocalorique négatif dans des films minces antiferroélectriques et nous proposons un nouveau mécanisme pour comprendre la réponse calorique dans antiferroïques en général incluant antiferroélectrique et antiferromagnétique. Par ailleurs, pour la première fois en utilisant une caméra infra-rouge, nous effectuons la mesure résolue spatialement sur l'effet électrocalorique dans des condensateurs multicouches, l'un des systèmes les plus étudiés considérés comme le prototype électrocalorique le plus prometteur. Nos résultats fournissent la première preuve expérimentale directe sur le flux de chaleur électrocalorique à la fois temporellement et spatialement dans un dispositif électrocalorique spécifique. En outre, pour la première fois, nous concevons un cycle de réfrigération multicalorique combinant effet électrocalorique avec des effets élastocaloriques/magnétocaloriques via des matériaux ferroélectriques. Nous avons réalisé ce cycle multicalorique pour résoudre un problème réel et de longue date, à savoir une grande hystérésis magnétique qui a empêché l'utilisation pourtant prometteuse de FeRh découvert il y a près de 26 ans en tant que matériau magnétocalorique. Nous espérons que cette thèse fournira non seulement des connaissances utiles pour comprendre fondamentalement l'effet calorique à l'état solide dans les matériaux ferroïques et ce qui est véritablement mesuré, mais pourra aussi servir de guide pratique pour exploiter et développer les ferrocalorics vers la conception de dispositifs appropriés.

Title : Multicaloric effect in ferroic materials

Keywords : electrocaloric effect, ferroelectric, solid-state refrigeration, mechanocaloric effect, multicaloric effect, multiferroic

Abstract : Solid-state caloric materials, which undergo an adiabatic temperature change or isothermal entropy change when some external stimulus (electric field, magnetic field, stress and pressure) is applied or withdrawn, are promising for solid-state refrigeration, as an alternative to hazardous gases used in conventional cooling devices invented a hundred years ago. Given that the highly refined vapor-compression refrigeration systems asymptotically approach their theoretical efficiency limit in addition to the concern on environment, there has been a recent upsurge in worldwide search for new refrigeration solution which is economical and environmentally friendly. The most prominent calorics are ferroically ordered materials (ferroelectric, ferroelastic and ferromagnetic/antiferromagnetic) that often exhibit giant caloric effects near their ferroic transitions. In this thesis, we present our theoretical and experimental results on electrocaloric effect, elastocaloric effect, barocaloric effect and magnetocaloric effect in different ferroic materials. Our findings show that all these caloric effects may appear promising with low environmental impact. We address ferroelectrics emerging as ideal materials which permit both giant elastocaloric, electrocaloric and barocaloric responses near room temperature. For the first

time, we find a large negative electrocaloric effect in antiferroelectric thin films and we propose a new mechanism to understand the caloric response in antiferroics including antiferroelectric and antiferromagnetic. In addition, for the first time using Infra-red camera we carry out spatially-resolved measurement on electrocaloric effect in multilayer capacitors, one of the most studied systems which are regarded as the most promising electrocaloric prototype. Our findings provide the first direct experimental evidence on the electrocaloric heat flux both temporally and spatially in a specific electrocaloric device. Moreover, for the first time, we design a multicaloric refrigeration cycle combining electrocaloric effect with elastocaloric/magnetocaloric effects bridged by ferroelectric materials. We realized such multicaloric cycle to solve a real and longstanding problem, i.e., a large hysteresis that impeded reversibility in an otherwise promising magnetocaloric material FeRh discovered almost 26 years ago. We hope that this thesis will not only provide a useful background to fundamentally understand the solid-state caloric effect in ferroics and what we are really measuring, but also may act as a practical guide to exploit and develop ferrocalorics towards design of suitable devices.

*To my dear parents who give unquestionable love and selfless support
to encourage myself to pursue my childish dreams in fairy tale.*

ACKNOWLEDGEMENTS

First of all, I would like to send my special thanks to the Jury members including Mimoun El Marssi, Zdravko Kutnjak, Xavier Moya, Jean-Michel Kiat and B. Dkhil for sparing their valuable time to review and examine my thesis. I appreciate their positive recommendation giving credit to the theoretical and experimental results in this manuscript. Their recognitions and nice suggestions are encouraging, which marks my Ph.D defense as an unforgettable memory in my life.

Before I came to CentraleSupélec pursuing my Ph.D study, I was impressed by one sentence: “*I have known more people whose lives have been ruined by getting a Ph.D. in physics than by drugs.*” Personal investment as a Ph.D. is an important period of life and I am sure that every Ph.D. including myself suffers from intensive scientific training and tasks during this 3-5 years. To me, it was really a big challenge especially at the very beginning.

Fortunately, I am not alone while my supervisor, Brahim Dkhil, was always there and ready to help. He is the kind of professor who has magic to ensure that his students are voluntarily enjoying coming to the lab. My sincere appreciation to Brahim: who allowed me changing my Ph.D. topic from “Control and tuning of ferroic properties using active piezoelectric substrates” to “Multicaloric effect in ferroic materials”. Interestingly, the last chapter in this manuscript describes our work exactly on control and tuning of ferroic properties (magnetocaloric effect) using active piezoelectric substrates; who was always the first expert audience to my immature results and conceived and expertly supervised this work. Although he was very busy, Brahim always found time to make fruitful discussions with me and advised me thoroughly at every stage of this manuscript.

I thank Laurent Bellaiche and Jim Scott for expert advice and support, particularly with my work on electrocaloric and elastocaloric effects. From Laurent’s short and concise advice, I learned basic concepts and principles about the piezocaloric effect and relaxors. From Jim’s critical comments and straightforward suggestions, I earned deeper understandings of electrocaloric and elastocaloric effects. They are the distinguished professors who nicely taught me how to be professional and serious to my original data.

I thank Zhengdong Luo, Wenping Geng and Lee C. Phillips for their experimental support and useful discussions to achieve my original theoretical predictions. I am very impressed by their hard work and always benefit from our collaborations. In particular, I would thank Lee for his critical comments and arguments on multicaloric effect, which kept me still awake even in deep nights to avoid making any stupid mistakes...I thank Jie Wei for his experimental support on

ceramic fabrication and characterization. I thank Manuel Bibes and Agnès Barthélémy for their support on the project of multicaloric effect. I thank Richard Mattana for characterizing the samples by SQUID magnetometry. I thank Vincent Garcia for sharing his knowledge of experimental measurement on ferroelectric tunnel junctions. I thank Rasa Pirc, Nikola Novak, and Zdravko Kutnjak for providing their experimental data of the heat capacity and fruitful discussions. I thank Pierre-Eymeric Janolin and Igor Kornev for discussions. I thank Xingyuan Wang, M. Baris Okata, I. Burç Misirlioğlu, and S. Pamir Alpay for their fruitful suggestions. I thank Mehmet Sanlialp and Doru C. Lupascu for their support on DSC technique. I thank Emmanuel Defay and Jens Kreisel for their support on infra-red camera. Specially for Emmanuel for his critical comments and nice suggestions, which improves significantly my understandings of electrocaloric heat flux in multilayer capacitors. I thank Xiangjian Meng and Anquan Jiang for their support on the project on electrocaloric effect. I thank Shengguo Lu, Yang Bai, Bo Li, Jie Wang, Honghui Wu, Zhongjian Xie, Xavier Moya, Sam Crossley, Alex Avramenko, Qi Zhang, Qiming Zhang and Qing Wang for useful discussions at conferences.

I am grateful to every member at SPMS lab and appreciate the nice and friendly atmosphere at lab, office room and coffee room: PhD students including Charlotte Cochard, Camille Exare, Romain Fayot, Charles Paillard, Désirée Ciria, Cintia Hartmann, Fabien Briec, Mohamed Ben Hassine, Xiaofai Bai, Wen Jing Li, Gentien Thorner, Bobo Tian, Chenyi Li, Yiming Cao, Xiao Xu, Xiaoxuan Shi, Halyna Volkova, and Zeyin Yan; all laboratory team: Pierre-Eymeric Janolin, Ingrid Canero-Infante, Igor Kornev, Nicolas Guiblin, Jean-Michel Kiat, Christine Vinée-Jacquín, Pascale Gemeiner, Jean-Michel Gillet, Guilhem Dezanneau, Pierre Becker, Sandrine Geiger, Hichem Dammak, Pascale Salvini, Michel Jouan, Thierry Martin, Agnès Bénard, Claire Roussel, Hubert Jubeau, Quy Dao Nguyen, Gianguido Baldinozzi, Anne Spasojevic, Gilles Boemare, and Xavier Bril. I am also thankful to my friends who shares their best time with me including cooking, traveling and so on: Ming Luo, Jun Tao, Wen Wu, Wei Gao, Pujian Mao, Chen Zhao, Hang Zhao, Xin Wei, Chen Shen, Xin Song, Wei Ai, Mengyang Liu, Zhongsen Li, Zhaofu Hong, Jing Peng, Jinyan Liu, Shouyu Ma, Xing Liu, Minhao Yang, Xue Bai, Yu Liu, Wei Zhang, Haijiao Ma, Yongfeng Tong, Wenxin Chang, Zhengxuan Fan, Jigang Lu, Cong Xin, Peng Chen, and Delong He.

I wish to thank the China Scholarship Council (CSC) for funding my stay in France.

I dedicate this work to my dear parents and my lovely Zhuoxi Yu, who always supported and encouraged me to, keeping me carrying on, no matter what kind of difficulties encountered.

Finally, I quote Paul Valéry by his verse in *Le cimetière marin*: “*Le vent se lève, il faut tenter de vivre*”. Although my life may have been partially ruined by getting a Ph.D. in physics, I never regret my choice and I will keep myself going and enjoying in my further scientific activities.

Yang Liu at SPMS
25 May 2016

CONTENTS

| | |
|---|-----------|
| Introduction | 1 |
| 1 Fundamentals of solid-state caloric effect | 5 |
| 1.1 Brief summary of history about solid-state caloric effects | 5 |
| 1.2 Brief introduction to ferroic materials | 11 |
| 1.3 Thermodynamics of caloric effects | 13 |
| 1.4 Indirect methods | 17 |
| 1.5 Direct measurements | 18 |
| 1.6 Multicaloric effect | 18 |
| 1.7 Thermodynamic refrigeration cycles | 21 |
| 1.8 Caloric parameters | 22 |
| 2 Review on direct and indirect measurements on electrocaloric effect | 24 |
| 2.1 Introduction | 24 |
| 2.2 Indirect measurements | 26 |
| 2.2.1 Basic thermodynamic description of electrocaloric refrigeration | 26 |
| 2.2.2 Selection of isothermal $P - T$ curves | 29 |
| 2.2.3 Negative electrocaloric effect in antiferroelectrics | 32 |
| 2.2.4 Electrocaloric effect in relaxors | 38 |
| 2.2.5 First-order phase transition | 39 |
| 2.2.6 Heat capacity and kinetics | 41 |
| 2.2.7 Depolarizing field | 43 |
| 2.2.8 Clausius-Clapeyron method | 44 |
| 2.3 Direct measurements | 44 |
| 2.3.1 Thermocouple and thermometer | 48 |
| 2.3.2 Differential Scanning Calorimetry | 48 |
| 2.3.3 Specifically designed calorimeters | 49 |
| 2.3.4 Infra-red camera | 50 |
| 2.3.5 Scanning thermal microscopy | 53 |
| 2.4 Closing Remarks | 53 |

| | | |
|----------|--|------------|
| 3 | Electrocaloric effect in ferroelectrics and antiferroelectrics | 55 |
| 3.1 | Electrocaloric effect in ferroelectric tunnel junctions | 55 |
| 3.1.1 | Ferroelectric tunnel junctions: the role of built-in electric field | 55 |
| 3.1.2 | Electrocaloric effect in symmetric ferroelectric tunnel junctions | 69 |
| 3.1.3 | Electrocaloric effect in asymmetric ferroelectric tunnel junctions | 75 |
| 3.1.4 | Mechanically-mediated electrocaloric effect in symmetric ferroelectric tunnel junctions | 82 |
| 3.2 | Negative electrocaloric effect in antiferroelectric La-doped $\text{Pb}(\text{ZrTi})\text{O}_3$ thin films near room temperature | 90 |
| 3.3 | Enhanced electrocaloric effect in lead-free $\text{BaTi}_x\text{Sn}_{1-x}\text{O}_3$ ceramics near room temperature | 103 |
| 4 | Direct imaging of electrocaloric heat flux in multilayer capacitors | 111 |
| 4.1 | Brief introduction | 111 |
| 4.2 | Experimental set-up | 113 |
| 4.3 | Spatially resolved imaging of electrocaloric effect in multilayer capacitors #1 | 115 |
| 4.4 | Spatially resolved imaging of electrocaloric effect in multilayer capacitors #2 | 125 |
| 4.5 | Spatially resolved imaging of electrocaloric effect in multilayer capacitors #3 | 134 |
| 4.6 | Electrocaloric heat flux in multilayer capacitors | 134 |
| 4.7 | Summary | 150 |
| 5 | Elastocaloric effect in ferroelectrics | 151 |
| 5.1 | Elastocaloric effect in ultrathin ferroelectric films near room temperature | 151 |
| 5.1.1 | Thermodynamical model | 151 |
| 5.1.2 | Thermal expansion coefficient and Poisson's ratio | 154 |
| 5.1.3 | Elastocaloric effect in ferroelectric ultrathin films | 156 |
| 5.1.4 | Ideal refrigeration cycle | 161 |
| 5.1.5 | Comments on elastocaloric effect | 165 |
| 5.2 | Influence of epitaxial strain on elastocaloric effect in ferroelectric thin films | 166 |
| 5.3 | Giant elastocaloric strength in BaTiO_3 in single crystals | 173 |
| 5.3.1 | Brief introduction | 173 |
| 5.3.2 | Landau theory of elastocaloric effect | 174 |
| 5.3.3 | Elastocaloric effect in BaTiO_3 single crystals | 175 |
| 5.3.4 | Stress-mediated electrocaloric effect in BaTiO_3 single crystals | 180 |
| 5.4 | Conclusions | 181 |
| 6 | Barocaloric effect in ferroelectrics | 183 |
| 6.1 | Barocaloric effect in BaTiO_3 single crystals | 183 |
| 6.2 | Pressure-mediated electrocaloric effect in BaTiO_3 single crystals | 188 |
| 6.3 | Summary | 189 |

| | |
|--|------------|
| 7 Multicaloric effect in FeRh/BaTiO₃ heterostructure | 190 |
| 7.1 Large reversible caloric effect in FeRh thin films via a dual-stimulus multicaloric cycle | 190 |
| 7.2 Giant electric-field induced mechanocaloric effect in hybrid FeRh/BaTiO ₃ heterostructure | 198 |
| 7.3 Summary | 204 |
| 8 Conclusions and perspectives | 205 |
| 8.1 Conclusions | 205 |
| 8.2 Perspectives | 209 |
| Bibliography | 212 |
| Publications | 235 |

INTRODUCTION

Current cooling technology is mainly supported by the vapor-compression refrigeration invented a hundred years ago. It has played a significant role in industry, agriculture, lifestyle, settlement patterns and so on. For instance, many commercial applications, including, but not limited to, are available today: household refrigerators, industrial freezers, cryogenics, and air conditioning. However, the highly refined vapor-compression refrigeration systems asymptotically approach their theoretical efficiency limit [1]. In addition, refrigeration is one ($\sim 15\%$) of the main sources of electricity consumption in the world [2] and therefore contributes to worldwide green house gas CO₂ emissions [3]. Moreover, vapor-compression refrigerants themselves such as hydrochlorofluorocarbons (HCFCs) are one of the main sinks of green house gas emissions with significantly larger global warming potential compared to CO₂ [3]. As a result, there has been a recent upsurge in worldwide search for high-efficiency alternative cooling technology which is economical and environmentally friendly.

In this context, solid-state caloric materials, which undergo an adiabatic temperature change or isothermal entropy change when some external stimulus is applied or withdrawn, are highly sought after for new refrigeration solutions to replace current vapor-cycle cooling technologies [4–6]. The most prominent calorics are ferroically ordered materials that often exhibit “giant” caloric effects near their ferroic transitions [7, 8]. Depending on the external stimulus, effects [8] may be called magnetocaloric (magnetic field), electrocaloric (electric field), elastocaloric (uniaxial stress) or barocaloric (hydrostatic pressure), the last two being very similar and now considered together as “mechanocaloric” effects [8]. All these caloric effects appear promising as they may deliver higher energy efficiency with low environmental impact compared to vapor compression refrigeration [4–6]. Many great breakthroughs in the fields of Condensed Matter Physics and Materials Science have been achieved so far followed by a sustained and coordinated effort by the international caloric community. For instance, a milestone discovery of giant room-temperature magnetocaloric effect [9] was announced by Karl A. Gschneidner, Jr. and Vitalij K. Pecharsk in 1997, which resulted in an exponential increase in scientific publications. At the same time, exciting news has been revealed by significant engineering developments aiming at commercial applications: about 60 magnetocaloric prototypes have been developed all over the world [6]. While research in electrocaloric and mechanocaloric effects are their early stages, how to select the required materials and design prototypes as efficient as magnetocaloric counterparts would be the central focus in current stage [5, 6]. Importantly, multiferroic materials [8, 10] permitting more than one type of caloric effect have great promise in multicaloric effect driven simulta-

neously or sequentially in a single sample. This may lead to search for hitherto unobserved caloric effect e.g. elastocaloric and barocaloric effects in ferroelectrics and ferromagnetics. Due to the strong coupling between different ferroic orders, the multicaloric effect may be larger than any of the single caloric effect. Interestingly, tuning and optimization of one single caloric (i.e., magnetocaloric or electrocaloric) in multicaloric materials by using mechanical stress can be also expected to be feasible in this regard [8].

Despite the foregoing advances from Materials Science and Industrial Engineering, several key challenges and open questions still exist:

1.) A large driving magnetic field (>2 T) is usually needed during the adiabatic magnetization process to ensure the large cooling capability and high efficiency of the magnetic refrigeration, which inevitably requires uneconomic investments on the clumsy magnets. This is not affordable for market applications [4, 6].

2.) First-order ferroic phase transition has shown a great success in inducing giant caloric effects. However, thermal hysteresis, which is usually large accompanied by the first-order phase transition, results in high loss of heat during caloric cooling cycles [7, 8]. Severe hysteresis loss can lead to a dramatic degradation of caloric response versus refrigeration cycles. Therefore, these parasitic losses at the material level must be minimized as much as possible for practical device design [4–6]. It was reported that the magnetic hysteresis loss can be reduced by using hydrostatic pressure [11] or electric field [12] thanks to the cross-response of magnetocaloric materials. However, questions remain regarding this approach: is the magnetic hysteresis loss really reduced or simply transferred into other form i.e. mechanical loss? If the later case dominates, is this mechanical loss important enough to prevent potential cooling applications?

3.) A giant magnetocaloric effect was discovered near room temperature in near-equiatomic FeRh alloys [13] some years before the benchmark study in $\text{Gd}_5\text{Si}_2\text{Ge}_2$ [9] that launched the field. However, FeRh has attracted significantly less interest in cooling applications mainly due to irreversibility in magnetocaloric cycles associated with the large hysteresis of its first-order metamagnetic phase transition [14]. This irreversibility has been for instance believed to be the key drawback for consideration of FeRh alloy as magnetocaloric cooler for almost 26 years. One may concern: could it be possibly overcome or not?

4.) Multicaloric effect [8, 10] can exploit multiple sources of entropy and be driven by multiple stimuli, however, it has yet to be realized, and its advantage over conventional cycles is not clear.

5.) The first breakthrough in electrocaloric effect was achieved in antiferroelectric thin films of $\text{PbZr}_{0.95}\text{Ti}_{0.05}\text{O}_3$ in 2006 (Ref. [15]). One natural question may concern about the effect of film thickness, depolarizing field, and electrode materials on the electrocaloric effect, which is still not clear.

6.) Interestingly and unexpectedly, recent experimental studies showed that relaxor ferroelectrics [16] and antiferroelectric ceramics [17] may permit a negative electrocaloric effect: materials cool when an electric field is applied, whereas they warm when the field is withdrawn. This unusual effect may enlarge the electrocaloric family and enhance the cooling efficiency in combination with conventional (positive) electrocaloric effect. Nevertheless, the mechanism underlying the negative electrocaloric effect is still elusive, and recent findings in the literature appear controversial.

7.) One open question still remains in searching for novel caloric materials in ferroic family: is there any overlooked ferroic member which can permit giant caloric effects? For instance, martensitic shape memory alloys are most intensively studied and promising elastocaloric materials due to reversible solid-to-solid martensitic-like phase transition [18]. Can ferroelectric also hold giant elastocaloric effect [19]? As the size of current shape-memory alloys shrinks towards the nano-scale, numerous problems and instabilities arise, including fatigue, micro-cracking and oxidation [20]. In this regard, ferroelectric thin films may have potential advantages if large elastocaloric effect exists in these thin films. Similar exploration of barocaloric effect in ferroelectric is also ambitious since it is known that ferroelectrics usually show strong pressure dependence of transition temperature [21]. Ferroelectric barocaloric may widen the barocaloric family as barocaloric effect is often related to a property of some magnetic materials.

8.) Although heat flux in a specific material/device is of great importance to the design of devices, electrocaloric heat flow behavior is generally unknown.

All these challenges and open questions are obviously of importance and thus motivated this PhD research work: *Multicaloric effect in ferroic materials*. The manuscript is organized in the following way:

The first chapter Chapter 1 on *Fundamentals of solid-state caloric effect*, basic caloric thermodynamic potentials are presented and described. Brief information is also provided about history of solid-state calorics, ferroic materials, indirect and direct measurements, multicaloric effect, thermodynamic refrigeration cycles and caloric parameters.

Chapter 2 is a comprehensive summary and careful reexamination of electrocaloric measurement approaches to justify the assumptions used in different measurement techniques. It is dedicated to cover recent important and rapid advances from both the indirect and direct measurements and provides critical insights relevant for quantifying electrocaloric effect.

Chapter 3 on *Electrocaloric effect in ferroelectrics and antiferroelectrics* introduces different electrocaloric materials in terms of material forms and types. Three typical materials: ultrathin ferroelectric thin films, antiferroelectric La-doped $\text{Pb}(\text{ZrTi})\text{O}_3$ thin films and lead-free $\text{BaTi}_x\text{Sn}_{1-x}\text{O}_3$ ceramics are highlighted and presented with their basic thermodynamic properties. This chapter provides detailed answers to aforementioned Challenges 2, 5 and 6.

Chapter 4 on *Spatially resolved imaging of electrocaloric effect and the resultant heat flux in multilayer capacitors using infra-red camera* is dedicated to provide direct electrocaloric measurement results in electrocaloric prototype device using infra-red camera both temporally and spatially. The distribution of electrocaloric response and direction of electrocaloric heat flux are directly imaged in this chapter. In addition, the frequency dependence of electrocaloric properties in multilayer capacitors is also included. This chapter therefore experimentally responds to aforementioned open questions in Challenge 8.

Chapter 5 and Chapter 6 theoretically respond to aforementioned open questions in Challenge 7.

Chapter 5 deals with *Elastocaloric effect in ferroelectrics*, which predicts that both ferroelectric thin films and single crystals can actually have large elastocaloric effect, which is comparable to their electrocaloric effect.

Chapter 6 devoted to *Barocaloric effect in ferroelectrics*, which predicts giant barocaloric effect in ferroelectric single-crystal BaTiO_3 near room temperature. In addition, pressure-

mediated electrocaloric effect in BaTiO₃ single crystals is also discussed.

Finally, Chapter 7 on *Multicaloric effect in FeRh/BaTiO₃ heterostructure*, which gives an experimental solution to aforementioned Challenges 1-4. A novel dual-stimulus magnetic-electric refrigeration cycle to overcome the irreversibility in magnetic FeRh thin films via coupling to a ferroelectric BaTiO₃ substrate is proposed and realized. This multicaloric cycle can experimentally yield larger reversible caloric effects than either stimulus alone. The magnetic hysteretic losses appear at first to be almost fully reduced (by 96%), but we show the losses are simply transferred into an elastic cycle, contrary to common belief [8, 11]. In addition, purely electric-field driven caloric effect in hybrid magnetoelectric heterostructure is also addressed, which shows great promise in overcoming especially the Challenge 1.

In end, Chapter 8 on *Conclusion and perspectives* summarize the main conclusion of this thesis and provides perspectives for further studies.

- CHAPTER 1 -

FUNDAMENTALS OF SOLID-STATE CALORIC EFFECT

1.1 BRIEF SUMMARY OF HISTORY ABOUT SOLID-STATE CALORIC EFFECTS

As stated in the Introduction, the search for alternative solid-state refrigeration materials to hazardous gases in conventional and cryogenic cooling devices is one of the most active fields of condensed matter and material science. We briefly summarize the events in the history of magnetocaloric effect (Table. 1.1), electrocaloric effect (Table. 1.2), elastocaloric effect (Table. 1.3), and barocaloric effect (Table. 1.4). It is shown that elastocaloric effect is the oldest-known ferroic caloric effect: John Gough from England detected it in Indian rubber (a shape memory polymer) in 1805 (Ref. [53]). Then the French and Swiss physicists Weiss and Piccard [22] and rather Warburg [81] discovered the magnetocaloric effect in nickel in 1917. This important historical fact who discovered the magnetocaloric effect was recently clarified by Smith [82]. 13 years later, the electrical analog to magnetocaloric effect, the electrocaloric effect was firstly found in Rochelle salt by Kobeko and Kurchatov [37]. The last caloric family member called barocaloric effect was described and experimentally verified in rare-earth compound $\text{Pr}_{1-x}\text{La}_x\text{NiO}_3$ in 1998 (Ref. [67]).

Table 1.1: Events in the history of magnetocaloric effect (MCE).

| Year | Events | Refs |
|------|---|------|
| 1917 | Discovery of MCE in nickel near the Curie temperature | [22] |
| 1926 | Fundamental principle of adiabatic demagnetization by Debye | [23] |
| 1927 | Fundamental principle of adiabatic demagnetization by Giauque | [24] |
| 1933 | Cryogenic MCE was experimentally proven by Giauque and MacDougall | [25] |
| 1935 | Discovery of ferromagnetism in gadolinium | [26] |
| 1976 | Magnetic heat pumping near room temperature based on gadolinium | [27] |
| 1982 | Active magnetic regenerator patented by Barclay and Steyert | [28] |
| 1990 | Discovery of giant room-temperature MCE in $\text{Fe}_{49}\text{Rh}_{51}$ | [13] |
| 1997 | Report of large MCE in perovskite-type manganese oxides | [29] |
| 1997 | Giant MCE in $\text{Gd}_5\text{Si}_2\text{Ge}_2$ near room temperature | [9] |
| 2001 | Giant room-temperature MCE of $\text{MnAs}_{1-x}\text{Sb}_x$ | [30] |
| 2001 | Discovery of giant room-temperature MCE in $\text{Ni}_{52.6}\text{Mn}_{23.1}\text{Ga}_{24.3}$ | [31] |
| 2002 | Giant room-temperature MCE reported in $\text{MnFeP}_{0.45}\text{As}_{0.55}$ | [32] |
| 2003 | Reduction of hysteresis losses in $\text{Gd}_5\text{Si}_2\text{Ge}_2$ by the addition of iron | [32] |
| 2003 | Giant room-temperature MCE in $\text{La}(\text{Fe}_x\text{Si}_{1-x})_{1.3}\text{H}_y$ | [33] |
| 2005 | Giant negative MCE in $\text{Ni}_{50}\text{Mn}_{37}\text{Sn}_{13}$ at room temperature | [34] |
| 2010 | Giant room-temperature MCE in $\text{MnCoGeB}_{0.02}$ | [35] |
| 2012 | Giant MCE driven by structural transitions in $\text{Ni}_{45.2}\text{Mn}_{36.7}\text{In}_{13}\text{Co}_{5.1}$ | [11] |
| 2013 | Giant extrinsic MCE in $\text{La}_{0.7}\text{Ca}_{0.3}\text{MnO}_3$ films due to strain | [36] |
| 2014 | Electric field control of the MCE in $\text{Ni}_{44}\text{Mn}_{36.7}\text{In}_{14.1}\text{Co}_{5.2}$ | [12] |

Table 1.2: Events in the history of electrocaloric effect (ECE).

| Year | Events | Refs |
|------|---|----------|
| 1930 | First report of ECE in Rochelle Salt by Kobeko and Kurchatov | [37] |
| 1956 | First cryogenic electrocaloric concept proposed in SrTiO ₃ ceramics | [38] |
| 1961 | First measurement on cryogenic ECE in SrTiO ₃ and CdTiO ₃ ceramics | [39] |
| 1962 | Largest ECE found at Curie Temperature | [40] |
| 1963 | Quantitative measurement of ECE in Rochelle Salt | [41] |
| 1968 | ECE measured in doped-PZT | [42] |
| 1979 | First cryogenic electrocaloric refrigerator concept | [43] |
| 1981 | ECE in Pb _{0.99} Nb _{0.02} (Zr _{0.75} Sn _{0.20} Ti _{0.05})O ₃ ceramics | [44] |
| 2002 | ECE in PbSc _{0.5} Ta _{0.5} O ₃ ceramics | [45] |
| 2006 | Discovery of giant ECE in PbZr _{0.95} Ti _{0.05} O ₃ thin films | [15] |
| 2008 | Report of large ECE in P(VDF-TrFE) thin films | [46] |
| 2010 | First negative ECE measured in relaxor ferroelectrics | [16] |
| 2011 | Negative ECE reported in antiferroelectric ceramics | [17] |
| 2012 | First report of ECE in ultrathin ferroelectric films | [47] |
| 2013 | Giant electrocaloric strength in single-crystal BaTiO ₃ | [48] |
| 2014 | Bridging EsCE and ECE by mechanical stress in ferroelectrics | [49, 50] |
| 2015 | Giant negative ECE in antiferroelectric thin films | [51] |
| 2015 | Colossal ECE in ferroelectric polymer nanocomposites | [52] |

Table 1.3: Events in the history of elastocaloric effect (EsCE).

| Year | Events | Refs |
|------|---|----------|
| 1805 | First recorded evidence of EsCE found in India rubber | [53] |
| 1855 | Thermodynamic interpretation of thermoelastic properties of matter | [54] |
| 1859 | EsCE observed in some metals and dry woods | [55] |
| 1957 | EsCE termed as piezocaloric effect in textbook by Nye | [56] |
| 1980 | Thermal effect in Cu-based alloy | [57] |
| 1985 | Thermal effect in Ni-Ti-based alloy | [58] |
| 1992 | First EsCE in Fe ₄₉ Rh ₅₁ alloy proposed for cooling applications | [59] |
| 2004 | EsC refrigeration concept using Ni-Ti-based alloy proposed | [60] |
| 2008 | EsCE of Cu-based shape-memory alloy | [61] |
| 2012 | Demonstration of high efficiency EsC cooling using NiTi wires | [62] |
| 2012 | Prediction of giant EsCE in ferroelectric Ba _{0.5} Sr _{0.5} TiO ₃ alloys | [19] |
| 2013 | Significant EsCE was detected in a Fe-31.2Pd (at. %) single crystals | [63] |
| 2014 | Prediction of giant EsCE in ferroelectric ultrathin films | [50] |
| 2015 | Prediction of giant elastocaloric strength in BaTiO ₃ single crystals | [64] |
| 2015 | Demonstration of EsCE in ferroelectric ceramics and relaxors | [65, 66] |

Table 1.4: Events in the history of barocaloric effect(BCE).

| Year | Events | Refs |
|------|--|------|
| 1998 | Concept of barocaloric cooling proposed in rare-earth compound | [67] |
| 2003 | Direct measurements on BCEs in rare-earth compounds | [68] |
| 2010 | Discovery of giant BCE in magnetic shape-memory alloy | [69] |
| 2010 | BCE reported in magnetocaloric manganites | [70] |
| 2011 | Negative BCE in La-Fe-Si-Co compound | [71] |
| 2011 | BCE reported in $\text{Rb}_x(\text{NH}_4)_{1-x}\text{HSO}_4$ ferroelectric solid solutions | [72] |
| 2011 | Possible concept of device using barocaloric cooling | [73] |
| 2012 | BCE in the magnetocaloric prototype $\text{Gd}_5\text{Sr}_2\text{Ge}_2$ | [74] |
| 2012 | BCE investigated in ferroelectric PbTiO_3 ceramics | [75] |
| 2014 | Prediction of giant BCE in BaTiO_3 single crystals | [76] |
| 2014 | Discovery of giant BCE in frustrated itinerant antiferromagnet | [77] |
| 2014 | Discovery of giant BCE in FeRh alloy | [78] |
| 2015 | Giant BCE at low pressure in ferrielectric ammonium sulphate | [79] |
| 2016 | Report on BCE in Polyvinylidene di-fluoride-based polymers | [80] |

There is no deny that magnetocaloric effect is the superstar among the caloric family. It has shown great success in cryogenic applications (see Table. 1.1). Suggested independently by Debye [23] and Giauque [24], adiabatic demagnetization method was proposed to achieve the temperatures below one kelvin. Several years later, Giauque and MacDougall successfully employed this method to produce temperatures near absolute zero [25]. This great contribution earned Giauque the Nobel Prize in chemistry for his low-temperature studies. To date, this cryogenic technology is still used in scientific laboratories to produce millikelvin temperatures. Room-temperature magnetocaloric cooling applications are stimulated by Karl A. Gschneidner, Jr. and Vitalij K. Pecharsk in 1997 who discovered giant magnetocaloric effect near 276 K in a first-order phase transition material called $\text{Gd}_5\text{Si}_2\text{Ge}_2$ alloy better than the Gd with second-order phase transition [9]. This is widely accepted as a milestone in the field of magnetocaloric effect [4, 6, 8]. Surprisingly, a giant room-temperature magnetocaloric effect has already been reported in $\text{Fe}_{49}\text{Rh}_{51}$ by Soviet scientists in 1990 (Ref. [13]). The first-order phase transition was reported near 308 K in $\text{Fe}_{49}\text{Rh}_{51}$ [13] which is nearer to room temperature compared to $\text{Gd}_5\text{Si}_2\text{Ge}_2$ [9]. Moreover, the magnetocaloric parameters in $\text{Fe}_{49}\text{Rh}_{51}$ are more competitive than those in $\text{Gd}_5\text{Si}_2\text{Ge}_2$ [14]. As the magnetic field favours the ferromagnetic phase, the sign of magnetocaloric effect is negative, which means adiabatic application of external magnetic field will lead to cooling of FeRh. This negative magnetocaloric effect is also larger than that in ferromagnetic Ni-Mn-Sn alloys [34] while the later was regarded as a significant breakthrough. The impressive caloric response in FeRh is due to its sharp first-order phase transition from antiferromagnetic phase to ferromagnetic phase. However, it is also this sharp metamagnetic transition associated a broad thermal hysteresis that leads to the irreversibility of the magnetocaloric effect with regard to alternating magnetic field [9, 14]. This is one main reason why

$\text{Fe}_{49}\text{Rh}_{51}$ was considered useless in cooling applications for almost 26 years. Indeed, the issue of relative large thermal hysteresis in $\text{Gd}_5\text{Si}_2\text{Ge}_2$ was addressed in 2003 by Provenzano *et al.* [83] who demonstrated a significant reduction (by more than 90 per cent) of the hysteretic losses by doping of Fe. Nevertheless, the significance of work on $\text{Gd}_5\text{Si}_2\text{Ge}_2$ was undoubtedly realized during 1990s and 2000s and thus stimulated enthusiastic research activities.

The investigations on electrocaloric effect can be dated back to 1930 (Ref. [37]). However, it did not attract much attention for quite a long time because this effect is too small to be of interest for practical cooling applications [5, 8, 84] (see Table. 1.2). For instance, many studies related to ferroelectric/antiferroelectric ceramics emerged since 1930 while the best electrocaloric effect data yielded an adiabatic temperature change of less 2.5 K in $\text{Pb}_{0.99}\text{Nb}_{0.02}(\text{Zr}_{0.75}\text{Sn}_{0.20}\text{Ti}_{0.05})\text{O}_3$ ceramics in 1981 (Ref. [44]). Later, a modest electrocaloric effect of ~ 2.4 K was reported in $\text{PbSc}_{0.5}\text{Ta}_{0.5}\text{O}_3$ ceramics in 2002 (Ref. [45]). We have to wait for 2006 when a Science paper [15] inspired both fundamental physics and exciting device applications for electrocaloric effect. Indeed, Mischenko *et al.* reported a giant electrocaloric effect with an adiabatic temperature change of 12 K in antiferroelectric $\text{PbZr}_{0.95}\text{Ti}_{0.05}\text{O}_3$ ceramic thin films under a high electric field of 780 kV/cm (Ref. [15]). Two years later, another breakthrough was reported with a giant electrocaloric effect in organic P(VDF-TrFE) thin films [46]. More recently, it is found that mechanical stress can act as a bridge to bring both electrocaloric and elastocaloric effects work either simultaneously [49] or sequentially [50]. It is usually expected that applying an electric field on any dielectric material results in the ordering of electrical dipoles and therefore this process should always be accompanied by the heating of the material in adiabatic conditions. This physical image was changed since negative electrocaloric effect was found in relaxor ferroelectric [16] and antiferroelectric ceramics [17]. The magnitude of the negative electrocaloric effect can be enhanced in antiferroelectric thin films [51]. Together, both positive and negative electrocaloric effect can coexist in antiferroelectrics depending on the magnitude of applied electric field [51]. Most excitingly, a colossal electrocaloric effect was reported very recently in ferroelectric polymer nanocomposites taking advantage of the significantly enhanced breakdown field [52]. The electrocaloric properties of nanocomposites even surpasses those of the recently reported giant magnetocaloric effect, which demonstrates the promising role of electrocaloric effect in next-generation refrigeration.

Elastocaloric/barocaloric refrigeration is similar to conventional vapor-compression type since they both use stress/pressure to induce a phase transition and achieve cooling thanks to latent heat of phase transition. The main difference lies in the form of the refrigerant. It is liquid/vapor for vapor-compression refrigeration, and solid/solid for elastocaloric and barocaloric cooling. Although the elastocaloric effect is the oldest-known caloric member [53], its real scientific research was initialized from the studies on thermal effect related to stress-induced martensite formation in shape-memory alloys [57, 58] (see Table. 1.1). However, these studies simply concentrated on the origin of thermal effects without consideration of issues associated with cooling applications [6]. The first experimental evidence on the giant elastocaloric effect was reported in 1992 (Ref. [59]). Interestingly, once again it is $\text{Fe}_{49}\text{Rh}_{51}$. Nikitin *et al.* reported the maximal elastocaloric temperature change of about -8.7 K while the maximal isothermal entropy change is about 12 J/kg K under a tensile stress of 529 MPa [59]. The entropy changes induced by stress and magnetic fields have both a positive sign, indicating negative elastocaloric and mag-

netocaloric effects in $\text{Fe}_{49}\text{Rh}_{51}$ alloys. In other words, applying a tensile stress or magnetic field adiabatically will cool the sample down. It was reported that the elastocaloric effect in $\text{Fe}_{49}\text{Rh}_{51}$ alloys is mainly due to the electronic entropy change during the antiferromagnetic-ferromagnetic transition but not the contribution by magnetoelastic interaction [85]. The transition is very sharp resulting in an extremely narrow operational temperature window (<10 K). The maximal driving stress is nearly twice as that used in shape memory alloys. Indeed, stimulated by 2008 PRL paper [61], ferroelastic shape memory alloys are the most intensively studied and promising elastocaloric materials due to their excellent superelasticity and broad operational temperature window [18]. For instance, for Ni-Ti alloys, the largest elastocaloric temperature change was reported as 25.5 K and 17 K for heating and cooling process, respectively [62]. They estimated the coefficient of performance (*COP*) of 56.5% and 83.7% of the Carnot cycle values for tension and compression, which represents the second highest among all the solid-state based cooling technologies [62]. Moreover, issue of fatigue has also attracted considerable attention [86].

Ferroelastic ferroelectric bulk [19, 49] and thin films [50] were predicted to have remarkable elastocaloric properties comparable with ferroelastic martensites, which further expands the elastocaloric family. The giant elastocaloric effect predicted in ferroelectric materials including bulk and thin films may open an alternative direction to search suitable elastocaloric materials for desired device applications. External stress or electric field may also find opportunities to tune the electrocaloric effect or elastocaloric effect due to strong coupling between strain and polarization in ferroelectrics [19, 49, 50]. Interestingly, experimental demonstration of elastocaloric effect in ferroelectric ceramics [65] and relaxors [66] has been reported very recently.

Barocaloric effect is the youngest in the caloric family and was often regarded as a property of magnetic materials. This can be seen more clearly in Table 1.4 showing that the very first barocalorics are all magnetic materials. More recently, large barocaloric effects were found in Ni-Mn-In magnetic shape-memory alloy [69], magnetocaloric prototype $\text{Gd}_5\text{Sr}_2\text{Ge}_2$ [74], frustrated itinerant antiferromagnet Mn_3GaN [77] and FeRh [78]. In addition, large negative barocaloric effect was reported in magnetocaloric La-Fe-Si-Co compound [71]. Interestingly, barocaloric effect has also attracted attention in ferroelectric community. For instance, barocaloric effect was studied in $\text{Rb}_x(\text{NH}_4)_{1-x}\text{HSO}_4$ ferroelectric solid solutions and ferroelectric PbTiO_3 ceramics [72]. However, the magnitude is too small ($\ll 1$ K). More efforts need to be made to enhance the barocaloric response as highlighted by recent theoretical predictions in BaTiO_3 single crystals [76]. Experimentally, recent findings demonstrated the noticeable barocaloric effect in ferroelectric ammonium sulphate [79] and polyvinylidene di-fluoride-based polymers [80]. Research in barocaloric effect is actually at a very early stage. Barocaloric refrigeration process was only conceptually suggested [73] and many technical problems have to be solved before a real prototype is built.

As a summary, research in magnetocaloric effect in terms of scientific publications and prototype heat pump devices is more mature than other ferroic caloric effects. Its application on cryogenic technology helped Giauque to win the Nobel Prize and room-temperature applications are now close to be realized [4, 6]. All the other caloric effects appear promising, though their research is still on the early stage. For instance, the application of giant electrocaloric effect is not limited to on-chip cooling or other nano-electronics embodiments as proposed originally in thin films [15, 46]. Electrocaloric cooling will be probably limited to situations with small temperature

ranges and modest cooling rates and loads. However, their other attributes such as low power (voltage < 25 V), inexpensive components and modest size may be advantageous. For instance, there are also other products where constant but modest temperatures are required: transplant organs for surgery must be transported long distances and neither frozen nor allowed to warm but kept at a constant temperature, e.g., ~ 4 °C. Other applications exist where size, weight, and power consumption are paramount, such as refrigerant-free devices in commercial satellites. In general it is useful to keep in mind that medical applications and aerospace or aircraft devices involve different priorities for performance parameters. Moreover, while magnetocalorics and bulk electrocalorics, elastocalorics or barocalorics require large external stimuli, here these giant electrocaloric and elastocaloric thin films only need significantly smaller stimuli to operate.

1.2 BRIEF INTRODUCTION TO FERROIC MATERIALS

Phase transitions are a powerful tool to achieve giant caloric effects in ferroic materials in which the generalized displacements (magnetization, polarization, strain, and volume) can be strongly tuned under a moderate external stimulus [7, 8, 18]. As a result, caloric effects concern a broad family including ferroelectrics/antiferroelectrics, ferromagnetic/antiferromagnetic/magnetic materials, ferroelastics/martensitic shape-memory alloys, and multiferroics subjected to a moderate magnetic field (magnetocaloric effect), electric field (electrocaloric effect), hydrostatic pressure (barocaloric effect), or uniaxial stress (elastocaloric effect). In particular, we mainly focus on ferroic materials in this manuscript. Ferroic materials can be divided into four different families depending on their symmetry properties with respect to time reversal and space inversion (see Table 1.5). Ferroic order parameter (magnetization, polarization, deformation and toroidal moment) can be switched from two opposite values by the application of a magnetic field, electric field, strain and source vector, respectively [87].

Ferromagnetics refer to materials which exhibit spontaneous magnetization (ferromagnetism). Typical ferromagnetic magnetocaloric is the well-known gadolinium (Gd) with its second-order phase transition [88]. The Curie temperature indicating the transition from ferromagnetic phase to paramagnetic phase is at room temperature (~ 294 K) for gadolinium [88]. Therefore, gadolinium is regarded as a kind of reference material due to the large magnetization. First-order magnetic transition, such as antiferromagnetic/ferromagnetic [13], ferromagnetic/ferromagnetic [9], ferromagnetic/paramagnetic [33] and so on, has been demonstrated to be of great use to achieve remarkably enhanced magnetocaloric response. It stimulates a upsurge to search and design a magnetic material with its phase transition temperature close to room temperature. Efforts should also be made to ensure that magnetocalorics have a hysteresis as small as possible in order to maintain the high performance and efficiency of magnetocaloric refrigeration [4, 6].

According to the definition of ferroelectricity, the spontaneous polarization of the ferroelectric materials is switchable under an ac electric field [89]. The term of ferroelectricity was originally used in analogy to ferromagnetism as both materials exhibit hysteresis behavior. Ferroelectricity was first discovered in Rochelle salt in 1920 (Ref. [90]) and accordingly the electrocaloric effect was found in the same material ten years later [37]. Ferroelectrics are usually considered to be prime candidates for electrocaloric cooling applications [5] since ferroelectrics undergo a phase

Table 1.5: Four primary ferroic orders in ferroic family

| Ferroic | Order parameter | External stimulus | IS ^{a)} | TRS ^{b)} |
|---------------|-----------------|-------------------|------------------|-------------------|
| Ferromagnetic | magnetization | magnetic field | preserved | broken |
| Ferroelectric | polarization | electric field | broken | preserved |
| Ferroelastic | deformation | strain | preserved | preserved |
| Ferrotoroidic | toroidal moment | source vector | broken | broken |

^{a)}IS indicates Inversion symmetry while ^{b)}TRS indicates Time-reversal symmetry.

transition from a high-temperature paraelectric phase with high-symmetry to a low-symmetry polarized phase at low temperature, accompanied by a remarkable change in the polarization either in a continuous manner (second-order phase transition) or discontinuous way (first-order phase transition). Antiferroelectric materials are also attractive for electrocaloric cooling applications as the first breakthrough in the field of electrocaloric effect was reported in antiferroelectric thin films [15]. However, the phase transition from antiferroelectric phase to ferroelectric phase was deliberately avoided by applying a large electric field in this work [15]. Indeed, even the definition of antiferroelectricity is elusive [91] and therefore is not discussed here. In addition, relaxor ferroelectrics [92] are receiving considerable attention and electric field-induced relaxor-ferroelectric phase transition and so-called polar nanoregions play an important role in determining the electrocaloric properties in relaxor [5].

Ferroelastics are materials that exhibit hysteretic stress-strain relationships [93]. Most ferroelectrics are also ferroelastic. Exceptions such as KTiOPO_4 are non-ferroelastic ferroelectrics because they do not change crystal class at their ferroelectric-paraelectric transitions; e.g., for KTiOPO_4 the transition is orthorhombic-orthorhombic. Conversely, many ferroelastics are not ferroelectric [94]. Good examples are the rare-earth pentaphosphates MP_5O_{14} ($\text{M}=\text{La}, \text{Nd}, \text{Pr} \dots \text{Tb}$) [95, 96]. One of the best pure ferroelastics for possible cooling devices near room temperature is probably $\text{LaP}_5\text{O}_{14}$ [97], because (1) miniscule stresses are required for its orthorhombic-monoclinic transition; (2) this material is cheap and non-toxic; and (3) no cracking will occur during cycles and the transition is of second order. Note that the transition of $\text{LaP}_5\text{O}_{14}$ is displacive and not order-disorder, which however entails a smaller entropy change [97]. Ferroelastic martensites as mentioned above are regarded as the most promising elastocaloric materials. Considering classical ferroelectric materials, e.g., BaTiO_3 [19] and PbTiO_3 [49], are extrinsic ferroelastics in which ferroelastic behavior is driven by the ferroelectric one. As a result, an appreciable elastocaloric effect can be only observed in the ferroelectric phase of the material. Indeed, recent first-principle calculations predicted that $\text{BaSr}_{0.5}\text{Ti}_{0.5}\text{O}_3$ solid solutions [19] and PbTiO_3 bulk [49] show comparable elastocaloric effect (> 10 K) under a high tensile stress field over 1 GPa, which is in the same range of temperature change for ferroelastic martensites.

We note that ferroelectric switching retains good potential for electrocaloric devices. However, ferroelastic switching is quite subtle and qualitatively different from that in pure ferroelectrics (such as KTiOPO_4). To be ferroelastic, as shown by Toledano in 1974 (Ref. [94]), the crystal class must change at the transition (treating hexagonal and rhombohedral as a “superclass” and

Laue type I and Laue type II tetragonals as different). The important thing is that the high- and low-temperature phases must have different non-zero piezoelectric tensor elements, e.g. C_{16} in the case of Laue Types I and II. In addition, ferroelastic switching from $+\sigma_3$ to $-\sigma_3$ (where σ_3 is stress) is glassy, with extremely complex transient domain structures. This causes violation of the Kittel relationship between thickness and domain width, and curved walls. Such “domain glasses” can possess large entropies and hence should be explored further.

Multiferroics refer to a relatively rare class of multifunctional materials that simultaneously exhibit several ferroic orders among ferromagnetic/antiferromagnetic, ferroelectric and ferroelastic and ferrotoroidic [87, 98]. Naturally, coexistence of several caloric effects is expected in multiferroics. The promise of multiferroic in caloric cooling applications (multicaloric effect) is the potential to take advantage of the multiple forms of the entropy. For instance, the elastocaloric effect can coexist or even couple with the intrinsic electrocaloric effect in the same ferroelectric material [19, 49]. Indeed, enhanced electrocaloric effect under hydrostatic pressure/uniaxial stress was reported in relaxor ferroelectrics [99] and LiNbO_3 [100]. Moreover, the multicaloric effect with stress and electric fields applied simultaneously was found to far exceed either single caloric effect in PbTiO_3 [49]. Therefore, combining mechanically- and electrically-induced phase transitions properly is feasible to obtain improved caloric properties in ferroelectrics [50]. More importantly, given that multiferroics may allow strong coupling between different ferroic orders, this opens a novel route to optimize the multicaloric effect. In this regard, we pay our attention to magnetoelectric multiferroic materials [101] and heterostructures [102] which were intensively studied during the last decade. It is known that magnetoelectric effect in single-phase multiferroics is too small and cannot be comparable to that in composite compounds or heterostructures. For instance, the largest magnetoelectric coupling was reported in hybrid $\text{FeRh}/\text{BaTiO}_3$ heterostructure [103], which is larger than previous reports by at least one order of magnitude. Recalling the history of caloric effect, FeRh is extremely unique: it is the first-order magnetocaloric material reported to have a giant magnetocaloric effect [13] while it is also the first material to demonstrate the elastocaloric cooling [59]. In addition, it is also a giant barocaloric material [78]. However, as addressed before, FeRh attracted almost no interest due to large hysteresis accompanied by the first-order phase transition [14]. We will revisit the magnetocaloric effect in FeRh and try to solve this roadblock on the way to practical application of FeRh in Chapter 7.

1.3 THERMODYNAMICS OF CALORIC EFFECTS

According to the first law of thermodynamics, the internal energy dU in a crystal is given by

$$dU = dW + dQ, \quad (1.1)$$

where dW , which is a small amount of work done per unit volume in changing the magnetization by small amounts dM (3 components) and/or altering the electric displacements by small amounts dD (3 components), and/or changing the strains by small amounts du (9 components) [or altering volume by small amounts dV (1 component)], is given by

$$dW = \mu_0 H dM + E dD + \sigma du \{-pdV\}, \quad (1.2)$$

where H (3 components) is the magnetic field, E (3 components) is the electric field, σ (9 components) is the stress and p is the hydrostatic pressure (1 component). By the second law of thermodynamics, for a reversible change, a small amount of heat dQ flowing into the crystal can be expressed as

$$dQ = TdS, \quad (1.3)$$

where T is the temperature and S is the entropy. Hence Eq. (1.1) becomes

$$dU = \mu_0 HdM + EdD + \sigma du\{-pdV\} + TdS. \quad (1.4)$$

Instead of the function U , which is convenient for independent variables $[M, D, u, (V), S]$, a new and more useful function Φ (Legendre transformation) can be defined by

$$\Phi = U - \mu_0 HM - ED - \sigma u\{+pV\} - TS. \quad (1.5)$$

Then, by differentiating and using Eq. (1.4),

$$d\Phi = -\mu_0 MdH - DdE - u d\sigma\{+Vdp\} - SdT. \quad (1.6)$$

Since Φ is a function of state defined by independent variables $[H, E, \sigma, (p), T]$, it follows that

$$\frac{1}{\mu_0} \left(\frac{\partial \Phi}{\partial H} \right)_{T, E, \sigma(p)} = -M, \quad (1.7)$$

$$\left(\frac{\partial \Phi}{\partial E} \right)_{T, H, \sigma(p)} = -D, \quad (1.8)$$

$$\left(\frac{\partial \Phi}{\partial \sigma} \right)_{T, H, E} = -u, \quad (1.9)$$

$$\left(\frac{\partial \Phi}{\partial p} \right)_{T, H, E} = V, \quad (1.10)$$

$$\left(\frac{\partial \Phi}{\partial T} \right)_{H, E, \sigma(p)} = -S. \quad (1.11)$$

Differentiating Eqs. (1.7)-(1.11), the Maxwell relations can be derived.

$$-\frac{1}{\mu_0} \left(\frac{\partial^2 \Phi}{\partial H \partial T} \right)_{E, \sigma(p)} = \left(\frac{\partial M}{\partial T} \right)_H = \frac{1}{\mu_0} \left(\frac{\partial S}{\partial H} \right)_T, \quad (1.12)$$

$$-\left(\frac{\partial^2 \Phi}{\partial E \partial T} \right)_{H, \sigma(p)} = \left(\frac{\partial D}{\partial T} \right)_E = \left(\frac{\partial S}{\partial E} \right)_T = p_{pyro}, \quad (1.13)$$

$$-\left(\frac{\partial^2\Phi}{\partial\sigma\partial T}\right)_{H,E} = \left(\frac{\partial u}{\partial T}\right)_\sigma = \left(\frac{\partial S}{\partial\sigma}\right)_T = \alpha, \quad (1.14)$$

$$-\left(\frac{\partial^2\Phi}{\partial p\partial T}\right)_{H,E} = -\left(\frac{\partial V}{\partial T}\right)_p = \left(\frac{\partial S}{\partial p}\right)_T = -\alpha V, \quad (1.15)$$

$$-\left(\frac{\partial^2\Phi}{\partial\sigma\partial E}\right)_T = \left(\frac{\partial u}{\partial E}\right)_\sigma = \left(\frac{\partial D}{\partial\sigma}\right)_E = d_{pizo}, \quad (1.16)$$

$$-\frac{1}{\mu_0}\left(\frac{\partial^2\Phi}{\partial M\partial E}\right)_T = \left(\frac{\partial M}{\partial E}\right)_H = \frac{1}{\mu_0}\left(\frac{\partial D}{\partial H}\right)_E = \frac{1}{\mu_0}\alpha_{ME}. \quad (1.17)$$

These relations establish the facts:

- (i) the coefficients for thermal expansion α are the same as those for the elastocaloric effect;
- (ii) the coefficients for the pyroelectric effect p_{pyro} are the same as those for the electrocaloric effect;
- (iii) the coefficients for the converse piezoelectric effect d_{pizo} are numerically equal to the ones for the direct effect;
- (iv) multicaloric effect [10] can be possible due to magnetoelectric coupling (α_{ME} is the magnetoelectric coupling coefficient).

The differential changes of the entropy $S_{H,E,\sigma,(p),T}$ can be described as follows

$$dS = \frac{C}{T}dT + \left(\frac{\partial S}{\partial H}\right)_T + \left(\frac{\partial S}{\partial E}\right)_T + \left(\frac{\partial S}{\partial\sigma}\right)_T\left\{-\left(\frac{\partial S}{\partial p}\right)_T\right\}, \quad (1.18)$$

where we have used the Maxwell relations [Eqs. (1.12)-(1.15)]. C is the volumic heat capacity of the system under constant fields H , E and σ , (p) through the relation $C = T\left(\frac{\partial S}{\partial T}\right)_{H,E,\sigma,(p)}$. As a result, the magnetocaloric entropy change ΔS_H upon application of a magnetic field in isothermal conditions can be determined by:

$$\Delta S_H = \mu_0 \int_0^H \left(\frac{\partial M}{\partial T}\right)_H dH. \quad (1.19)$$

Analogously, electrocaloric entropy change ΔS_E in response to isothermal application of an electric field is given by:

$$\Delta S_E = \int_0^E \left(\frac{\partial D}{\partial T}\right)_E dE. \quad (1.20)$$

Isothermal entropy change ΔS_σ due to elastocaloric effect can be determined by:

$$\Delta S_\sigma = \int_0^\sigma \left(\frac{\partial u}{\partial T}\right)_\sigma d\sigma. \quad (1.21)$$

Barocaloric entropy change ΔS_p in isothermal condition can be expressed as:

$$\Delta S_p = - \int_0^p \left(\frac{\partial V}{\partial T}\right)_p dp. \quad (1.22)$$

In addition to isothermal entropy change $\Delta S_Y(Y = H, E, \sigma, p)$ mentioned above, another caloric parameter named as adiabatic temperature change $\Delta T_Y(Y = H, E, \sigma, p)$ can be simply derived from Eq. (1.18) according to the adiabatic condition ($dQ=0$):

$$\Delta T_H = -\mu_0 \int_0^H \frac{T}{C_H} \left(\frac{\partial M}{\partial T} \right)_H dH, \quad (1.23)$$

$$\Delta T_E = - \int_0^E \frac{T}{C_E} \left(\frac{\partial D}{\partial T} \right)_E dE, \quad (1.24)$$

$$\Delta T_\sigma = - \int_0^\sigma \frac{T}{C_\sigma} \left(\frac{\partial u}{\partial T} \right)_\sigma d\sigma, \quad (1.25)$$

$$\Delta T_p = \int_0^p \frac{T}{C_p} \left(\frac{\partial V}{\partial T} \right)_p dp. \quad (1.26)$$

In particular, in ferroelectrics, the relation $D \sim P$ is usually met when the depolarizing field is negligible. Therefore, evaluating the electrocaloric effect using polarization P as the order parameter is widely used in the literature such that:

$$\Delta S_E = \int_0^E \left(\frac{\partial P}{\partial T} \right)_E dE, \quad (1.27)$$

$$\Delta T_E = - \int_0^E \frac{T}{C_E} \left(\frac{\partial P}{\partial T} \right)_E dE. \quad (1.28)$$

Eqs. (1.19)-(1.26) suggest that a noticeable caloric effect can be observed in materials for which the generalized displacements (M , D , u , V) depend strongly on the temperature. In general, strong temperature dependence of the generalized displacements is only observed near the phase transition. This is also the main reason why caloric effect is usually negligible when it is far away from the phase transition point [4–6]. It is worth mentioning that the key requirement for caloric effect to be giant is the existence of a first-order-like phase transition in most cases and the second-order-type phase transitions are always related to small or moderate caloric effects. Second-order-type phase transition is limited fundamentally by the modest change of the generalized displacements with temperature since the generalized displacements decay continuously to zero as the transition temperature is approached. On the contrary, the caloric effect is remarkably enhanced in materials undergoing discontinuous (first-order) phase transitions. Despite large caloric properties can be achieved near first-order transition, an appreciable thermal hysteresis is usually observed due to the large latent heat of transition. Moreover, these irreversibilities and/or nonequilibrium dissipative effects inevitably are detrimental for cooling applications as they can directly lead to heat losses in each cooling cycle. This obviously reduces the cooling efficiency of the material. In this regard, changing the phase transition from first order toward second order may eliminate the hysteresis completely. Therefore, it may be desired to search promising materials either whose transition is first-order with a very small hysteresis loss (second-order like phase transition) or with a second order transition while the caloric response could be still large enough for practical applications.

1.4 INDIRECT METHODS

According to Eqs. (1.19)-(1.26), one can calculate the caloric effects based on the data from the temperature dependence of the generalized displacements obtained either from theory or experiment [4–6]. This is a well-known indirect method mainly based on Maxwell relationships. Indeed, there is still debate on the validity of this method. This topic in the field of electrocalorics will be discussed in detail in Chapter 2.

In addition to indirect method based on Maxwell relationships, Clausius-Clapeyron method is also frequently used for only the first-order phase transition [8]. This approach represents a nominally equivalent indirect method as that based on Maxwell relationships. In this approach, the temperature dependence of equilibrium transition temperature T_0 and then values of entropy changes for the fully driven transition can be obtained using the Clausius-Clapeyron equation below, in which order parameter changes across first-order phase transitions is denoted by the subscript “0”.

$$\Delta S_H = -\mu_0 \Delta M_0 (dT_0/dH)^{-1}, \quad (1.29)$$

$$\Delta S_E = \Delta D_0 (dT_0/dE)^{-1}, \quad (1.30)$$

$$\Delta S_\sigma = -\Delta u_0 (dT_0/d\sigma)^{-1}, \quad (1.31)$$

$$\Delta T_p = \Delta V_0 (dT_0/dp)^{-1}. \quad (1.32)$$

The discontinuity in the entropy can be treated by using Clausius-Clapeyron equation. For instance, Mañosa *et al.* evaluated the effect of irreversible contributions associated with the first-order transition and modified the Clausius-Clapeyron equation as follow: [104]

$$\frac{dY}{dT} = -\frac{\Delta S}{\Delta T} + \frac{D}{\Delta x} \frac{dE_{diss}}{dT} \quad (1.33)$$

where E_{diss} is the dissipated energy which can be estimated as $E_{diss} = (Y - Y_0)\Delta x$, where Y_0 is the equilibrium transition field at temperature T . Δx is the discontinuity in the generalized displacement (e.g., u). If E_{diss} is assumed to be weakly dependent on temperature, and the last term in Eq. (1.33) is small, which suggests that Clausius-Clapeyron equation is still a good approximation. Moreover, they demonstrated that Eqs. (1.21) and (1.25) can be still valid especially in shape-memory alloys with small dissipative effects.

Finally, there are other indirect approaches called as quasidirect methods mainly including heat-capacity method and heat-flux method [8, 18]. These two methods are usually realized by modified differential scanning calorimetry.

For heat-capacity method, the key experimental data is the experimental dependence of heat capacity in initial Y_i and final fields Y_f ($Y = H, E, \sigma$ or p). Accordingly, the governing principle is given by: [8]

$$\Delta S(T, Y_f - Y_i) = \int_{T_i}^{T_f} \frac{C(T', Y_f) - C(T', Y_i)}{T'} dT'. \quad (1.34)$$

This method as simple as the one based on Maxwell relations is useful for rapid characterization of new materials. However, it only necessarily reproduces the intrinsic entropy change as long as the hysteresis of the transition is correctly taken into account in the experimental procedure. An alternative route to obtain the isothermal entropy is heat-flux method determined by: [18]

$$\Delta S(Y, T_f - T_i) = \int_{T_i}^{T_f} \frac{1}{T} \frac{Q(\dot{Y})}{\dot{T}} dT, \quad (1.35)$$

where \dot{Q} and \dot{T} are the heat flux and the cooling (or heating) rate, respectively. If the experiments are done at constant temperature by sweeping the external field, The field-induced entropy-change can be determined by:

$$\Delta S(T, Y_f - Y_i) = \frac{1}{T} \int_{Y_i}^{Y_f} \frac{Q(\dot{Y})}{\dot{Y}} dY, \quad (1.36)$$

where \dot{Y} is the field rate.

1.5 DIRECT MEASUREMENTS

Direct measurement means a direct determination of the temperature change of the sample when the external stimulus is applied/removed adiabatically [4–6]. Usually the direct measurements are implemented by using thermocouple, infra-red sensor/camera, scanning thermal microscopy and so on. The direct approach can inspire confidence for design of devices. However, in practical case there are several factors making it difficult to achieve the perfect adiabatical conditions. For instance, thermal isolation of the sample is the key factor. In ideal case, an instantaneous increase and decrease of the magnetic field should be met for measuring magnetocaloric effect, which is in contrast to the isothermal measurement carried out under nearly equilibrium conditions. However, in real measurements, it is usually required that the characteristic time constant for the application (or removal) of the field should be significantly smaller than the time constant for heat exchange between sample and ambient environment. This can be achieved in bulk in most cases but fails in thin films with substrates. Good thermal contact between the sample and the thermocouple is also required. Most importantly, reasonable calibration has always to be considered to compensate for unavoidable thermal losses during the measurements. Nevertheless, most experimental data reported in the literature are obtained by homemade instruments and some of data vary significantly even for the same material. In this context, it is of importance to compare the results by different techniques. Further information on direct measurement on electrocaloric effect can be found in Chapter 2.

1.6 MULTICALORIC EFFECT

Vopson proposed multicaloric effect to address the promise of multiferroic in taking advantage of the multiple forms of the entropy [10]. Note that multicaloric effects refer to not only the case

that more than one type of stimuli is applied simultaneously, but also include the case that the different stimuli are applied sequentially [8]. Here we present one example of how multicaloric effect works fundamentally. Considering a multiferroic material upon adiabatic application of an electric field. Obviously, two contributions to the total multicaloric effect: electrical entropy corresponds to electrocaloric effect while additional magnetic entropy change induced through magnetoelectric coupling. Therefore, Vopson simply replaced the external magnetic field in Eq. (1.19) by electric field via linear magnetoelectric coupling: [10]

$$\mu_0\chi dH = \alpha_{ME}dE, \quad (1.37)$$

where $\chi = (\frac{\partial M}{\partial H})_T$ is the volume magnetic susceptibility. Therefore, the total entropy change can be determined as follows:

$$\Delta S_E = \int_0^E [(\frac{\partial D}{\partial T})_E + \frac{\alpha_{ME}}{\chi}(\frac{\partial M}{\partial T})_E]dE. \quad (1.38)$$

Accordingly, the total temperature change in adiabatic condition can be expressed as

$$\Delta T_E = - \int_0^E \frac{T}{C_E} [(\frac{\partial D}{\partial T})_E + \frac{\alpha_{ME}}{\chi}(\frac{\partial M}{\partial T})_E]dE. \quad (1.39)$$

Therefore, it is expected that enhanced caloric response can be achieved in multiferroic materials. In addition, higher-order magnetoelectric couplings such as $1/2\alpha_{ME}P^2M^2$ may also contribute to entropy change, as addressed by Planes *et al.* recently in a phenomenological Landau model [105].

These additional terms in Eqs. (1.38) and (1.39) can be derived from Helmholtz free energy $F = U - TS$ [106] by introducing $dU = TdS + \mu_0HdM$ (where H is the induced magnetic field rather than external field), one can obtain the differential Helmholtz free energy as

$$dF = -SdT + \mu_0HdM = -SdT + \mu_0H(\frac{\partial M}{\partial E})dE. \quad (1.40)$$

Replacing $\mu_0(\frac{\partial M}{\partial E})$ by the magnetoelectric coupling coefficient α_{ME} , dF can be written as

$$dF = -SdT + \alpha_{ME}HdE. \quad (1.41)$$

It can be seen clearly that the magnetoelectric coupling energy ($\alpha_{ME}HdE$) is included in the differential Helmholtz free energy. Note that H is phenomenologically equivalent to the induced magnetic field via magnetoelectric coupling and magnetic order change is controlled by the electric field rather than the external magnetic field. The Helmholtz free energy should be defined by two independent variables (T, E) rather than ($T, M(E)$) used in Binek and Burobina' paper [106]. It is inappropriate to use (T, M) as the thermodynamic variables because the magnetization is indeed a function of the applied electric field. Therefore, the equation of state is corrected as

$$H = H(T, E). \quad (1.42)$$

Obviously, the magnetization $M(T, E)$ depends on both the temperature and electric field just like $H(T, E)$. If the temperature is fixed, applying an electric field will induce a change in the magnetization and thus magnetic entropy change.

Then the Maxwell relation based on Helmholtz free energy is obtained:

$$\left(\frac{\partial S}{\partial E}\right)_T = -\alpha_{ME}\left(\frac{\partial H}{\partial T}\right)_E. \quad (1.43)$$

Integration of Eq. (1.43) yields:

$$\Delta S_E = -\int_0^E \alpha_{ME}\left(\frac{\partial H}{\partial T}\right)_E dE. \quad (1.44)$$

Using thermodynamic identities, we may obtain from Eq. (1.44)

$$\Delta S_E = -\int_0^E \alpha_{ME}\left(\frac{\partial H}{\partial M}\right)_T\left(\frac{\partial M}{\partial T}\right)_E dE = -\int_0^E \frac{\alpha_{ME}}{\chi}\left(\frac{\partial M}{\partial T}\right)_E dE. \quad (1.45)$$

This is as equal as the case derived from Gibbs free energy but with different signs.

The idea that multiferroic can permit enhanced multiple entropy change sounds physical. However, the approaches provided above need further considerations. The concern mainly comes from the replacing treatment of “external” magnetic field via linear magnetoelectric couplings relationship in Eq. (1.37). Indeed, near the phase transition, every physical property changes significantly and is electric field dependent. Using constant values to estimate the entropy change is technically unjustified. Moreover, the magnetoelectric coupling coefficient used in Eq. (1.39) under adiabatic condition may differ significantly from that used in Eq. (1.38) under isothermal condition due to thermally mediated magnetoelectric effect in multiferroics [107]. This important temperature mediated mechanism, which was highlighted by recent first-principles calculations, was completely overlooked in previous works [10, 106]. Indeed, the linear adiabatic magnetoelectric coupling coefficient can be determined by: [107]

$$\mu_0\left(\frac{\partial M}{\partial E}\right)_{S,H} = \mu_0\left(\frac{\partial M}{\partial T}\right)_{E,H}\left(\frac{\partial T}{\partial E}\right)_{S,H} + \mu_0\left(\frac{\partial M}{\partial E}\right)_{T,H}. \quad (1.46)$$

Interestingly, it is shown that even the isothermal magnetoelectric coupling coefficient $\mu_0\left(\frac{\partial M}{\partial E}\right)_{T,H}$ is zero, the adiabatic one may not necessarily be zero due to the first term in Eq. (1.46). As a result, Eq. (1.39) actually underestimates the final outcome and thus needs to be modified as follows:

$$\Delta T_E = -\int_0^E \frac{T}{C_E}\left[\left(\frac{\partial D}{\partial T}\right)_E + \mu_0\frac{\left(\frac{\partial M}{\partial T}\right)_E\left(\frac{\partial T}{\partial E}\right)_S + \left(\frac{\partial M}{\partial E}\right)_T}{\chi}\left(\frac{\partial M}{\partial T}\right)_E\right]dE. \quad (1.47)$$

Similarly, for the caloric effect driven by magnetic field in multiferroics can be also obtained considering the linear magnetically induced magneto-electric coupling $\varepsilon_0\chi^E dE = \mu_0\alpha'_{ME}dH$ (χ^E is the electric susceptibility and $\alpha'_{ME} = \left(\frac{\partial D}{\partial H}\right)_T$):

$$\Delta S_H = \mu_0\int_0^H \left[\left(\frac{\partial M}{\partial T}\right)_H + \frac{\alpha'_{ME}}{\varepsilon_0\chi^E}\left(\frac{\partial D}{\partial T}\right)_H\right]dH, \quad (1.48)$$

and

$$\Delta T_H = -\mu_0 \int_0^H \frac{T}{C_H} \left[\left(\frac{\partial M}{\partial T} \right)_H + \frac{(\frac{\partial D}{\partial T})_H (\frac{\partial T}{\partial H})_S + \alpha'_{ME}}{\epsilon_0 \chi^E} \left(\frac{\partial D}{\partial T} \right)_H \right] dH. \quad (1.49)$$

Indeed, Eqs. (1.38), and (1.47)-(1.49) have provided basic insights into achieve the largest multicaloric effect in multiferroics. Obviously, it requires that both isentropic and isothermal magnetoelectric couplings should be as large as possible. This fails in most of single phase multiferroic as the isothermal magnetoelectric coupling is really weak up to now [87, 98, 101, 102]. However, isentropic magnetoelectric coupling mediated by temperature may be significantly larger and does not require strong intrinsic couplings between magnetic and electric order parameters. In addition, both magnetocaloric and electrocaloric effects alone should be large as possible as they can further enhance isentropic magnetoelectric coupling and thus enhance multicaloric effect. In particular, large multicaloric effect is expected in composite materials in which significantly larger isothermal magnetoelectric effect was demonstrated in these materials compared to that in single phase compounds [87, 98, 101, 102]. On the basis of Eqs. (1.38), and (1.47)-(1.49), the worldwide research in multicaloric effect has just started in multiferroics.

1.7 THERMODYNAMIC REFRIGERATION CYCLES

In general, a refrigerator should not only include the caloric materials and the driving action systems but also have a hot/cold exchange system and a system related to a heat transfer fluid [4, 6]. Heat exchange can be realized by the cyclic action of refrigeration cycle. Figure. 1.1 summarizes three typical thermodynamic refrigeration cycles in terms of a total entropy-temperature (S, T) diagram: Carnot, Brayton, and Ericsson cycles [4, 6].

An Carnot cycle consists of two adiabatic steps (A-B and C-D associated with adiabatic application or removal of external fields) with no fluid flow and two isothermal steps (B-C and D-A related to isothermal application or removal of external fields) with a fluid flow. Refrigerant capacity defined as $R = \Delta S \Delta T$ depicts the heat which can be transferred between the cold and hot sinks in one ideal refrigeration cycle. Pure Carnot-type refrigerators (i.e., magnetic refrigerators) are nonregenerative and usually used in low temperatures (<20 K) [4].

For higher temperatures applications, lattice entropy of solids are dominated, Brayton, and Ericsson cycles can be used. Thermodynamic Brayton cycles can be described as follows: (A-B) adiabatic application of external stimulus (with no fluid flow); (B-C) isofield cooling of caloric material; (C-D) adiabatic removal of external stimulus (with no fluid flow); and (D-A) isofield heating of the caloric material. Ericsson cycles differ from Brayton ones mainly from the facts that external stimulus is isothermally applied or removed. In both cases, isofield processes are needed, which requires heat regeneration to increase the temperature span of the refrigeration device. This is because the caloric response of solids is limited to a maximum adiabatic temperature change <10 K, which is not sufficient for practical cooling applications. A heat regenerator has to be added into regenerative thermodynamic cycle in order to widen the temperature change window. According to textbooks [4, 6], a heat regenerator defined as a type of indirect heat exchanger where the heat is periodically stored and transferred from/to a thermal storage medium (regenerative material) by a working (heat-transfer) fluid.

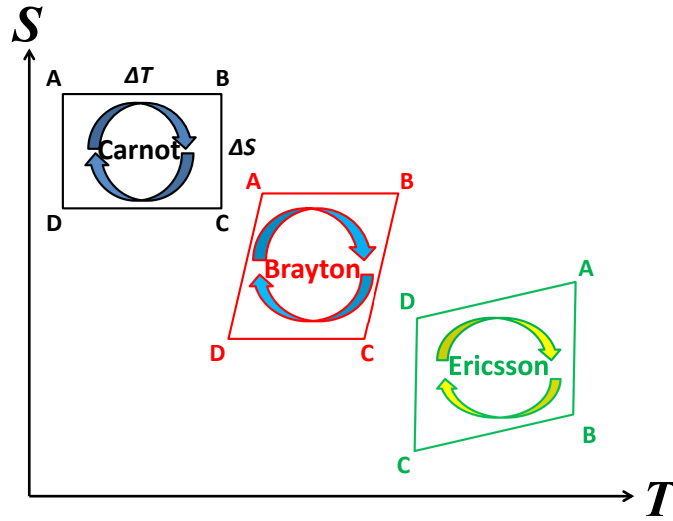


Figure 1.1: Schematic of Carnot, Brayton, and Ericsson cycles in space of total entropy-temperature ($S - T$).

Let us take the regenerative magnetocaloric refrigeration as an example [4, 6]. Magnetocaloric materials heat up when placed into a magnetic field and cooled down when removed. During hot period, fluid from cold heat exchanger to hot heat exchanger flows through the regenerative material. The fluid heats up by absorbing heat from the magnetocaloric material while the material cools down. Then the hot heat exchanger transfers the heat surroundings. During cooling period, another fluid from hot heat exchanger to cool heat exchanger flows through the regenerative material. This leads to heating of magnetocaloric material and cooling of fluid. Then cold heat exchanger absorbs heat from the surroundings (food, beer and so on). With continuous circulation of fluid from cold to heat exchangers, heat is pumped from inside cooler to outside air by forming a periodic steady working state.

Brayton-like, Ericsson-like and Carnot-like or even hybrid Brayton-Ericsson-like regenerative cycles have been used to design active magnetic regeneration [4, 6]. As a result, about 60 magnetocaloric refrigerator prototypes has been built to date. Optimization and development of prototypes are still desired such as the operating frequencies and reproducibilities. On the contrary, the first electrocaloric refrigerator prototypes are still rare and far from being competitive with magnetocaloric or vapor-compression cooling devices, while no elastocaloric or barocaloric prototypes have been reported yet [6].

1.8 CALORIC PARAMETERS

Solid-state caloric material is mainly characterized in terms of isothermal entropy change ΔS and adiabatic temperature change ΔT . For practical cooling applications, refrigerant capacity [108] defined as $R = -\int_{T_1}^{T_2} \Delta S(T) dT$ and coefficient of performance COP defined as the

ratio between the extracted heat with respect to the input work one refrigeration cycle are two key caloric parameters to evaluate the refrigeration efficiency. We note that considering the real devices, numerous engineering problems strongly correlated to the material properties arise in terms of parasitic thermal losses, fatigue and so on. In this regard, *COP* rather than material efficiency can be still used to characterize the performance of devices since *COP* is related to the thermodynamic refrigeration cycle taking into account practical contributions.

- CHAPTER 2 -

REVIEW ON DIRECT AND INDIRECT MEASUREMENTS ON ELECTROCALORIC EFFECT

2.1 INTRODUCTION

In electrically responsive materials, reversible thermal changes can be driven when electric field is applied or removed either adiabatically or isothermally [5]. This phenomenon is called the electrocaloric effect, which is considered as a new refrigeration solution to replace current vapor-cycle cooling technologies [5, 8, 84, 109–117]. It is now known that electrocaloric materials often exhibit the largest response near their phase transitions [8, 84]. However, this effect did not attract as much attention as its magnetic counterpart, magnetocaloric effect [5, 8, 84, 117], because the magnitude of the electrocaloric effect was too small to be of interest for practical cooling applications [84]. Since its discovery in Rochelle Salt in 1930 (Ref. [37]), many studies related to ferroelectric/antiferroelectric/relaxor ceramics were reported, but the best electrocaloric effect data yielded an adiabatic temperature change of less 2.5 K in $\text{Pb}_{0.99}\text{Nb}_{0.02}(\text{Zr}_{0.75}\text{Sn}_{0.20}\text{Ti}_{0.05})\text{O}_3$ ceramics in 1981 (Ref. [44]). In addition, a similar electrocaloric effect of 2.4 K was reported in $\text{PbSc}_{0.5}\text{Ta}_{0.5}\text{O}_3$ ceramics in 2002 (Ref. [45]). It is not until 2006 that a Science paper [15] inspired both fundamental physics and exciting device applications for electrocaloric effect. Mischenko *et al.* at Cambridge reported a giant electrocaloric effect with an adiabatic temperature change of about 12 K in antiferroelectric $\text{PbZr}_{0.95}\text{Ti}_{0.05}\text{O}_3$ ceramic thin films under a high electric field of 780 kV/cm (Ref. [15]). Two years later, another breakthrough related to a giant electrocaloric effect in organic P(VDF-TrFE) thin films was announced by the Penn State group of Zhang [46]. In these two pioneering works [15, 46], high electric fields could be achieved in the thin films (i.e. $E = V/h$ with thickness h decreasing for a given voltage V , E increases), which naturally frees the primary limit by the electric breakdown strength of the bulk materials. As a result, significantly enhanced electrocaloric response can be obtained.

Both studies [15, 46] employed indirect measurement to characterize the electrocaloric effects. Since then the indirect measurement, based on the Maxwell relations has become a well-established practice in the field [5, 8, 84, 109–117]. This approach is useful for rapid selection of electrocaloric materials. However, uncertainties can arise when improper methods are used in

such approach. In this regard, a direct measurement is quite necessary to inspire the confidence of measured electrocaloric effect for practical applications [5]. Direct measurement means a direct determination of the electrocaloric temperature change of the sample when the external electric field is applied or removed adiabatically. Usually the direct measurements are performed by using a thermocouple, differential scanning calorimeter (DSC), infra-red (IR) camera, scanning thermal microscopy and specifically designed calorimeters [5]. According to the literature, most experimental data reported are obtained by specific homemade calorimeters and some of the data vary significantly even for the same class of materials [5, 111]. In this context, it is of importance to compare the results measured using different experimental techniques. For instance, commercially available techniques such as IR cameras or other calorimeters may be helpful to allow a standard practice between different groups at least at the materials level. This can avoid any overestimation or underestimation of the electrocaloric effect and would provide a reliable basis for developments of electrocaloric prototypes.

Although the goal is to arrive towards commercial applications, research in the field of electrocaloric effect is still at its early stage. Current publications mainly focus on properties of materials and only few works are devoted to the design of electrocaloric prototypes for applications [5, 6, 117]. In contrast, significant engineering developments have been achieved in magnetocaloric refrigeration: about 60 magnetocaloric prototypes have been developed all over the world during the past two decades [6]. A part of delay encountered in the field of electrocaloric is due to the way of extracting the electrocaloric data and their reliability. Therefore, it is of great importance to gain insights into the different (indirect and/or direct) approaches and address their basic characteristics. Summarizing recent developments on indirect and direct measurements on electrocaloric effect will also provide a useful background and practical guide to understand and exploit the electrocaloric effect. Therefore, this review is intending to bring an overview on the current electrocaloric measurements in complement to other excellent works i.e. a recent book [5] and other reviews [8, 84, 109–117], which we strongly recommend to readers. We address recent developments that were not systematically and comprehensively discussed or focused on in previous works [5, 8, 84, 109–117] especially during the past two years such as selection of $P(E)$ loops, negative electrocaloric effect in antiferroelectrics, controversial debate on the indirect method in relaxors, the important role of field dependence of specific heat and so on. Our aim is to gain deeper insights into electrocaloric effect by addressing the indirect method based on Maxwell relations while emphasizing the direct measurements to set a solid foundation for developing the electrocaloric prototypes. The review is organized as follows: the first section (Section 2.2) is devoted to indirect measurement where basic thermodynamic descriptions of electrocalorics are presented and discussed. It includes introduction to electrocaloric refrigeration and indirect method based on Maxwell relation, selection of the isothermal $P - T$ curves, negative electrocaloric effect in antiferroelectrics, applications of the Maxwell method to relaxors and first-order phase transitions, the role of heat capacity, kinetics and the depolarizing field, and brief information about Clausius-Clapeyron method. It also physically involves the typical entropy change profile with respect to electric field in the most studied electrocalorics like normal ferroelectrics, antiferroelectrics and relaxors. The second section (Section 2.3) concerns direct measurements. Four typical techniques used recently such as thermocouple, DSC, specifically designed calorimeters, and scanning thermal microscopy are briefly reviewed while

IR camera is particularly addressed. Finally, this chapter ends by closing remarks.

2.2 INDIRECT MEASUREMENTS

2.2.1 Basic thermodynamic description of electrocaloric refrigeration

There are three typical thermodynamic refrigeration cycles: Carnot, Brayton, and Ericsson cycles which were used to present basic thermodynamic features of magnetic refrigeration [6]. Here we use electrical analog to depict electrocaloric refrigeration through electrocaloric Brayton-like cycle (see Fig. 2.1), which was discussed in Scott's review [84] and used in electrocaloric cooling or heat pumping devices (Refs. [118–120] and references therein). Discussions about the Ericsson-like (Ericsson cycles differ from Brayton ones mainly from the facts that external stimulus is isothermally applied or removed) [5] and Carnot-like cycles (consists of two adiabatic steps and two isothermal steps) [121] can be also found elsewhere. Note that electrocaloric refrigeration based on electrocaloric effect is reported to achieve higher coefficient of performance (COP , defined as the ratio between the extracted heat with respect to the input work) over 50% of Carnot efficiency [122]. According to Fig. 2.1, thermodynamic Brayton cycles can be described as follows: (A-B) adiabatic application of external electric field (with no contact with any sink); (B-C) isofield cooling of the electrocaloric material (with contact with the cold sink); (C-D) adiabatic removal of the external field (with no contact with any sink); and (D-A) isofield heating of the electrocaloric material (with contact with the hot sink). The specific electrical work corresponds to area bounded by the surface A-B-C-D while the maximum extracted heat of the electrical Brayton refrigeration cycle is denoted as Q_R , i.e. inside the surface 1-2-D-A. Therefore, the coefficient of performance COP can be defined as $COP_B = Q_R/|W|$. Considering an ideal Carnot cycle, the COP can be written as $COP_C = T_R/T_H - T_R$, where T_R and T_H indicate temperature of cold and hot reservoirs, respectively. The relative efficiency of a refrigerator with respect to an ideal Carnot cycle can be defined as $\eta = COP/COP_C$. Now let us concentrate the basic thermodynamic description of the electrocaloric effect. Based on the Maxwell relationship $(\frac{\partial S}{\partial E})_T = (\frac{\partial P}{\partial T})_E$, the reversible electrocaloric change in temperature ΔT ($\equiv \Delta T_E$ in this Chapter) of an electrically responsive material due to a change in external electric field $\Delta E = E_2 - E_1$ under adiabatic conditions can be determined by:

$$\Delta T = - \int_{E_1}^{E_2} \frac{T}{C(E, T)\rho} \left(\frac{\partial P}{\partial T}\right)_E dE, \quad (2.1)$$

where T is the temperature; P , the polarization; ρ , the mass density; and $C(E, T)$, the heat capacity, all depend on both electric field and temperature. Note that another quantity called isothermal entropy change $\Delta S_E = \int_{E_1}^{E_2} (\frac{\partial P}{\partial T})_E dE$, is equally important to depict the electrocaloric effect. However, its important role is not widely recognized in the literature since ΔS is directly related to the absorbed or ejected heat in response to isothermal application or removal of electric field [8]. The entropy behavior will be discussed in detail later in several typical electrocalorics. According to Eq. (2.1), ΔT is usually maximized near the phase transition, where thermally driven changes in measured polarization P arising from changes in the magnitude

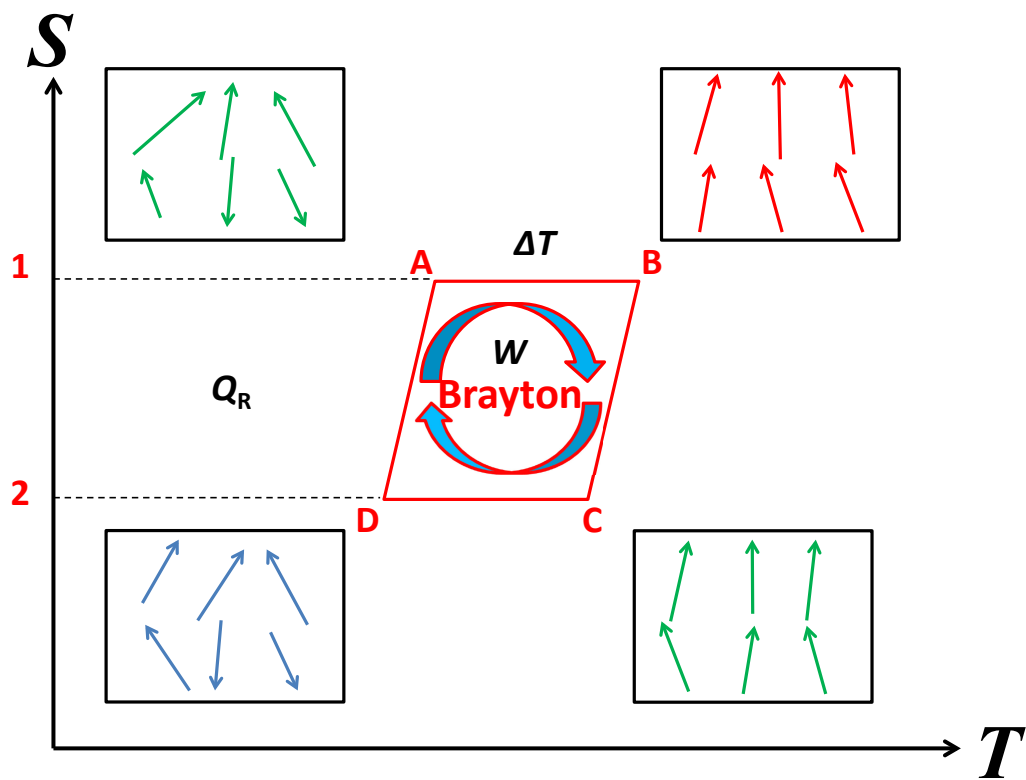


Figure 2.1: Schematic of ideal electrocaloric Brayton refrigeration cycle in space of total entropy-temperature.

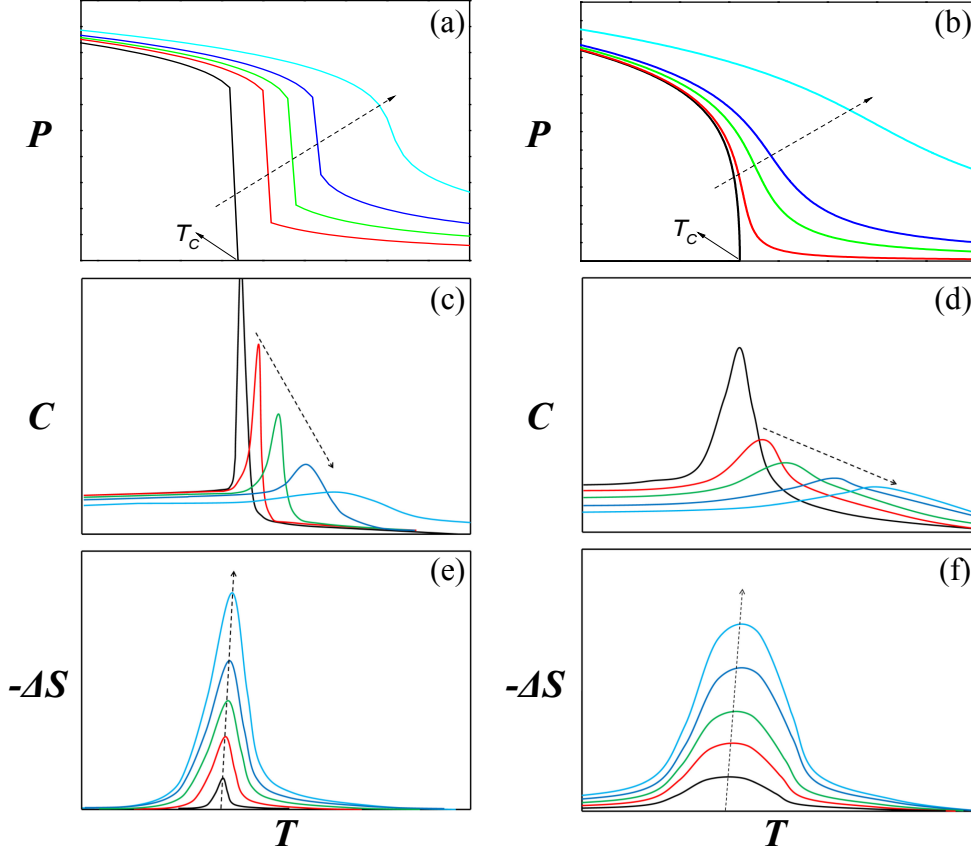


Figure 2.2: Polarization versus temperature curves under various magnitudes of external electric fields: (a) first-order phase transition and (b) second-order phase transition. Temperature dependence of heat capacity under different electric fields for (c) first-order phase transition and (d) second-order phase transition. Isothermal entropy change as a function of temperature for (e) first-order phase transition and (e) second-order phase transition. The dashed arrows indicate the increasing trend of electric fields.

$(\frac{\partial P}{\partial T})_E$ are largest. Recalling the features of phase transition, P changes discontinuously at the transition temperature T_C for first-order phase transition, while for second order type, it decays continuously with temperature increasing until T_C [see Figs. 2.2(a) and 2.2(b)]. In this regard, electrocaloric response is usually significantly stronger in materials undergoing first order phase transitions than those with second order [see Figs. 2.2(e) and 2.2(f)]; a tricritical point is often optimum.

As long as $P(E, T)$ is precisely known, it simply becomes a mathematical problem to calculate its derivative, its integral and thus ΔT . This approach can naturally include the boundary conditions and/or coupling to the strains etc. (for example, in thin films) and therefore is a standard practice in this field [116, 123, 124]. However, in practical situations, precise determination of $P(E, T)$ and its derivative $(\frac{\partial P}{\partial T})_E$ is challenging especially for discontinuous first-order phase transitions and causes several concerns (see Section 2.2.2 and Section 2.2.5). Moreover,

the specific heat $C(E, T)$ in Eq. (2.1) is both temperature- and field-dependent. In particular, compared to zero-field heat capacity $C(0)$, $C(E, T)$ usually experiences a significant change under ultrahigh electric fields regardless of the nature of phase transition [see Figs. 2.2(c) and 2.2(d)]. However, $C(E, T)$ is usually taken as a constant i.e. zero-field $C(0)$ in the literature. This unwarranted assumption may lead to serious systematic errors, which will be discussed in Section 2.2.6. Moreover, usually application of an electric field would lead to the ordering of electrical dipoles accompanied by reduction of entropy regardless of the nature of phase transition [see Figs. 2.2(e) and 2.2(f)]. This thermal phenomenon corresponds to positive (conventional) electrocaloric effect. In addition, the electrocaloric response induced by a first-order phase transition is sharper than that corresponding to second-order transition. In other words, as shown in Figs. 2.2(e) and 2.2(f), the magnitude of electrocaloric effect associated with first-order phase transition can be significantly larger than that accompanied by second-order phase transition, whereas the working temperature window becomes narrower using a first-order phase transition.

2.2.2 Selection of isothermal $P - T$ curves

As mentioned in Section 2.2.1, the electrocaloric effect can be derived based on the data from the temperature dependence of the polarization (isothermal $P - T$ curves) obtained either from theory or experiment. Fig. 2.3 shows antiferroelectric $P(E)$ loops measured at room temperature. In experiments, upper branches of $P(E)$ loops ($E > 0$), in which the ferroelectric or antiferroelectric domain configurations are not significantly modified due to the large electric field, are usually selected to ensure that the indirect method based on Maxwell relations is reliable [15]. In the case of lower branches, the electric field threshold is not high enough ($E > 0$) and undesired ferroelectric switching occurs. In addition, in antiferroelectrics there may be some lower-voltage regions of upper legs of the hysteresis cycle (which we denote as “lower” branches in Fig. 2.3) which are also associated with polarization switching and remarkable change in the domain configurations. The concern about using the lower hysteresis leg or this “lower” part of upper branches to calculate ΔT is that significantly smaller electrocaloric effect may be predicted. For instance, experimental results in BaTiO_3 single crystals showed that electrocaloric responses derived from the lower branches show 50% smaller values than that from the upper branches or the result from direct measurement [48].

This finding was attributed to the dramatic change in ferroelectric domain configurations when a modest electric field is applied [48]. However, according to the following analysis, there are at least two overlooked factors which demands further considerations. (1) The role of electric field dependence of specific heat [123, 125] was not taken into account. This may also lead to remarkable underestimation of electrocaloric responses when a constant heat capacity is used in Eq. (2.1) (see Section 2.2.6). In other words, the use of upper and lower branches $P(E)$ loops to calculate ΔT both suffers from this important factor; (2) direct measurement results [48, 126] indicate that the electrical hysteresis losses may play an important role leading to an asymmetry between the electrocaloric heating (lower branches with electrical field increasing) and cooling responses (upper branches corresponding to decreasing electric field). To be more specific, if the upper branches (excluding the “lower” regions in Fig. 2.3) may correspond to the intrinsic electrocaloric cooling (precluding the contributions from ferroelectric switching and

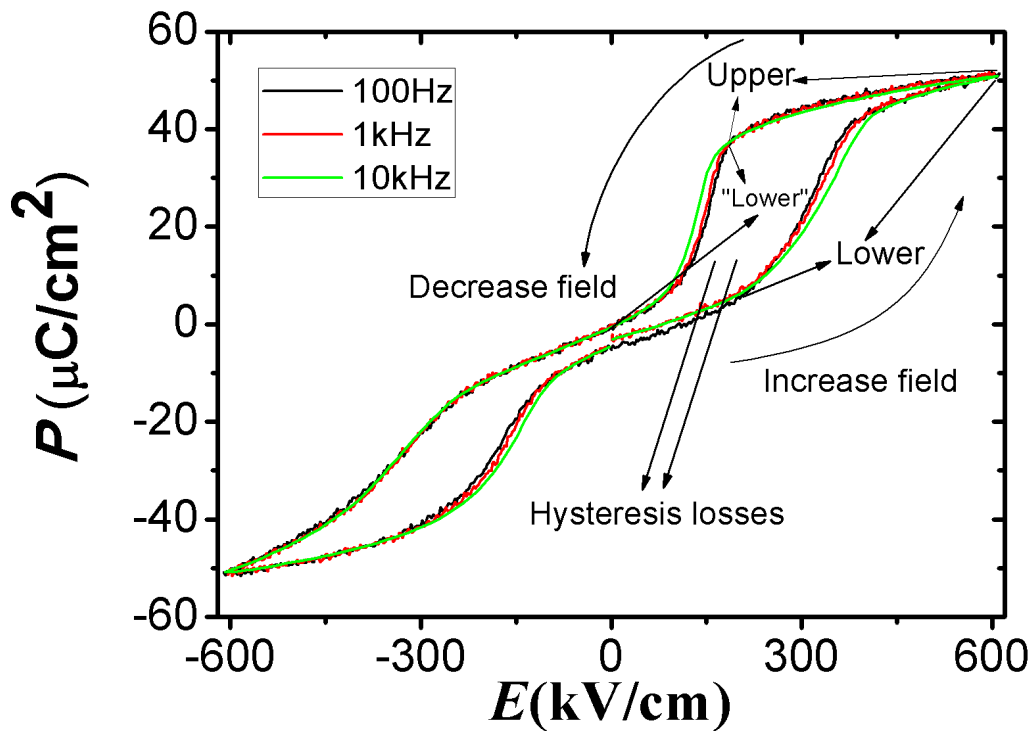


Figure 2.3: $P(E)$ loops of antiferroelectric $(\text{Pb}_{0.97}\text{La}_{0.02})(\text{Zr}_{0.95}\text{Ti}_{0.05})\text{O}_3$ thin films measured under different frequencies at room temperature. The single phase films were fabricated on a Pt(111)/Ti/SiO₂/Si substrate using sol-gel spin coating and the thickness is about 650 nm. Lower, “lower” and upper branches are specifically indicated. The arrows act as a guide to eyes. It can be seen that the frequency has a negligible influence on shape of $P(E)$ loops here.

hysteresis losses) when the field is removed, the lower branches in turn would reflect the extrinsic contributions from the hysteresis losses to the electrocaloric heating since the change in domain configuration such as domain growth/switching is responsible for the $P(E)$ hysteresis loops. As a result, the electrocaloric heating temperature change (lower branches) may be larger than the magnitude of the cooling peak temperature (upper branches), which was observed in recent direct measurements on organic thick films [126] and also BaTiO₃ single crystals [48]. Therefore, we argue that the foregoing underestimation of ΔT by using lower branches could arise as a result of hysteresis losses. As hysteresis losses strongly depend on the magnitude of external fields, their contributions to extract ΔT become less dominated with the field decreasing. This evidence implies that remarkable discrepancies between upper and lower branches can be only observed under high electric fields. As a result, it may further support that the reasonable estimations can be obtained even though a significant domain configuration change exists i.e. near the antiferroelectric-to-ferroelectric switching regions [51]. In addition, Joule heating especially under high fields can also result in a similar asymmetry [127]. Just as addressed in the review [84], the materials will get hotter and hotter if the Joule heating is dominated and no cooling effect will eventually be obtained.

We also note that even the ferroelectric switching in ferroelectric or antiferroelectric is a complex phenomenon, and the electrocaloric effect during ferroelectric switching is poorly understood since it is related to kinetic factors. Indeed, the ferroelectric switching mechanism is usually described by nucleation of new domains followed by their sideways growth. Yet in many materials nucleation is the rate-limiting step. It therefore still requires more efforts to provide solid experimental evidence or theoretical insights. In order to avoid ferroelectric switching, Crossley suggested an alternative approach in terms of $P(E)$ loops. However, factors such as applied frequency are not taken into account and analyzed. Indeed, the shape of $P(E)$ loops also depends on the measured frequency (see Fig. 2.3), which is often ignored in the literature and will be discussed in Section 2.2.6.

$P(E)$ loops are measured at a constant temperature and for different temperatures when the sample is cooled or heated. In standard practice, fourth(or sixth)-order polynomial [15] or Gaussian fittings [46] to $P - T$ curves are carried out to infer ΔT in Eq. (2.1). It is usually required that the temperature interval should be small enough to ensure that isothermal $P - T$ curves are as smooth as possible. Otherwise, very strange electrocaloric responses might be obtained such as remarkable shifts of electrocaloric peak positions, significant variation in the values of predicted ΔT introduced by different smoothing approaches and erroneous prediction of electrocaloric peak even without any phase transitions [129].

Special concern for antiferroelectrics when selecting $P - T$ curves is to exclude the contributions from isentropic-like polarization rotations [51]. To be more specific, in antiferroelectric region ($E_1=0$ kV/cm), Eq. (2.1) actually not only takes into account the contribution arising from the change in the magnitude of the staggered polarization $P_A = P_a - P_b$ [130] (where P_a and P_b are the polarizations of two sublattices) but also that resulting from the polarization rotations driven by changes in the directions of the dipoles being not collinear with the electric field. The former part is the truly physical contribution to the entropy change, while the later plays a negligible role even though it may be accompanied by a modest polarization rise during the initial application of a low electric field (well below antiferroelectric-ferroelectric transition

field E_{AFE-FE}). Therefore, Eq. (2.1) may overestimate the electrocaloric effect ($E_1=0$ kV/cm) in antiferroelectrics as it artificially includes the contribution from isentropic-like polarization rotation during the initial poling process ($E \ll E_{AFE-FE}$), which should be subtracted [51]. One common treatment using Eq. (2.1) is to deliberately apply a high electric field E_1 (much larger than antiferroelectric-ferroelectric transition field E_{AFE-FE}) to stabilize the ferroelectric regime (Ref. [15]). After that, a larger electric field $E_2 > E_1$ is applied to induce the positive (conventional) electrocaloric response. In this case, using the upper branches subjected to high electric fields might avoid the controversy using of lower branches as proposed in Ref. [48]. However, the phase transition from antiferroelectric phase to ferroelectric phase is not employed to optimize the electrocaloric response in antiferroelectrics simply because it is energetically too expensive and inefficient.

2.2.3 Negative electrocaloric effect in antiferroelectrics

Recent publications in antiferroelectric materials either simply followed the foregoing strategy $E_1 > E_{AFE-FE}$ (Refs. [15, 131, 132] and references therein) or studied the electrocaloric response for the case of $E_1=0$ (Refs. [17, 51, 129, 133–138] and references therein) in order to use the electric-induced antiferroelectric-to-ferroelectric phase transition. However, recent findings ($E_1=0$) in the literature appear controversial with respect to positive or negative electrocaloric effect. A negative electrocaloric effect means materials will cool rather than warm in the case of positive electrocaloric effect when an electric field is applied adiabatically, whereas they warm when the field is withdrawn adiabatically. Specifically, a giant positive electrocaloric effect of 45.3 K at 17 °C (it is always positive within the temperature of interest) was predicted in antiferroelectric $\text{Pb}_{0.8}\text{Ba}_{0.2}\text{ZrO}_3$ thin films using indirect measurements [133] while a moderate negative electrocaloric effect (about -0.5 K to -1.5 K depending on the field) was observed by direct measurements in prototypical PbZrO_3 (Ref. [137]) and $\text{Pb}_{0.94}\text{Ba}_{0.06}\text{ZrO}_3$ (Ref. [138]) ceramics near room temperature. A negative electrocaloric effect was predicted in (Na,Bi)TiO₃-based ceramics by indirect measurements [17, 136] while recent direct measurements on similar ceramic compositions near the morphotropic phase boundary showed significant discrepancies between the direct and indirect electrocaloric measurements [139]. Moreover, a giant negative electrocaloric effect (about -5 K) was demonstrated in La-doped $\text{Pb}(\text{Zr}_{0.95}\text{Ti}_{0.05})\text{O}_3$ thin films (0.65 μm) near room temperature using indirect method [51] while only positive electrocaloric effect was reported in La-doped $\text{Pb}(\text{Zr}_{0.85}\text{Ti}_{0.15})\text{O}_3$ thin films (1 μm) within the whole temperature of interest including both room temperature and higher temperatures [135]. These inconsistencies in the literature may be probably attributed to (1) the unjustified nature of antiferroelectricity [some $P(E)$ loops even show evidence of ferroelectricity or slim relaxor type!] without further evidence of microscopic structure, (2) inaccurate fits of $(\frac{\partial P}{\partial T})_E$ or without considering the field- and temperature dependent specific heat and measurement frequency (see Section 2.2.6). The first concern may be a key reason why only positive electrocaloric effects were observed in antiferroelectric compounds using indirect measurements. The second concern may likely account for the quantitative discrepancies between direct and indirect measurements. As mentioned in the Section 2.2.2, it may be risky to use Eq. (2.1) in antiferroelectrics where the transition is between antiferroelectric and ferroelectric phases. Moreover, simply choosing the

measured (average) polarization as primary ferroic order parameter may be questionable since the relevant order parameter in antiferroelectric state is the staggered polarization rather the average polarization [130]. While very similar concerns about the magnetic order parameters in antiferromagnetics were raised by Gschneidner *et al.* [140], treating the measured magnetization as the primary order parameter is frequently used in the magnetocaloric community [13, 34, 141–145, 147]. It seems that the indirect method might still yield reasonable estimations about direct measurement results. For instance, it was reported that the direct measurement results in FeRh compounds can be well reproduced by indirect method based on the magnetization measurements [147].

The entropy change $\Delta S(E)$ under an applied field in an antiferroelectric is not always negative, as shown in Figs. 2.2(e) and 2.2(f) in normal ferroelectric (E does not increase the existing antiferroelectric order). This may lead to a negative electrocaloric effect, changing our general understandings of electrocaloric effect [51, 129, 137, 138]. One can already realize that, for the case of normal ferroelectrics [Figs. 2.2(e) and 2.2(f)], applying a (conjugate) field E always reduces entropy by further aligning dipoles, therefore leading to a conventional (positive) electrocaloric effect according to Eq. (2.1) and once recalling that $(\frac{\partial S}{\partial E})_T = (\frac{\partial P}{\partial T})_E$. Therefore this process should always be accompanied by a decrease in entropy, as shown in Figs. 2.2(e) and 2.2(f). A negative electrocaloric effect, however, indicates that electrocaloric entropy increases when an external electric field applied isothermally and become smaller when the field is withdrawn.

Indeed, being able to observe negative electrocaloric effect in antiferroelectric under a moderate electric field is reasonable and understandable if one recalls the magnetic analog (called negative magnetocaloric effect) which was found in antiferromagnetic FeRh alloys 26 years ago [13]. In order to understand physically this electrically induced thermal effect in antiferroelectrics, using Kittel model, Pirc *et al.* predicted a crossover temperature above which the low-temperature negative electrocaloric effect transforms into high-temperature positive type [137]. This was qualitatively confirmed by recent experimental works in antiferroelectric thin films [51] together with Young's pioneering work [129]. Moreover, a possible mechanism was proposed to explain the origin of the negative electrocaloric effect in antiferroelectric when subjected to a modest electric field under isothermal conditions [51]. To be more specific, the non-collinear responses of dipoles in antiferroelectrics to an applied electric field lead to the increase of the entropy components perpendicular to the direction of the electric field with the entropy component along the direction of electric field nearly unchanged (see Fig. 2.4). As a result, the application of a modest electric field in antiferroelectrics will generally increase the entropy by misaligning (canting) the dipoles, therefore generating the negative electrocaloric effect [51]. We also note that this collective non-collinear response of antiferroelectric dipoles is different from the initial random arrangement of dipoles as aforementioned.

Furthermore, since both antiferroelectric state and ferroelectric state are ordered with nominally different order parameters, the existence of negative electrocaloric effect in antiferroelectrics seems to be reasonable. Entropy clearly plays the key role in electrocaloric properties. Let us qualitatively analyze the electric-field-induced entropy change in antiferroelectrics as depicted in Fig. 2.5 as follows. It is known that a ferroelectric order can be always stabilized from an antiferroelectric state and more easily at relatively higher temperatures and higher electric

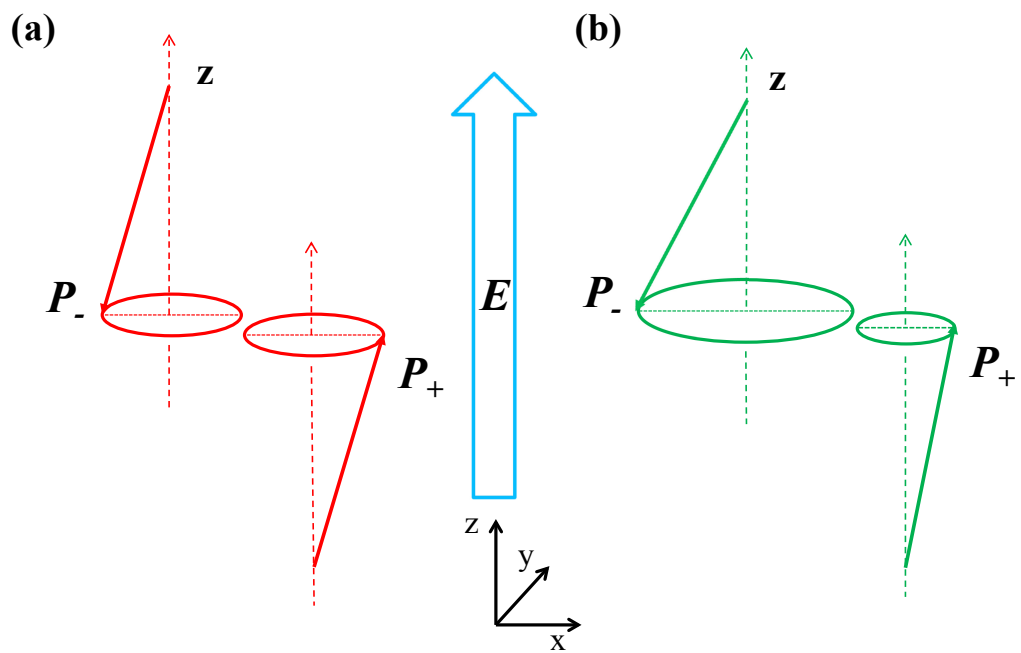


Figure 2.4: Schematic of a possible mechanism of negative electrocaloric effect in antiferroelectric: (a) without any electric field and (b) under a modest electric field. Due to temperature fluctuations, local polarization P locally moves around, roughly in cones. The dipoles are collinear only on average and the cones have the same radii without any field.

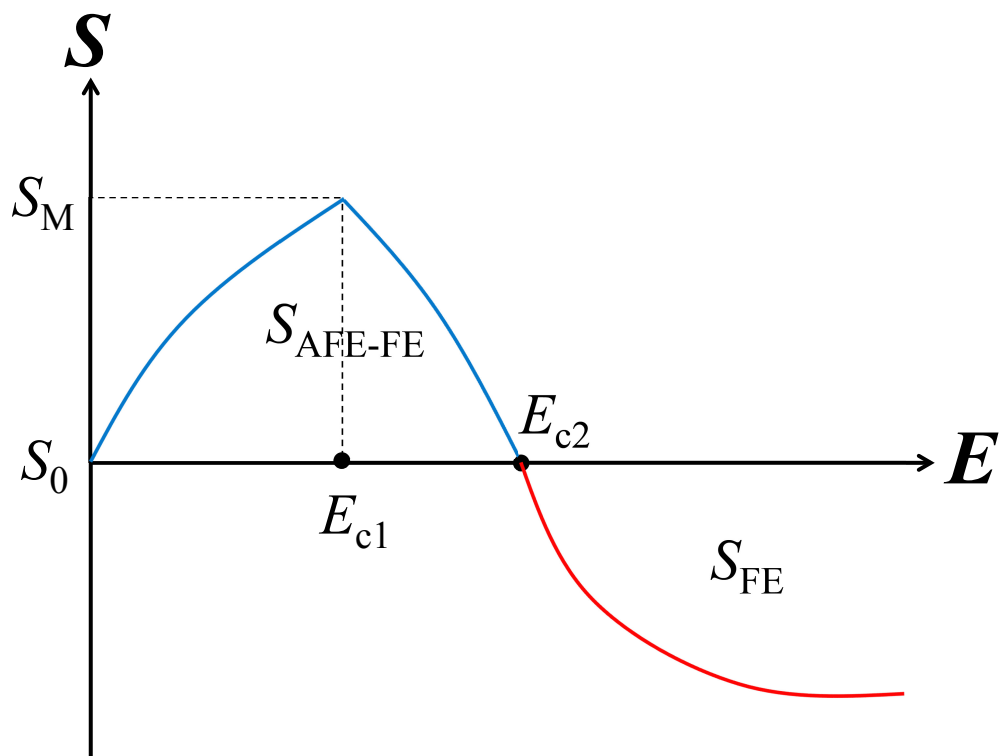


Figure 2.5: Schematic of the principle of the electric-field-induced entropy change in antiferroelectrics.

fields [51, 130]. Without any external fields, the antiferroelectric state is stabilized with a nominal entropy $S_{AFE}(E = 0)$ (which is deliberately set to be a constant S_0 in our following analysis). When the electric field is applied isothermally ($E_1 = 0$), local antiferroelectrically arranged dipoles will rotate and align along the direction of electric field until local phase switches from antiferroelectric domain configuration to ferroelectric-like type in the antiferroelectric matrix assuming a first-order phase transition. In this case, the whole system becomes “disordered” or less ordered with an intermediate entropy as S_{AFE-FE} which is larger than S_0 . This provides a simple and common physical image for the origin of negative electrocaloric effect in antiferroelectrics under a modest electric field. The upper bound magnitude of negative electrocaloric response S_M is limited by the competition between antiferroelectric and ferroelectric orders. With the electric field up to a critical electric field $E_{c1} (\approx E_{AFE-FE})$, the entropy contribution from ferroelectric order becomes more appreciable and comparable to its antiferroelectric counterpart. The electric field decreases the antipolar order while increases polar one, which means that antipolar entropy contribution increases while polar one decreases. In this regard, the whole system becomes ordered again accompanied by a decrease in the entropy S_{AFE-FE} . The entropy behavior ends within a ferroelectric regime S_{FE} ($E > E_{c2}$) where negative electrocaloric effect is completely compensated by the positive electrocaloric one and the sign of electrocaloric effect changes to positive.

The physical description proposed above is not restricted in understanding the thermal behavior in antiferroelectrics but can be also useful to explain the non-monotonical magnetocaloric behavior in antiferromagnetic materials when subjected to field-induced phase transition from an antiferromagnetic phase to a ferromagnetic phase [142–145]. To simplify, in Fig. 2.6 we do not consider any specific information such as the material and the direction of fields but focus on the general physical behavior of an antiferroic system. The magnetocaloric or electrocaloric entropy change ΔS with a positive sign at lower temperatures $T < T_C$ (1) firstly experiences an increase in its magnitude (becoming more positive) with magnetic or electric field; (2) $|\Delta S|$ then decreases when a critical magnetic or electric field is reached; (3) ΔS changes its sign from positive to negative, which indicates that the nature of magnetocaloric or electrocaloric effect changes from negative type to positive type [also see positive electrocaloric entropy change in Figs. 2.2(e) and 2.2(f)]. In the higher temperatures near the Curie temperature, entropy change is always negative indicating positive caloric response due to the field induced transition from a paraelectric or paramagnetic phase to a ferroelectric or ferromagnetic phase.

Regarding antiferroelectrics, the analysis above implies a subtle coupling between antiferroelectric and ferroelectric polarizations; and their structural instabilities might be at the heart of this complex mechanism [148]. Indeed, recent first-principles calculations predicted the existence of a so-called scaling law of ΔT for the fields below E_{AFE-FE} in PbZrO_3 [146]. However, the computational results failed to reproduce several typical experimental behaviors: [51, 129] the remarkable shift of polarization peak with temperature under various electric fields, the shift of negative ΔT peak with temperature under various electric fields, the sign reversal under ultrahigh electric fields. In addition, relaxor ferroelectrics were also found to display a modest negative electrocaloric effect in a limited temperature change, which will be discussed in the next Section. 2.2.4. The potential interest for negative electrocaloric or magnetocaloric effect is not only to develop a new class of caloric materials in solid-state caloric family, but also to enhance

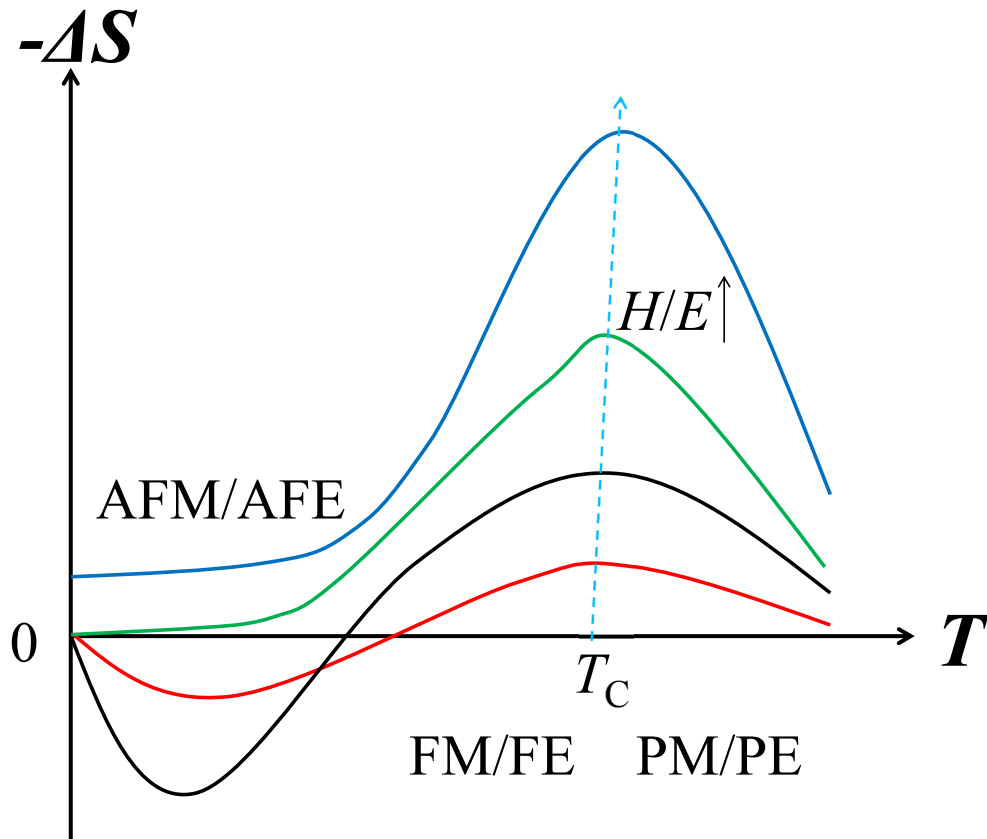


Figure 2.6: Schematic of the principle about the temperature dependence of magnetocaloric/electrocaloric entropy change under various magnetic/electric fields. AFM/AFE indicates antiferromagnetic/antiferroelectric, FM/FE refers to ferromagnetic/ferroelectric, and PM/PE indicates paramagnetic/paraelectric, respectively. T_C is the Curie temperature corresponds to the high-temperature transition from PM/PE phase to FM/FE phase. At the low temperature, AFM/AFE is stabilized without any fields.

the cooling efficiency if both negative and positive caloric effects can be combined properly. At a final glance, we will discuss an example of negative electrocaloric found in antiferroelectric thin films in Section 3.2 of Chapter 3.

2.2.4 Electrocaloric effect in relaxors

Relaxors are characterized by strong dielectric constant anomalies in which temperature of the susceptibility maximum depends on the measurement frequency. It is believed that polar nanoregions caused such anomalies and that a classical ferroelectric long-range state is avoided because of the presence of random electric fields. There is still debate on the validity of electrocaloric data from the indirect approach based on the Maxwell relations especially for these relaxor ferroelectric materials. For instance, it was reported that the indirect method using Eq. (2.1) may not necessarily yield a reliable basis for electrocaloric response in the relaxors [139, 149–152]. Note that relaxors are known to be not mechanical, polar, or thermal equilibrium and therefore it is technically unjustified to use the Maxwell relations in relaxors whose $S(E)$ is generally unknown. The interest of relaxors for electrocaloric studies originated from the following considerations: The magnitude of ΔT in relaxors is highly competitive with that in normal ferroelectrics [5, 111]; the operational temperature window can be quite wide [46, 149–152]; a dual broad peak was observed [153–157]; there are small electrical and thermal losses [46]; the non-equilibrium state of polar phase and the coexistence of numerous polar phases may provide multiple sources of entropy change especially near the critical composition [158, 159], which is also applicable in normal ferroelectric solid solutions with critical point [160–162].

Recently, a theoretical model without the use of Maxwell relations was proposed to describe the electrocaloric effect in relaxor ferroelectrics [163]. The total entropy of a polar material was divided into two parts: one is dipolar degrees of freedom or polar nanoregions, which corresponds to polar contributions and thus is electric-field-dependent. The other component results from the lattice, which is a field-independent contribution (phonons, electrons, etc). Another assumption is that the dipolar free energy can be written in the standard Landau form. Therefore, following the thermodynamic relations as describe in Ref. [163], the electrocaloric effect $\Delta T = T_2 - T_1$ in response to an applied field E can be implicitly derived from [69]:

$$T_2 = T_1 \exp\left\{\frac{1}{2C_{latt}}[a_1(T_2)P^2(E, T_2) - a_1(T_1)P^2(0, T_1)]\right\}, \quad (2.2)$$

where C_{latt} is the lattice heat capacity per unit volume and assumed to be nonsingular and dependent weakly on the temperature. $a_1 = da/dT$, where a is a temperature dependent Landau free energy expansion coefficient. As a result, this model can explain the maximum electrocaloric strength observed near the critical point where the first-order phase transition transforms into second-order type (tricritical point) as the field increases [125, 152, 163, 164] and is also applicable to normal ferroelectrics [164]. In addition, based on this framework, theoretical descriptions of the elastocaloric [64] and barocaloric effects [76] associated with uniaxial stress and hydrostatic pressure were reported recently. The interest in these predictions is to demonstrate the promise of ferroelectrics in mechanocaloric cooling applications together with recent and rapid developments in this field (Ref. [19, 49, 50, 65, 66, 75, 79, 80, 165, 166] and references therein).

Indeed, this model [see Eq. (2.2)] can be also used to justify the negative electrocaloric effect found in relaxors as long as the parameters such as polarization and heat capacity are precisely known. Efforts in relaxors require further investigations. For instance, from the theoretical point of view, first-principles calculations combined with non-equilibrium molecular dynamics can be used to determine the electrocaloric effect without the use of Maxwell relations [167]. It was reported that single crystals $\text{PbMg}_{1/3}\text{Nb}_{2/3}\text{O}_3\text{-PbTiO}_3$ (PMN-PT) were also found to display a negative electrocaloric effect [156, 168]. For instance, negative electrocaloric effect with a quite small magnitude of about 0.025 K was firstly evidenced around 60 °C in $\langle 011 \rangle$ -oriented PMN-28PT single crystals under an electric field of 9 kV/cm [156]. Later on, $\langle 001 \rangle$ -oriented PMN-30PT single crystals were studied in details by both indirect measurement and direct measurement based on DSC calorimetry [168]. The findings confirmed the existence of negative electrocaloric effect near a relatively narrow region [75-95 °C]. Moreover, both the indirect and direct measurement results agree with each other within the experimental errors even for relaxors [168]. The origin of this effect in relaxors was theoretically studied by using a one dimensional statistical mechanical lattice model and the change in electrocaloric sign was attributed to the variation in free energies driven by electric field [169]. Nevertheless, in contrast to these results, no negative electrocaloric response was found in ceramics made of the same material PMN-30PT [152]. According to recent theoretical developments in relaxors [for instance $\text{Ba}(\text{Zr}_x\text{Ti}_{1-x})\text{O}_3$ relaxors], there is a dielectric peak around a specific temperature, T_m , associated with the application of weak dc electric fields [170]. No macroscopic paraelectric-to-ferroelectric transition occurs in this material down to the lowest possible temperatures. Such behavior therefore implies that the (induced) polarization decreases as the temperature decreases below T_m when applying these weak fields, which thus should result in the negative electrocaloric effect according to Eq. (2.1). Finally, theoretical insights using *ab initio* calculations are highly desired to understand particularly the origin of the negative electrocaloric effect in antiferroelectrics and relaxors.

The microscopy model we described in Section 2.2.3 may be applied to relaxors. Indeed, relaxors can be seen as a similar system where polar state should fight against the random fields (rather than antiferroic interactions).

2.2.5 First-order phase transition

Strictly speaking, Eq. (2.1) is not valid in the case of first-order phase transition (these are not thermodynamically reversible [112]). Recalling the phase diagram in the space of (P, T) , the polarization exhibits a discontinuous change at a critical temperature T_C corresponding to the first-order phase transition [Fig. 2.2(a)]. Both $(\frac{\partial P}{\partial T})_E$ and heat capacity [Fig. 2.2(c)] are rather challenging to define. In experiments, the phase transition usually occurs in a specific temperature range with phase coexistence. Latent heat referring to the heat energy rejected or absorbed within the coexistence range of two phases is an import factor describing the first-order phase transition, whose contribution to electrocaloric response fails to be taken into account in Eq. (2.1) (Ref. [171]). Typically, a noticeable thermal hysteresis is often observed when the first-order phase transition is driven by cooling and heating processes [123]. However, few experimental studies were conducted to consider this aspect of the electrocaloric response [172]

while most of results were obtained through single thermal path by either cooling or heating the samples. In the ideally isothermal condition, the electrical hysteretic losses should also be considered when the field is applied and removed. In this case, relaxor has a positive flavor due to its slim $P(E)$ loops, which are not as sensitive to temperature compared to normal ferroelectrics [5]. On the contrary, the hysteresis loss in antiferroelectrics could be problematic in addition to its great volume change near the antiferroelectric-to-ferroelectric phase transition [51, 130].

Both the thermal and electrical losses contribute to the final electrocaloric response. Moreover, if these two factors are dominant, the electrocaloric effect may be irreversible and it would exist for only a few cycles. This degradation (“fatigue”) is surely detrimental to any cooling applications. Similar issues have attracted much more attention for magnetocaloric refrigeration [11, 83, 117, 173–176] while investigation on electrocaloric counterpart is in its infancy stage [5, 8, 84, 109–117]. Quantitative analysis of contributions of thermal and electrical losses to the electrocaloric effect is of great importance especially for design of electrocaloric prototype devices.

According to the analysis above, great caution should be made to include every detailed information regarding the discontinuity in $P(E, T)$ associated with first-order phase transition when one may try to fit $P(E, T)$ with some polynomials [116, 129]. This is challenging. Taking into account the discontinuous change of the polarization at the phase transition, electrocaloric entropy change ΔS was suggested to be modified as follows: [5, 112]

$$\Delta S_E = \int_0^E \left(\frac{\partial D}{\partial T} \right)_E dE - \Delta D \left(\frac{\partial E}{\partial T} \right). \quad (2.3)$$

From Eq. (2.3), the Maxwell relation can be expressed in two forms: one in which dS is proportional to dE and the other form in which dS is proportional to the change of the displacement dD having a proportional factor of $\left(\frac{\partial E}{\partial T} \right)$. Note that Eq. (2.3) is also an approximate expression and it seems technically complex, which has not been employed in experimental works yet.

First-principles-based simulations were carried out to testify the applicability of the Maxwell relations. Ponomareva and Lisenkov demonstrated that the indirect approach based on the Maxwell relations provides an accurate and reliable basis for electrocaloric effect as long as Eq. (2.1) is accurately integrated [177]. To the contrary, according to Rose and Cohen’s computations, Eq. (2.1) is an exact expression and both indirect and direct approaches must agree within the error of experiments or simulations but not necessarily depend on detailed numerical integration techniques [100]. Note that both simulations [100, 177] started from the first-order phase transition; however, neither of them took into account the field- and temperature-dependent heat capacity and reported any dissipative non-equilibrium effects resulting from latent heat associated with the first-order phase transitions. These important factors were included in a more recent computational framework [171] that demonstrated that the indirect approach can only be only valid as long as the first order transition is not crossed. They also found that systematic errors by using indirect approach may arise due to inaccurate fits of $\left(\frac{\partial P}{\partial T} \right)_E$ as we discussed above and the use of a constant specific heat which we will address in the next section (Section 2.2.6). The theoretical approach [171] by Marathe *et al.* represents an important advance to quantify the electrocaloric effect by using *ab initio* calculations. One practical route to further theoretical explorations is suggested to carry out theoretical simulations which can be directly compared to the experimentally available data.

2.2.6 Heat capacity and kinetics

Assuming a constant value of heat capacity $C(E, T)$ in Eq. (2.1) despite the phase transition is often used in the literature since this treatment may still yield a reasonable estimate of the electrocaloric effect [8]. Indeed, the heat capacity measured at zero electric field can be significantly different from those at modest and strong fields. This field- and temperature-dependence of heat capacity may raise concern about the simple treatment widely used in the literature. Previous thermodynamic calculations [123] showed that heat capacity $C(E, T)$ peak (or divergence) near the phase transition in normal ferroelectric (like BaTiO₃) thin films will be smeared at high electric fields with a shift in its peak position towards higher temperatures [see Fig. 2.2(c)]. This behavior in normal ferroelectric BaTiO₃ is confirmed by the first principles-based calculations very recently [171]. In addition, the field-dependence of heat capacity in Ba_xSr_{1-x}TiO₃ (x from 0 to 1) at various temperatures was also calculated using Green's functions and the results imply that the value of heat capacity experiences a remarkable decrease with increasing field [178].

Moreover, it is known that latent heat associated with first-order phase transition will be fully released as long as the field is high enough. This indicates that a smearing of phase transition from first-order nature to second-order type should be observed by experiments. As a result, the heat capacity peak should decrease significantly since the latent heat is determined by the area of this peak, which was experimentally observed in KDP [179] and theoretically predicted in BaTiO₃ [123, 171]. This behavior is also confirmed in BaTiO₃ [125, 164] and PMN-PT [180, 181] single crystals by using a high-resolution calorimeter with ac and relaxation modes. According to these recent calorimetric measurements, together with foregoing theoretical findings, it is reasonable to conclude here that the heat capacity is not constant but strongly dependent on the electric field and also changes with temperature.

Let us now reexamine the assumption that heat capacity is electric-field independent. According to the analysis aforementioned [see Figs. 2.2(c) and 2.2(d)], the relation $C(E, T) < C(0, T)$ is usually satisfied, and any discrepancies become more significant in the case of ultrahigh electric field which drives the giant electrocaloric effect near the phase transition. The real physical contribution of heat capacity to the integral in Eq. (2.1) is overestimated. Therefore, ΔT estimated using $C(0, T)$ or $C(0)$ should be smaller than the true electrocaloric response. This simple treatment can lead to underestimations of the real ΔT , which was ignored by most of the studies in the literature [5]. Indeed, even for quasi-direct measurement using DSC calorimetry, numerous concerns exist when heat data is used to calculate ΔT according to the simple relation $T\Delta S = C(0)\Delta T$, which will be discussed in detail in the Section 2.3.2. Given that field-dependent heat capacity can be also a source of underestimations of ΔT , further works are highly desired to determine the role of ferroelectric switching, field-dependent heat capacity and hysteresis loss.

Regarding the lower branches of $P(E)$ loops mentioned above, it is related to a very complex dynamic process associated with domain switching and growth mechanism [182]. Indeed, the Maxwell relations approach gives trends in the caloric effects since it assumes thermal equilibrium, but most of the experiments are time-dependent. The kinetics is rarely mentioned in the literature. Indeed, the use of the Maxwell relations may cause an overestimation on average of approximately 40% (see Ref. [183]). The first recognition of the time and frequency depen-

dence of the electrocaloric effect was independently made in Ref. [183] and Chapter 7 of a recent book [5]. The important point is that the polarization $P(t, f)$ is relaxational with time t . And the hysteresis loops are usually recorded within a millisecond or less (the frequency is typically 1 kHz or even larger), probably corresponding to the condition between isothermal and adiabatic regime which is neither isothermal nor adiabatic. This likely leads to systematic errors of ΔT , which was justified and reexamined in detail by Young [129]. Moreover, the instrument temperature response also has an integration time and normally these two times are not the same. In such a case, the Maxwell relations must be explicitly time dependent. Another concern about Eq. (2.1) is the different relaxation time for heat capacity and polarization; these often differ and both are different from the rise time of the applied field in the experiments. Hence the electrocaloric response depends upon three characteristic times. Future device optimization must frequency-match the detector response time and the polarization decay time.

It is known that shape of $P(E)$ loops depends on measurement frequency [182] and the frequency has important effect on P_{max} in a specific electric field and thus the calculated ΔT . This complicates the calculations of ΔT or ΔS based on Eq. (2.1) compared to magnetocaloric analog whereas the magnetic field does not have a frequency. For instance, as shown in Fig. 2.3, the measurement frequency has a negligible influence on $P(E)$ loops and therefore results in a trivial effect on the predicted ΔT in antiferroelectric PLZT $[(\text{Pb}_{0.97}\text{La}_{0.02})(\text{Zr}_{0.95}\text{Ti}_{0.05})\text{O}_3]$ thin films [51]. On the contrary, $P(E)$ loops of BaTiO_3 single crystals show a remarkable dependence on measured frequency at 100 °C (near to Curie temperature of about 130 °C) [184]. As a result, the predicted ΔT based on Eq. (2.1) conclusion that electrocaloric effect in BaTiO_3 single crystals is strongly dependent on electric field frequency. Moreover, it was recently suggested by Crossley *et al.* that sufficiently low frequency measurement might be useful to achieve near isothermal conditions and was reported to support the validity of the indirect method even in relaxors [185]. However, $P(E)$ loops at other frequencies were not reported and similar comparison of loops (see Fig. 2.3) between different frequencies is lacking. In this context, careful reexamination of the experimental data is strongly recommended in the future studies.

In addition, deeper insights into the contributions of ferroelectric switching [186, 187], domain growth [188, 189], and domain wall [190–193] to the electrocaloric effect are highly desired in order to provide basic understandings. For instance, a recent study using non-adiabatic direct measurement on PZT-5 ceramics showed that ΔT displays a hysteresis behavior with E and the sign of electrocaloric effect reverses at coercive field where polarization switching occurs [186]. Using phase field method, similar $\Delta T - E$ curves were predicted in PbTiO_3 nanoparticle in which vortex domain switching was considered [187]. Moreover, phase field theory predicted a sign reversal of electrocaloric response at the domain walls (180 degree in Ref. [188] and 90 degree in Ref. [189]). However, this does not necessarily indicate the coexistence of both negative and positive electrocaloric effects can really exist. The existence of remarkable ΔT gradient across the domain walls will immediately lead to fast heat exchange between different domains and therefore only a pure positive or negative electrocaloric effect should be observed with a significantly reduced ΔT .

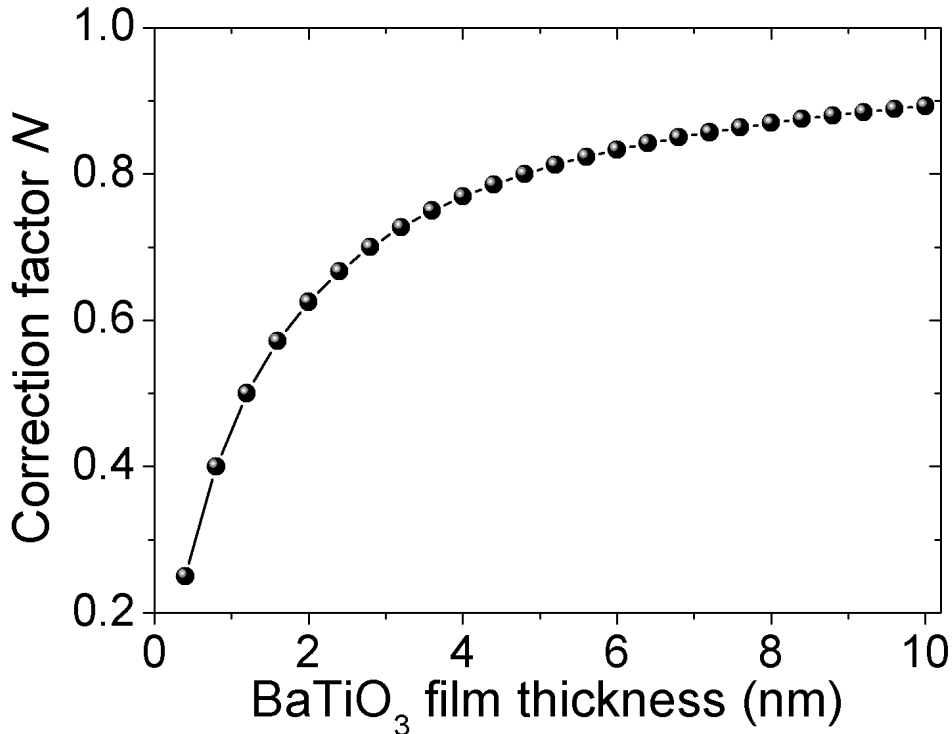


Figure 2.7: The thickness dependence of the correction factor N originated from the depolarizing field in epitaxial (001)-oriented BaTiO₃ thin films.

2.2.7 Depolarizing field

It is known that in magnetocaloric refrigeration, the magnetocaloric response usually needs to be corrected by taking into account the demagnetizing field [194–198]. Considering the case of the depolarizing field in ferroelectrics, its influence on electrocaloric properties is ignored in most studies. This is because for strongly polar materials, such as ferroelectrics, $D \sim P$, one can have $(\frac{\partial D}{\partial T})_E \approx (\frac{\partial P}{\partial T})_E$ and therefore may validate the use of Eq. (2.1). However, this is not the case for ultrathin films in which the depolarizing field due to incomplete screening from the electrode has to be taken into account [199]. The electrocaloric effect in ultrathin ferroelectric films was systematically studied by taking into account the film thickness, electrode, mechanical stress and depolarizing field [47, 166, 200, 201]. For instance, Liu *et al.* [166] found that such approximation is only valid for a film thickness h being relatively big ($h > 4.8$ nm). The correction factor N (see Fig. 2.7) describing the deviation between the two derivatives such that $(\frac{\partial D}{\partial T})_E = N(\frac{\partial P}{\partial T})_E$ is introduced [166]. N can be written as $N = 1 - \frac{2\varepsilon_b\lambda}{h\varepsilon_0 + 2\lambda\varepsilon_b}$ where the second term arising exactly from the contribution of depolarizing field [47, 166, 200, 201] (ε_b is the background dielectric constant, and ε_0 is the permittivity of free space. λ is the effective screening length of ferroelectric/electrode interface). When h decreases down to the

critical thickness h_c , N experiences a sharp drop, which clearly indicates that the effect of the depolarizing field becomes dominant (see Section 3.1.4).

Tuning the electrocaloric effect by adjusting the magnitude of the residual depolarizing field has been reported recently in $\text{Pb}(\text{Zr}_{0.4}\text{Ti}_{0.6})\text{O}_3$ nanodots by Prosandeev *et al.* [167]. Similarly, the depolarizing field is found to play a major role in determining the electrocaloric properties and is especially detrimental for the thinner films since it cancels out a large part of the external electric field [166]. This conclusion is reached by considering only the single domain configuration. Moreover, Glazkova *et al.* revealed a positive effect of residual depolarizing field on the electrocaloric effect, which is attributed to formation of nanodomain in ultrathin ferroelectric thin films [202]. Also note that strict Maxwell relation $(\frac{\partial S}{\partial E})_T = (\frac{\partial D}{\partial T})_E$ was also frequently employed to derive ΔT in organic materials (Refs. [46, 149] and references therein) while there are also some studies using the relation $(\frac{\partial S}{\partial E})_T \approx (\frac{\partial P}{\partial T})_E$ even in nanoscale organic films [203]. The difference in calculating ΔT originated from these two different relations was unknown since it was not explicitly discussed in these works (Refs. [46, 149, 203] and references therein).

2.2.8 Clausius-Clapeyron method

In addition to indirect method based on the Maxwell relationships, Clausius-Clapeyron method can be also used for first-order phase transition [8]. This approach represents a nominally equivalent indirect method as that based on the Maxwell relationships, and it remains rarely employed to extract the electrocaloric effect in the literature. Moreover, the Clausius-Clapeyron equation can be used to evaluate the contributions from the latent heat of the first order phase transition which is not included in Eq. (2.1) (Ref. [171]). In this approach, the temperature dependence of equilibrium transition temperature T_0 and then values of entropy changes for the fully driven transition can be obtained using the Clausius-Clapeyron equation below [Eq. (2.4)], in which order parameter changes across first-order phase transitions is denoted by the subscript “0”: [8]

$$\Delta S_E = \Delta D_0(dT_0/dE)^{-1}, \quad (2.4)$$

2.3 DIRECT MEASUREMENTS

At first glance, the direct approach measurement can inspire more confidence for the design of electrocaloric devices. However, in practical cases there are several factors making it difficult to achieve perfect adiabatic conditions. This difficulty in using direct method can be readily seen according to the statistic result obtained from Web of Science as summarized in Fig. 2.8. Specifically, experimental studies using direct measurements only comprise less than 15% (about 50 articles) of the total articles entitled “electrocaloric” while most works (about 85%) were conducted by using indirect measurements. Most works are carried out to search new materials and improve their properties, whereas only few concepts for electrocaloric refrigeration and heat pump have been proposed (see the review in Ref. [117] or Chapter 10 in Ref. [6]). These data not only imply that direct measurement is challenging but also clearly reflects the current research

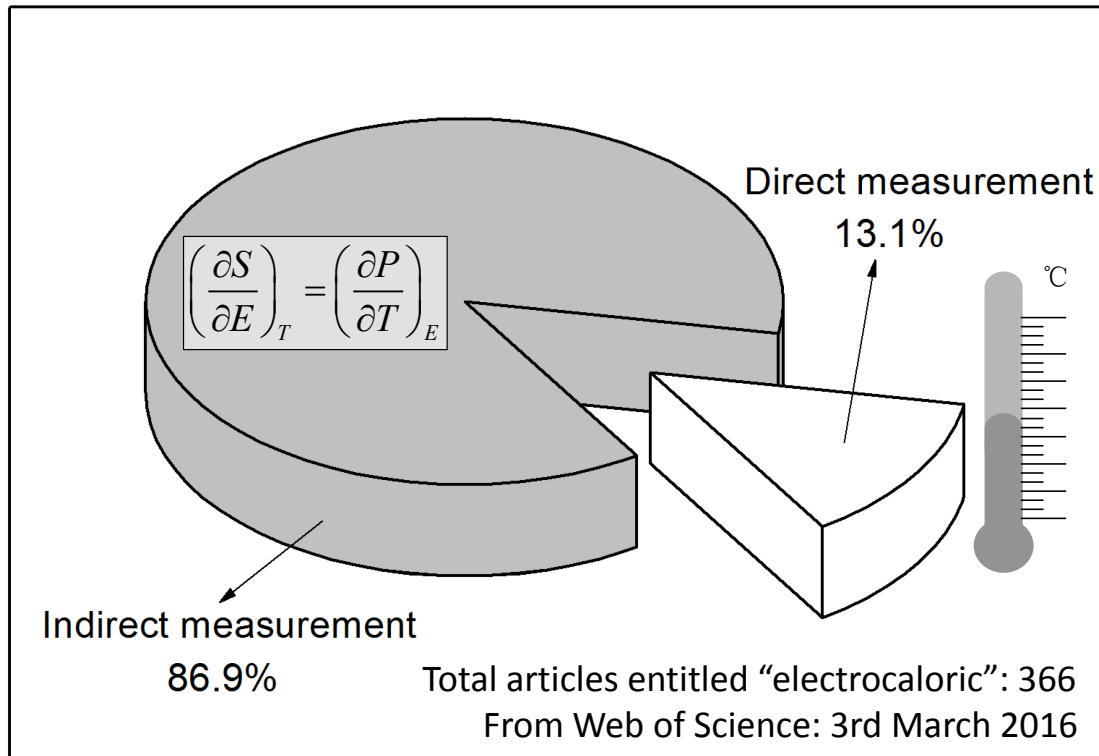


Figure 2.8: Statistic result on the electrocaloric publications including direct and indirect measurements according to the Web of Science.

stage of the electrocaloric effect. This is also one reason why indirect measurements dominate this review. Because the topic of electrocaloric effect is increasing interest since 2006 (see Figure 1 in Ref. [8]), Fig. 2.8 also underlines the need to pursue more efforts into the direct measurements and design of electrocaloric cooling devices. Previous sections have provided critical insights into the indirect measurements, which should be useful to understand and quantify the electrocaloric effect. Regarding the direct measurements which have been reviewed in detail in previous publications [5, 111, 116], here we only give a brief overview of several direct techniques in order to avoid unnecessary repetition. Specifically, we will mainly focus on IR camera.

Typical result by direct measurement (such as thermocouple or thermometer, specifically designed calorimeter, IR camera, scanning thermal microscopy and so on) is schematically shown in Fig. 2.9. The thermal isolation of the sample is the key factor in the direct measurements. For instance, in perfectly adiabatic conditions, the sample temperature should remain constant after the electrocaloric effect is activated (dashed line in Fig. 2.9), and the electric field is applied or removed instantaneously in contrast to the isothermal measurement carried out under nearly equilibrium conditions. However, in practical situations, the thermal exchange between the elec-

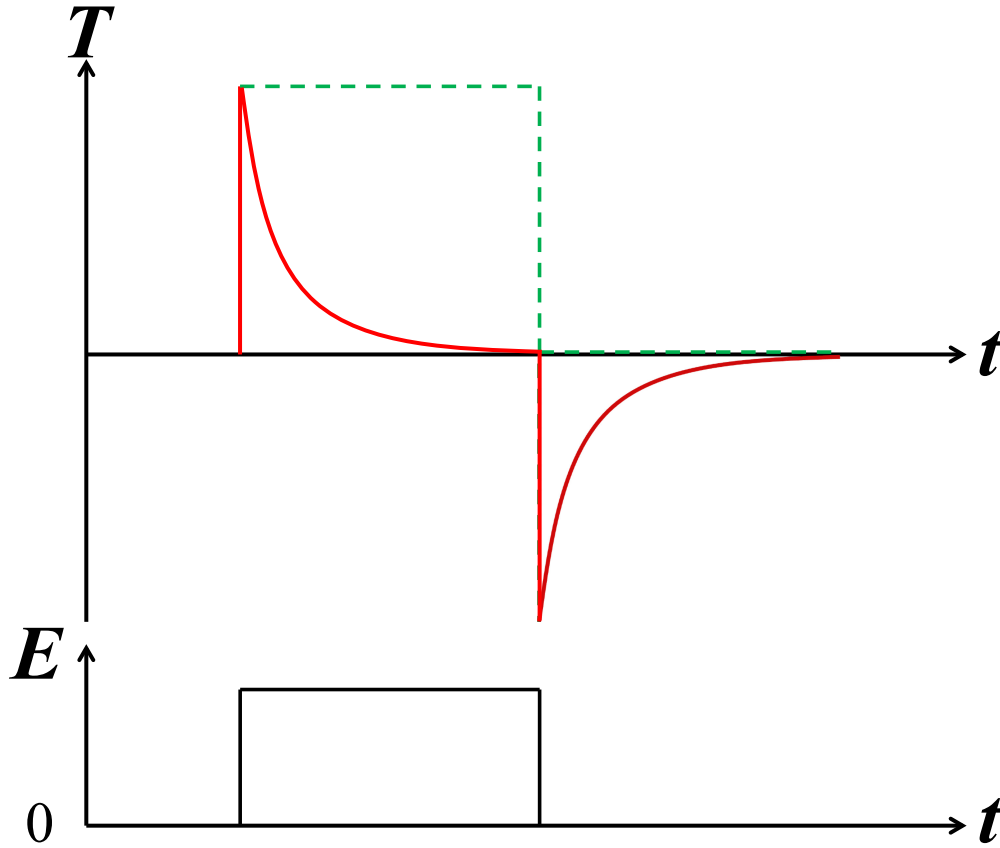


Figure 2.9: Typical electrocaloric effect as a function of time measured directly under near adiabatic conditions; the dashed line indicates the ideal electrocaloric response under perfectly adiabatic conditions.

trocaloric materials and the surroundings always exists, which leads to exponential decay of the electrocaloric peak with measurement time (see solid line in Fig. 2.9). In this case, it is usually required that the characteristic time constant for the application (or removal) of the field should be significantly smaller than the time constant for heat exchange between sample and ambient environment in order to achieve near adiabatic conditions. This requirement can be met in bulk in most cases but fails in thin films with substrates, which makes direct determination of electrocaloric temperature change extremely challenging in thin films. As a result, it can be seen in Table 2.1 that only two experimental results were reported on nanoscale thin films [204, 205] during the past ten years while most other works carried out direct measurement on thick films with a thickness of few micrometers or bulk, including ceramics and single crystals. It would either require the device to be engineered with a thinner substrate, a thermal barrier and a greater film volume fraction, or demand technological achievements to get precise thermal measurements (as in pyroelectric detector devices). More importantly, reasonable calibration has always to be considered to compensate for unavoidable thermal losses during the measurements.

Table 2.1: Comparison of typical results by direct measurement on electrocaloric effect in thin and thick films

| Material | h [μm] | T [$^{\circ}\text{C}$] | ΔE [kV/cm] | ΔT [K] | $\Delta T/\Delta E$ [K cm/kV] | Method |
|--|--------------------------|-------------------------------|-----------------------|-------------------|----------------------------------|-------------|
| (Pb _{0.86} La _{0.08})(Zr _{0.65} Ti _{0.35})O ₃ | 0.45 | 45 | 1200 | 40 | 0.033 | SC[204] |
| PbZr _{0.8} Ti _{0.2} O ₃ | 0.15 | 25 | 67 | 0.1 | 0.0015 | SC[205] |
| BaZr _{0.8} Ti _{0.2} O ₃ | 12 | 40 | 97 | 4.9 | 0.051 | SC[206] |
| 0.9PMN-0.1PT | 13 | 25 | 105 | 0.23 | 0.0022 | SThM[185] |
| (Cd _{0.83} Pb _{0.17}) ₂ Nb ₂ O ₇ MLCs | 45 | -179 | 100 | 0.8 | 0.008 | SC[207] |
| Pb(Sc _{0.5} Ta _{0.5})O ₃ MLCs ^{a)} | 64-72 | 18 | 125 | 3.5 | 0.028 | SC[45] |
| Doped BaTiO ₃ MLCs | 6.5 | 47 | 300 | 0.5 | 0.0017 | TC[208] |
| BaTiO ₃ MLCs | 1.4 | 80 | 176 | 1.8 | 0.010 | DSC[209] |
| BaTiO ₃ MLCs | 1.4 | 80 | 800 | 7.1 | 0.0089 | DSC[210] |
| P(VDF-TrFE) 68/32 mol. % | 10-15 | 33 | 1600 | 20 | 0.0125 | SC[204] |
| P(VDF-TrFE-CFE) ^{b)} | 4-6 | 30 | 1500 | 16 | 0.011 | SC[211] |
| P(VDF-TrFE-CFE) ^{c)} | 50 | 27 | 1000 | 4 | 0.004 | DSC/IR[212] |
| P(VDF-TrFE-CFE) ^{d)} | 11-12 | 25 | 900 | 5.2 | 0.0058 | IR[213] |
| Terpolymer/BNNSs/BST67 ^{e)} | 6 | 30 | 2500 | 50.5 | 0.0202 | SC[214] |
| P(VDF-TrFE) /BST75 ^{f)} | 80 | 79 | 600 | 2.5 | 0.0042 | DSC[215] |
| Terpolymer ^{g)} /PMN-PT | 7-15 | 30 | 1800 | 31 | 0.017 | SC[52] |
| Polymer ^{h)} /graphene | 11 | 25 | 400 | 5.2 | 0.013 | SC[216] |

^{a)} Pb(Sc_{0.5}Ta_{0.5})O₃ was modified by doping Co and Sb; ^{b)} The terpolymer P(VDF-TrFE-CFE) content is 59.2/33.6/7.2 mol.%; ^{c)} The terpolymer P(VDF-TrFE-CFE) was purchased from Piezotech SA with the composition not reported; ^{d)} The terpolymer P(VDF-TrFE-CFE) content is 62.6/29.4/8 mol.%; ^{e)} Terpolymer refers to the relaxor ferroelectric P(VDF-TrFE-CFE) with a composition of 62.3/29.9/7.8 mol.%, BNNSs refers to Boron nitride nanosheets (9 vol.%) and BST67 refers to Ba_{0.67}Sr_{0.33}TiO₃ (8 vol.%); ^{f)} P(VDF-TrFE) 52/48 mol.% and Ba_{0.75}Sr_{0.25}TiO₃ (10 vol.%); ^{g)} Terpolymer refers to P(VDF-TrFE-CFE) (59.4/33.4/7.2 mol.%) and PMN-PT refers to 0.9PMN-0.1PT nanoparticles with the content of 37.5 wt%; ^{h)} (VDF-TrFE-CFE)/P(VDF-TrFE) 90/10 wt.% blend and graphene (1.0 wt.%). In the method column, SC, SThM, TC, DSC and IR indicate specific calorimeters, scanning thermal microscopy, thermocouple, scanning thermal microscopy and infra-red camera.

2.3.1 Thermocouple and thermometer

A thermocouple (based on thermoelectric effect) or thermometer (based on various principles) is a simple device to determine the temperature and electrocaloric temperature change. Usually, it is attached on a bulk sample using thermally conducting paste in order to meet good thermal contact between the sample and the thermocouple/thermometer [48, 153, 154, 156, 208, 217]. Otherwise, thermal losses may lead to the measurements conducted in non-adiabatic conditions [186]. Thermocouple or thermometer by itself cannot be used to provide reliable determination of the electrocaloric effect in thin films and is sensitively influenced by the surroundings. However, thermocouple or thermometer can be integrated into calorimeter system (i.e. high-resolution calorimeter [116, 152, 204, 218], and scanning thermal microscopy [185, 217]) as one of the key elements to achieve high-resolution probe of the electrocaloric effect even in thin films.

2.3.2 Differential Scanning Calorimetry

Modified DSC calorimetry can provide a good and precise characterization of electrocaloric heat of samples in quasi-isothermal conditions. Different from the standard mode measuring zero-field heat capacity, modified DSC calorimetry evaluates the heat flow dQ/dE by applying an electric field at a controlled temperature [48, 139, 151, 168, 209, 210, 212]. The electrocaloric heat can be then obtained by $Q = \int_0^E dQ/dE' dE'$, which corresponds to the area of the exothermic (endothermic) peak. Therefore, the entropy change can be determined by $\Delta S = Q/T$. To obtain the temperature dependence of heat flow, this procedure is repeated at different measurement temperatures from cooling or heating. Due to the thermal conduction of the apparatus, a long waiting period is usually required to stabilize the temperature before the electrocaloric measurement starts. Therefore, this approach is a slow measurement. The thermal losses from imperfect thermal contact between a sample and DSC sensors should be taken into account [139, 151, 168]. In addition, a quasi-direct method by measuring the heat flow dQ/dT at fixed finite field was also reported [48]. Further information about various DSC setups can be found elsewhere (Refs. [48, 139, 151, 168, 209, 210, 212] and references therein).

As long as the temperature dependence of entropy change is given by the DSC method, the temperature change is often calculated by $\Delta T = T\Delta S/C(0)$ where a constant zero-field and temperature-independent $C(0)$ is used (Refs. [48, 139, 151, 168, 209, 210, 212] and references therein). As we analyzed in Section 2.2.6, this inappropriate assumption is not supported by recent experimental and theoretical evidence [123, 125, 164, 171, 178–181]. Indeed, a very similar issue was already discussed comprehensively in the magnetocaloric community. For instance, Pecharsky and Gschneidner addressed in detail [219] that the unrealistic assumption (that heat capacity is magnetic-field independent) may fail to yield a reasonable approximation for magnetocaloric temperature change. Moreover, they suggested an approach by combining heat capacity and magnetization data to extract temperature change. And even for obtaining the entropy change by integrating the measured heat from DSC, the deleterious effects of intrinsically inaccurate heat capacity should also be eliminated or minimized with caution especially for first-order transition [220]. One practical route to ensure reasonable and useful data obtained

by DSC is to compare it with other direct measurements or from indirect data based on proper isothermal curves. This demands to modify the application mode of DSC further to determine the field-dependence of heat capacity or combine other techniques available.

2.3.3 Specifically designed calorimeters

A specific calorimeter sensor was developed by Zhang's group [204]. The operational principle is to compare the electrocaloric heat originated from samples to the heat generated by a reference resistor. The reference resistor heater attached to the samples with the same integrated areas produces a Joule heat which can be detected by IR sensor or heat flux sensor. For instance, the voltage signal peaks, detected by the heat flux sensor and then amplified by the low-noise preamplifier, can be observed by the oscilloscope (Refs. [52, 214] and references therein). The integrated areas of the peaks correspond to the amount of heat released or absorbed by the reference resistor (Refs. [52, 214] and references therein). When the electrocaloric effect is induced in the samples, the electrocaloric heat released or absorbed is then calibrated by this reference resistor and ΔT can be finally obtained through simple calculations. This technique is useful for bulk samples and thick films ($>1 \mu\text{m}$). Another specific calorimeter called high-resolution calorimeter was recently developed by Kutnjak *et al.* to directly measure the electrocaloric effect [116, 125, 152, 164, 204, 218]. High-resolution calorimeter was firstly used to determine the field-dependence of latent heat to study the phase transitions in relaxors [180]. The latent heat can be extracted by comparing results of ac mode and the relaxation mode [116, 125, 180, 181, 221]. Moreover, the modified calorimeter is shown to be useful not only in probing the electrocaloric response for bulk including single crystals and ceramics [116, 125, 137, 138, 152, 164, 218] but also for thin films [204]. The readers are recommended for further details to [5, 116].

In addition to these two specific calorimeters, there are other examples available according to the literature. For instance, laser-based calorimeter using temperature-dependent reflectance measurements of the top metal (additionally sputtered on the top electrode of the thin films) was used to characterize the electrocaloric effect directly in nanometer-scale thin films [205]. The experimental results revealed an invisible contribution arising from elastocaloric effect related to substrate clamping through the piezoelectric coefficient of thin films, which is not necessarily taken into account into Eq. (2.1) (see Ref. [205]). In other words, Eq. (2.1) using the polarization as the order parameter under proper mechanical boundary conditions [123, 124] may fail to describe the electrocaloric effect. Finally, a homemade calorimeter using a microfabricated resistance thermometer (integrated onto the substrate) was developed by Jia *et al.* to provide direct measurement on electrocaloric effect in organic thick films [126]. In addition, a new pyroelectric method was proposed to measure the pyroelectric coefficient through pyroelectric current measurement and electrocaloric response through the converse relation between electrocaloric effect and pyroelectric effect [222, 223].

2.3.4 Infra-red camera

Compact and fast IR camera (see the experimental setup in Fig. 2.10) can provide an accurate and sensitive imaging of caloric effects both temporally and spatially [62, 86, 212, 213, 217, 224–227]. Typically, the camera consists of an arrangement of lenses with a digital detector semiconductor (i.e., InSb) having a broadband spectral sensitivity of several micrometers. Thermal images captured by the camera usually have an effective spatial resolution of several micrometers with a thermal sensitivity of about 25 mK. The IR camera is calibrated with black-body calibration by the provider. For caloric measurements, the frame frequency describing the capability of the camera to capture thermal change is one of the key parameters since it is correlated to the measurement conditions. For instance, higher frequencies (i.e. 100 Hz) can ensure the adiabatic conditions in most of measurements on bulk materials [62, 86, 212, 213, 217, 224–227]. In this case, the camera is sensitive enough to capture thermal change in each pixel in near adiabatic conditions.

To ensure the high accuracy in temperature measurements, it is usually required that the surface of samples is flat since the surface emissivity is strongly related to its roughness. In the case of a rough surface, the corresponding thermal image recorded by the camera will represent a false profile of inhomogeneity in temperature before the caloric effect is driven by an external stimulus [217]. This can be overcome by measuring the intensity of the thermal radiation at two adjacent temperatures and interpolating linearly but at expense of the high accuracy temperature measurements [217]. This can be also achieved by manually adjusting the emissivity of different selected regions without compromising the resolution of camera (see Chapter 4), which corresponds to setting the temperature of sample to a specific measurement temperature. As mentioned above, IR camera has been frequently used to measure the magnetocaloric, elastocaloric and electrocaloric effects according to the literature [62, 86, 212, 213, 217, 224–227]. Recent studies specifically demonstrated that IR imaging as a function of real time and magnitude of stimulus can provide reliable data for caloric response with good precision [62, 212, 217, 225]. For instance, in order to ensure the reliability of this technique, data obtained by IR camera are compared with those from the thermocouple [62, 217, 225] and DSC measurements [212] and were found to be consistent. A non-contact IR camera is compact and fast compared to other techniques i.e., DSC, and its use is rather simple. More importantly, IR camera can directly image spatial caloric response, which is the main advantage over other techniques such as DSC, thermocouple, and other specifically designed calorimeters. An IR camera is very sensitive to the surroundings; the people who are carrying out this kind of measurement not mentioning the inevitable temperature variation in a day. This makes temperature dependence of measurement difficult since the temperature fluctuations can directly contribute to the thermal images of the camera if no thermal shield is arranged. In addition, IR measurement is usually limited in a temperature window [about 0-100 °C] near room temperature.

In addition to temporal resolved measurement, spatial thermal image captured by IR camera is an ideal noncontact tool to explore the distribution of temperature profiles subjected to external stimulus such as uniaxial stress [225–228]. In this case the thermal response is correlated with structural degrees of freedom of materials, which can be very useful to study the microstructure dynamics such as nucleation [225, 227]. Spatially resolved measurements have been conducted to

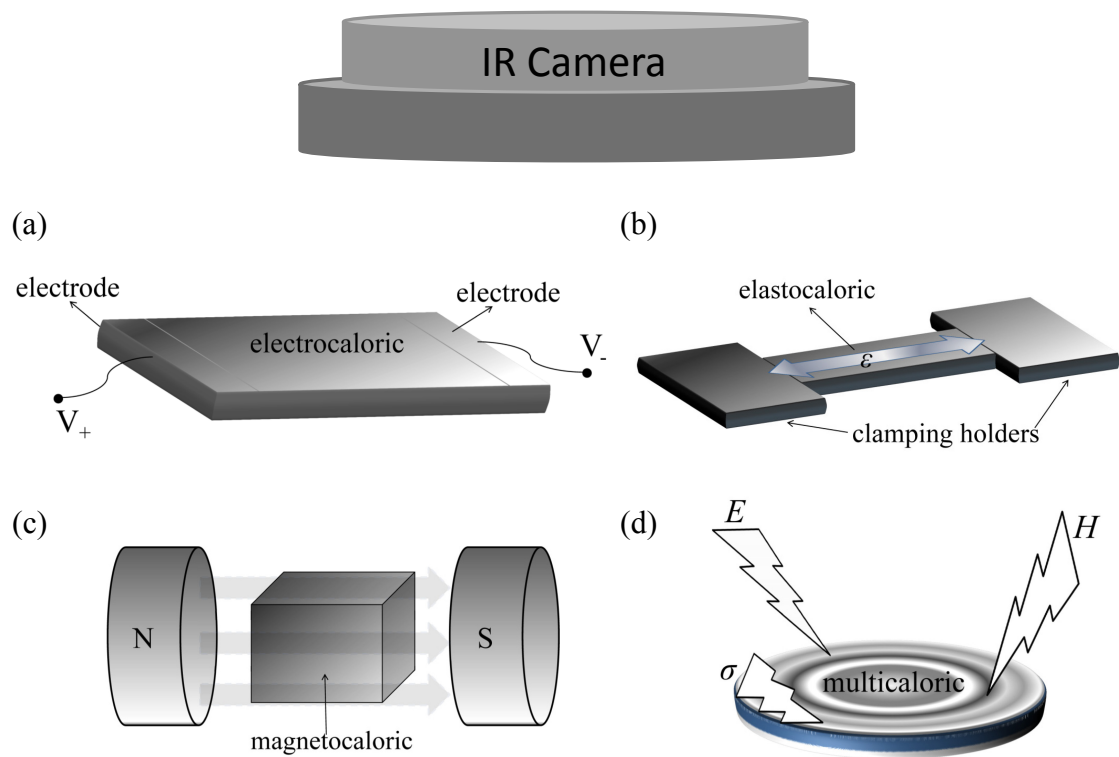


Figure 2.10: Schematics of IR measurement set-up for direct image of (a) electrocaloric effect, (b) elastocaloric effect (ϵ is strain and the arrow indicates its direction), (c) magnetocaloric effect (H refers to magnetic field from the magnets) and (d) multicaloric effect (σ indicates uniaxial stress), respectively.

study the local inhomogeneities of elastocaloric and magnetocaloric responses [224–227]. However, similar studies on electrocaloric effect are rarely reported. In turn, electrocaloric effect is always characterized by an isotropic ΔT with a homogeneous distribution along the sample in the literature except for very few studies [217, 229, 230]. For instance, it was reported that uniaxial $\text{Sr}_{0.75}\text{Ba}_{0.25}\text{Nb}_2\text{O}_6$ and $\text{Pb}(\text{Mg}_{1/3}\text{Nb}_{2/3})\text{O}_3\text{-PbTiO}_3$ relaxor single crystals display anisotropy of electrocaloric cooling (about 0.20–0.25 K) due to strong anisotropic polar direction [229] and different crystal orientations [230], respectively. In addition, extrinsic variation of electrocaloric effect (approximately 0.2 K) due to specific geometry in multilayer capacitors was observed between the metallic terminals and electrocaloric active ceramic regions in multilayer capacitors [217]. This underlines that spatially distributed electrocaloric effect should exist over the multilayer capacitors in contrast to theoretical assumptions [231, 232]. Moreover, using IR camera Liu *et al.* revealed the existence of a significant variation of electrocaloric effect up to 0.285 K between central region and the region near the terminals (see Chapter 4). This result corresponds to about 50% of the average value in the sample, which is larger than the previous ones on anisotropy and inhomogeneity of electrocaloric cooling [217, 229, 230].

Let us briefly recall that current interest in design of electrocaloric prototypes is mainly based on multilayer capacitors. The multilayer capacitors consist of around 200 ceramic layers of thickness about 10 μm separated by interdigitated inner electrodes with a thickness of several μm . The electrocaloric effect in multilayer capacitors was already reported [45, 207]. But it is only recently that the promise of multilayer capacitors in practical electrocaloric refrigeration was addressed [121, 208, 209, 231] and was regarded as one of the main breakthroughs in this field [84]. Using multilayer capacitors is a successful compromise allowing high breakdown field and relative large electrocaloric active volume. Moreover, electrocaloric refrigerator prototypes based on multilayer capacitors were designed confirming the potential of multilayer capacitors for real cooling applications [118, 119, 121, 233]. In this case, IR camera is a powerful tool to detect the dynamic performances of multilayer capacitors i.e. the electrocaloric response under the external fields with different shapes and frequencies [234], the contributions of Joule heating [127, 235] as well as the electrocaloric fatigue properties under cyclic operating. These unexplored data are extremely desirable to the design of electrocaloric prototypes.

Note that understandings of the heat flow behavior in specific caloric prototype device are crucial to optimize the refrigeration efficiency [176]. For instance, control of heat flux direction in active magnetic regeneration in an effective manner can be very useful to enhance the operating frequency and thus the power density of the device [236]. Direct thermal mapping captured by IR camera allows analyzing quantitatively the dynamic heat flux in one specific prototype devices according to distributions of adiabatic temperature change. For instance, the electrocaloric heat flow in multilayer capacitors is found to be mainly bidirectional but is transferring inhomogeneously between the central ceramic layers and the terminals (see Chapter 4). To be specific, the electrocaloric heat is mainly transferred in a path along interdigitated inner electrodes away from (towards) the terminals and it is weakly dissipated in the direction along the terminals in a complex manner. Further studies to directly quantify this inhomogeneous heat flux are desirable by solving the heat equations. As a result, a sustained cooling power of 0.037 kW/m^2 is experimentally obtained based on spatially resolved imaging of temperature gradient, which is smaller than recent theoretical simulations [208, 231]. In addition, we note that IR camera

is also capable of measuring the multicaloric effect [see Fig. 2.10(d)] driven by either single stimulus [10] or multiple stimuli (applied/removed simultaneously or sequentially) [8].

2.3.5 Scanning thermal microscopy

Based on scanning probe microscopy, scanning thermal microscopy is a useful technique permitting the thermal probing of the submicron heat transfer behavior of materials and devices [237, 238]. Recently, Kar-Narayan *et al.* introduced this approach for directly measuring the electrocaloric effect in multilayer capacitors [217] and relaxor thin films [185]. In the measurement set-up, the atomic force microscope tip is not in contact with the samples. A small resistance thermometer deposited in the tip is used to detect the temperature change through tip-sample heat transfer when the electric field is applied and removed. It was also found that the measured temperature change and its shape with respect to time strongly depend on the distance between tip and is specifically measured region in both studies [185, 217]. The measurement can be conducted quickly with a resolution of temperature being 80 mK [217]. Scanning of the tip can therefore provide the spatial resolution of electrocaloric response of the sample, like the IR camera. Near adiabatic conditions can be met when active electrocaloric active volume is large, e.g. in multilayer capacitors [217]. However, measurements in thin films (13 and 38 μm) suffer from non-adiabatic conditions due to the rapid heat exchange between the film and underneath substrate [185]. Obviously, further works exploiting this technique are needed in future.

2.4 CLOSING REMARKS

Critical insights into the indirect approach which is widely used without criticism are summarized here incorporating recent theoretical and experimental advances, which is dedicated to prolong any unnecessary misunderstandings or feud. The role of field dependence of heat capacity is addressed while no definitive answer to a reliable approach to select proper $P(E)$ loops is provided. Generally, it is yet required to take into account the important effects such as ferroelectric switching, kinetics such as measurement frequency, electrical hysteresis losses between application and removal of electric field, thermal hysteresis associated with first-order phase transition between cooling and heating processes and so on. This obviously demands further studies. Nevertheless, indirect measurement based on Maxwell relation could provide general trends to analyze the behavior of electrocaloric responses and might be useful to compare different results obtained from the same class of materials. It may be still useful acting as an approximate tool to estimate the electrocaloric effect at current research stage.

Ultimately, direct measurements of heat and temperature change are highly desired for indisputable proof of electrocaloric effect at this stage. In particular, we address the promise of IR camera in directly imaging electrocaloric effect from material characterization to design of electrocaloric prototypes. The commercial feature makes this technique competitive for providing a reliable experimental data, at least comparable from a research group to another. Finally, we hope that our review can be found useful in some aspects and read as an inspiration for the fast

growing interest in the field of electrocalorics.

- CHAPTER 3 -

ELECTROCALORIC EFFECT IN FERROELECTRICS AND ANTIFERROELECTRICS

In this chapter, we firstly present our detailed results on electrocaloric effect in ferroelectric tunnel junctions in Section 3.1. Then, we show the negative electrocaloric effect in antiferroelectric La-doped $\text{Pb}(\text{ZrTi})\text{O}_3$ thin films in Section 3.2. Finally, we discuss the electrocaloric properties of lead-free ceramics in Section 3.3. All these works conducted either theoretically or experimentally focus on room-temperature electrocaloric effect exploited for fundamental insights for designing electrocaloric cooling devices.

3.1 ELECTROCALORIC EFFECT IN FERROELECTRIC TUNNEL JUNCTIONS

3.1.1 Ferroelectric tunnel junctions: the role of built-in electric field

3.1.1.1 Introduction

Ferroelectric tunnel junctions (FTJs) that are composed of ferroelectric thin films of a few unit cells sandwiched between two electrodes (in most cases the top and bottom electrodes are different) have attracted much more attention during the last decade [239–242]. It is generally believed that the interplay between ferroelectricity and quantum-mechanical tunneling plays a key role in determining tunnel electroresistance (TER) or tunneling current and the TER effect usually takes place upon polarization reversal. Due to the strong coupling of ferroelectric polarization and the applied field, the electric-field control of TER or tunneling current [239–241, 243–250], spin polarization [251–265], and electrocaloric effect [47] can be achieved, which makes ferroelectrics promising candidates for nondestructive ferroelectric storage [239–249], ferroelectric memristor [250], spintronics (magnetization) [251–265], or electrocaloric [47] devices. Meanwhile, another mechanically (including strain or strain gradient) induced TER is found recently, which also shows its potential applications in mechanical sensors, transducers and low-energy archive data storage devices [266, 267]. Note that having different electrodes for the

FTJs (some experiments use conductive atomic force microscope tips instead of the top electrodes) is usually required for a large effect at low bias voltage, although the FTJs with the same electrodes may also display interesting performances [240, 243, 248, 257]. Also note that all the functionalities in these devices are strongly related to the thermodynamic stability and switching ability of FTJs [47, 239–241, 243–267]. Therefore, a fundamental understanding of ferroelectricity of FTJs, especially their size effects, is crucial at the current stage of research.

Unfortunately, no consensus has been achieved on whether there exists a critical thickness h_c below which the ferroelectricity disappears in FTJs, especially for those with different top and bottom electrodes. It is believed that an electrostatic depolarizing field caused by dipoles at the ferroelectric-metal interfaces is responsible for the size effect [199, 268–272]. However, recent theoretical studies suggest that the choice of electrode material may lead to smearing of size effect or even vanishing of h_c [273–277]. For example, it was reported that choosing Pt as electrodes would induce a strong interfacial enhancement of the ferroelectricity in Pt/BaTiO₃(BTO)/Pt FTJs, where h_c is only an 0.08 BTO unit cell [273]. In addition, the results of a modified thermodynamic model [274, 275] and first-principles calculations [276, 277] both indicate that the BTO barrier with dissimilar electrodes, i.e., Pt and SrRuO₃ (SRO) electrodes, might be free of deleterious size effects. In contrast, it has been reported that asymmetric combination of the electrodes (including the same electrodes with different terminations) will result in the destabilization of one polarization state making the asymmetric FTJs non-ferroelectric [271, 278]. And the up-to-date studies reported that the fixed interface dipoles near the ferroelectric/electrode interface is considered the main reason for that detrimental effect [279, 280]. Considering the importance of the physics in FTJs with dissimilar top and bottom electrodes, we are strongly motivated to investigate the size effect in such asymmetric FTJs.

It was pointed out as early as 1963 that the contribution of different electronic and chemical environments of the asymmetric electrode/ferroelectric interfaces would induce a large long-range electrostatic built-in electric field \vec{E}_{bi} in ferroelectric thin films [281]. \vec{E}_{bi} becomes more significant in asymmetric FTJs and should be taken in to account. [271, 272] In this study, we use a multiscale thermodynamic model [47, 271, 272] to investigate the effect of such built-in electric field on the phase transition of asymmetric FTJs by neglecting the short-range interface dipoles. As a result, we discover an unusual ferroelectric-“polar non-ferroelectric” phase transition in asymmetric FTJs. Then, we make a detailed analysis of the contribution of the built-in electric field to ferroelectric phase transition, i.e., h_c , what happens below h_c , transition temperature T_c , and temperature dependence of dielectric response of the asymmetric FTJs.

3.1.1.2 Multiscale thermodynamic model

We concentrate on a short-circuited (001) single-domain ferroelectric plate of thickness h sandwiched between different electrodes. The ferroelectric films are fully strained and grown on thick (001) substrate with the polar axis lying normal to the ferroelectric-electrode interfaces [270–272]. We denote the two interfaces as 1 and 2, with surface normals \vec{n}_1 and $\vec{n}_2 = -\vec{n}_1$ pointing into the electrodes. The configurations are schematically shown in Fig. 3.1. The exact value

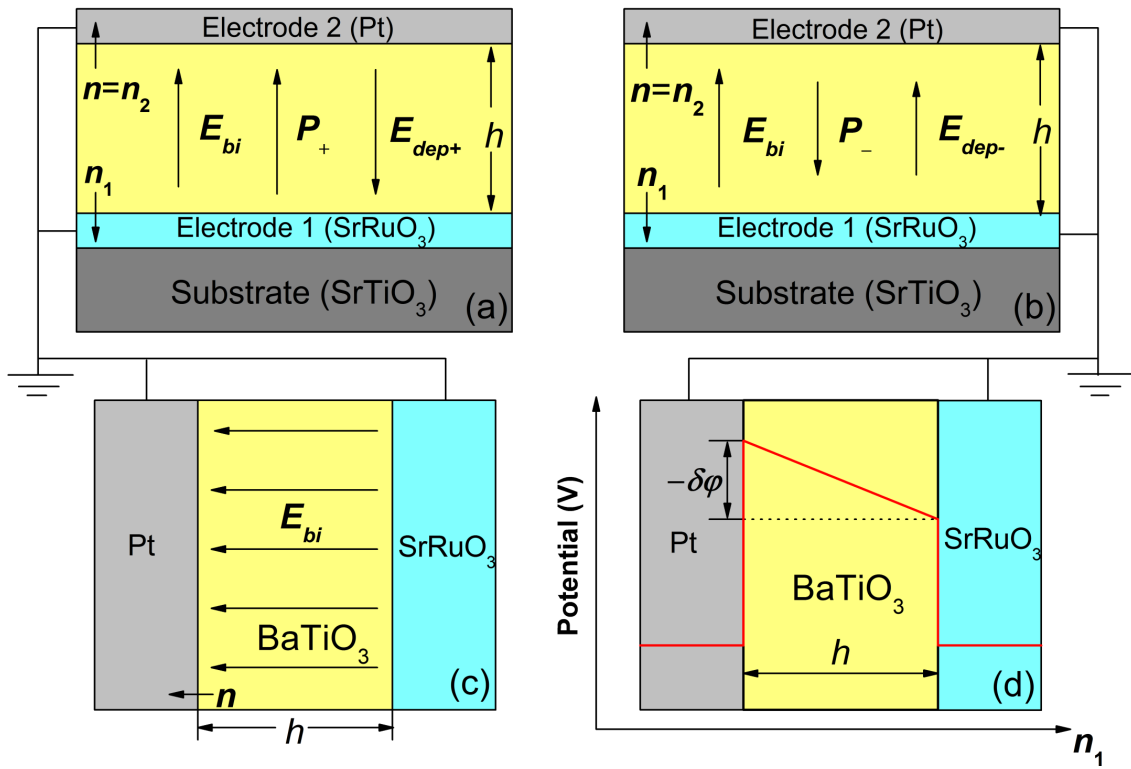


Figure 3.1: Schematic configurations of the system considered in the present calculations for the asymmetric FTJs: P_+ state (a); P_- state (b); \vec{E}_{bi} (c) and the corresponding potential profile at zero polarization (red line) (d).

and direction of \vec{E}_{bi} can be determined as [271, 272]

$$\vec{E}_{bi} = -\frac{\Delta\varphi_2 - \Delta\varphi_1}{h}\vec{n} = -\frac{\delta\varphi}{h}\vec{n} \text{ and } \vec{n} = \vec{n}_2 = -\vec{n}_1, \quad (3.1)$$

where $\Delta\varphi_i$ which is the work function steps for ferroelectric-electrode i interface at zero polarization is simply defined as the potential difference between the ferroelectric and the electrode i [271, 272]. With the help of first-principles calculations, one could easily obtain $\Delta\varphi_i$ through the analysis of the electrostatic potential of FTJs where ferroelectric films are in the paraelectric state [271, 272].

Then, the free energy per unit surface of the ferroelectric layer is presented as [271, 272]

$$\begin{aligned} F &= h\Phi + \Phi_S = \left(\frac{1}{2}\alpha_1^*P^2 + \frac{1}{4}\alpha_{11}^*P^4 + \frac{1}{6}\alpha_{111}P^6\right. \\ &+ \frac{1}{8}\alpha_{1111}P^8 + \frac{u_m^2}{S_{11} + S_{12}} - \frac{1}{2}\vec{E}_{dep} \cdot \vec{P} - \vec{E}_{bi} \cdot \vec{P} \\ &\left. - \vec{E} \cdot \vec{P}\right)h + (\zeta_1 - \zeta_2)\vec{n} \cdot \vec{P} + \frac{1}{2}(\eta_1 + \eta_2)P^2, \end{aligned} \quad (3.2)$$

where α_i^* are Landau coefficients. The renormalized coefficients α_1^* and α_{11}^* which take into account the epitaxial strain u_m and the two-dimensional clamping of the substrate are $\alpha_1^* = \alpha_1 - 4u_m Q_{12}/(S_{11} + S_{12})$, $\alpha_{11}^* = \alpha_{11} + 4Q_{12}^2/(S_{11} + S_{12})$, where α_i are the unconstrained bulk dielectric stiffness coefficients, and only α_1 is temperature dependent, given by the Curie-Weiss law such that $\alpha_1 = (T - T_0)/\varepsilon_0 C$, and T_0 and C are the Curie-Weiss temperature and constant, respectively. u_m is the epitaxial strain. S_{mn} and Q_{mn} are the elastic compliances and electrostrictive coefficients, respectively. ζ_i and η_i are the first- and second-order coefficients of the surface energy Φ_S expansion for the two ferroelectric-electrode interfaces [271, 272]. \vec{E} is the applied electric field along the polar axis. \vec{E}_{dep} is the depolarizing field which can be determined from the short-circuit condition such that: [271, 272]

$$\vec{E}_{dep} = -\frac{\lambda_1 + \lambda_2}{h\varepsilon_0 + (\lambda_1 + \lambda_2)\varepsilon_b}\vec{P}, \quad (3.3)$$

where ε_0 is the permittivity of vacuum space, and ε_b indicates the background (i.e. without contribution of the spontaneous polarization) dielectric constant. λ_i are the effective screening lengths of the two interfaces and are dependent on the polarization direction if the electronic and chemical environments of ferroelectric/electrode interfaces are different [271, 272]. For the two opposite polarization orientations, the direction dependence of λ_i will induce the asymmetry in potential energy and hence will produce the TER effect, besides the depolarizing field effect due to the polarization difference between two opposite orientations [239–242]. However, we ignore such an effect due to the lack of information about the direction dependence of λ_i and we mainly focus on the role of the built-in field in this study. Note that $\delta\varphi$ and $\delta\zeta = (\zeta_2 - \zeta_1)$ are thickness and polarization independent and \vec{E}_{bi} is indeed a long-range internal-bias field which has the effect of poling the ferroelectric film [271, 272, 281]. In asymmetric FTJs, such asymmetry parameters $\delta\varphi$ and $\delta\zeta$ can introduce a potential energy profile difference and therefore induce the TER effect [239–242].

Table 3.1: The parameters used in this work.

| Parameters | Values(in SI units) | Reference |
|-----------------|------------------------------|------------|
| α_1 | $8.248(T - 115) \times 10^5$ | [283] |
| α_{11} | -8.388×10^8 | [283] |
| α_{111} | 7.764×10^9 | [283] |
| α_{1111} | 3.0904×10^{11} | [283] |
| S_{11} | 8.3×10^{-12} | [284] |
| S_{12} | -2.7×10^{-12} | [284] |
| Q_{12} | -0.045 | [284] |
| λ_{SRO} | 1.2×10^{-11} | [273] |
| λ_{Pt} | 3×10^{-13} | [273] |
| u_m | -0.02458 | - |
| ε_0 | 8.85×10^{-12} | - |
| ε_b | $\sim 50\varepsilon_0$ | [274, 275] |

The equilibrium polarization can be derived from the condition of thermodynamic equilibrium:

$$\frac{\partial F}{\partial P} = 0. \quad (3.4)$$

The dielectric constant ε under an applied field E whose direction is along the polar axis can be determined as: [275]

$$\varepsilon = \frac{1}{h\varepsilon_0} \left(\frac{\partial^2 F}{\partial^2 P} \right)^{-1}. \quad (3.5)$$

The multiscale thermodynamic model used in this study combines first-principles calculations and phenomenological theory and its detailed description can be found elsewhere [271, 272]. In a previous study, it is reported that \vec{E}_{bi} could result in a smearing of the phase transition and an internal-bias-induced piezoelectric response above T_c in asymmetric FTJs [271]. However, adding to the forgoing controversy on the size effects, further analysis of the effect of a built-in field on the ferroelectric transition in asymmetric FTJs is still absent. Inserting Eq. (3.1) into Eq. (3.2) results in a term that encompasses an odd power of the polarization: $\vec{E}_{bi} \cdot \vec{P}$, which leads to asymmetric thermodynamic potentials. We shall show that this term which behaves mathematically as identically as the phenomenological term suggested by Bratkovsky and Levanyuk [282] will result in an unusual ferroelectric-“polar non-ferroelectric” phase transition in asymmetric FTJs.

3.1.1.3 Size effects

For a quantitative analysis, we consider a fully strained BTO film sandwiched between Pt (electrode 2) and SRO (electrode 1) epitaxially grown on (001) SrTiO₃ (STO) substrates. We

neglect the energy difference of the asymmetric surfaces, i.e., by setting $\zeta_1 = \zeta_2$, $\eta_1 = \eta_2 = 0.113$ (Refs. [271, 272]), to ensure that the effect of \vec{E}_{bi} is clearly observable from the calculations since it is reported that surface effects are generally much smaller than that of \vec{E}_{bi} [274, 275]. All the parameters we used are listed in Table. 3.1. Note that the background dielectric constant ε_b is taken from Refs. [274, 275] which is distinct from $7\varepsilon_0$ used in Refs. [271, 272]. In fact, there is no consensus on its exact value, especially by the theoretical researchers. In this study, we have made some comparisons with the previous studies in Refs. [274, 275], so selecting $50\varepsilon_0$ is reasonable and does not change the main results of this work. The approximated parameters in this work need more rigorous treatment by the first-principles calculations or experimental confirmation in the future.

We first examine the effect of \vec{E}_{bi} on the ferroelectricity of asymmetric FTJs. Previous studies indicate that the direction of \vec{E}_{bi} in asymmetric Pt/BTO/SRO FTJs points to a Pt electrode with higher work function [274–276]. All recent results show indeed that a strong preference for one polarization state, namely P_+ while P_- disappears at “ h_c ” [274–280]. According to the definition of ferroelectricity, the spontaneous polarization of the ferroelectric materials is switchable under an ac electric field [89]. However, knowing that the spontaneous polarization of ferroelectric materials is switchable under an ac electric field [89], recent reports [274–277] are rather confusing and remain incomplete on this point. Indeed, in addition to the aforementioned divergence in the size effects, two different transition temperatures at which the two polarization states reach zero are obtained (see Ref. [275]), which may be confusing since there should be only one finite phase transition temperature for disappearance of ferroelectricity. In order to avoid such confusions, we used the classical definition of ferroelectricity [89] in the following parts.

We make further analysis of the physical formulation of h_c in asymmetric FTJs. Note that Eq. (3.4) is a nonlinear equation and yields “at most” three solutions P , two of them corresponding to minima and the other one to a saddle point (unstable state). Whether the solution is a minimum, a maximum, or a saddle point can be revealed through inspecting the eigenvalues of the Hessian matrix of the total free energy F . Because the asymmetric FTJ is internally biased, i.e., the energy degeneracy between positive P_+ and negative P_- is lifted, one of the minima corresponds to the equilibrium state (the global minimum) of the system (the direction of which is along \vec{E}_{bi}) and the other minima corresponds to a metastable state (a local minimum) of the system. It means that the presence of two different electrodes in asymmetric FTJs results in a preferred polarization orientation of the ferroelectric plate. Having found all P solutions as a function of h , one can clearly see that metastable state and unstable state solutions become closer to each other and coincide at finite h , henceforth the number of solutions P drops from three to one. According to the bistable property of ferroelectric materials, this finite h is just h_c (Ref. [89]). As long as there are three P solutions, two of these three solutions correspond to stable/metastable polarizations so that two orientations of polarization are possible in the BTO layer and thus it is ferroelectric. Switching the asymmetric FTJ into its unfavored high-energy polarization may be difficult. If there is the only P solution corresponding to the unstable state, although it attains a finite value, it is not ferroelectric anymore and may be called “paraelectric”. Indeed, it would be more appropriate to consider it as “polar non-ferroelectric” since P has a unique finite value [285–287]. FTJs with no built-in field $\delta\varphi = 0$ will exhibit two energetically

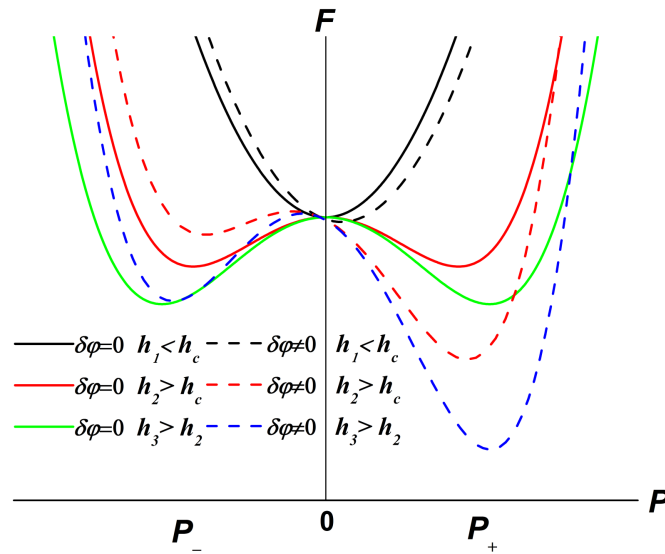


Figure 3.2: Schematic representation of the variation in total free energy with respect to polarization with different BTO barrier thicknesses in asymmetric Pt/BTO/SRO tunnel junctions with/without consideration of the built-in field in zero applied field.

equivalent stable polarization states (P_+ and P_-) along with an unstable polarization state at $P = 0$ below h_c . All the foregoing discussions can be clearly and easily understood in the schematic representation of $F - P$ curves with different BTO thicknesses as shown in Fig. 3.2, which is quite similar with the results of ferroelectric thin films with/without consideration of the fixed interface dipoles near the asymmetric ferroelectric/electrode interface [278–280] or ferroelectric superlattices with/without interfacial space charges [287]. Together with previous results [279, 280], we conclude that whether the \vec{E}_{bi} is considered as a long-range field or a short-range surface one, it cannot induce the vanishing of h_c in asymmetric FTJs, which is in contrast with other works [274–277].

Note that the “polar non-ferroelectric” phase is actually a pyroelectric phase because there is a non-switchable polarization in this phase. This kind of phase transition has once been reported in ferroelectric thin films with asymmetric electrodes [271, 278–280] or ferroelectric superlattices with interfacial space charge [285–287]. As we discussed in the formation of h_c , the “polar non-ferroelectric” phase indeed always corresponds to the unstable state (see Fig. 3.2) and this kind of non-switchable polarization may not be stable at all. However, breaking up the system into 180° domain stripes is unambiguously ruled out due to the long-range pinned field \vec{E}_{bi} . In plane vortex formation [288, 289] is also inhibited because the large compressive strain favors more 180° domain stripes [289]. The ferromagneticlike closure domains are predicted to form in ultrathin ferroelectric films or ferroelectric capacitors even below h_c (Refs. [290–292]) and are experimentally confirmed well above h_c recently [293, 294]. However, typical ferroelectric closure domains [290–294] are also not expected in “polar non-ferroelectric” phase where 180° domains in the closure domain structure should be suppressed. But local rotations

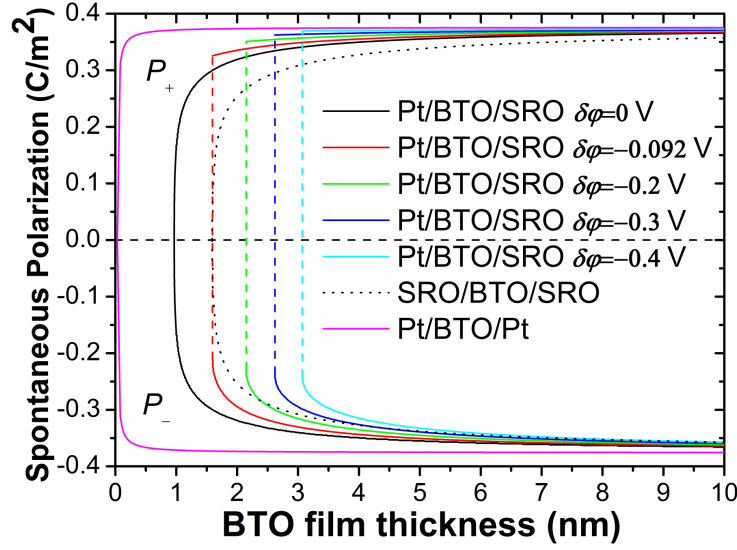


Figure 3.3: Spontaneous polarization of the asymmetric Pt/BTO/SRO tunnel junctions as a function of BTO layer thickness with $\delta\varphi=0$ V, -0.092 V, -0.2 V, -0.3 V and 0.4 V in zero applied field at 0 K, respectively. The results of symmetric SRO/BTO/SRO and Pt/BTO/Pt tunnel junctions at 0 K [47] are also added for comparison.

of non-switchable polarization ($<90^\circ$) are still likely to occur and result in a closure-like domain structure since the local change of the direction of the non-switchable polarization especially near the ferroelectric/electrode interface is helpful to minimize the system energy [290–292]. Although such closure-like domains can be favored below h_c (<3 nm at least), it is clear that the ferroelectric barrier as a whole is not ferroelectric according to our forgoing analysis that shows the polarization is not switchable under external electric fields. While a detailed analysis of the built-in field effect on domain formation is beyond the scope of this study, we suggest that more rigorous simulations should be made in the future. It can be seen that the asymmetric FTJs below h_c can not be used for ferroelectric memory applications in which two thermodynamic stable polarization states are needed to encode “0” and “1” in Boolean algebra [89, 199, 268–272]. However, based on our calculation, one should expect a resistance change below h_c between the non-switchable polarization state and the other one being ferroelectrically dead. This result agrees well with recent works on Pt/BTO/Pt FTJs that even below h_c , the resistance of the FTJ would change by a factor of 3 due to the interface bonding and barrier decay rate effects [243]. We argue that the TER effect below h_c suggested in our work may be essentially attributed to the asymmetric modification of the potential barrier by the nonzero barrier height ($-\delta\varphi$) [see Eqs. (3.1)-(3.4)] which even exists at zero polarization as shown in Fig. 3.1(d). Further theoretical and experimental efforts should be made to confirm these predictions.

The quantitative results of the foregoing analysis are directly given in Fig. 3.3. It can be seen that h_c exists regardless of symmetric or asymmetric structures. As expected, the curves of P_+ and P_- are symmetric with respect to $P = 0$ at $\delta\varphi = 0$ where h_c is about 1 nm which is smaller than that of SRO/BTO/SRO, i.e., 1.6 nm (Refs. [47, 273]). When $\delta\varphi \neq 0$, the

supposed degeneracy between P_+ and P_- occurs, i.e., P_+ is enhanced while P_- is reduced so the coordinate of the center of the hysteresis loop along the polarization axis [$1/2(P_+ + P_-)$] is shifted along the direction of P_+ . It is shown that such a displacement of the hysteresis loop along the polarization axis becomes more significant as the strength of \vec{E}_{bi} increases. It may be attributed to the imprint caused by \vec{E}_{bi} such that the whole shape of the hysteresis loop will shift along the direction of the field axis which is antiparallel to the direction of \vec{E}_{bi} (Ref. [89]). Besides, it is found that as $\delta\varphi$ increases, h_c increases, which indicates that \vec{E}_{bi} can enhance the size of h_c . Thus, whether h_c of Pt/BTO/SRO junction is larger or smaller than that in the SRO/BTO/SRO counterpart strongly depends on the exact value of $\delta\varphi$ as shown in Fig. 3.3.

For the symmetric structures (SRO/BTO/SRO and Pt/BTO/Pt FTJs), one can easily see in Fig. 3.3 that single domain in the ferroelectric layer destabilizes as the film thickness is decreased due to the depolarizing field effect [47, 199, 268–272]. And it is shown in Fig. 3.3 that Pt/BTO/Pt FTJ whose h_c is merely 0.08 BTO unit cell is nearly free of deleterious size effects [47], which agrees well with the result of first-principles calculations [273]. h_c of SRO/BTO/SRO FTJ is about four BTO unit cells, which is well consistent well with our previous results [47]. The qualitative result that h_c of Pt/BTO/Pt FTJ is smaller than that of SRO/BTO/SRO FTJ in this work is well consistent with those of first-principles calculations [273] and the lattice model [295, 296]. However, our results are in contrast with previous works [269, 274, 275] predicting h_c of SRO/BTO/SRO FTJ to be smaller than that of Pt/BTO/Pt FTJ. In these previous works [274, 275], the Mehta *et al.*' electrostatic theory about the depolarizing field ($\vec{E}_{dep} = -\frac{\vec{P}}{\epsilon_b}(1 - \frac{h/\epsilon_b}{l_{s1}/\epsilon_{e1} + l_{s2}/\epsilon_{e2} + h/\epsilon_b})$ where l_{s1} and l_{s2} are Thomas-Fermi screening lengths and ϵ_{e1} and ϵ_{e2} are dielectric constants of electrode 1 and 2) is used [268] while in our work we used the “effective screening length” model to describe the depolarizing field [see Eq. (3.3)]. Note that we used the same parameters as Refs. [274, 275] except for the model of depolarizing field (see Table. 3.1). The distinct results are understandable since it is generally accepted that imperfect screening should be characterized by effective screening length [see Eq. (3.3)] rather than Thomas-Fermi one in Mehta *et al.*' model [297]. In fact, the effective screening length at Pt/BTO interface is only 0.03 Å (Ref. [273]) much smaller than that of Thomas-Fermi one ~ 0.4 Å (Ref. [269]), so a significantly reduced depolarizing field is expected and it would result in nearly no h_c in Pt/BTO/Pt FTJs. A previous study attributes this freedom of size effects in the Pt/BTO/Pt structure to the “negative dead layer” near the Pt/BTO interface [273], while we argue that it may result directly from the fact that the effective screening length of the Pt electrode is extremely small since Bratkovsky and Levanyuk suggested the “dead layer” model is totally equivalent as to consider an electrode with a finite screening length [298]. Here, we ignore the effect of the extrinsic “dead layer” formed between metal electrode (i.e., Au or Pt) and a perovskite ferroelectric [i.e., Pb(ZrTi)O₃ or BTO]. Indeed, Lou and Wang found that the “dead layer” between Pt and Pb(ZrTi)O₃ is extrinsic and could be removed almost completely by doping 2% Mn [299]. Experimentally, many researchers found that SRO/BTO/SRO capacitors (as well as other perovskite ferroelectric structures with conductive oxide electrodes) are free from passive layers [269, 300, 301]. Recently, a very interesting experimental result demonstrates that the RuO₂/BaO terminations at BTO/SRO interface, which is assumed as many pinned interface dipoles and plays a detrimental role in stabilizing a switchable ferroelectric polarization, can be overcome by depositing a very thin layer of SrTiO₃ between the BTO layer and SRO

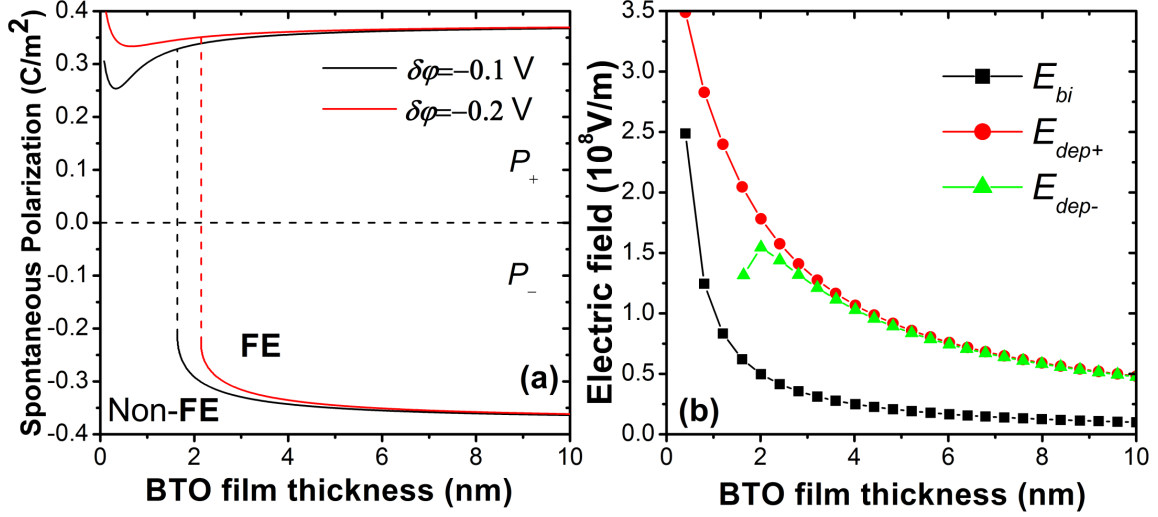


Figure 3.4: (a): Polarization state P_{\pm} of the asymmetric Pt/BTO/SRO tunnel junctions as a function of BTO layer thickness with $\delta\varphi = -0.1$ V and -0.2 V in zero applied field at 0 K, respectively. The dash lines mark the boundary between polar non-ferroelectric and ferroelectric phases for different values of $\delta\varphi$; (b): Dependence of the strengths of the built-in field E_{bi} and depolarizing field for different directions, E_{dep+} and E_{dep-} on the BTO layer thickness with $\delta\varphi = -0.1$ V at 0 K. FE in (a) and (b) indicate ferroelectric.

electrode [279, 280]. Nonetheless, it is still unclear whether such pinned interface dipoles are intrinsic and can be found in other ferroelectric/electrode interfaces [i.e., SRO/PbTiO₃ (PTO) and Pt/BTO].

In the asymmetric structures in Fig. 3.3, it is shown that in comparison with $\delta\varphi = 0$ in asymmetric Pt/BTO/SRO FTJs, h_c is significantly enhanced, as $\delta\varphi$ increases, which is in good agreement with the recent results regarding \vec{E}_{bi} as short-range interface field [279], and is similar with the previous results [275]. Note that $\delta\varphi$ is intrinsic and determined strictly by the electronic and chemical environments of ferroelectric/electrode interfaces but not by any potential drop through the FTJ which “creates” an applied field [271, 272, 281, 282]. Changing $\delta\varphi$ is simply due to the lack of its exact value and for the purpose of studying the effect of \vec{E}_{bi} in asymmetric FTJs, which is similar to the previous method [274, 275]. This method [274, 275] indeed does not mean that any asymmetric electrodes are considered here, since the electrode is

replaced, the electrode/ferroelectric interface parameters in Eqs. (3.1)-(3.3) such as λ_i and other interface parameters will also change. The variation of P_+ in Pt/BTO/SRO FTJs as a function of the whole BTO layer thickness with $\delta\varphi=-0.1$ V and -0.2 V at 0 K is shown in Fig. 3.4(a). It is found that below the critical thickness P_+ state shows an interesting recovery of a polar non-ferroelectric polarization, in contrast to P_- state [see Fig. 3.4(a)], becoming less significant when $\delta\varphi \sim <-0.2$ V. Note that such recovery has been reported in ferroelectric superlattices with asymmetric electrodes and demonstrated to be independent of the interfacial space charge [285]. Although such a recovery of polar non-ferroelectric polarization in BTO layer does not mean the recovery of ferroelectricity as it is not switchable, it is necessary to realize its origin. We plot the build-in field E_{bi} and depolarizing field for different directions, E_{dep+} and E_{dep-} , as a function of the BTO film thickness considering $\delta\varphi=-0.1$ V as an example in Fig. 3.4(b). For the condition of P_- state as schematically illustrated in Fig. 3.1(b), E_{dep-} shows the typical behavior as the FTJ with the same electrodes [199, 269, 270, 295], which means that E_{dep-} plays a key role forcing the single domain in the ferroelectric layer to destabilize as the film thickness is decreased. E_{bi} with the same direction of E_{dep-} helps then to speed up such destabilization, therefore enhancing the critical thickness. For the P_+ state, E_{dep+} and E_{bi} are in the opposite directions, as depicted in Fig. 3.1(a), and both the strengths of E_{dep+} and E_{bi} increase as the BTO layer thickness is decreased [Fig. 3.4(b)], which means that E_{dep+} is partially canceled by E_{bi} . The strength of this partial compensation becomes stronger with the film thickness decreasing (see the slopes of $E_{bi} - h$ and $E_{dep+} - h$ curves)[Fig. 3.4(b)]. Therefore, E_{bi} is fighting against E_{dep+} allowing the polarization to recover into a polar non-ferroelectric polarization. This recovery of polar non-ferroelectric polarization forces the system to a higher energy state which strongly supports our foregoing predictions of local rotations of non-switchable polarization ($<90^\circ$) and the formation of closure-like domain structure to minimize the system energy.

The critical thickness h_c under different ambient temperatures T as a function of $(-\delta\varphi)$ in asymmetric Pt/BTO/SRO FTJs is shown in Fig. 3.5. It can be seen that h_c decreases with T increasing. And it is found that for other T , the asymmetric Pt/BTO/SRO FTJs show a similar behavior of enhancement of h_c by increasing the strength of \vec{E}_{bi} as shown in Fig. 3.3 at 0 K.

3.1.1.4 Transition temperature and dielectric response

The transition temperature T_c of the asymmetric FTJs is extremely important, especially for the device applications. Figure. 3.6 summarizes T_c as a function of BTO thickness in epitaxial asymmetric Pt/BTO/SRO FTJs at various values of $\delta\varphi$. It is shown that T_c in asymmetric Pt/BTO/SRO FTJs monotonically decreases with the BTO layer thickness decreasing, which is similar to the behavior of symmetric SRO/BTO/SRO or Pt/BTO/Pt FTJs [47]. Moreover, T_c decreases more significantly for thinner BTO barrier layer thickness (see the slope of $T_c - h$ curves in Fig. 3.6). At a given BTO layer thickness, it is found in Fig. 3.7 that T_c decreases as $\delta\varphi$ becomes more negative, which means a larger built-in field can force the phase transition to occur at lower temperatures. The transition temperature T_c is strongly sensitive to the $\delta\varphi$ change especially for the thinner BTO barrier [see the slope of $T_c - (-\delta\varphi)$ curves in Fig. 3.7]. It can be clearly seen that the ferroelectric transition temperature is suppressed as the built-in field is increased for different BTO thicknesses. Usually, the TER effect is always significantly larger for

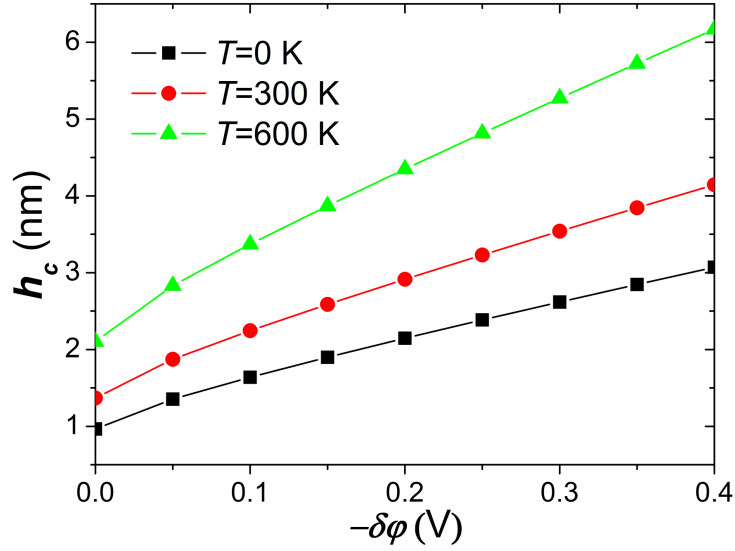


Figure 3.5: The variation in critical thickness h_c in epitaxial asymmetric Pt/BTO/SRO tunnel junctions as a function of $-\delta\phi$ at three different temperatures: 0 K, 300 K, and 600 K, respectively ($E=0$ kV/cm).

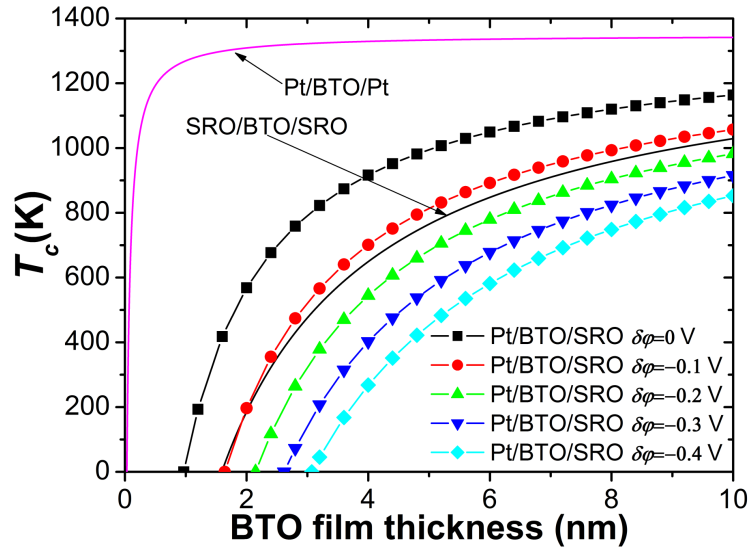


Figure 3.6: The transition temperature T_c as a function of BTO layer thickness in epitaxial asymmetric Pt/BTO/SRO tunnel junctions at various values of $\delta\phi$ with no applied field. The results of symmetric SRO/BTO/SRO and Pt/BTO/Pt tunnel junctions [47] are also provided for comparison.

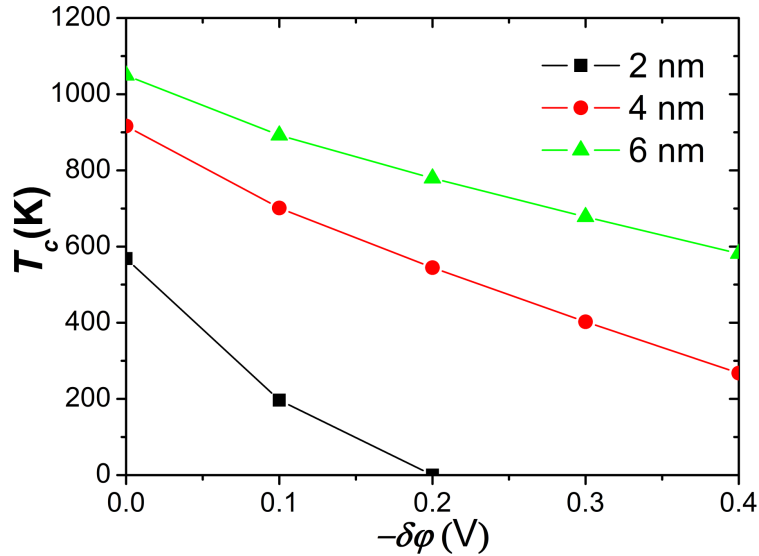


Figure 3.7: The transition temperature T_c as a function of $(-\delta\varphi)$ in epitaxial asymmetric Pt/BTO/SRO tunnel junctions with three different BTO layer thicknesses: 2 nm, 4 nm and 6 nm, respectively ($E=0$ kV/cm).

thicker barrier with larger polarization [241, 244]. Here we find that a fundamental limit (which is more drastic for thinner ferroelectric barrier thickness) on the work temperature of FTJ-type or capacitor-type devices should also be simultaneously taken into account together with the ferroelectric barrier thickness or polarization value. In addition and interestingly, since the electrocaloric effect is always the strongest close to the ferroelectric-paraelectric transition [84], such tuning of T_c by \vec{E}_{bi} should be also considered in potential asymmetric FTJs for the room temperature solid-state refrigeration (see Section 3.1.3). Moreover, the fact that large tunneling current in asymmetric FTJs [245] results in significant Joule heating should also be included in the design of future devices.

The dielectric response ε_+ (\vec{E} is parallel to \vec{E}_{bi}) and ε_- (\vec{E} is antiparallel to \vec{E}_{bi}) of Pt/BTO/SRO FTJs (consider the 5-nm-thick BTO film as an example) as a function of T at different $\delta\varphi$ is shown in Figs. 3.8(a) and 3.8(b). Several key parameters with different $\delta\varphi$ in Fig. 3.8(a) are extracted in Table. 3.2: T_{max} corresponds to the temperature where ε_+ reaches its maximum, ε_{max+} ; ε_{min+} simply means the minimal value of ε_+ ; $\delta\varepsilon_d$ is in somehow the diffuseness of the transition. It can be seen that when $\delta\varphi = 0$, ε_+ shows a sharp peak near T_c . However, a gradual decrease in ε_{max} and $\delta\varepsilon_d$ is seen upon increasing \vec{E}_{bi} , which is well consistent with the results of smearing of T_c by increasing \vec{E}_{bi} in Fig. 3.6 (see the slope of $T_c - h$ curves in Fig. 3.6). The diffusive transition response in ε_+ clearly shows smearing of the phase transition as a result of \vec{E}_{bi} , which verifies the predictions of Tagantsev *et al.* [271, 272]. and Bratkovsky *et al.* [282]. In addition, it is shown T_{max} is shifted to higher temperatures due to \vec{E}_{bi} . As the strength of \vec{E}_{bi} increases, the smearing of phase transition and the shift of T_{max} becomes more significant. On the other hand, the applied field can not fully compensate the built-in field, resulting in a

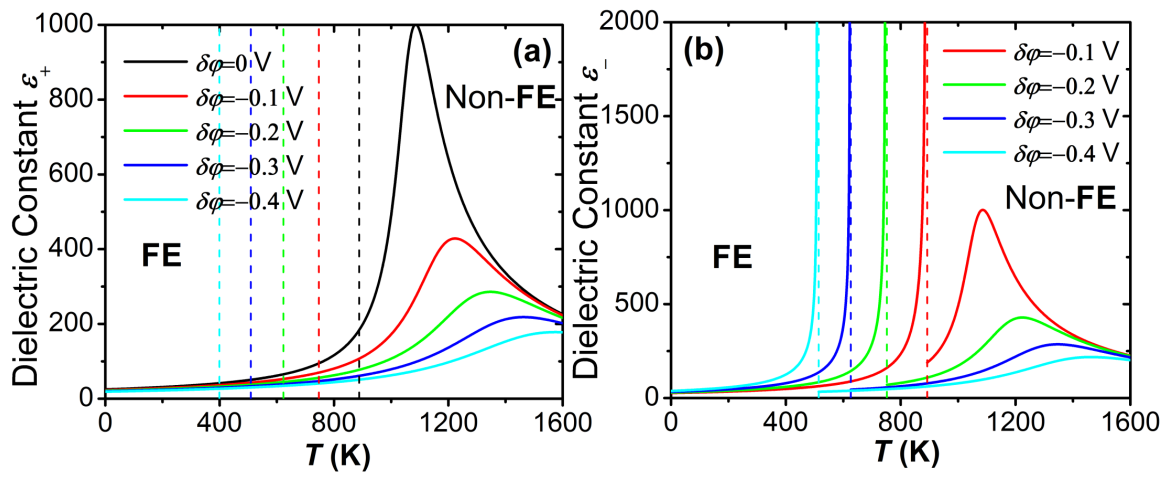


Figure 3.8: Dielectric constants ϵ_+ (a) and ϵ_- (b) as a function of temperature T at various values of $\delta\phi$ in asymmetric Pt/BTO/SRO tunnel junctions where BTO layer thickness h is 5 nm ($E=100$ kV/cm). The dash lines mark the boundary between polar non-ferroelectric and ferroelectric phases for different values of $\delta\phi$. FE in (a) and (b) indicate ferroelectric.

Table 3.2: The different parameters extracted from Fig. 3.8(a).

| $\delta\varphi(\text{V})$ | $T_{max}(\text{K})$ | ε_{max+} | ε_{min+} | $\delta\varepsilon_d = (\varepsilon_{max+} - \varepsilon_{min+})/2$ |
|---------------------------|---------------------|----------------------|----------------------|---|
| 0 | 1086 | 1001.4 | 24.8 | 513.1 |
| -0.1 | 1223 | 428.5 | 23.0 | 225.7 |
| -0.2 | 1345 | 285.8 | 21.4 | 153.6 |
| -0.3 | 1465 | 218.3 | 20.1 | 119.2 |
| -0.4 | 1574 | 178.1 | 18.9 | 98.5 |

discontinuous phase transition from the ferroelectric phase to the polar non-ferroelectric phase with temperature increasing as depicted in dielectric response ε_- in Fig. 3.8(b), which is distinct from the continuous counterpart of ε_+ as shown in Fig. 3.8(a). P_- abruptly changes its sign near the transition point resulting in a dielectric peak and a similar smearing of ε_- by increasing the strength of \vec{E}_{bi} is found. Furthermore, it is found that although the transition temperatures for two directions are different, they both decrease as the built-in field increases, which is consistent with the results without any external field (see Fig. 3.6), which indicates that the built-in field forces the transition to take place at a reduced temperature.

3.1.1.5 Comments on the built-in field effect

We make further comments on the built-in field effect in asymmetric FTJs. The main assumption in this study is that $\delta\varphi$ does not change during the polarization reversal [271, 272]. The presence of $\delta\varphi$ which results in an asymmetric potential energy and barrier height differences by switching the polarization will induce the TER effect [239–241]. Note that the switching of the polarization in the asymmetric FTJs may change the value of $\delta\varphi$ [243, 257, 278, 302, 303]. However, according to our analysis, the variation in $\delta\varphi$ (even changing its sign occurs during the polarization reversal) does not alter the main results of this study due to its induced broken spatial inversion symmetry of FTJs. In addition to the built-in field, if the surface term $\delta\zeta = (\zeta_2 - \zeta_1)$ is nonzero, the main conclusions of this paper will not change as well.

3.1.2 Electrocaloric effect in symmetric ferroelectric tunnel junctions

The investigations on electrocaloric effect—the cooling of a crystal by the application of an external electric field—can be dated back to 1930 (Ref. [5, 84]), however, it is not until 2006 that a Science paper [15] inspired both fundamental physics and exciting device applications for electrocaloric effect. Mischenko *et al.* at Cambridge reported a giant electrocaloric effect with an adiabatic temperature change of 12 K in $\text{PbZr}_{0.95}\text{Ti}_{0.05}\text{O}_3$ ceramic thin films under a high electric field of 780 kV/cm (Ref. [15]). Since then, the giant electrocaloric effect was successively observed in the relaxor ferroelectric films ($\text{PbMg}_{1/3}\text{Nb}_{2/3}\text{O}_3$ - PbTiO_3) [172, 304], ferroelectric polymer thin films $[\text{P}(\text{VDF-TrFE})]_{(55/45)}$ [46], and lead-free $\text{SrBi}_2\text{Ta}_2\text{O}_9$ thin films [305], where

high electric field in the ferroelectric thin films could be achieved to free the primary limit by the electric breakdown strength of the specimen. For practical cooling devices, it is of great importance to exploit a kind of potential electrocaloric material which is environmentally friendly and working at room temperature [84, 110]. One leading material is relaxor ferroelectric family such as high-energy-electron-irradiated-poly [P(VDF-TrFE)] (68/32) relaxor copolymer and the La-doped Pb(ZrTi)O₃ relaxor ceramic thin films which perform much better than the normal ferroelectric counterparts [204].

Theoretically, Landau-Devonshire theory has been developed to evaluate the effects of clamping [123, 306], applied field [307], and domain walls [192] on electrocaloric effect where electrode and film thickness are totally ignored. In addition, an alternative first principles study using Monte Carlo atomistic simulations theory is helpful to understanding of the general problem of electrocaloric effect [308]. In this letter, we study the intrinsic electrocaloric effect in ultrathin ferroelectric capacitors by using a multiscale thermodynamic model-which combines phenomenology and first-principles calculations-recently developed by Tagantsev *et al.* [271, 272] (see Section 3.1.1). Here, we report that the ultrathin ferroelectric capacitors which could permit ultrahigh applied field is just another promising candidate for lead-free room-temperature solid-state refrigeration [84].

We focus on an electroded and short-circuited (001) single-domain BTO plate of thickness h , whose polar axis lies normal to the ferroelectric-electrode interfaces. We restrict ourselves to the case of the ultrathin ferroelectric capacitors grown on thick STO substrate. We only consider the case for symmetric ferroelectric-electrode interfaces, and set $\zeta_1 = \zeta_2$, $\eta_1 = \eta_2 = \eta$ ($\eta_{SRO} = 0.113$ and $\eta_{Pt} = 0.0034$), $\lambda_1 = \lambda_2 = \lambda$, and $\Delta\varphi_1 = \Delta\varphi_2$. The equilibrium polarization P^0 can be derived from the condition of thermodynamic equilibrium following Eq. (3.4). Then, the electrocaloric coefficient p_{pyro} can be obtained by Eq. (1.13). The electrocaloric change in temperature upon application of an electric field can be determined by Eq. (1.28) and we use the approximate relation $D \sim P$. Heat capacity $C_E = 2.53 \times 10^6$ J/K m³ is taken from Ref. [208].

First, since the electrocaloric effect is always strongest close to the ferroelectric-paraelectric transition [84, 110], the transition temperature T_c is of great importance. Figure. 3.9 summarizes T_c (Let α_1^* be zero) as a function of BTO thickness. The Raman data of multidomain BTO films without electrodes [309] is also given. It is found that the critical thickness for T_c reaching 0 K in SRO/BTO/SRO capacitors is 1.592 nm a little smaller than uncapped BTO thin films (1.6 nm in Ref. [309]), and T_c vs h for monodomain BTO on SRO shifts to a higher temperature than 180° domain BTO on STO (except for 2.4 nm). This is reasonable since the conducting SRO electrode lowers the energy of the single-domain state, producing a direct transition from unpolarized to monodomain polarized at a higher T_c , which agrees well with the experimental results of PTO counterpart [310]. For the condition under Pt electrodes, it is found that T_c is much larger than that under SRO due to the much smaller λ . The critical thickness in Pt/BTO/Pt capacitors is 0.08 BTO unit cell, which is consistent well with the previous result of first-principles calculations [273]. Although higher T_c means larger polarization under Pt than SRO, it is not desirable for electrocaloric effect because dramatic change of T_c occurs in extremely narrow thickness range (within one BTO unit cell) and the T_c for one BTO unit cell only is about 1156 K which is too high for application. On the other hand, it is shown that T_c in SRO/BTO/SRO capacitors can be tuned by the BTO layer thickness, which suggests artificial

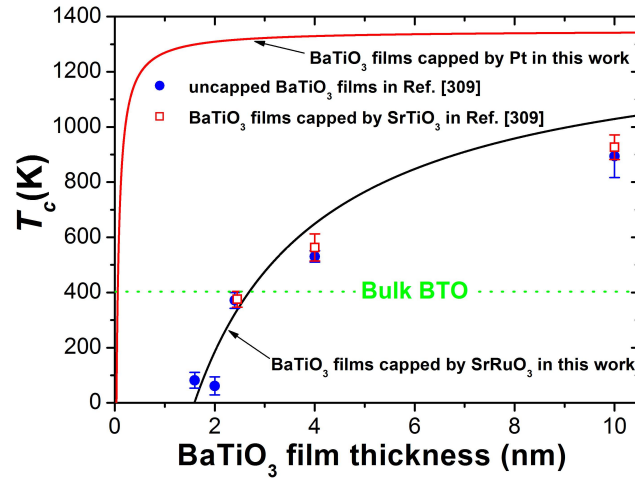


Figure 3.9: The transition temperature T_c as a function of BTO layer thickness, as determined from Raman data (symbols) in Ref. [309]. The solid lines are the results of calculation results in epitaxial SRO/BTO/SRO and Pt/BTO/Pt capacitors with short-circuit boundary conditions.

tuning of working temperature of the capacitors is possible.

Second, we choose a 2.4-nm BTO film as its T_c (322.47 K) is close to room temperature as clearly seen in the curves in space of equilibrium polarization versus temperature in Fig. 3.10. With no electric field, the polarization continuously drops to zero as the temperature increases, which is in agreement with second-order nature of phase transition. It is also shown that electric field favouring the ferroelectric phase can induce a significant change of polarization. Moreover, this change is always the largest near the T_c , indicating that the maximum electrocaloric effect near the transition temperature.

The electrocaloric coefficient as a function of temperature is illustrated in Fig. 3.11. It is shown that $p_{pyro}(T_M) = 9.5 \times 10^{-4} \text{ C/m}^2\text{K}$ for $\Delta E = 100 \text{ kV/cm}$ is smaller than that of $\text{Pb}(\text{ZrTi})\text{O}_3$ [$p_{pyro}(T_M) \sim 1.5 \times 10^{-3} \text{ C/m}^2\text{K}$] [307] and bulk BTO [$p_{pyro}(T_M) = 1.2 \times 10^{-3} \text{ C/m}^2\text{K}$] [306] under the same ΔE , however, is comparable with the clamped BTO films [$p_{pyro}(T_M) = 9.2 \times 10^{-4} \text{ C/m}^2\text{K}$ under $\Delta E = 100 \text{ kV/cm}$] [306]. It should be noted that the temperature T_M where the maximum of electrocaloric coefficient occurs increases significantly with the enhancement of electric field, which is consistent with the previous results of $\text{Pb}(\text{ZrTi})\text{O}_3$ [307]. What's more, it is found that T_M is also enhanced by increasing BTO layer thickness (see the inset of Fig. 3.11), which agrees well with the behavior of $T_c - h$ in Fig. 3.9. Note that T_M shift induced by both the electric field and film thickness may impose a fundamental limit for ultrathin ferroelectric capacitor as a room-temperature solid-state refrigeration, however, according to Eq. (1.28), electrocaloric temperature change is not only dependent on the amount of p_{pyro} (let alone p_{pyro} is still large enough around room temperature), but also strongly related to the magnitude of the applied electric field. As will be shown that a giant electrocaloric effect can be still induced at room temperature by ultrahigh electric field in ultrathin ferroelectric capacitors. The $p_{pyro} - T$

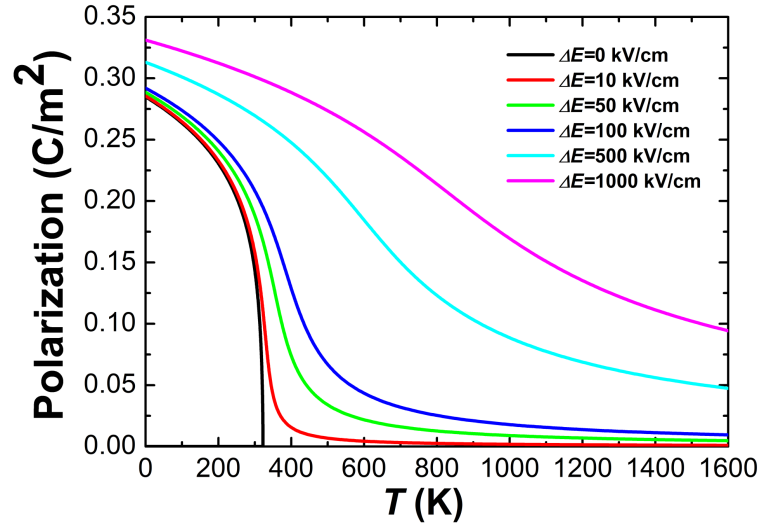


Figure 3.10: Temperature dependence of polarization epitaxial SRO/BTO/SRO capacitors under different electric fields ($h=2.4$ nm).

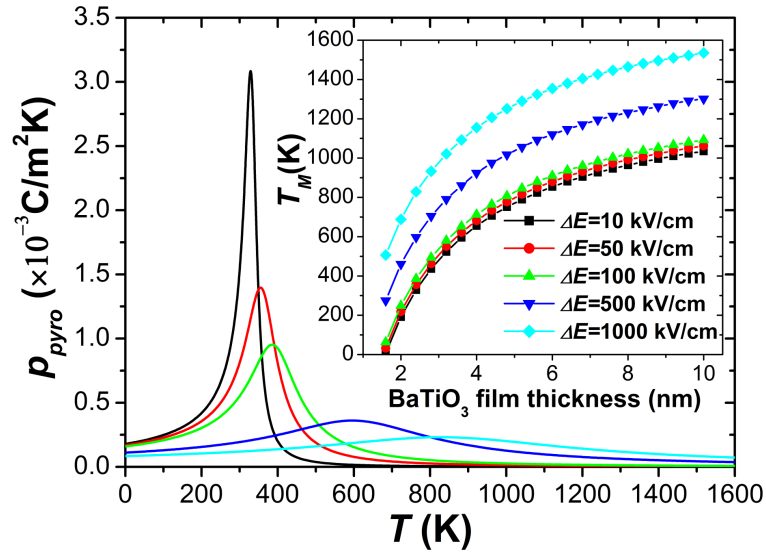


Figure 3.11: The electrocaloric coefficient p_{pyro} as a function of temperature T under different values of ΔE ($\Delta E = E_b - E_a$, where E_a is zero) for a 2.4-nm-thick BTO film capped with two identical SRO electrodes. The inset depicts the BTO thickness dependence of T_M where the EC coefficient p_{pyro} reaches its maximum in epitaxial SRO/BTO/SRO capacitors under different values of ΔE .

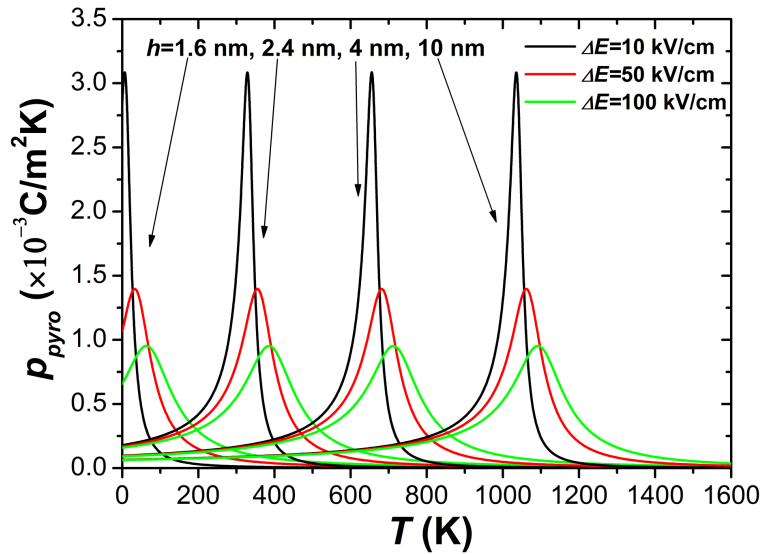


Figure 3.12: The electrocaloric coefficient p_{pyro} due to applied ΔE as a function of temperature T in epitaxial ultrathin SRO/BTO/SRO capacitors with different thicknesses of the BTO layer: 1.6 nm, 2.4 nm, 4 nm and 10 nm, respectively.

curve for different BTO layer thicknesses is shown in Fig. 3.12. It is found that the intrinsic profiles and magnitudes of p_{pyro} are not modified by either the film thickness or $p_{pyro} - T$ curve [not simply $p_{pyro}(T_M) - T$ in Fig. 3.11] in the ferroelectric phase (above critical thickness); they are merely shifted to higher temperatures with increasing the BTO layer thickness.

Furthermore, the comparison of electrocaloric effect between the ferroelectric (above critical thickness) and paraelectric phase (below critical thickness) is directly provided. It is found that the electrocaloric coefficient in the ferroelectric phase is much larger than that in the paraelectric phase as shown in Figs. 3.13(a)-3.13(c). Note that when $h=0.4, 0.8, 1.2$ nm, films are in paraelectric phase (see Fig. 3.9). Our results suggest that the ultrathin films in the paraelectric phase (below critical thickness) are not desirable because of the significant degradation of approximately one to two orders of magnitude in their electrocaloric coefficient. This is mainly due to the small polarization change induced by electric field in this region. Note that the electric-field-induced T_M shift is still observed in SRO/BTO/SRO capacitors with three BTO unit cells [see Fig. 3.13(c)]. For the BTO layer with only one or two unit cells, p_{pyro} decreases monotonously with the temperature increasing and increases as ΔE increases.

Finally, giant electrocaloric effect in SRO/BTO/SRO capacitors is shown in Fig. 3.13(d) in the form of $\Delta T_E - T$ curves. Note that the peak of ΔT_E shows a shift to a higher working temperature which is in good agreement with $p - T$ curves in Fig. 3.10. The peak value of ΔT_E is 5 K at 360 K under a high electric field of 1000 kV/cm. At around room temperature (300 K), it is shown that ΔT_E for $\Delta E = 100$ kV/cm is 1.1 K, which is comparable with that in bulk BTO (0.8 K) [306] and that in clamped BTO films (0.83 K) [306], but much larger than that in fully strained $\text{PbZr}_{1-x}\text{Ti}_x\text{O}_3$ ($0.65 \leq x \leq 1.0$) films (~ 0.2 K) [192]. Further estimations of the ratio

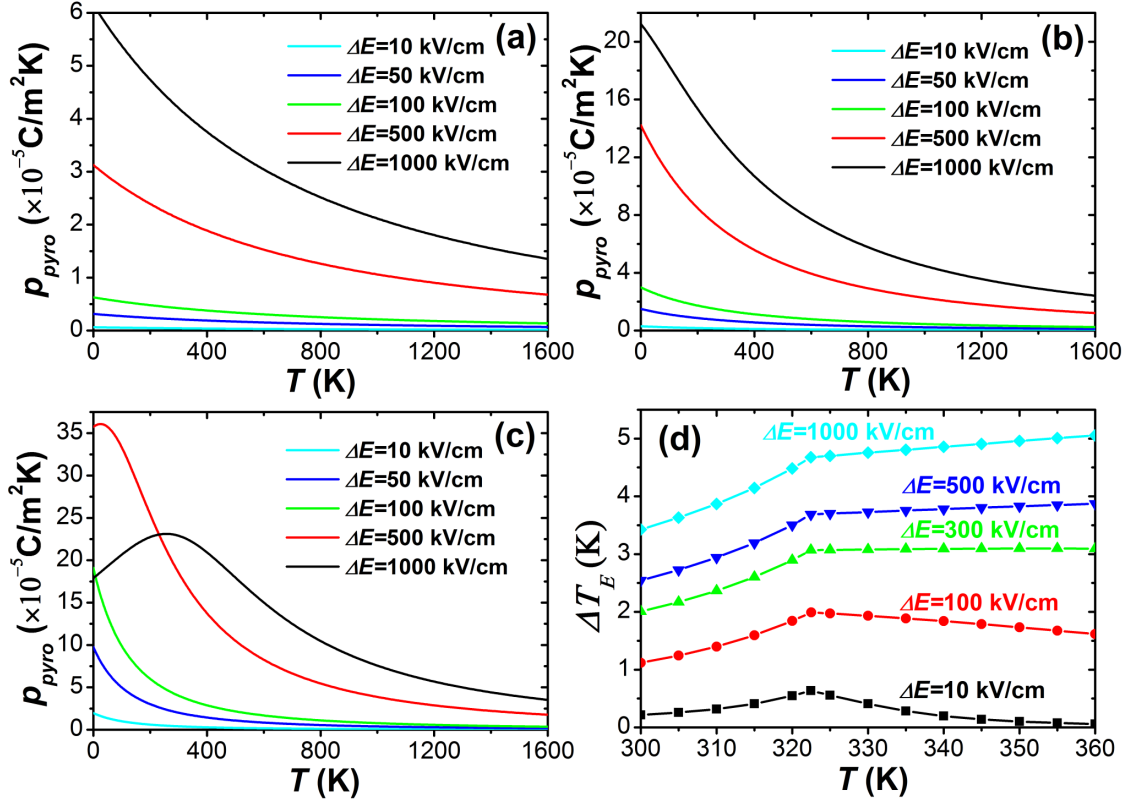


Figure 3.13: Temperature dependence of the electrocaloric coefficient p_{pyro} in response to applied ΔE in epitaxial ultrathin SRO/BTO/SRO capacitors with three different thicknesses of the BTO layer: (a) 0.4 nm, (b) 0.8 nm, and (c) 1.2 nm; (d): Predictions of electrocaloric temperature change ΔT_E as a function of working temperature T for a 2.4-nm-thick BTO film capped with two identical SRO electrodes at various electric field changes ΔE .

of ΔT_E over ΔE in three forms of BTO shown above under the same condition of temperature and applied electric field show that they are similar and in the same order of magnitude, which suggests that such a large strain in ultrathin BTO films cannot alter the electrocaloric effect significantly. However, the fully strained ultrathin films could bear a much higher applied field, which is helpful in increasing the electrocaloric effect [84]. For example, at 300 K, it is found that ΔT_E is 3.5 K under 0.24 V (15 K/V), which is significantly enhanced by the ultrahigh electric field. Experimentally, it was reported that thin BTO films (77 nm) may permit a giant applied field (i.e., > 13000 kV/cm) [311]. If the ultrathin BTO film (2.4 nm) in this study could hold a field as large as 10000 kV/cm, ΔT_E at 300 K would be 9 K. As the films become thinner, heat capacity C_E in Eq. (1.28) decreases as well, and ΔT_E would be enhanced even further. Thus, giant electrocaloric effect in ultrathin ferroelectric capacitor is quite possible to be achieved. In addition, for the BTO films (2.4 nm) under high field, the important tunnel electroresistance should be taken into account [244]. However, such a quantum tunnelling corresponding to a very large resistance [244] is usually quite small, i.e., a tunnelling current of ~ 2.4 nA under the electric field of 1000 kV/cm. This value yields negligible Joule heating ($< \sim \times 10^{-3}$ K) which would not affect the main results of this study.

Up to now, most research concentrate on the size effect of ultrathin ferroelectric capacitors mainly for the application of ferroelectric tunnel junctions or high density ferroelectric storage, here we report that ultrathin ferroelectric capacitors have another advantage that the self-electrocaloric effect could provide themselves a comfortable working temperature, and they may also be grown on small chips in computer as an environmentally friendly room-temperature solid-state refrigeration. Furthermore, interesting multilayer capacitors [208, 209, 231] would be helpful for ultrathin ferroelectric capacitors to improve the capability of absorbing heat. Although in practice there are still many challenges such as high leakage [84] or pinholes which would induce many short-circuited hotspots in ultrathin films resulting in no electrocaloric effect at all [244], we believe that our results will stimulate further work on growing high-quality ultrathin perovskite films, and measuring the thickness dependence of the electrocaloric effect in these films.

3.1.3 Electrocaloric effect in asymmetric ferroelectric tunnel junctions

As addressed in Section 3.1.1, FTJs are gaining increasing interest due to their great potential applications in next generation memory/logic devices [239]. In FTJs, the TER effect—a change in resistance of the junction associated with the reversal of ferroelectric polarization—can be achieved [240, 241, 312]. Only very recently, TER effect was experimentally demonstrated and the application of an external bias voltage can switch resistance between two states: high resistance (OFF) and low resistance (ON) states [244, 245, 313]. Based on this effect, a non-volatile bi-stable device with non-destructive readout operation was reported [246]. In addition to the electrostatic effect, TER effect can be also induced by changing the width of the barrier based on converse piezoelectric effect [240, 248, 314], ferroelectric field effect [315], interface magnetoelectric effect [316] and so on.

For TER effect in FTJs, ultrahigh electric fields are usually used in ultrathin ferroelectric films, especially during the writing process. For instance, an electric field of 1.5 GV/m can be produced

upon an application of a typical writing voltage of 3 V for a ferroelectric barrier thickness of 2 nm. As a matter of fact one may ask whether a large or even giant electrocaloric response can be obtained in FTJs under such large external fields which can not be achieved in ferroelectric bulk and relatively thicker films [15, 18, 46, 84, 110–112, 149, 158, 163, 203, 204, 304, 317]. This is of crucial interest for both fundamental research and practical applications [84].

Actually, an intrinsic giant electrocaloric effect was already demonstrated in symmetric FTJs in Section 3.1.2. However, the selected electrode materials are usually different and the role of the depolarizing field should be explicitly addressed. Moreover, in practice, even for the same electrode materials, the terminations near the ferroelectric/electrode interfaces may be different [200, 264, 271, 281, 318], which results in asymmetrically electronic and chemical environments of the electrode/ferroelectric interfaces. This is particularly true for FTJs containing only a few ferroelectric unit cells, in which a large internal field (also called the built-in field) can be generated due to the work function difference between the two ferroelectric/electrode interfaces [200, 271, 281, 318]. In this Section, taking into account the contributions of the depolarizing field, built-in electric field, interface and surface energies, electrocaloric effect in (001)-oriented Pt/BTO/SRO FTJs is quantitatively presented using a multiscale thermodynamic based calculations. Let us consider the epitaxial (001) single-domain Pt/BTO/SRO FTJs grown on thick STO substrates as shown in Fig. 3.14. Two asymmetric electrode/ferroelectric interfaces of SRO/BTO and BTO/Pt are denoted as 1 and 2, respectively, with surface normals \vec{n}_1 and $\vec{n}_2 = -\vec{n}_1$ pointing towards the electrodes. Note that the AO-BO₂ stacking sequence is usually preserved at the interfaces in a heterostructure with SRO electrode [264] and Pt₂-BaO type is reported to induce an overall enhancement of the ferroelectricity of BTO films [273, 303]. Therefore, we focus on the particular interface terminations of the SrO-TiO₂ type for SRO electrodes, and the Pt₂-BaO type for Pt electrodes. For other geometries of the ferroelectric/electrode interfaces [264, 271, 318], further calculations can be done based on the methodology used in this work. In the following, we use the multiscale thermodynamic model as stated in Section. 2.1.1.2 to study the electrocaloric effect in asymmetric FTJs.

Based on a simple electrostatic model [241] and experimental evidence [245], the junction is in ON (low resistance) or OFF (high resistance) states for polarization pointing towards SRO or Pt, respectively, which is indicated in Fig. 3.14. Due to the internal built-in electric field, spatial inversion symmetry of FTJs is broken, which can be seen clearly from the asymmetric thermodynamic potentials in Eq. (3.2). Usually, electrocaloric properties do not have direction, therefore, do not show any direction dependence. However, the existence of the built-in field in FTJs can lead to the asymmetric ferroelectric properties which strongly depend on the direction of the polarization [200, 271, 318]. As a result, the electrocaloric temperature change under adiabatic application of an electric field for the two opposite polarization orientations can be different, just like the TER effect [239–242, 244–246, 248, 312–316] revealed in FTJs. We denote the adiabatic electrocaloric temperature change of ON (OFF) state as ΔT_{ON} (ΔT_{OFF}) following Eq. (1.24), which can be written as:

$$\Delta T_{ON/OFF} = -T \int_{E_a}^{E_b} \frac{1}{C_E} \left(\frac{\partial D_{ON/OFF}^0}{\partial T} \right)_{E,\sigma} dE, \quad (3.6)$$

where $\vec{D}_{ON/OFF}^0 = \varepsilon_b(\vec{E}_{dep,ON/OFF} + \vec{E} + \vec{E}_{bi}) + \vec{P}_{ON/OFF}^0$ is the equilibrium electric displace-

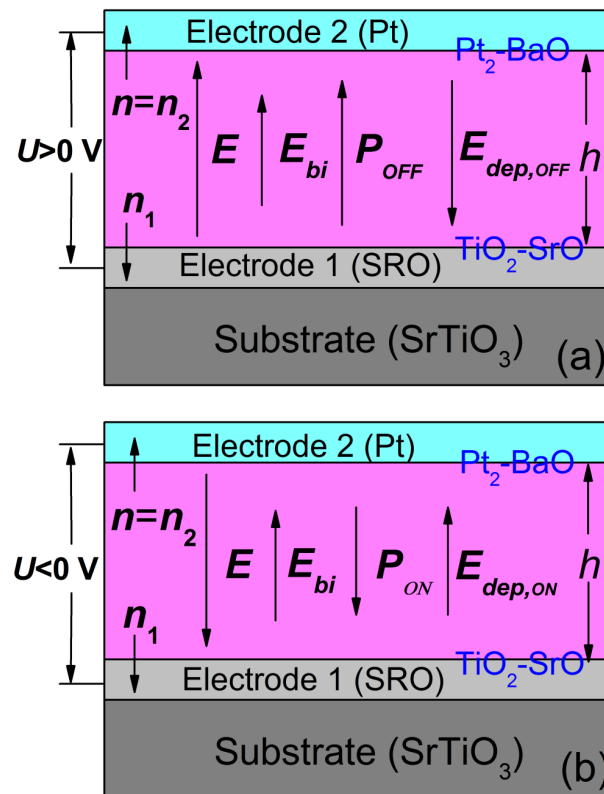


Figure 3.14: Sketch of (a) OFF and (b) ON states in (001)-oriented Pt/BTO/SRO FTJs under adiabatic application of an electric field along the polarization direction.

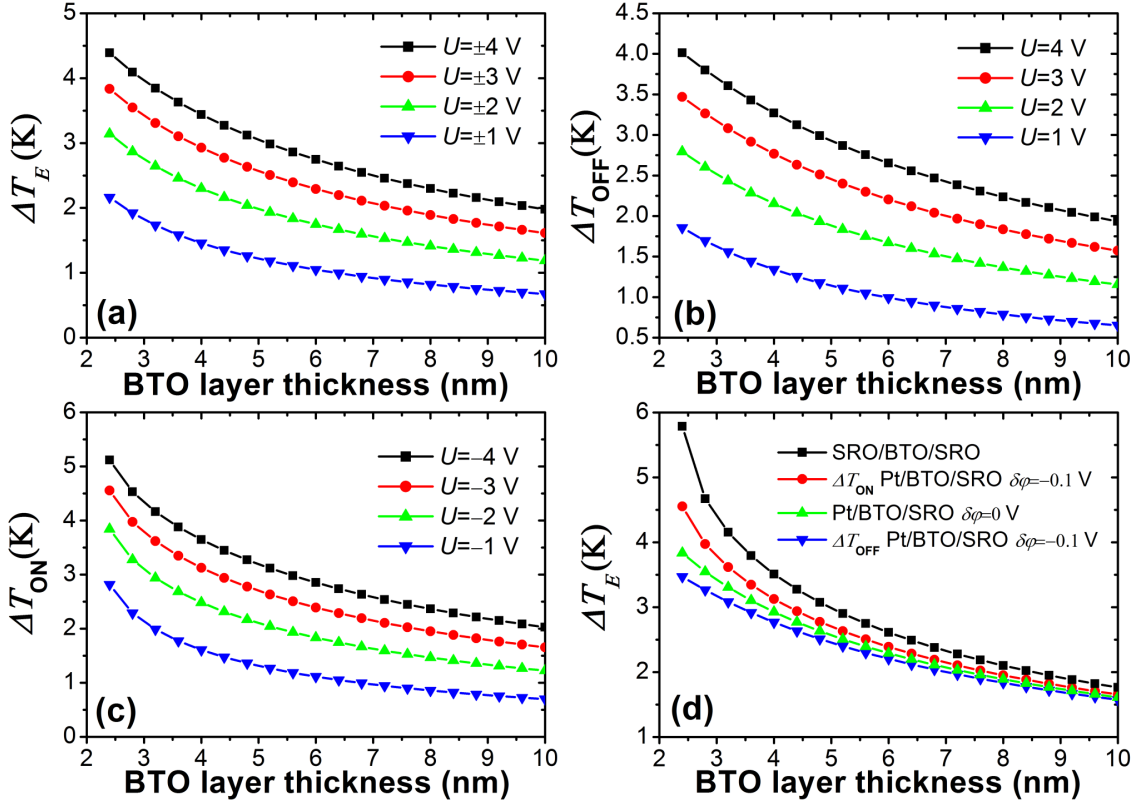


Figure 3.15: The thickness-dependent adiabatic electrocaloric temperature change in response to some applied voltages $U = \Delta E h$ in (001)-oriented Pt/BTO/SRO FTJs for different states: (a) without the built-in field; (b) OFF and (c) ON states taking into account the built-in field; (d): comparison between (a), (b), (c) and the results of symmetric SRO/BTO/SRO FTJs ($|U| = 3$ V).

ment of ON and OFF states, respectively, under a fixed electric field. C_E is the heat capacity under constant electric field and $\Delta E = E_b - E_a$ is the field change (E_a is set to zero). Note that strict Maxwell relation $(\frac{\partial S}{\partial E})_{T,\sigma} = (\frac{\partial D^0}{\partial T})_{E,\sigma}$ rather than the approximate $(\frac{\partial S}{\partial E})_{T,\sigma} = (\frac{\partial P^0}{\partial T})_{E,\sigma}$ is used in order to explicitly include the effect of the depolarizing field, where S is the entropy and σ is the stress. Although the approximate Maxwell relation $(\frac{\partial S}{\partial E})_{T,\sigma} = (\frac{\partial P^0}{\partial T})_{E,\sigma}$ is widely used in literature, such approximation $P^0 \sim D^0$ is only valid for relatively thicker films, which will be discussed in Section 3.1.4. All the parameters we used are the same as Section 3.1.1 and Section 3.1.2.

Let us concentrate on the room-temperature electrocaloric properties of Pt/BTO/SRO FTJs. The critical thickness at 0 K is about 1.64 nm. This means that the instability of ferroelectric phase occurs approximately at four unit-cells, which agrees well with the results of first-principles calculations [318]. Also the theoretical behaviors of the polarization [200] agree well with the results predicted by first-principles calculations [318]. Furthermore, ferroelectricity is found to

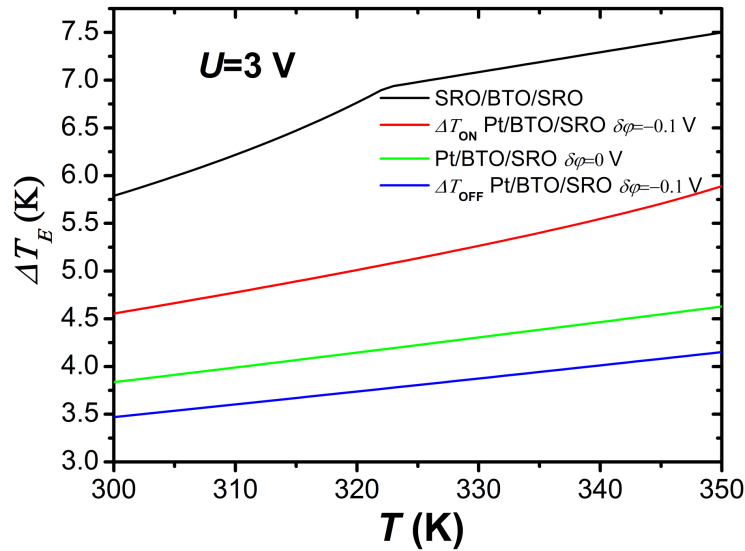


Figure 3.16: The temperature-dependent adiabatic electrocaloric temperature change in (001)-oriented Pt/BTO/SRO FTJs ($h=2.4$ nm, $|U|=3$ V) with/without considering the effect of the built-in field. The results of symmetric SRO/BTO/SRO FTJs under the same conditions are also added.

remain stable down to 2.4 nm at room temperature, which is in line with a recent experimental evidence [245]. For the Pt/BTO/SRO FTJs free from any built-in field, the a value of the critical thickness would be smaller, of about three unit-cells at 0 K [200]. We also note that in order to further relate our theoretical predictions to the experimental measurements, we have paid a particular attention to the writing progress in FTJs, in which larger electric stimulus can be achieved compared to that in the reading progress [244–246, 314–316]. Then, it is more suitable to use the electric stimulus in terms of applied voltage ($U=\Delta E h$) rather than electric field ΔE . Electrocaloric properties in Pt/BTO/SRO FTJs without/with considering the effect of the built-in field are given in Figs. 3.15(a)-3.15(c). As expected, it can be seen in Fig. 3.1(a) that electrocaloric response does not show any direction dependence for OFF and ON states without introducing the built-in field. In this case, the largest ΔT_E is about 3.8 K for $h=2.4$ nm under a typical voltage of 3 V, which is smaller than 5.8 K found in symmetric SRO/BTO/SRO FTJs [47]. This is essentially due to a much higher phase transition temperature in Pt/BTO/SRO junctions compared with that in SRO/BTO/SRO junctions for a given BTO thickness [200]. For the conditions taking into account the effect of the built-in field, direction-dependent electrocaloric properties, namely ΔT_{OFF} and ΔT_{ON} are shown in Figs. 3.15(b) and 3.15(c), respectively. It appears that both ΔT_{OFF} and ΔT_{ON} under a given external voltage decrease as the BTO film thickness increases due to the reduction of the applied field. It is found that ΔT_{OFF} is reduced while ΔT_{ON} is enhanced compared to the results without the built-in field for all given thicknesses. This can be seen more clearly in Fig. 3.15(d) and the difference between ΔT_{ON} and ΔT_{OFF} becomes increasingly larger, reaching over 1 K as the BTO film thickness decreases. Interestingly, ΔT_E versus thickness evolves in an opposite variation trend compared

Table 3.3: Comparison of electrocaloric properties of Pt/BTO/SRO FTJs developed here with those in the literature.

| Samples | T [K] | ΔT_E [K] | ΔE [kV/cm] | $\Delta T_E/\Delta E$ [mK cm/kV] | $\Delta T_E/\Delta U$ [K/V] | R [J/cm ³] | Refs |
|--|------------|---------------------|-----------------------|-------------------------------------|--------------------------------|-----------------------------|-------|
| PbZr _{0.95} Ti _{0.05} O ₃ ^{CF} | 495 | 12 | 480 | 25 | 0.48 | ~0.74 | [15] |
| P(VDF-TrFE) ^{PF} | 353 | 12.5 | 2000 | 6.25 | ~0.16 | ~1.33 | [46] |
| BTO ^{SC} | 402 | 0.9 | 12 | 75 | ~0.015 | ~0.010 | [48] |
| doped BTO ^{CMLC} | 350 | 0.5 | 300 | 1.7 | ~0.0037 | ~0.0020 | [231] |
| BTO ^{CMLC} | 353 | 7.1 | 800 | 9 | ~0.030 | ~0.395 | [210] |
| BTO ^C | 312 | 4.5 | 145 | 31 | ~0.003 | ~0.21 | [150] |
| BTO ^{UTF} | 300 | 5.8 | 12500 | 0.46 | 1.93 | ~0.28 | [47] |
| BTO (OFF) ^{UTF} | 300 | 3.5 | 12500 | 0.28 | 1.17 | ~0.10 | Here |
| BTO (ON) ^{UTF} | 300 | 4.6 | 12500 | 0.37 | 1.53 | ~0.18 | Here |

CF, PF, SC, CMLC, C, and UTF indicate ceramic film, polymer film, single crystal, ceramic MLC, ceramic and ultrathin film, respectively.

to TER ratio versus thickness [241, 244, 245]. Obviously, this change in electrocaloric response for the two opposite polarization orientations is the consequence of the built-in field and can be understood as follows. The built-in field \vec{E}_{bi} is antiparallel with P_{ON}^0 and therefore reduces it, while \vec{E}_{bi} is parallel with P_{OFF}^0 and thus enhances it [200, 318]. As a result, an external electric field with the same magnitude can induce a larger polarization change in the ON state than in the OFF state. Though ΔT_{ON} is enhanced compared with the case without the built-in field in Pt/BTO/SRO junctions, it remains still about 1 K smaller than that in SRO/BTO/SRO junctions, as shown in Fig. 3.15(d).

Thanks to the ultrahigh breakdown fields in these ultrathin films, the electrocaloric effect in Pt/BTO/SRO junctions is considerably enhanced, and is larger than most of the theoretical and experimental results in BTO-based samples near room temperature (see Table. 3.3). For instance, 0.90 K was reported in BTO single crystals ($\Delta E=12$ kV/cm at 402 K) [48], ~0.82 K in BTO films ($\Delta E=100$ kV/cm at 300 K) [123, 306], ~0.45 K in doped BTO multilayer capacitors (MLCs) ($\Delta E=300$ kV/cm at 300 K) [231], 1.3 K in BTO MLCs ($\Delta E=176$ kV/cm at 313 K), [209] 1.4 K in BTO ceramics ($\Delta E=10$ kV/cm at 400 K) [319], and 4.5 K in modified BTO ceramics ($\Delta E=145$ kV/cm at 312 K) [150]. And the result obtained in this work is close to the largest one i.e., 7.1 K reported in BTO MLCs ($\Delta E=800$ kV/cm at 353 K) [210]. Note that although the ultrahigh electric field (>1.5 GV/m) is expected to induce a larger electrocaloric effect in FTJs, our study quantitatively demonstrates that its contribution to the enhancement of ΔT_E is not so significant. Indeed, ΔT_E in Pt/BTO/SRO junctions could only reach less than half of those obtained (~12 K) in PbZr_{0.95}Ti_{0.05}O₃ films [15] and P(VDF-TrFE) polymer films [46, 317]. It was reported that the electrocaloric strength $|\Delta T_E|/|\Delta E|$ in ferroelectric thin films is usually smaller than that in bulk [48, 111]. Here we find that $|\Delta T_E|/|\Delta E|$ decreases even further as the film thickness decreases to only a few nanometers (see Table. 3.3). Note that

the second-order nature of the phase transition ($\alpha_{11}^* > 0$) in Pt/BTO/SRO junctions may also give rise to this reduced $|\Delta T_E|/|\Delta E|$. Nevertheless in counterpart, large hysteresis losses usually associated with first-order transition which are detrimental for refrigerant capacity, which can be naturally avoided in such junctions.

The temperature-dependent electrocaloric properties in response to a typical writing voltage of 3 V for different cases are summarized in Fig. 3.16. It is shown that the adiabatic temperature change rises as the temperature increases. It is found that electrocaloric response shows the lowest sensitivity to temperature in the OFF state, while it shows the highest temperature sensitivity for SRO/BTO/SRO junctions (see Fig. 3.16). However, ΔT_{OFF} is the smallest among different states. Indeed, the change in ΔT_E with temperature (from 300 K to 350 K) is in a range smaller than 2 K, which demonstrates a wide working temperature window of a potential device made of Pt/BTO/SRO tunnel junctions. In addition, the electrocaloric strength $|\Delta T_E|/|\Delta E|$ obtained in Pt/BTO/SRO junctions is found to be more than one order of magnitude smaller than those reported in BTO single crystal and other relatively thick films. Note that the relevant figure of merit for applications of electrocaloric effects depends on the external voltage applied rather than the electric field generated [15, 84]. Indeed, the electrocaloric parameter $|\Delta T_E|/|\Delta U|$ (1.53 K/V) is found to exceed the previous best results obtained in $\text{PbZr}_{0.95}\text{Ti}_{0.05}\text{O}_3$ films (0.48 K/V) (see Table. 3.3). Moreover, it only requires an operational voltage of ~ 3 V, which is strongly reduced compared to 25 V in $\text{PbZr}_{0.95}\text{Ti}_{0.05}\text{O}_3$ films [15] and $\gg 5$ V in BTO MLCs [231]. Our findings therefore imply promising potential of FTJs for tuning electrocaloric effect from high voltages achievable in laboratories to the standard silicon logic level of 5 V, which can be designed as battery-powered integrated microelectronic on-chip devices [84, 231].

For practical applications of any caloric effects, the refrigerant capacity R is of great importance, as it describes how much heat can be transferred between the cold and hot sources in an ideal refrigeration cycle. The refrigerant capacity is defined as $R = \int_{\Delta T_E} \Delta S_E dT \simeq \Delta S_E \Delta T_E$ [108, 110]. Table. 3.3 compares R obtained in this work with those in other typical electrocaloric materials. Interestingly, it is shown that R of the ON state (0.18 J/cm^3) is found to be larger than that of the OFF state (0.10 J/cm^3) in Pt/BTO/SRO junctions. And these R values are much larger than those in BTO single crystals [48] and doped BTO MLCs [231], and are comparable with those of BTO MLCs [210] and modified BTO ceramics [150]. Note that the refrigerant capacity R in Pt/BTO/SRO junctions is much smaller than those in non-BTO-based samples, especially that (1.33 J/cm^3) in P(VDF-TrFE) polymer films [46]. Moreover, due to the tiny volume of the ultrathin capacitor, the total heat that the FTJs can absorb or restore is very small. Therefore, to enhance the efficiency, we suggest the use of MLC structure [209, 231] based on BTO FTJ elements with a relatively large surface area.

Obviously, in real situations, Joule heating warrants further theoretical and experimental considerations. If large Joule heating is induced during the writing progress, no refrigeration will occur [84]. In other words, the ultrathin films would become hotter, not colder, upon the removal of the electric field. Also thermionic injection could contribute more significantly due to its strong temperature dependence [312]. As a result, the resistance would decrease significantly, provided that quantum tunneling is non-sensitive to temperature [240, 245, 246]. For the electrocaloric effects, however, the temperature of ultrathin films increases upon the application of an external voltage, while the temperature decreases upon the removal of the electric field. If

the effect of Joule heating can be ignored and not affecting the performance of the device, the temperature of the sample should stay unchanged after many writing cycles. Based on above analysis, the variation in resistance can somehow reflect the effect of Joule heating. This Joule heating issue can be addressed from two aspects. On one hand, recent experimental results support that the effect of Joule heating is negligible since the resistance variations were not observed even after many writing cycles [246, 315]. On the other hand, even if Joule heating is large, the corresponding change in temperature can be effectively minimized by using high resistance (OFF) state ($> \sim 1 \times 10^7 \Omega$) for electrocaloric applications. In addition, caloric effects in FTJs may be further enhanced by taking advantage of the electrocaloric and elastocaloric effects by applying an electric field and external stress. And the later caloric response, elastocaloric or piezocaloric effect, was recently predicted to be giant in ferroelectric $\text{Ba}_{0.5}\text{Sr}_{0.5}\text{TiO}_3$ alloys [19] and PTO bulk [49]. Most importantly, our recent findings show that the electrocaloric properties of SRO/BTO/SRO symmetric FTJs can be significantly improved in relatively thick films under compressively loaded conditions compared with the unloaded case [166].

In summary, we have studied intrinsic electrocaloric effect in asymmetric Pt/BTO/SRO FTJs by using a multiscale thermodynamic model. Compared with superconductor tunnel junctions which can be employed as low-temperature electronic on-chip coolers with a sub-kelvin temperature change [320], our study highlights the potential use of asymmetric FTJs for solid-state refrigerator at room temperature with a temperature change of several kelvins ($> 4.5 \text{ K}$) and a low operational voltage ($< 5 \text{ V}$). Hopefully, our study will encourage further theoretical works and experimental investigations to measure the electrocaloric response of asymmetric FTJs.

3.1.4 Mechanically-mediated electrocaloric effect in symmetric ferroelectric tunnel junctions

In Section 3.1.2 and Section 3.1.3, we have studied the room-temperature electrocaloric effect in FTJs, the phase transition we used is mainly the ferroelectric-to-paraelectric type due to the size effect as addressed in Section 3.1.1. Interestingly, the transition temperature of such capacitors and consequently their working temperature can be tuned by varying BTO barrier thickness [47]. Moreover, the transition temperature of the epitaxial thin films can be systematically tuned via applying an external stress [321]. Interestingly, a significant enhancement of the Curie temperature and the electrocaloric effect subjected to a tensile stress was reported on bulk PTO [49]. However, due to its high Curie temperature, the working temperature of bulk PTO is limited to a high-temperature range above about 700 K, not mentioning the need of alternative eco-friendly materials. Additionally, a giant extrinsic magnetocaloric effect in $\text{La}_{0.7}\text{Ca}_{0.3}\text{MnO}_3$ films due to a strain-mediated feedback from a BTO substrate near its first-order phase transition was found recently [36]. These two studies [36, 49] underline the potential applications of the external stress/strain into tuning structural transitions to enhance giant caloric effects in a wider range of ferroics including different electrically and magnetically ordered materials. The present section is, therefore, motivated by investigating the influence of external stress on the phase transition, as well as the on electrocaloric effect of ultrathin ferroelectric capacitors.

In this Section, we developed a multiscale thermodynamic model [271, 272] (Section 3.1.1.2) considering a uniform local loading σ_3 (all tensors appear in Voigt notation) applied along the

z direction whereas the shear stresses σ_4 and σ_5 are neglected [321]. The loaded area has dimensions much smaller than those of the substrate surfaces but much larger than film thickness [321]. For a quantitative analysis, we only consider a (001) single-domain BTO film of thickness h capped between two SRO electrodes at room temperature. In particular, we restrict ourselves to the case of capacitors grown on thick (001) STO substrate. In this case, a large compressive misfit strain u_0 is generated by the lattice mismatch between the film and the underlying substrate, i.e., $u_0 = (a_s - a_0)/a_s$, where a_s is the effective lattice constant of the substrate, and a_0 is the equivalent cubic cell constant of the free-standing film. Such large compressive u_0 ensures that the phase transition only occurs from the paraelectric phase ($P_x=P_y=P_z=0$) to the ferroelectric tetragonal phase ($P_x=P_y=0, P=P_z \neq 0$) even under a moderate stress according to the phase diagram of epitaxial BTO films at room temperature [321]. The modified free energy per unit surface of the ferroelectric film can be expressed as [271, 272, 321]

$$\begin{aligned}
 F &= h\Phi + \Phi_S = \left[\frac{1}{2}\alpha_1^* P^2 + \frac{1}{4}\alpha_{11}^* P^4 + \frac{1}{6}\alpha_{111} P^6 + \frac{1}{8}\alpha_{1111} P^8 \right. \\
 &\quad \left. - \frac{1}{2}\vec{E}_{dep} \cdot \vec{P} - \vec{E} \cdot \vec{P} + \frac{(u_m - S_{12}\sigma_3)^2}{S_{11} + S_{12}} - \frac{1}{2}S_{11}\sigma_3^2 \right] h + \eta P^2,
 \end{aligned} \tag{3.7}$$

where

$$\alpha_1^* = \alpha_1 - \frac{4Q_{12}}{S_{11} + S_{12}} u_m - 2(Q_{11} - \frac{2Q_{12}S_{12}}{S_{11} + S_{12}})\sigma_3, \tag{3.8}$$

$$\alpha_{11}^* = \alpha_{11} + \frac{4Q_{12}^2}{S_{11} + S_{12}} \tag{3.9}$$

are the renormalized Landau coefficients. α_{ijkl} are the dielectric stiffness coefficients at constant stress, and only α_1 is temperature dependent through the Curie-Weiss law $\alpha_1 = (T - T_0)/\varepsilon_0 C$, T_0 and C being the Curie temperature and constant, respectively. S_{mn} are the elastic compliances of the film and Q_{mn} are the electrostrictive coefficients of the film. u_m is the misfit strain in the loaded case which is the sum of the unloaded u_0 and the substrate deformations Δu_m . Δu_m can be written as $\Delta u_m = [s_{12} + (s_{11} - 2s_{12})(s_{11} + s_{12})/s_{11}]\sigma_3$, where s_{mn} are the elastic compliances of a cubic substrate [321]. Note that in this work a uniform stress applied perpendicular to the top surface of the film is considered, ruling out the flexoelectric effect caused by strain gradients [322]. η is the second-order coefficient of the surface energy Φ_S expansion for ferroelectric/electrode interfaces. \vec{E} is the applied electric field along the polar axis. \vec{E}_{dep} is the depolarizing field which can be determined from the short-circuit condition: [271, 272]

$$\vec{E}_{dep} = -\frac{2\lambda}{h\varepsilon_0 + 2\lambda\varepsilon_b} \vec{P}, \tag{3.10}$$

where ε_0 is the permittivity of free space, and ε_b is the background dielectric constant. λ is the effective screening length of BTO/SRO interface.

The equilibrium polarization P^0 can be derived from the condition of thermodynamic equilibrium: $\partial F/\partial P = 0$. Then, the electrocaloric coefficient p can be obtained as follows

$$\begin{aligned} p = \left(\frac{\partial S}{\partial E}\right)_{T,\sigma_3} &= \left(\frac{\partial D^0}{\partial T}\right)_{E,\sigma_3} = N \left(\frac{\partial P^0}{\partial T}\right)_{E,\sigma_3}, \\ N &= 1 - \frac{2\varepsilon_b \lambda}{h\varepsilon_0 + 2\lambda\varepsilon_b}, \end{aligned} \quad (3.11)$$

where $\vec{D}^0 = \varepsilon_b(\vec{E}_{dep} + \vec{E}) + \vec{P}^0$ is the equilibrium electric displacement field under a fixed electric field. The electrocaloric temperature change ΔT_E upon adiabatic application of an electric field can be determined following Eq. (1.24):

$$\Delta T_E = -T \int_{E_a}^{E_b} \frac{1}{C_E} \left(\frac{\partial D^0}{\partial T}\right)_{E,\sigma_3} dE, \quad (3.12)$$

where C_E is the heat capacity under constant electric field and ΔE is the field change written as $\Delta E = E_b - E_a$, where E_a is set to zero in the following parts.

For the asymmetric ferroelectric/electrode interfaces, the built-in electric field and surface effects can be included (see Section 3.1.1 and Section 3.1.3). Note that this indirect approach based on Maxwell relation failed to explain the electrocaloric responses in relaxors [149, 150]. However, for normal ferroelectrics as used here, recent theoretical results demonstrated that the indirect approach should always agree with the direct measurement in describing the electrocaloric response within the error of experiments or simulations [100, 177]. All the parameters we used can be found in previous sections. The mechanical boundary conditions (the two-dimensional clamping of the film by the substrate) transform the nature of the phase transition from first order ($\alpha_{11} < 0$) to second order ($\alpha_{11}^* > 0$) according to Eq. (3.9). Although second-order phase transitions are always related to small or moderate caloric effects [18], a giant elastocaloric (also called piezocaloric) effect in principle cannot be strictly ruled out. In this work, we only focus on the loaded equilibrium state after the stress has been applied for a long time.

The uniaxial stress used in this study is in a range of $[-5 \text{ GPa}, 5 \text{ GPa}]$ which is larger than that $[-1 \text{ GPa}, 1 \text{ GPa}]$ applied onto the bulk $\text{Ba}_{0.5}\text{Sr}_{0.5}\text{TiO}_3$ alloys [19] and $[-2 \text{ GPa}, 2 \text{ GPa}]$ used for PbTiO_3 bulk [49]. For bulks, 5 GPa stress represents a very high stress probably high enough to break the sample. However, for thin films, stress being even larger than 5 GPa is reachable [321, 322]. This contrast can be understood as follows. For instance, to achieve a uniform (not local) stress of 5 GPa in a bulk, it requires a force of $5 \times 10^4 \text{ N}$ acting on a typical surface area of 10 mm^2 , which is equivalent to load a very heavy object (5000 kg) onto such a small surface. Obviously, it is rather difficult to reach this situation. In contrast, it was already reported that a very large local stress of about 5 GPa can be achieved in ultrathin BTO films with a sharp tip of a scanning probe microscope (considering the tip-surface contact area as a disk of 10 nm in radius and a mechanical load of 1400 nN) [322]. Therefore, for thin films, a uniform stress of 5 GPa could be readily achieved by applying a mechanical force of 0.005 N using a relatively large tip, i.e., $1 \times 1 \mu\text{m}^2$ on the top surface of $10 \times 10 \mu\text{m}^2$ capacitor. Note that the stress value is well below the threshold ($\sim 20 \text{ GPa}$) for irreversible plastic damage of the BTO surface [323].

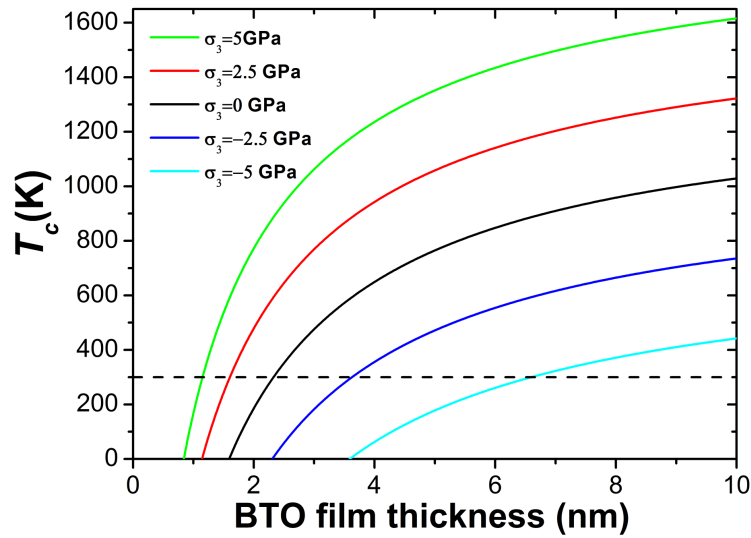


Figure 3.17: The transition temperature T_c as a function of the BTO film thickness in epitaxial SRO/BTO/SRO capacitors with externally controlled stress values σ_3 . The dashed line depicts the temperature of 300 K as a guide for the room temperature.

The effect of an external stress and the mechanical boundary conditions can result in a change in the phase transition temperature $T_c(\sigma_3, h)$. This can be obtained via setting $\alpha_1^* = 0$ in Eq. (3.8). Figure. 3.17 shows that T_c as a function of BTO thickness. It is found that T_c is very sensitive to the strength of σ_3 even under a modest stress. To be more specific, it is shown that compared to the unloaded case ($\sigma_3 = 0$ GPa), a tensile stress ($\sigma_3 > 0$ GPa) increases T_c while a compressive stress ($\sigma_3 < 0$ GPa) suppresses it. This is essentially attributed to the modifications of the effective misfit strain by applying the corresponding stress [321]. Apart from the film thickness, as an alternate degree of freedom, stress can systematically tune T_c being close to room temperature for certain thicknesses, which is desired for caloric applications. To achieve improved performance of the practical devices employing ultrathin ferroelectric capacitors, the change in T_c as a function of the applied stress found here should be taken into account.

Since we select the BTO film at the desired room temperature (300 K), the effect of an external stress and the mechanical boundary conditions then can result in a change in the critical thickness h_c below which the ferroelectric phase disappears. Figure. 3.18 shows that h_c as a function of BTO thickness. It can be seen that compressive stress ($\sigma_3 < 0$ GPa) increases the h_c value, while tensile stress ($\sigma_3 > 0$ GPa) decreases it but less significantly. For instance, $h_c \approx 3.6$ nm for $\sigma_3 = -2.5$ GPa, while $h_c \approx 1.6$ nm for $\sigma_3 = 2.5$ GPa, and we evaluate $h_c \approx 2.4$ nm for $\sigma_3 = 0$ GPa, which is in good agreement with the results of Raman spectroscopy [309]. This is essentially attributed to the modifications of the effective misfit strain by applying the corresponding stress [321]. It was reported that strain engineering can be extremely useful in enhancing ferroelectricity by using various substrates [324] or changing the thicknesses of thin film grown on a finite substrate [325]. Here we can achieve a similar kind of strain engineering by using

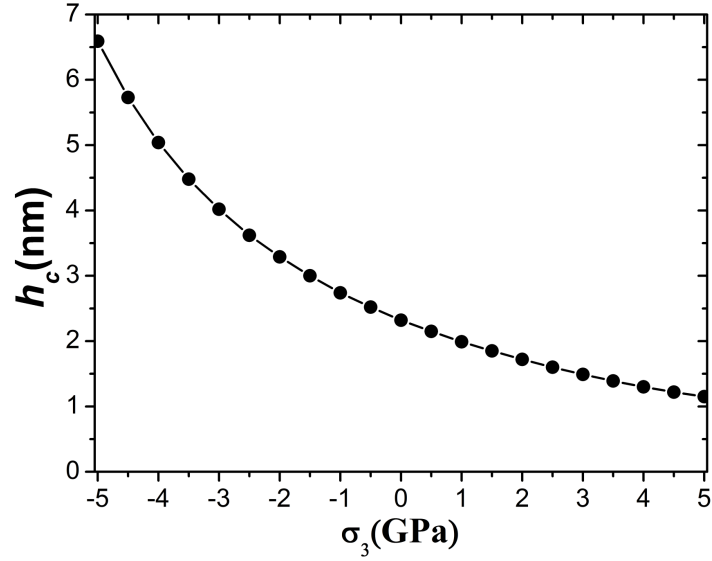


Figure 3.18: The critical thickness h_c as a function of external stress in epitaxial SRO/BTO/SRO capacitors at room temperature.

stress fields along the z -axis for ultrathin films grown on a fixed substrate. To achieve improved performance of the real devices employing ultrathin ferroelectric capacitors, the change in h_c as a function of the applied stress deduced from our calculations can be also taken into account.

The thickness dependence of ΔT_E at 300 K under different stresses is shown in Figs. 3.19(a)-3.19(c). It is found that there is a peak in ΔT_E near the critical thickness h_c , which is essentially due to the ferroelectric-paraelectric phase transition [47]. Compared with the unloaded case, the peak of ΔT_E is shifted to a larger (or smaller) h if a compressive (or tensile) stress is applied. This is attributed to the change in h_c which is induced by stress as shown in Fig. 3.18. The peak of ΔT_E is found to be sharp for the unloaded samples, which is a common feature in ferroelectric thin films, but unfortunately, is not desired for electrocaloric applications. Interestingly, a considerable broadening of ΔT_E in compressively stressed samples is found compared to either the unloaded or tensile cases, becoming more significant as the external electric field increases. Such wide thickness and temperature windows (which is about 60 K, and not shown here) are extremely desirable for practical applications of ferroelectric solid-state refrigeration. The largest value of ΔT_E in response to an electric field of 1000 kV/cm under compressively loaded conditions is 3.69 K which is higher than that (2.87 K) of the unloaded case [see Fig. 3.19(c)].

Another important feature found here is that a significant enhancement of ΔT_E is observed under compressive stress compared with the unloaded and tensile cases [Figs. 3.19(a)-3.19(c)]. In order to explain this result, we focus on the effect of depolarizing field. For strongly polar materials, such as ferroelectrics, $D \sim P$, one can have $(\partial D^0/\partial T)_{E,\sigma_3} \approx (\partial P^0/\partial T)_{E,\sigma_3}$. This equation is widely used in literature but the effect of depolarizing field is ignored. However, it is found that such approximation is only valid for a film thickness being relatively large ($h > 4.8$ nm) [see Fig. 3.19(d)]. When h decreases down to h_c , the ratio N describing the deviation

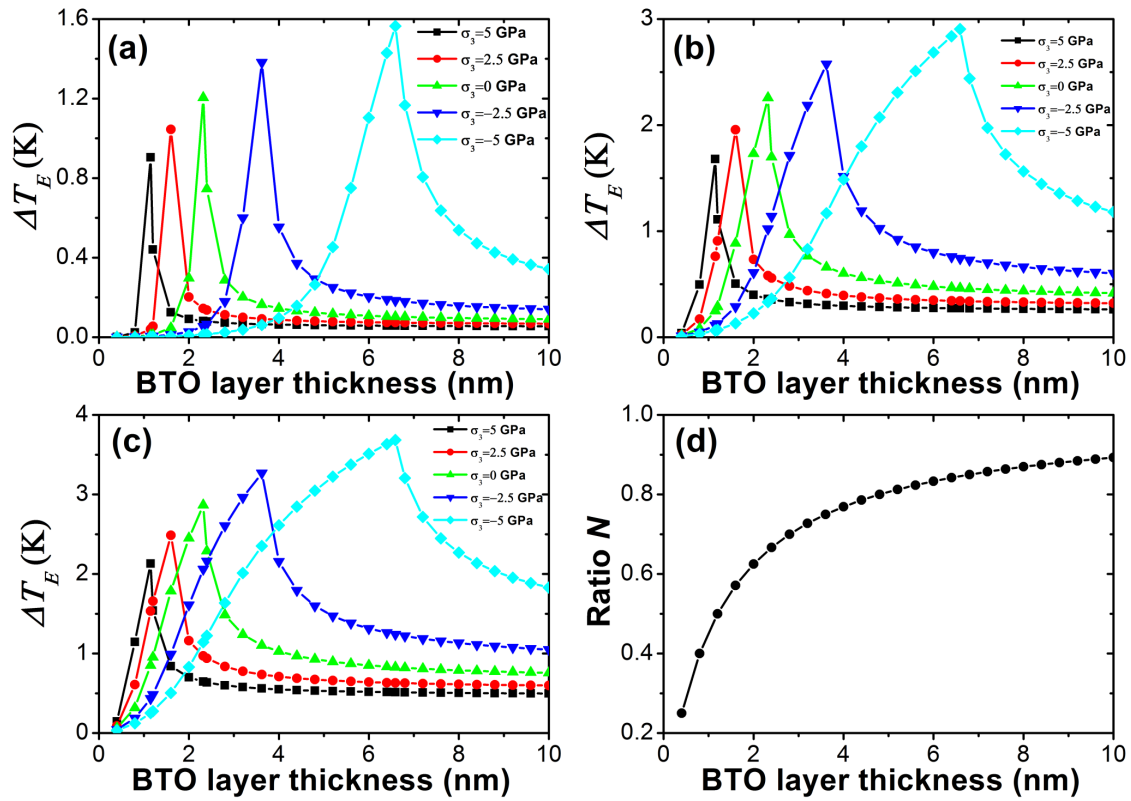


Figure 3.19: The room-temperature electrocaloric temperature change ΔT_E in response to $\Delta E = 100$ kV/cm (a), $\Delta E = 500$ kV/cm (b) and $\Delta E = 1000$ kV/cm (c) as a function of BTO film thickness h for the epitaxial SRO/BTO/SRO capacitors at various stress states: -5 , -2.5 , 0 , 2.5 , and 5 GPa, respectively; (d): The thickness dependence of the ratio N .

between the two derivatives [see Eq. (3.11)], experiences a sharp drop, which clearly suggests that the effect of the depolarizing field becomes dominant. It can be seen in Figs. 3.20(a) and 3.20(b) that the peak value of ΔT_E under different stresses remains almost unchanged for the thicknesses close to the critical ones at 300 K, if $(\partial P^0/\partial T)_{E,\sigma_3}$ is used to calculate ΔT_E as shown in Eq. (1.28). In this case, a remarkable broadening of ΔT_E under compressive stress is still observed in Figs. 3.20(a) and 3.20(b) which is similar with the results shown in Figs. 3.19(a) and 3.19(b). Moreover, it is found that the peak values of ΔT_E in Figs. 3.19(a)-3.19(c) follow exactly the same variation trend as that of the ratio N as BTO film thickness increases. This is mainly due to effect of the depolarizing field, which plays a less dominant role in thicker BTO films in reducing the electrocaloric properties. As a result, the modification of ΔT_E peak is due to the effect of the depolarizing field while the broadening or shrinking of ΔT_E is attributed to the effect of applied stress.

Note that the enhancement of the electrocaloric effect caused by stress especially in the nonpolar state was explained by an additional piezocaloric effect induced by the electric field [49]. In this recent work [49], though there is no piezocaloric effect in the nonpolar state, after being polarized by an external field the sample could show observable piezocaloric effect due to the strong coupling between polarization and strain in ferroelectric. This is obviously not the case in our study, since the piezocaloric effect is explicitly not considered. Moreover, though a significant enhancement of the Curie temperature of bulk PTO can be induced by a tensile stress, there is no perceptible peak shift of ΔT_E observed upon the application of the stress [49]. While in our case, it is found that a change in the critical thickness by applied stress in epitaxial SRO/BTO/SRO capacitors can result in a remarkable shift of ΔT_E peak [see Figs. 3.19(a)-3.19(c)]. Indeed, tuning the electrocaloric effect by adjusting the magnitude of the residual depolarizing field has been reported recently in $\text{Pb}(\text{Zr}_{0.4}\text{Ti}_{0.6})\text{O}_3$ nanodots by Prosandeev *et al.* [167]. Similarly, here we also find that the depolarizing field plays a major role in determining the electrocaloric properties of ultrathin BTO films.

Figure. 3.19(a) shows that the maximum ΔT_E under $\Delta E=100$ kV/cm (i.e., voltage=0.06 V) at 300 K is about 1.56 K for $h=6$ nm and $\sigma_3=-1$ GPa. Moreover, this value is larger than most of the theoretical and experimental data in BTO-based samples. For instance, ~ 1.00 K was reported in $\text{Ba}_{0.5}\text{Sr}_{0.5}\text{TiO}_3$ alloys ($\Delta E=100$ kV/cm at 300 K) [177, 308], 0.90 K in BTO single crystal ($\Delta E=12$ kV/cm at 402 K) [48], ~ 0.82 K in BTO films ($\Delta E=100$ kV/cm at 300 K) [123, 306], ~ 0.45 K in the doped BTO multilayer capacitors ($\Delta E=300$ kV/cm at 300 K) [208, 231] and 1.3 K in BTO multilayer capacitors ($\Delta E=176$ kV/cm at 313 K) [209]. And the result obtained in this work is about half of the largest one i.e., ~ 3.2 K reported in modified BTO ceramics ($\Delta E=100$ kV/cm at 342 K). Note that due to the ultrathin thickness of ferroelectric films [150], ultrahigh electric field, which can not be achieved in ferroelectric bulk and relatively thick films, can be used to further enhance ΔT_E (Ref. [47] or Section 3.1.2). In particular, the largest ΔT_E in ultrathin SRO/BTO/SRO capacitors is about 1.2 K under $\Delta E=100$ kV/cm for the unloaded case shown in Fig. 3.20(a). This value is larger than 0.82 K in BTO films at room temperature, in which the effect of the depolarizing field is not included [123, 306]. This enhancement of ΔT_E may be due to the sharp phase transition nature near the critical thickness, which can compensate the effects of the depolarizing field and the compressive misfit strain [123, 306], both lowering ΔT_E . In addition, although the electrocaloric strength $|\Delta T_E|/|\Delta E|$ of the ultrathin

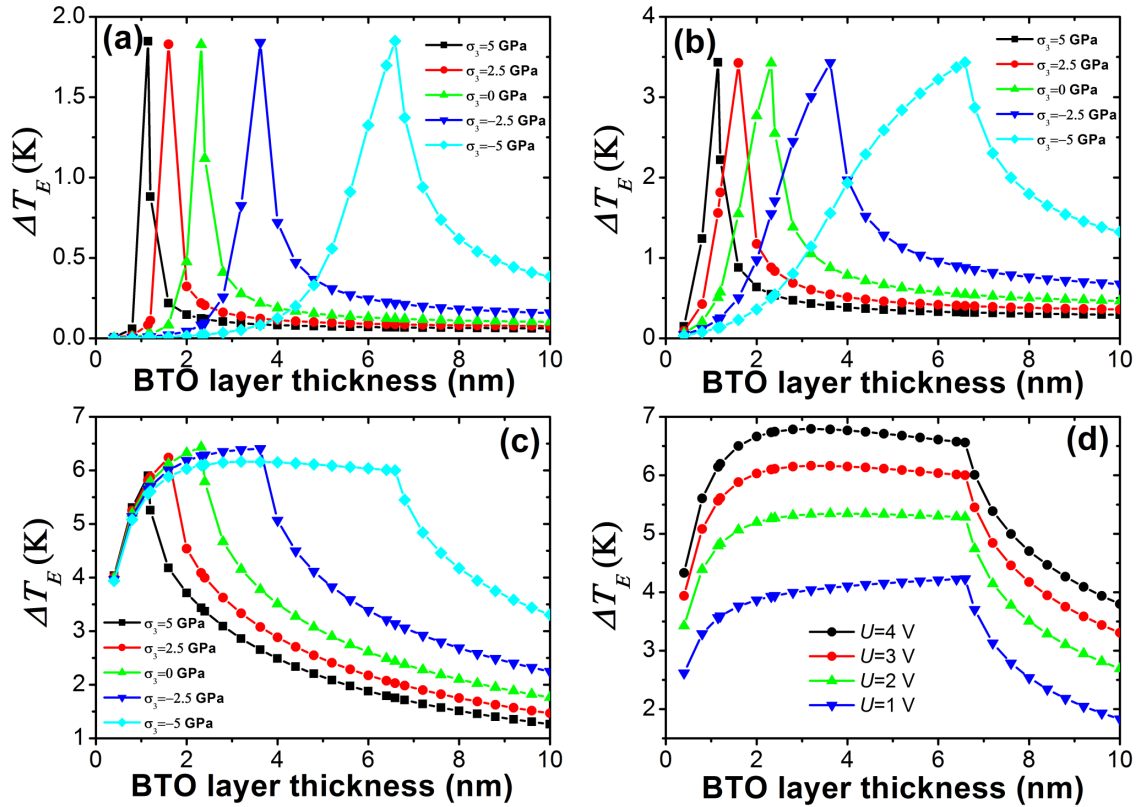


Figure 3.20: The room-temperature electrocaloric temperature change ΔT_E in response to $\Delta E = 100$ kV/cm (a), $\Delta E = 500$ kV/cm (b) as a function of BTO film thickness h for the epitaxial SRO/BTO/SRO capacitors at various stress states: -5 , -2.5 , 0 , 2.5 , and 5 GPa, respectively, in which depolarizing field is not explicitly included; (c): The thickness dependent ΔT_E in response to a typical voltage U of 3 V for the epitaxial SRO/BTO/SRO capacitors at various stress states at 300 K; (d): The thickness dependent ΔT_E for $\sigma_3 = -5$ GPa under different applied voltages U at 300 K.

films considered in this work is found to be more than one order of magnitude smaller than that reported in BTO single crystals [48], it only requires an extremely small operational voltage of ~ 0.06 V in ultrathin films, which is therefore energetically more efficient. Moreover, due to the second-order nature of the phase transition here, hysteresis losses, which are detrimental to refrigerant efficiency, are naturally overcome.

Finally, ΔT_E subjected to a typical writing voltage of ~ 3 V is shown in Fig. 3.20(c). The foregoing broadening of ΔT_E becomes wider and the largest ΔT_E is around 6 K for various σ_3 . Improved electrocaloric behaviors, especially in compressively stressed conditions, can be seen more clearly in Fig. 3.20(d). For instance, a relative wide operational thickness window (from 2 nm to 7 nm) for various applied voltages from 1 V to 4 V is found under compressive stress ($\sigma_3 = -5$ GPa) compared with the narrow one in the unloaded case. The wide thickness window therefore offers more choices for designing ultrathin samples with excellent electrocaloric performances. In contrast, for the cases under zero or tensile stress, strict requirements about the thickness of sample impose a limit for its practical applications. The largest ΔT_E obtained in this work ($\sigma_3 = -5$ GPa) is about 6.8 K under a voltage of 4 V which is close to the largest one i.e., 7.1 K reported in BTO multilayer capacitors ($\Delta E = 800$ kV/cm at 353 K) [210]. Note that no refrigeration will occur if large Joule heating is induced during the writing process [84]. We would like to address this important issue from two aspects. On the one hand, recent experimental results indicate that the effect of Joule heating is negligible since the resistance variations caused by fatigue were not observed even after many writing cycles [247, 315]. On the other hand, even if Joule heating is significant, the corresponding change in temperature could be effectively minimized by employing relatively thicker films and applying a compressive stress according to this study. In particular, for asymmetric ferroelectric tunnel junctions, the use of the high resistance state ($> \sim 1 \times 10^7 \Omega$) [247, 315] could be more helpful for electrocaloric applications.

In summary, we predict a giant mechanically-mediated electrocaloric effect in ultrathin ferroelectric capacitors by using a developed thermodynamic model. We find the electrocaloric properties of ultrathin ferroelectric capacitors can be significantly improved in compressively stressed systems. Since the compressive stress is easier to obtain compared with the tensile one, we hope that our study will stimulate further experimental works to directly measure the electrocaloric effect in such capacitors under compressive loading.

3.2 NEGATIVE ELECTROCALORIC EFFECT IN ANTIFERROELECTRIC LA-DOPED $\text{PB}(\text{ZrTi})\text{O}_3$ THIN FILMS NEAR ROOM TEMPERATURE

Electrocaloric refrigeration based on the electrocaloric effect has recently been regarded as a very promising alternative to the vapor-cycle cooling technologies invented a hundred years ago [5, 8, 84, 109–111]. Electrocaloric effect refers to the isothermal entropy or adiabatic temperature change of a dielectric material when an electric field is applied or removed. Usually an isothermal application of an electric field orders the dipoles, accompanied by a reduction of the corresponding entropy. A subsequent adiabatic depolarization randomizes the dipoles again, causing an increase in electrical entropy, which leads to the cooling of material in order to meet

the adiabatic condition [15, 46, 47, 123, 133, 172, 201, 204, 304, 326, 327].

Interestingly and unexpectedly, recent experimental studies showed that relaxor ferroelectrics [16, 168] and antiferroelectric ceramics [17, 134, 137] may permit a negative electrocaloric effect: materials cool when an electric field is applied, whereas they warm when the field is withdrawn. This unusual effect may enlarge the electrocaloric family and enhance the cooling efficiency in combination with conventional (positive) electrocaloric effect [5]. Nevertheless, the mechanism underlying the negative electrocaloric effect is still elusive, and recent findings in the literature appear controversial (see Table. 3.4). For instance, a direct electrocaloric measurement on typical antiferroelectric PbZrO₃ (PZO) ceramics displayed a negative temperature change ΔT_E of about 1 K under a large electric field of 100 kV/cm at 37 °C (Ref. [137]). In contrast, this negative electrocaloric effect was not found in thin films made of antiferroelectrics like Pb_{0.8}Ba_{0.2}ZrO₃ (PBZ) [133], Pb(Nb,Zr,Sn,Ti)O₃(PNZST), and (Pb,La)(Zr,Sn,Ti)O₃ (PLZST) [327] (note, however, that 0.9Bi_{0.5}Na_{0.5}TiO₃-0.1BaTiO₃ (BNT-0.1BT) thin films were predicted to exhibit a negative electrocaloric effect in Ref. [328]). Furthermore and surprisingly, single crystals of relaxor PbMg_{1/3}Nb_{2/3}O₃-0.30PbTiO₃ (PMN-0.3PT) were also found to display a negative electrocaloric effect [16, 168] while ceramics made of the same material do not [152]. Moreover, the negative electrocaloric effect reported so far is mainly restricted to bulk antiferroelectrics and relaxors, and its magnitude is relatively small ($|\Delta T_E| < 2$ K) (Table. 3.4), which is too small for commercial electrocaloric refrigerators [5, 8, 84, 110, 111]. Here we report a giant negative electrocaloric effect with a significantly enhanced $|\Delta T_E|$ of over 5 K in La-doped Pb(Zr_{0.95}Ti_{0.05})O₃ (PZT95/05) thin films near room temperature.

In this work, typical antiferroelectric (Pb_{0.97}La_{0.02})(Zr_{0.95}Ti_{0.05})O₃ (denoted as PLZT2/95/05 for short) thin films were fabricated on a Pt(111)/Ti/SiO₂/Si substrate using sol-gel spin-coating [15]. The top electrodes (platinum squares of about 90 μm×90 μm) were deposited through transmission electron microscopy grids by dc sputtering. The PLZT2/95/05 film structure was determined by X-Ray diffraction (XRD) (Bruker D8 Advance) using Cu K_α radiation. The film thickness was measured by cross-section scanning electron microscopy (SEM) (ZEISS SIGMA HD). Dielectric measurements were conducted using an Agilent E4980A LCR meter at $U=50$ mV. Measurements of $P(E)$ loops and leakage current $I(E)$ were carried out using a Radiant ferroelectric workstation. Note that the work done in this section is done in strong collaboration with Wenping Geng and Anquan Jiang from Fudan University, Xiangjian Meng from Shanghai Institute of Technical Physics, Laurent Bellaiche from University of Arkansas and Jim Scott from University of St Andrews.

X-ray diffraction measurements show a pure orthorhombic antiferroelectric perovskite phase with a highly (100) preferred orientation in these PLZT2/95/05 thin films (see Fig. 3.21) [329]. The XRD refinement is carried out using the software JANA 2006. It is found that refinement with the $Pbam$ space group yields a reasonable fit to our experimental data (i.e., refined parameters $R_p = 2.07$, $wR_p = 2.71$, $cR_p = 4.49$). Refined lattice parameters for orthorhombic (O) phase in PLZT2/95/05 thin film are thus obtained as follows: $a_O = 5.835771$ Å, $b_O = 11.55898$ Å, $c_O = 8.226765$ Å. The film thickness measured by cross-section SEM is about 650 nm and the film is of a dense columnar structure as shown in Fig. 3.22.

$P(E)$ loops of the PLZT2/95/05 thin film at different temperatures on cooling. Evidence for antiferroelectricity is seen below 190 °C [Figs. 3.23(a)-3.23(c)]. Slim-loop ferroelectric phase

Table 3.4: Comparison of different electrocaloric effects in selected materials.

| Material ^{a)} | T [°C] | ΔT_E [K] | ΔE [kV/cm] | $ \Delta T_E/\Delta E $ [K cm/kV] | $ \Delta S_E $ [J/K kg] | $ R $ [J/kg] | Refs |
|--------------------------------|-------------|---------------------|-----------------------|--------------------------------------|----------------------------|-----------------|-------|
| PZT95/05 ^{Cf} | 222 | 12 | 480 | 0.0250 | 8 | 96 | [15] |
| P(VDF-TrFE)55/45 ^{Cf} | 80 | 12.6 | 2090 | 0.0060 | 60 | 758 | [46] |
| PMN-0.35PT ^{Cf} | 140 | 31 | 747 | 0.0415 | — | — | [326] |
| P(VDF-TrFE)68/32 ^{Cf} | 33 | 20 | 1600 | 0.0125 | 95 | 1900 | [204] |
| PLZT8/65/35 ^{Cf} | 45 | 40 | 1200 | 0.0333 | 50 | 2000 | [204] |
| PBZ ^{Cf} | 17 | 45.3 | 598 | 0.0758 | 46.9 | 2125 | [133] |
| PNZST ^{Cf} | 50 | 5.5 | 139 | 0.0396 | — | — | [327] |
| PLZST ^{Cf} | 32 | 3.8 | 80 | 0.0475 | — | — | [327] |
| PLZT2/95/05 ^{Cf} | 220 | 8.5 | 754 | 0.0113 | — | — | [132] |
| PZO ^{Cf} | 235 | 7.7 | 400 | 0.0193 | — | — | [131] |
| BNT-0.1BT ^{If} | 50 | -3.3 | 517 | 0.0064 | — | — | [328] |
| PMN-0.30PT ^{Ibc} | 80 | -0.15 | 10 | 0.0150 | — | — | [168] |
| BNT ^{Ibc} | 25 | -0.12 | 50 | 0.0024 | — | — | [17] |
| NBT ^{Ibc} | 20 | -1.6 | 70 | 0.0229 | — | — | [134] |
| PZO ^{Ibc} | 37 | -1.05 | 100 | 0.0105 | — | — | [137] |
| PLZT2/95/05 ^{If} | 30 | -5.0 | 308 | 0.0162 | — | — | Here |

^{a)} indicates the positive electrocaloric effect while I stands for negative electrocaloric effect; bs and bc correspond to single crystal and bulk ceramic, respectively, while f refers to thin films. P(VDF-TrFE)= poly(vinylidene fluoride-trifluoroethylene).

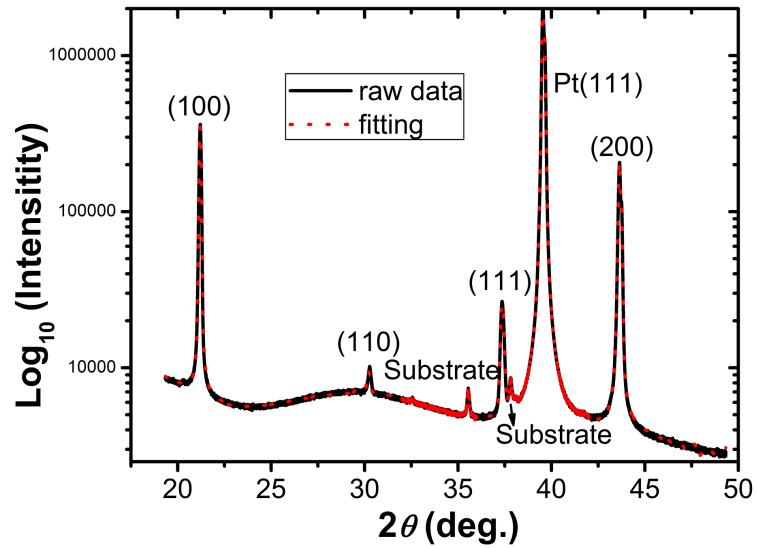


Figure 3.21: XRD pattern of the PLZT2/95/05 thin film.

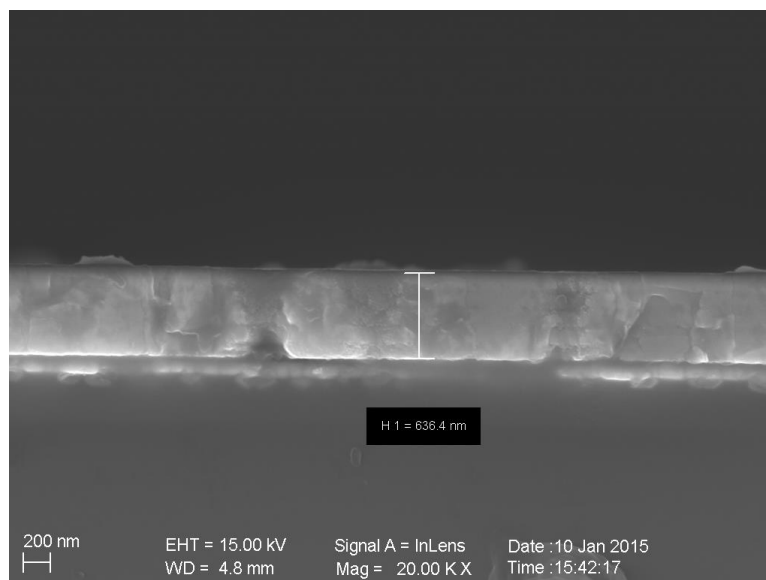


Figure 3.22: The cross-sectional SEM micrographs of the PLZT2/95/05 thin film.

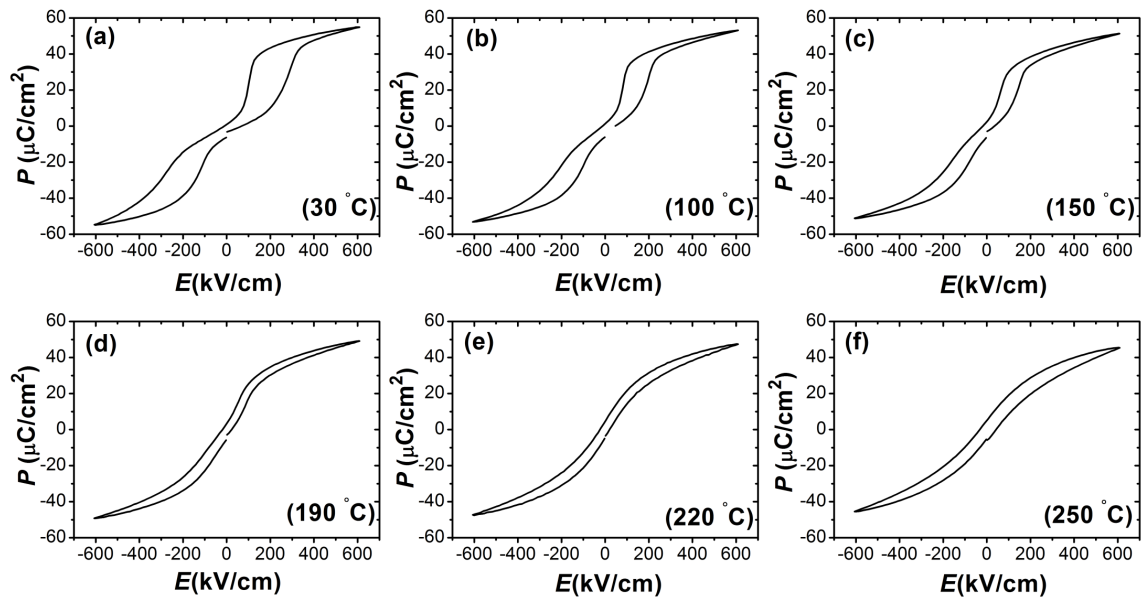


Figure 3.23: Typical $P(E)$ loops of the PLZT2/95/05 thin film at different temperatures on cooling.

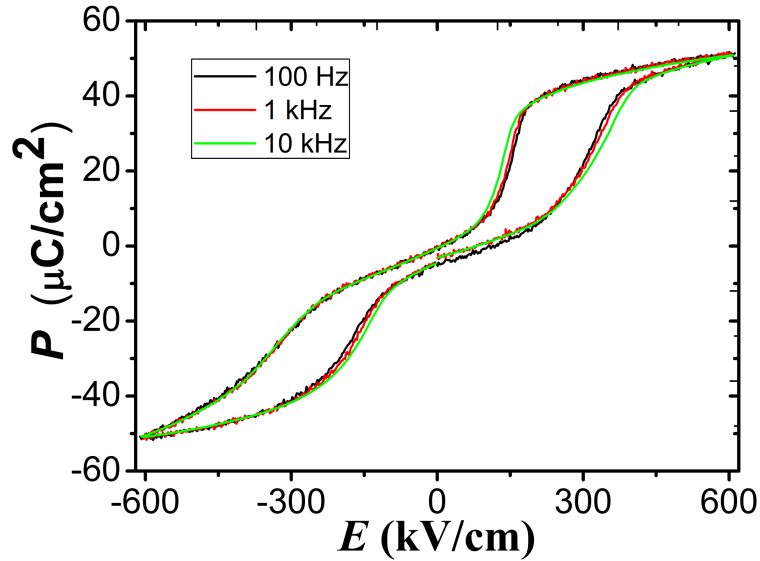


Figure 3.24: $P(E)$ loops of the PLZT2/95/05 thin film at room temperature measured at different frequencies.

is observed in the intermediate temperature range [~ 190 - 220 °C] [Fig. 3.23(e)]. No qualitative change corresponding to the ferroelectric to paraelectric transition is apparent in this case. Lossy paraelectric behavior is shown at 250 °C [Fig. 3.23(f)] which is well above this intermediate temperature range. The frequency for $P - E$ measurement is set as 10 kHz, which is the same as that reported in the 2006 Science paper (Ref. [15]). Note that we also have carried out the $P - E$ measurements under different frequencies and the corresponding results are shown in the Fig. 3.24. It can be clearly seen that the frequency has a negligible influence on the upper branches of $P(E)$ loops. Therefore, our determined polarization corresponds to the intrinsic properties of the system.

The dielectric data in Fig. 3.25(a) are maximum for a temperature of about 220 °C, which is in line with the ferroelectric Curie temperature T_C (225 °C) obtained in PLZT2/95/05 bulk material [330, 331], or about 222 °C in PLZT2/95/05 thick films [132]. No dielectric peak related to an intermediate transition from the antiferroelectric phase to the slim-loop ferroelectric phase reported in bulk material [330, 331] can be resolved in the whole temperature range studied; this is typical of antiferroelectric thin films [15, 132, 133].

Figure. 3.25(b) shows the temperature dependence of the polarization $P(T)$ under different applied electric field values E ranging from 0 to 615 kV/cm in PLZT2/95/05 thin films between 30 and 250 °C, which is determined from the upper branches of $P(E)$ loops ($E > 0$, $f=10$ kHz) taken at 10 K intervals during the cooling process. Upper branches of $P(E)$ loops, in which the configurations of antiferroelectric/ferroelectric domains are not significantly modified, are deliberately selected to ensure that the indirect method based on Maxwell relations is reliable [15, 46, 48, 304]. Typical ferroelectric behavior in terms of decreased polarization with temperature increasing ($\partial P/\partial T < 0$) can be observed in the temperature range studied only when $E \geq 415$

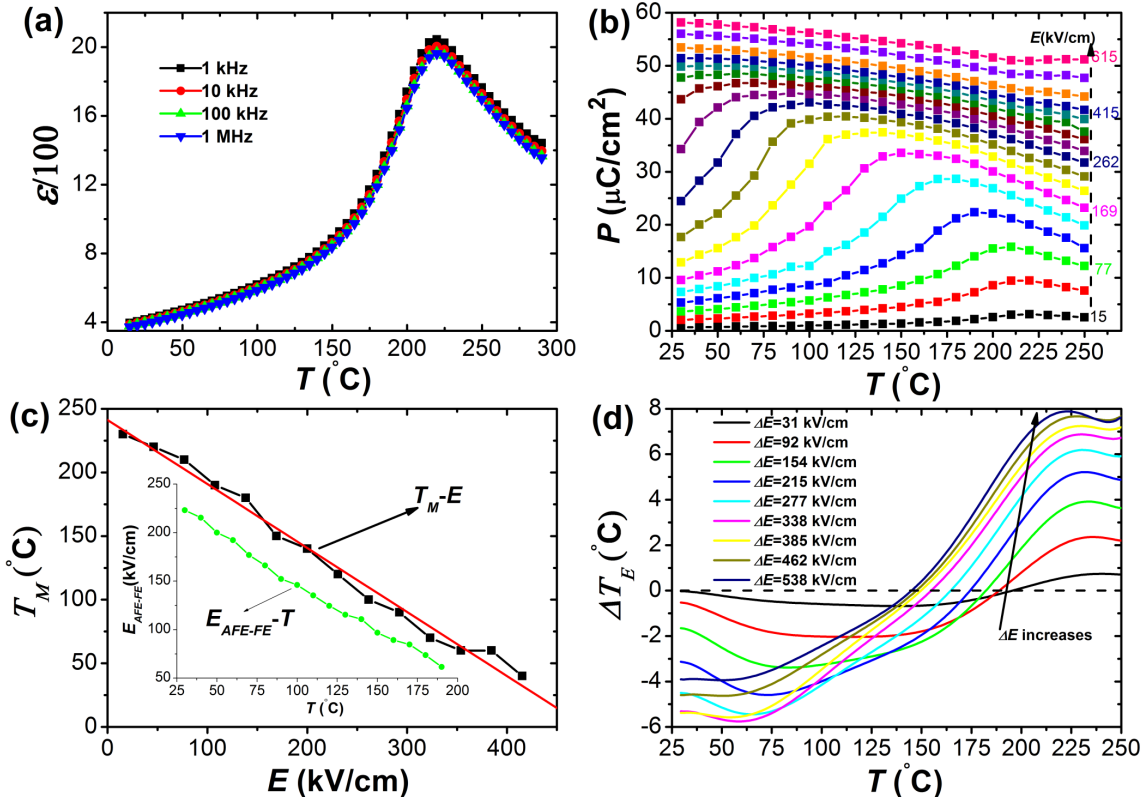


Figure 3.25: (a) Dielectric constant $\epsilon(T)$ in PLZT2/95/05 thin films on cooling. (b) Polarization $P(T)$ at selected external electric fields E during the cooling process. (c) Temperature of the polarization peak T_M as a function of electric field E . The solid red line represents a linear fit to the data. The inset depicts the temperature dependence of antiferroelectric-to-ferroelectric switching field $E_{\text{AFE-FE}}$. (d) Electrocaloric temperature change ΔT_E in response to application of different electric field changes $\Delta E = E_2 - E_1$ ($E_1 = 77$ kV/cm). The dashed line represents the zero in ΔT_E and the arrow depicts an increasing trend in ΔE .

kV/cm. Below this field of 415 kV/cm, the situation is more complex, with polarization non-monotonic with a peak at T_M . For $T < T_M$ polarization increases with temperature ($\partial P/\partial T > 0$), whereas above T_M it decreases ($\partial P/\partial T < 0$, as similar to the behavior of typical ferroelectric materials under high E). In this regard T_M determines the emergence of ferroelectric behavior, which is also supported by the strong temperature dependence of the phase switching field $E_{AFE \rightarrow FE}$, as shown in Fig. 3.25(c). $E_{AFE \rightarrow FE}$ decreases remarkably from 225 to 62 kV/cm as the temperature rises from 30 to 190 °C, which is typical for antiferroelectrics [130, 332]. Therefore Figure. 3.25(b) implies that the ferroelectric phase can be always stabilized more easily at relatively higher temperatures and higher electric fields $E (\gg E_{AFE \rightarrow FE})$. There is a significant shift of T_M toward lower temperatures with a large average rate $dT_M/dE \approx 0.5$ cm K/kV [see Fig. 3.25(c)], as shown in Fig. 3.25(b).

Based on the indirect method, the reversible electrocaloric change in temperature ΔT_E of a dielectric material in response to a change in external electric field $\Delta E = E_2 - E_1$ under adiabatic conditions can be determined by Eq. (1.28). Note that ΔT_E is usually maximized near the phase transition, where thermally driven changes in measured polarization P arising from changes in the magnitude are largest. One concern about Eq. (1.28) is the different relaxation times for heat capacity and polarization; these often differ and both are different from the rise time of the applied field in the experiments [5]. Hence the electrocaloric response depends upon three characteristic times. However, it is known that assuming a constant value of P despite the phase transition may still yield a reasonable estimate of electrocaloric effect [8]. We emphasize that the basic physical mechanism that permits the negative electrocaloric effect in relaxors and antiferroelectrics but not in ordinary ferroelectrics is not yet known. Entropy clearly plays a key role; and unlike the case with ferroelectrics, the entropy change $S(E)$ under an applied field in an antiferroelectric is not always negative (E does not increase the existing antiferroelectric order). Relaxors are more complex and not in thermal equilibrium, so $S(E)$ is generally unknown. The theory of Pirc *et al.* [137] is a good beginning, but we lack yet the experimental parameters required to fit that model. In addition, Eq. (1.28) is not strictly valid in the case of first-order phase transition [333]. However, our dielectric data together with the following results on negative electrocaloric effect may indicate a second-order-like phase transition likely due to interfacial strain or other microscopic factors [15]. Therefore, the structural evolution during the application of an electric field and the cooling/heating process are highly desired to confirm the nature of the transition, e.g., using diffraction techniques.

Following the pioneering work by Mischenko *et al.* (and using the values $\rho = 8.3$ g/cm³ and $C = 330$ J/K kg) [15], the electrocaloric temperature change ΔT_E obtained by numerical integration of Eq. (1.28) is shown in Fig. 3.25(d). Instead of deliberately applying a high electric field E_1 (much larger than $E_{AFE \rightarrow FE}$) to stabilize the ferroelectric regime, we rather consider the more complex case starting from antiferroelectric state ($E_1 = 0$). We deliberately set $E_1 = 77$ kV/cm, which is well below $E_{AFE \rightarrow FE}$ near room temperature [Fig. 3.25(c)], in order to avoid the isentropic contribution ($\Delta S_E = 0$) from the polarization rotations driven by changes in the directions of the local random antiferroelectric domains during the initial application of a low electric field [130, 332], which is similar to the treatment reported in the magnetocaloric effect [36]. As E_2 increases from 77 kV/cm, a negative ΔT_E peak is observed for different temperatures; it shifts significantly toward lower temperatures, accompanied by an increase in magnitude $|\Delta T_E|$.

Interestingly, a giant negative electrocaloric effect is clearly demonstrated with a maximum amplitude value of -5.76 K under a modest applied field of $\Delta E = E_2 - E_1 = 338$ kV/cm at 59°C . This corresponds to an upper bound $E_{2C} \approx 415$ kV/cm at which $\partial P/\partial T$ becomes negative [see Fig. 3.25(b)]. When E_2 increases further above E_{2C} , a significant reduction of $|\Delta T_E|$ is observed. This is due to the field-induced conventional electrocaloric effect ($\partial P/\partial T < 0$) which contributes above E_{2C} , compensating the negative electrocaloric effect.

As a result of the broad phase transition, a wide operational temperature window is also shown in Fig. 3.25(d). Moreover, our data highlight a crossover temperature above which the nature of electrocaloric effect transforms from negative to positive type. This finding is in qualitative agreement with the prediction based on the Kittel model [137]. Such a crossover was not observed in PZO ceramics, mainly due to the low electric breakdown field [137]. In addition, a conventional electrocaloric peak can be always observed near the zero-field Curie temperature of around 220°C [see Fig. 3.25(d)]; there is no need to apply a high electric field to ensure the conventional electrocaloric effect [15, 131, 132]. This is due to the fact that the relationship $\partial P/\partial T < 0$ is always satisfied near 220°C , which only allows conventional electrocaloric effect.

The main features discussed above can be seen more clearly in the $\Delta T_E - \Delta E$ curves as summarized in Fig. 3.26(a). It is found that conventional electrocaloric effect also has a larger electrocaloric magnitude $|\Delta T_E|$ and electrocaloric strength [51] $|\Delta T_E/\Delta E|$ than its negative counterpart under the same electric field change ΔE . However, in contrast to the high working temperatures (around 200°C) required in the conventional electrocaloric effect, the negative electrocaloric effect can be operated near room temperature. Compared with the negative electrocaloric effect reported in bulk [17, 134, 137, 168], our results show that ΔT_E is significantly enhanced because of the remarkably enhanced external electric field used in thin films [see Fig. 3.26(a) and Table. 3.4]. Nevertheless, the negative electrocaloric strength $|\Delta T_E/\Delta E|$ in PLZT2/95/05 films at 30°C remains smaller than that in PZO bulk [137] under the same electric field range, which is in line with previous studies [47, 200, 201]. Compared with previous result in thin films, our electrocaloric strength here is about 0.0162 K cm/kV at 30°C , which is over twice larger than that (about 0.0064 K cm/kV) obtained in BNT-0.1BT thin films at 50°C (Ref. [328]). This indicates a significant improvement in the electrocaloric properties reported in thin films.

Compared with other typical electrocaloric materials, it is shown here that the maximum electrocaloric magnitude $|\Delta T_{max}|$ in this work is moderate while the electrocaloric strength $|\Delta T_E/\Delta E|$ is comparable with that reported in conventional electrocaloric materials [Fig. 3.26(b) and Table. 3.4]. This underlines the need to pursue more effort into the negative electrocaloric effect [5]. It will be very interesting to combine both conventional and negative electrocaloric effects in one material or combine two or more electrocaloric materials together such as in nanocomposites [52, 214, 334] to further enhance the electrocaloric performances. In addition, exploring the elastocaloric effect [50] due to large strain change during the antiferroelectric-ferroelectric switching [130, 332] in antiferroelectric thin films can also be considered in the future. Although the hysteresis loss may be larger than that near $T_C(E = 0)$, the high electric-field-induced ferroelectric state reverts back to a low electric-field antiferroelectric state when the field E is turned off, which may contribute to reduction of potential hysteresis loss. Nevertheless, further discussions of any thermodynamic cycles of negative electrocaloric devices based

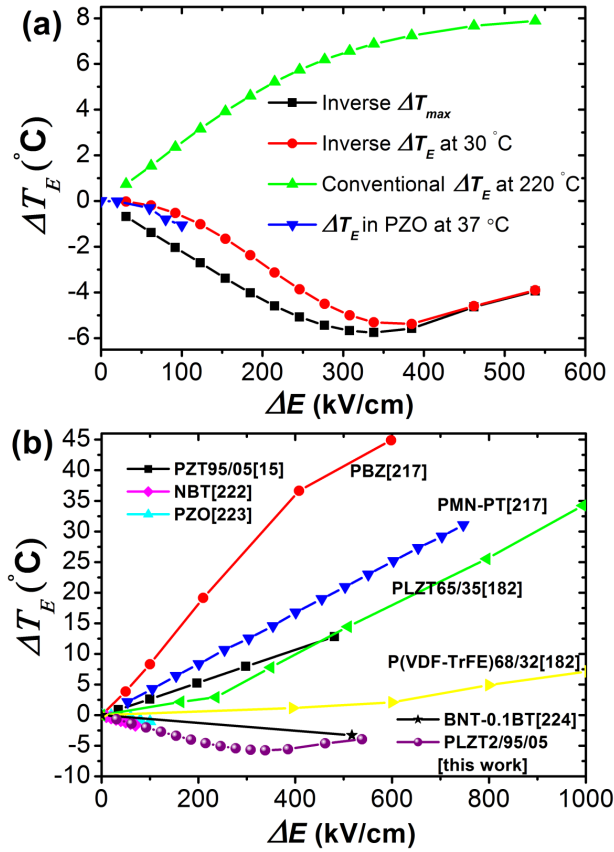


Figure 3.26: (a) The electrocaloric temperature change ΔT_E in PLZT2/95/05 thin films as a function of electric field change ΔE . ΔT_{max} is obtained from the negative electrocaloric peak shown in Fig. 3.25(d). The experimental result from PZO ceramics is also added for comparison. (b) Comparison of electrocaloric effect in several typical materials in the literature. All data were reported on thin films except for NBT [134] and PZO [137] ceramics.

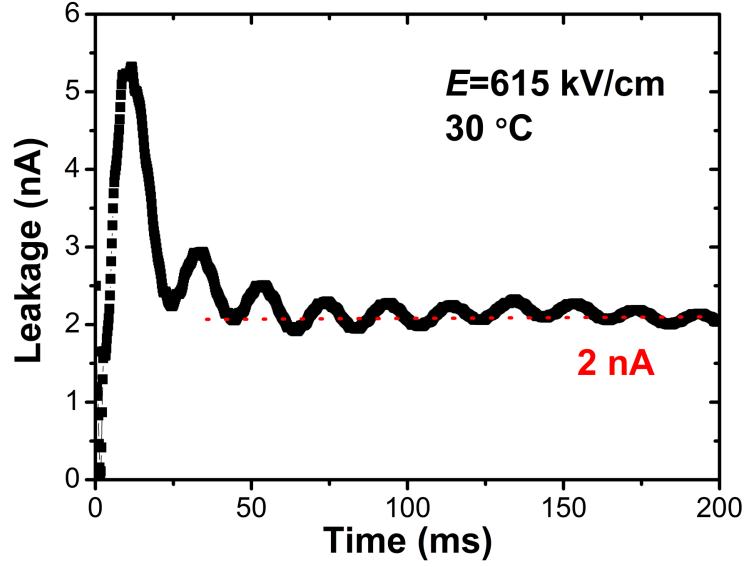


Figure 3.27: Leakage current in PLZT2/95/05 thin film at room temperature.

on antiferroelectric thin films are beyond the scope of this study, we suggest that direct measurements should first be made in the future to confirm our indirect measurements here. High electrocaloric resistance is expected especially under unipolar electrical cycling [329, 335], which is also desirable for the design of electrocaloric devices.

In addition, Joule heating can be negligible, as shown by the leakage current data in Fig. 3.27. In the very beginning (~ 10 ms), the sharp jump in the leakage current corresponds to the transient state during application of a constant DC bias voltage (60 V) across the sample. After that, the current decreases gradually to be steady as large as 2 nA, which is significantly smaller than that (50 nA) in Ref. [15]. Therefore, Joule heating can be negligible.

The primary findings here are mainly based on the Maxwell relationship approach and Eq. (1.28) without any consideration of microscopic details in our system (note that it independently agrees with the recent theoretical model proposed to describe the negative electrocaloric effect in antiferroelectric PZO [137]). Near the temperature at which $(\partial P/\partial T)_E = 0$ is satisfied, the conventional and negative electrocaloric effects will therefore cancel each other, which marks the transition from negative electrocaloric effect to the conventional electrocaloric effect as found in our study. More theoretical insights using *ab initio* calculations are highly desired to understand the origin of the negative electrocaloric effect in antiferroelectrics and relaxors (for instance, the subtle coupling between antiferroelectric, ferroelectric, and oxygen tilting instabilities discussed in detail in the first-principles-based work of Ref. [148] might be at the heart of this complex mechanism in our studied material). However, one can already realize that, for the case of ferroelectrics, applying a (conjugate) field E always reduces entropy by further aligning dipoles, therefore leading to a conventional (positive) electrocaloric effect according to Eq. (1.28) and once recalling that $(\partial S/\partial E)_T = (\partial P/\partial T)_E$. On the other hand and as schematized in Fig. 3.28 (or see Fig. 3.29), the application of a modest E in antiferroelectrics will generally increase the

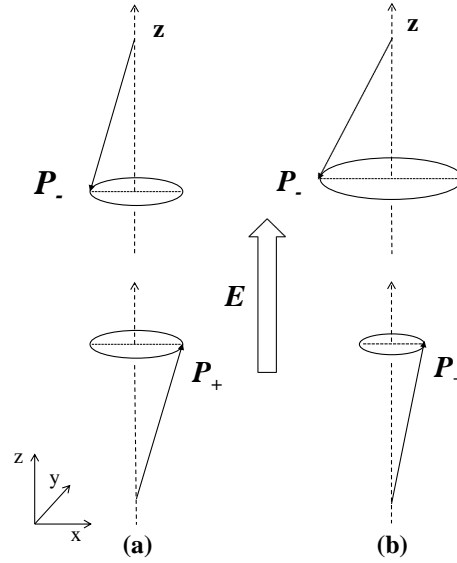


Figure 3.28: Schematic of a possible mechanism of negative electrocaloric effect in antiferroelectrics: (a) without any electric field and (b) under a modest electric field.

entropy by misaligning (canting) the dipoles, therefore generating the negative electrocaloric effect. To be more specific, at a finite T , the dipoles are collinear only on average. Due to temperature fluctuations, local polarization P local moves around, roughly in cones. The cones have the same radii, and their time average is such that $\overline{P(x)}$ and $\overline{P(y)}$ are zero [see Fig. 3.28(a)]. When an electric field is applied along the z axis, there is no significant change in the magnitude of polarization (the length of the arrows), but instead the fluctuation circle for the P_+ sublattice becomes narrower (increasing $\overline{P_+(z)}$) while that of the P_- sub-lattice becomes wider (thus decreasing $\overline{P_-(z)}$); see Fig. 3.28(b). This comes about primarily from the decrease (increase) in $P_{x,y}$, which also increases the entropy of the system since the total $\overline{P_x^2}$ increases. Algebraically, if two polarizations, i.e., P_+ and P_- increase and decrease by the same amount, \overline{P} remains unchanged but $\overline{P^2}$ increases. Considering the case of relaxors, recent first-principles calculations conducted in Ba(Zr _{x} Ti _{$1-x$})O₃ relaxors indicate that the dielectric response (denoted as χ^{CF} there) associated with the application of weak dc electric fields presents a peak around a specific temperature [170], T_m , while no macroscopic paraelectric-to-ferroelectric transition occurs in this material down to the lowest possible temperatures [as consistent with the fact that Ba(Zr _{x} Ti _{$1-x$})O₃ is a relaxor]. Such behavior therefore implies that the (induced) polarization decreases as the temperature decreases below T_m when applying these weak fields, which thus should result in the negative electrocaloric effect according to Eq. (1.28).

In summary, since most current studies focus on the electrocaloric effect in ferroelectric or relaxor materials for cooling applications, our study highlights the potential use of antiferroelectric thin films for room-temperature solid-state refrigerators. The giant negative electrocaloric effect in antiferroelectric thin films suggests novel combinations with conventional electrocaloric effect to enhance further the cooling efficiency.

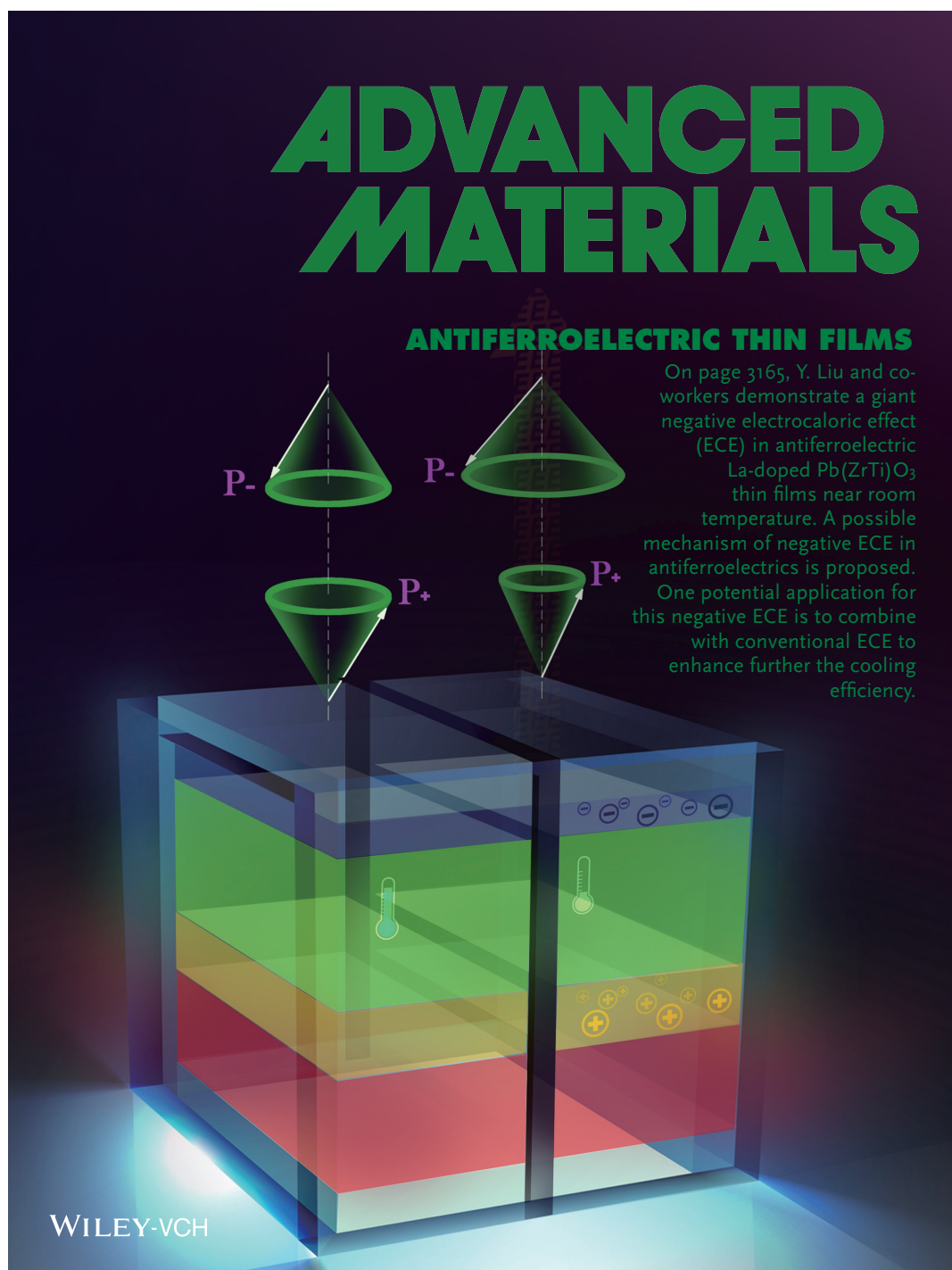


Figure 3.29: Frontispiece: Advanced Materials, Volume 27, Issue 20 May 27, 2015 Page 3164

3.3 ENHANCED ELECTROCALORIC EFFECT IN LEAD-FREE $\text{BaTi}_x\text{Sn}_{1-x}\text{O}_3$ CERAMICS NEAR ROOM TEMPERATURE

The idea of looking for multiphase materials to enhance the electrocaloric response was proposed by myself. The experimental results shown in this section were obtained by collaboration with Zhengdong Luo, Xiaojie Lou and other colleagues from Xi'an Jiaotong University.

To achieve high electrocaloric performances near room temperature, the use of phase transitions is revealed to be a powerful tool since the largest electrocaloric effect usually occurs near the phase transition. In addition, in order to tune the properties of electrocaloric materials, various approaches have been proposed, which include, but are not restricted to, tailoring the thickness of an electrocaloric film [15, 47, 201, 203], doping [336], changing the anisotropy/texture of the material [229], applying a stress field [50, 166] or a hydrostatic pressure [76], improving the material capability to enhance the electrical breakdown strength [150, 337, 338], and maximizing the number of coexisting phases near an invariant critical point (CP) [159] in the temperature-composition phase diagram. Moreover, considering the request of bulk materials for medium- or large-scale cooling facilities and household applications, it is crucial to improve the electrocaloric properties near room temperature in these materials [111, 150, 159, 160, 336, 337, 339]. In particular, concerning the physical upper bounds imposed on the electrocaloric effect of bulk polar solids, the intrinsic electrocaloric properties are expected to be significantly improved by operating the materials near the CP [158]. Similarly, a giant piezoelectricity was reported due to the nearly vanishing energy barrier for polarization rotation among the coexisting phases near quasi-CP [340, 341]. For ferroelectric materials with a critical point composition, high electrocaloric performances may also be obtained even under a modest electric field due to the small energy barrier. Therefore, by engineering the materials near the CP at room temperature as an effective means, we expect to obtain high room-temperature electrocaloric performance. Until now, most reported inorganic materials with outstanding electrocaloric performance contain toxic lead element while lead-free materials generally exhibit “inferior” electrocaloric responses [111, 342]. Nevertheless, because of the global restrictions of lead, there is an urgent need to develop lead-free electrocaloric materials. Among the lead-free electrocaloric bulk materials, prototypical barium titanate (BTO) in ceramic and single crystal forms is one of the most extensively studied compounds [48, 150, 160, 166, 208, 209, 337–339, 342]. However, for BTO-based materials, the observed maximum electrocaloric effect usually occurs far above room temperature [48, 166, 209, 342], and there are only a few reports focusing on tuning their working temperature towards room temperature [150, 337, 339]. In addition, the electrocaloric strength or responsivity defined as $\Delta T_E/\Delta E$, which is a crucial parameter for designing electrocaloric cooling devices, is relatively low in the aforementioned BTO-based ceramics compared to that in single crystals. The drawbacks of using single crystals for electrocaloric applications, however, are their complex growth method and even weaker endurance to large electric field in comparison with ceramics, not mentioning their higher price. Therefore, it is of interest to further search for lead-free alternatives in ceramic form with better electrocaloric performances near room temperature.

In this section, we present large electrocaloric responses near room temperature in lead-free solid solution ceramics $\text{BaTi}_{1-x}\text{Sn}_x\text{O}_3$ (BTSn). Remarkably, a recent work showed that dra-

matically improved dielectric and piezoelectric properties can be achieved near an unexpected quasi-quadruple point (QP) at which four phases, i.e., cubic (C), tetragonal (T), rhombohedral (R), and orthorhombic (O), coexist [341]. These improved properties at this critical point agree very well with the recent theoretical results [158]. Moreover, it was reported that ferroelectric BTSn thin films with Sn concentration of ~ 0.15 show excellent pyroelectric properties (750 nC/K cm^2) [343], which suggests that BTSn may be a promising electrocaloric material due to the intrinsic relationship between electrocaloric effect and pyroelectricity. Considering that great enhancement in both electromechanical and electrocaloric responses could be achieved at the critical point [125, 152, 158, 180, 340, 344], we expect that interesting electrocaloric effects in BTSn ceramics could be obtained in the vicinity of the QP composition. Therefore here, the electrocaloric properties in BTSn ceramics were thoroughly investigated. By using an indirect method, we found that the BTSn ceramics at the QP composition (i.e., $x=0.105$) indeed exhibit the largest electrocaloric response near its Curie temperature ($\sim 28 \text{ }^\circ\text{C}$) among all the compositions investigated, which is comparable with the best results reported previously on lead-free room-temperature electrocaloric materials. As a result, our findings not only expand the spectrum of room-temperature lead-free electrocaloric materials for future refrigeration applications but also may serve as a guide for revealing other electrocaloric material alternatives by looking for solid solutions having critical points.

In this study, three characteristic BTSn solid solutions were selected according to the phase diagram: [341] $x=x_{QP}=0.105$, which corresponds to the quasi-quadruple critical point, we localized precisely as the multiphase composition in this study compared to $x=0.11$ proposed in Ref. [341], $x=0.08 < x_{QP}$, exhibiting the C -to- T -to- O -to- R phase transitions sequence similar to that of pure BTO and $x=0.14 > x_{QP}$ corresponding to a sample having a bi-phase C -to- R phase transition. Therefore, $\text{BaTi}_{1-x}\text{Sn}_x\text{O}_3$ ceramics with $x=0.08, 0.105,$ and 0.14 were fabricated via the conventional solid-state reaction method using barium carbonate ($\text{BaCO}_3, 99.8\%$), titanium dioxide ($\text{TiO}_2, 99.8\%$) and stannic dioxide ($\text{SnO}_2, 99.9\%$) as starting products. The details of sample fabrication and sintering procedure can be found elsewhere [341]. The structural characteristics and degree of purity of all the samples were determined by XRD (Shimadzu 7000). The density of the sintered ceramics was obtained by Archimedes' method. The temperature dependence of dielectric permittivity was measured with a HIOKI 3532 LCR meter. The evolution of polarization-electric field (P - E) hysteresis loops with decreasing temperature was recorded by using a Radiant ferroelectric workstation. Thermal characteristics measurements of all the samples were conducted by using a differential scanning calorimeter (DSC, TA Instruments Q200).

Figure 3.30 shows the XRD patterns of the BTSn ceramics with $x=0.08, 0.105,$ and 0.14 recorded at room temperature, which clearly indicates the formation of a pure perovskite structure without any secondary phases.

The temperature dependence of dielectric permittivity recorded at 100 Hz and 1 V during the cooling process from $110 \text{ }^\circ\text{C}$ to $-20 \text{ }^\circ\text{C}$ for the three BTSn compositions is shown in Fig. 3.31. For better illustration, a rough phase diagram of BTSn adapted from Ref. [341] is shown in the inset of Fig. 3.31. Three permittivity anomalies indicated with arrows in Fig. 3.31 are the manifestations of three first order transitions, i.e., C - T , T - O , O - R , in BTSn with $x=0.08$. In contrast, BTSn with $x=0.14$ displays only a unique phase transition from the C phase to R phase at ~ 8

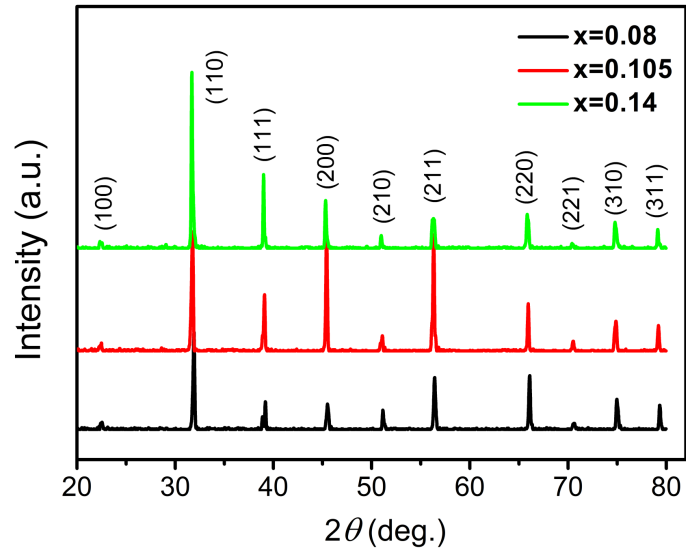


Figure 3.30: XRD patterns of the BTSn ceramics with $x=0.08$, 0.105 , and 0.14 , respectively.

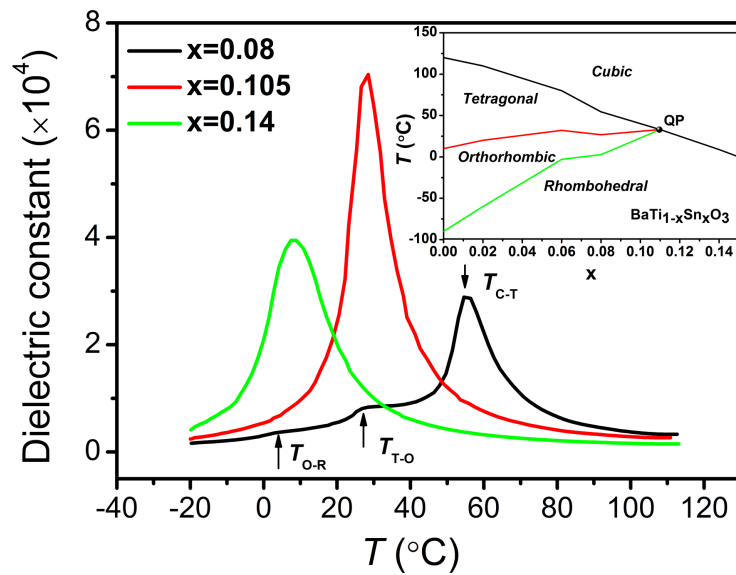


Figure 3.31: The temperature dependence of dielectric constant of all the BTSn ceramics during a cooling process, recorded by applying an electric stimulus of 1 V at 100 Hz on the sample. The arrows indicate the phase transition sequence of BTSn with $x=0.08$. The inset shows the phase diagram of BTSn ceramics with the Sn doping level ranging from 0% to 15%.

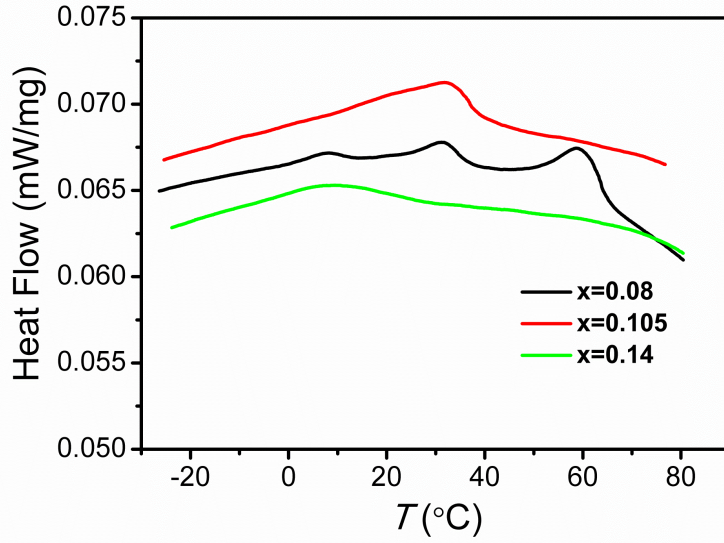


Figure 3.32: Heat flow of BTSn with different compositions ($x=0.08$, 0.105 , and 0.14) during the cooling process.

$^{\circ}\text{C}$. In case of the quasi-quadruple point composition $x_{QP}=0.105$, where C , T , O , and R phases coexist, there is also only one permittivity peak at $\sim 28^{\circ}\text{C}$. However, the permittivity value for x_{QP} is almost twice higher than that of the other two compositions, which reaches ~ 72000 and is in agreement with the improved dielectric and piezoelectric properties expected for this peculiar composition [341]. The quasi-quadruple point defined in our phase diagram presented in the inset of Fig. 3.31 is a point where four phases (C - T - O - R) nearly coexist together with the same Landau-Devonshire free energy [341]. The Gibbs phase rule is not necessarily violated for our case. Indeed, such a point in the temperature-composition phase diagram is difficult to exactly determine simply by our current dielectric and XRD measurements, and therefore needs further investigations. Nevertheless, multiphase points are unusual thermodynamic features [345], and the violation of the Gibbs phase rule has been reported in STO [346], $\text{Pb}(\text{Zr}_{1-x}\text{Ti}_x)\text{O}_3$ [347], and $\text{Eu}_x\text{Sr}_{1-x}\text{TiO}_3$ [348] phase diagrams. Obviously, further experimental studies on the origin of the quasi-quadruple point in BTSn solid solution ceramics are needed in the future.

Let us now consider the thermal properties of these three BTSn ceramics. The heat flow versus temperature data, obtained from the DSC measurements for the three samples during cooling process, are illustrated in Fig. 3.32. As expected and in good agreement with the dielectric results shown in Fig. 3.31 for BTSn ceramic with $x=0.08$, three exothermic peaks appear at around 9°C , 31°C , and 58°C , respectively, indicating the C - T - O - R phase transitions sequence, while only a single peak can be identified for both the QP composition, i.e., $x_{QP}=0.105$ and BTSn with $x=0.14$ from the DSC curves. Note that with increasing the Sn doping concentration, the exothermic peak is suppressed considerably and the phase transition becomes gradually diffused [339, 349, 350]. This temperature diffuseness may be also revealed on the dielectric data (see Fig. 3.31) when one compares the dielectric peaks of the ceramics with $x=0.105$ and

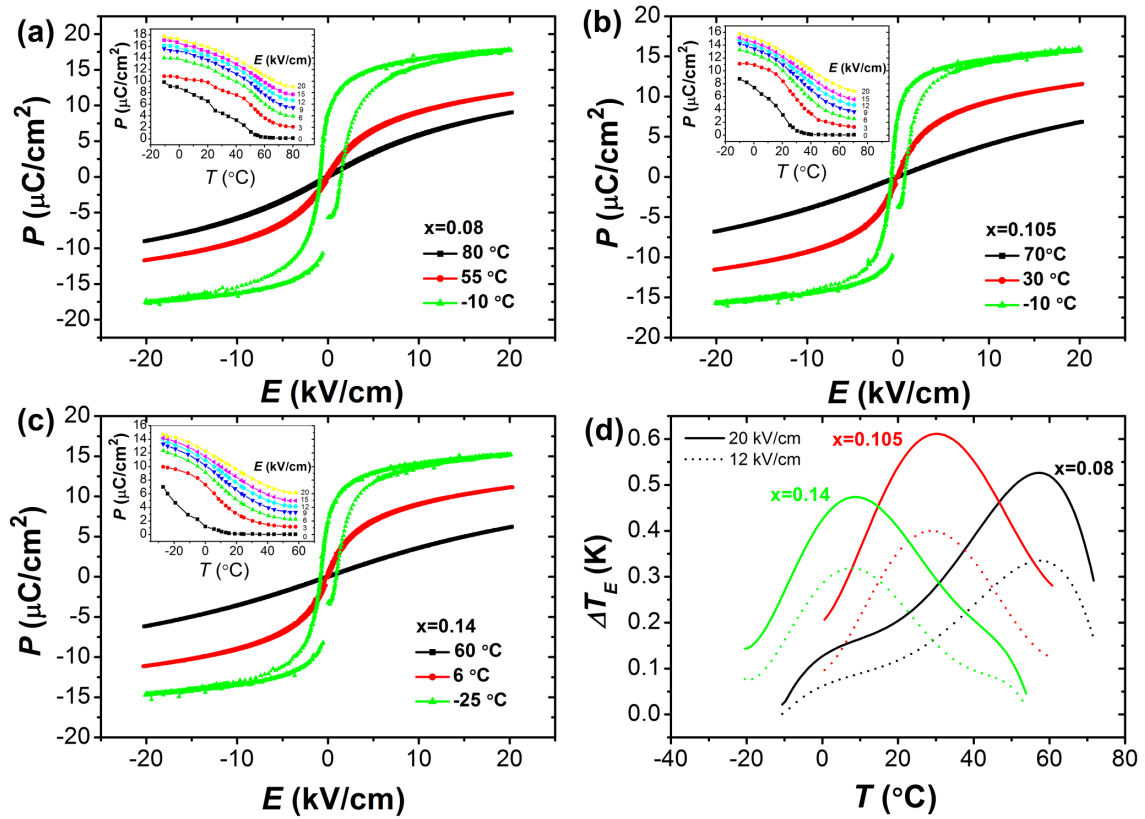


Figure 3.33: P - E hysteresis loops recorded at different temperatures under 20 kV/cm: (a) $x=0.08$, (b) $x=0.105$, and (c) $x=0.14$. The insets of (a)-(c) show the corresponding evolution of polarization versus temperature of the BTSn ceramics under various electric fields. (d) Electrocaloric effect in BTSn ceramics with different compositions.

$x=0.14$.

In order to estimate the electrocaloric properties of the BTSn ceramics, the temperature dependent P - E hysteresis loops shown exemplarily in Figs. 3.33(a)-3.33(c) were collected under different electric fields every 5 K during the cooling process. The hysteresis loops at given temperatures for each sample show typical characteristics attesting the phase transition from the paraelectric to the ferroelectric phase on cooling. The insets in Figs. 3.33(a)-3.33(c) display the evolution of the polarization (P) with temperature for different applied electric field values ranging from 0 to 20 kV/cm, in which P is extracted from the upper branch of the P - E hysteresis loops. At zero field, the polarization value starts to increase below the Curie temperature in agreement with the dielectric data (Fig. 3.31). By increasing the strength of the applied electric field, the polarization versus temperature curves become smoother and the observed inflection is shifted toward higher temperatures.

We use the well-known indirect method as presented before. The values of $(\frac{\partial P}{\partial T})_E$ for BTSn with different compositions were obtained from sixth-order polynomial fits to the cubic-spline interpolation of the polarization versus temperature data shown in the insets of Figs. 3.33(a)-3.33(c), respectively. The profile of ΔT_E versus temperature for BTSn with $x=0.08$, 0.105, and 0.14 under selected electric fields (i.e., 12 and 20 kV/cm) was deduced from Eq. (1.28) and is shown in Fig. 3.33(d). The heat capacity is measured as $C_p=2.25 \times 10^6$, 2.44×10^6 , and 2.22×10^6 J/K m³ for BTSn with $x=0.08$, 0.105, and 0.14, respectively.

One can see that the values of ΔT_E reach the maximum in the vicinity of the Curie temperature for each BTSn composition. As expected, the electrocaloric response is enhanced with increasing the magnitude of applied electric field and its maximum slightly shifts towards higher temperatures, which is in agreement with the variation of the polarization versus temperature curves with electric field. Most importantly and as anticipated, BTSn with the QP composition ($x_{QP}=0.105$) displays the highest ΔT_E value (0.61 K, under 20 kV/cm) near room temperature ($\sim 28^\circ\text{C}$). In contrast, the BTSn ceramics with $x=0.08$ and $x=0.14$ exhibit significantly reduced electrocaloric responses. The maximum ΔT_E for BTSn with $x=0.08$ is 0.52 K (at 58°C), corresponding to a reduction of $\sim 15\%$ compared with that of BTSn with $x=x_{QP}$ under the same electric field of 20 kV/cm, while the maximum ΔT_E for BTSn with $x=0.14$ is 0.47 K (at 9°C), corresponding to a reduction of $\sim 23\%$. Note that the phase transition temperature where the maximum electrocaloric response occurs can be tailored by varying the doping level as shown here. Thus, our work provides an effective means to tune the working temperature of electrocaloric materials.

The electrocaloric strength, expressed as $\Delta T_E/\Delta E$, is of great importance for practical cooling applications, especially for bulk materials where the available electric field is limited by the breakdown field [48, 111, 152]. Here, the values of $\Delta T_E/\Delta E$, deduced from the data in Fig. 3.33(d), are shown in Table. 3.5. As expected, the electrocaloric strength of BTSn with $x=x_{QP}$ (0.31 K mm/kV, under 20 kV/cm) is $\sim 19\%$ and $\sim 29\%$ larger than that of BTSn with $x=0.08$, and $x=0.14$, respectively (see Table. 3.5). The comparison of electrocaloric performance of the BTSn ceramics with that of other typical bulk electrocaloric materials is also shown in Table. 3.5. It is found that BTSn with $x=x_{QP}=0.105$ exhibits an appreciable electrocaloric temperature change ΔT_E , but especially an excellent electrocaloric strength $\Delta T_E/\Delta E$, compared to these reference materials. The electrocaloric properties of the BTSn ceramics fabricated in

Table 3.5: Comparison of electrocaloric properties of the BTSn ceramics prepared in this work with typical electrocaloric ceramics obtained in the literature.

| Material | T_0 [°C] ^{a)} | ΔE [kV/cm] | ΔT_E [K] | $\Delta T_E/\Delta E$ [K mm/kV] | Reference |
|--|-----------------------------|-----------------------|---------------------|------------------------------------|-----------|
| BTSn (x=0.08) | 58 | 20 | 0.52 | 0.26 | this work |
| BTSn (x=0.105) | 28 | 20 | 0.61 | 0.31 | this work |
| BTSn (x=0.14) | 9 | 20 | 0.47 | 0.24 | this work |
| $\text{Ba}_{0.7}\text{Sr}_{0.3}\text{Ti}_{0.997}\text{Mn}_{0.003}\text{O}_3$ ^{b)} | 30 | 120 | 2.53 | 0.21 | [337] |
| $0.94(\text{Na}_{0.5}\text{Bi}_{0.5})\text{TiO}_3$ -0.06BT ^{c)} | 100 | 50 | 1.5 | 0.3 | [136] |
| $\text{Ba}_{0.65}\text{Sr}_{0.35}\text{TiO}_3$ | 23 | 20 | 0.42 | 0.21 | [160] |
| Modified BZT | 39 | 145 | 4.5 | 0.31 | [150] |
| Doped BTO ceramic film | 80 | 300 | 0.5 | 0.017 | [208] |
| $\text{Ba}_{0.8}\text{Ca}_{0.2}\text{Zr}_{0.04}\text{Ti}_{0.96}\text{O}_3$ | 113 | 8 | 0.27 | 0.34 | [351] |
| PMN | 67 | 90 | 2.5 | 0.27 | [152] |
| PMN-30PT | 145 | 90 | 2.6 | 0.29 | [152] |

a) Phase transition temperature/temperature corresponding to largest electrocaloric effect.

b) Fabricated via the spark plasma sintering.

c) Fabricated via the sol-gel flame synthetic approach.

this work are comparable with the best values reported in lead-free bulk materials, i.e., the modified $\text{BaZr}_{0.15}\text{Ti}_{0.85}\text{O}_3$ (BZT) ceramics (4.5 K and 0.31 K mm/kV, under 145 kV/cm) [150] (see Table. 3.5) or also Ce doped (Sr,Ba) Nb_2O_6 single crystals (1.1 K and 0.32 K mm/kV, under 28 K mm/kV) [336]. Furthermore, the BTSn ceramics with x=0.105 in this work show a relatively high electrocaloric strength near room temperature (~ 28 °C), which therefore expand the spectrum of room-temperature lead-free electrocaloric material family (see Table. 3.5).

In order to understand the electrocaloric behaviors depicted in Fig. 3.33(d), let us recall the mechanisms proposed by Liu *et al.* [159] and Pirc *et al.* [158]. As analyzed by Pirc *et al.* [158], the theoretical maximum electrocaloric temperature change under saturation in an electrocaloric material only depends on the molar specific heat and the number of equilibrium orientations of polar states. Moreover, Liu *et al.* [159] very recently presented a detailed theoretical analysis emphasizing the entropy in a dipolar system, which can be written as

$$S = \sum_i \frac{k}{v_i} c_i \ln\left(\frac{c_i}{\Omega_i}\right), \quad (3.13)$$

where k is the Boltzmann constant, c_i denotes the volume fraction of the i th phase, v_i is the average volume associated with each dipolar unit in the i th phase, and Ω_i describes the number of polar-states in the i th phase. It can be seen from Eq. (3.13) that the entropy of an electrocaloric material depends on the total number of polar states in a specific phase, i.e., 12 polar states in an O phase, 8 polar states in a R phase, and 6 polar states in a T phase [159]. Considering BTSn with the QP composition (x=x_{QP}=0.105) in this work, the total number of

polar states due to the multiphase coexistence is considerably larger than BTSn with $x=0.08$ or 0.14 ; thus, one can expect a significantly enhanced entropy change at this critical x_{QP} composition. Moreover due to the flat energy landscape, the energy barrier for polarization rotation and phase transition is minimized near the critical point [125, 150, 180, 340], which implies that even a modest electric field can readily induce a remarkable polarization/entropy change and consequently a larger electrocaloric temperature change and a higher electrocaloric strength. Therefore, BTSn solid solution with its critical x_{QP} composition can be added to other systems having enhanced electrocaloric properties arising from phases coexistence, for instance, $0.7\text{BaZr}_{0.2}\text{Ti}_{0.8}\text{O}_3\text{-}0.3\text{Ba}_{0.7}\text{Ca}_{0.3}\text{TiO}_3$ (0.7BZT-0.3BCT) ceramics [160], $0.7\text{Pb}(\text{Mg}_{1/3}\text{Nb}_{2/3})\text{O}_3\text{-}0.3\text{PbTiO}_3$ (0.7PMN-0.3PT) single crystals, and $\text{PbZr}_{0.52}\text{Ti}_{0.48}\text{O}_3$ thin films [344], at their Morphotropic Phase Boundary (MPB) compositions or modified BZT ceramics [150] near the invariant critical point. As a matter of fact, our findings reinforce the idea of looking for materials having critical point composition and thus multiphase coexistence in order to obtain superior electrocaloric properties

In conclusion, lead-free BTSn ferroelectric ceramics in the vicinity of the QP composition were prepared by the conventional solid-state reaction method and their electrocaloric properties were systematically investigated in this work. The significantly enhanced electrocaloric effect (0.61 K) was obtained in BTSn with the QP composition $x=x_{QP}=0.105$ near room temperature ($\sim 28^\circ\text{C}$) under 20 kV/cm. Additionally, it is found that the electrocaloric strength for this peculiar x_{QP} composition is about 0.31 K mm/kV under a modest electric field of 20 kV/cm, which is comparable with the best results previously observed in lead-free ceramics [150]. The improved electrocaloric properties are attributed to the four-phase coexistence at the quasi-critical point composition and the associated flat energy landscape facilitating the rotation of the polarization. This work therefore reveals that the lead-free BTSn solid solution is a promising alternative for the development of eco-friendly room-temperature refrigeration in the future and provides a route towards better electrocaloric properties by highlighting the role of multiphase critical point compositions.

- CHAPTER 4 -

DIRECT IMAGING OF ELECTROCALORIC HEAT FLUX IN MULTILAYER CAPACITORS

Note that all the results presented in this chapter are achieved by strong cooperation and exchange with Emmanuel Defay who is working at Luxembourg Institute of Science and Technology (LIST). The experimental set-up related to the measurements using infra-red camera was managed by Emmanuel Defay.

4.1 BRIEF INTRODUCTION

According to Chapter 2, electrocaloric refrigerator prototypes based on multilayer capacitors (MLCs) (see the typical structure as shown in Fig. 4.1) were recently designed attesting the potential of MLCs for cooling applications [119, 121, 126, 233]. The promise of using MLCs is that heat flow can be conducted by the inner interdigitated electrodes [208, 231]. Previous works assumed a homogeneous distribution of temperature change in the electrocaloric active ceramic regions and the behavior of electrocaloric heat flux between the center of ceramic regions and the metallic terminals was unknown [231, 232]. Direct experiments are still lacking whereas understanding the heat flow behavior in specific caloric prototype devices is crucial to optimize refrigeration efficiency [117]. For instance, in active magnetic regeneration the control of heat flux direction has been shown to be very useful to enhance the operating frequency and thus the power density of the device [236]. Interestingly, infra-red (IR) imaging can nowadays enable a direct determination of caloric effects both temporally and spatially with good precision [62, 86, 212, 213, 217, 224–227]. Indeed, temperature inhomogeneity due to the inevitable variations in emissivity and photon collections in the terminals has already been evidenced in previous work [217]. Extrinsic variation of electrocaloric effect (~ 0.2 K) due to specific geometry in MLCs was observed between the terminals and ceramic regions in MLCs [217] (see MLC structure in Fig. 4.1). This underlines that spatially distributed electrocaloric effect should exist over MLCs (see Fig. 4.2) in contrast to theoretical assumption [231, 232], and its quantitative understanding is highly demanded for a better use of MLCs in future devices. However, due to the rough surface of the metallic terminals, it is difficult to extract any small spatial variations

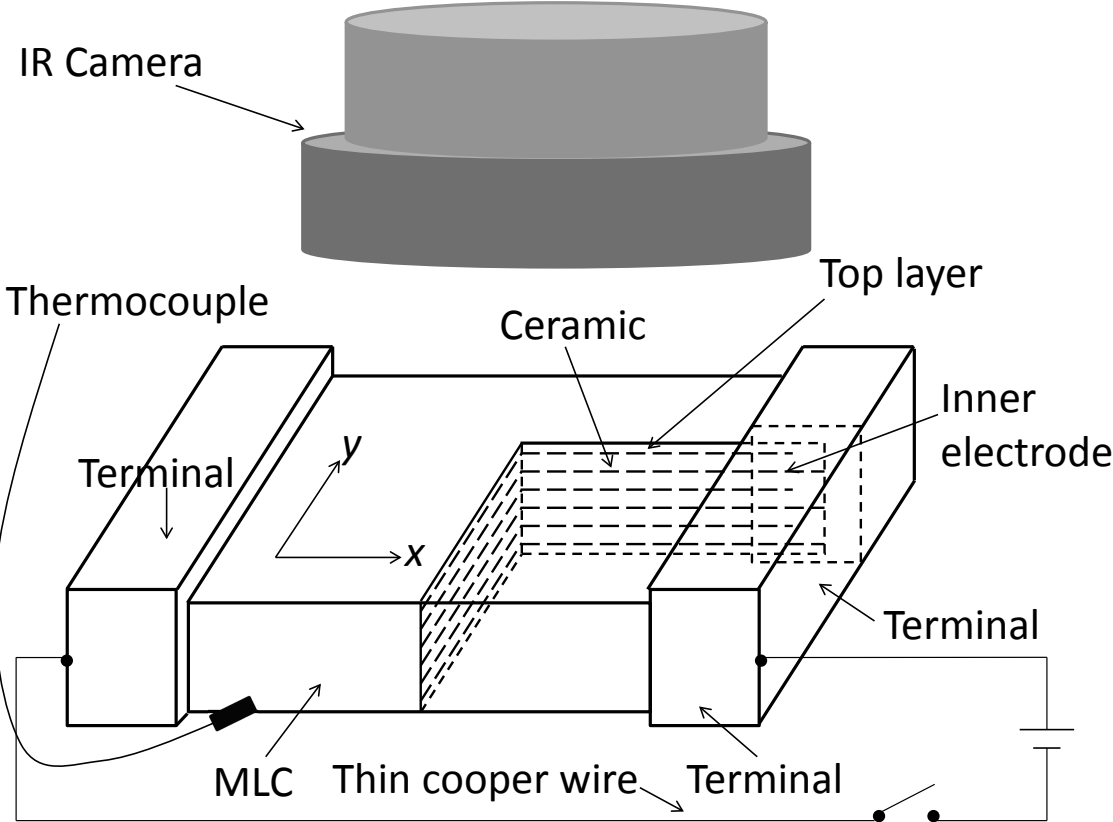


Figure 4.1: Schematic representation of measurement setup.

of electrocaloric effect. In this study, we focus on the flat electrocaloric active ceramic region in MLCs rather than the terminals, avoiding rough surface and poor emissivity with lots of reflections on terminals. Moreover, we develop the mode of IR measurements by setting the temperature of the MLC to a specific temperature determined by a thermocouple connected to the MLC (see Fig. 4.1). This can be achieved by manually adjusting the emissivity of different selected regions without necessarily compromising the resolution of the camera. Therefore, we may quantitatively image spatial distributions of electrocaloric effect and gain qualitative information about how the electrocaloric heat conducted between electrocaloric ceramic layers and terminals, which is obviously of great importance for the design of electrocaloric prototype based on MLCs [119, 121, 126, 233].

In this Chapter, we use an IR camera to directly image the variation of electrocaloric response in Ni-electroded commercial MLCs made of a proprietary BaTiO₃-based dielectric (Multicomp). We find the existence of a significant variation of electrocaloric effect up to 0.285 K between the central region and regions near the terminals. This variation corresponds to about 50% of the average value in the sample, which is larger than the previous ones on anisotropy/inhomogeneity of electrocaloric cooling [217, 229, 230]. Direct experimental evidence allows us to qualitatively analyze the dynamic electrocaloric flux which is found to be mainly transferring unidirectionally and inhomogeneously between the central ceramic regions and the terminals. We reveal the existence of measurable changes in electrocaloric effect from region to region including the central zones. Our findings offer a promising route to detect electrocaloric effect locally in a specific electrocaloric material/device by using IR imaging in order to design and optimize the prototype cooling device efficiency.

4.2 EXPERIMENTAL SET-UP

A sketch of the IR camera and MLC structure is presented in Fig. 4.1. The MLCs were purchased from Multicomp (MC1210F476Z6R3CT). The structure schematic is shown in Fig. 4.1. The MLCs consist of around 150 doped BaTiO₃ ceramic layers of thickness 11 μm separated by interdigitated Ni inner electrodes of thickness 2.0 μm . Tin is deposited onto the terminals in order to realize electrical connection by thin copper wires between the MLCs and generator (KEITHLEY). We choose three different fresh MLCs: namely MLC #1 with one side polished and the other side unpolished (we only measured the polished side); unpolished MLC #2 (we chose one unpolished side to measure) and MLC #3 with one side polished and the other side unpolished (we measured both sides). For the IR measurements, we used a FLIR X6580SC camera and an arrangement of lenses. The X6580sc camera features digital InSb detector corresponding to broadband spectral sensitivity of 1.5-5.1 μm . Thermal images captured by the camera have an effective spatial resolution of 6.5 μm with a thermal sensitivity of less than 25 mK (20 mK typical). The frame frequency of camera we used is 100 Hz, which is sensitive enough to capture thermal change in electrocaloric active MLCs (see Fig. 4.3). Moreover, the smallest frame frequency likely exhibits a remarkable variation of electrocaloric response, supporting that at higher frequencies (i.e. 100 Hz) the adiabatic regime can be always ensured. In order to determine the temperature of MLCs, a thermocouple was attached to MLCs using

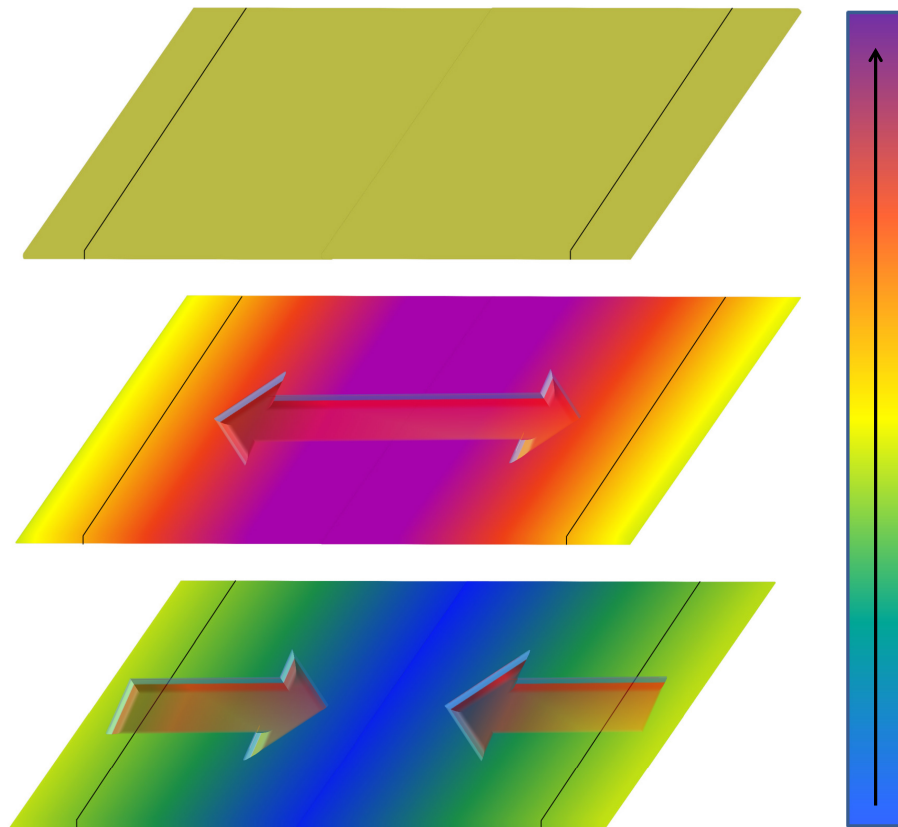


Figure 4.2: Schematic of heat transfer for the MLCs: top panel (no field), middle panel (field applied) and bottom panel (field removed). Solid black lines indicate the boundaries of the terminals. The black arrow indicates increasing temperature while the colored arrows refer to the direction of heat flow.

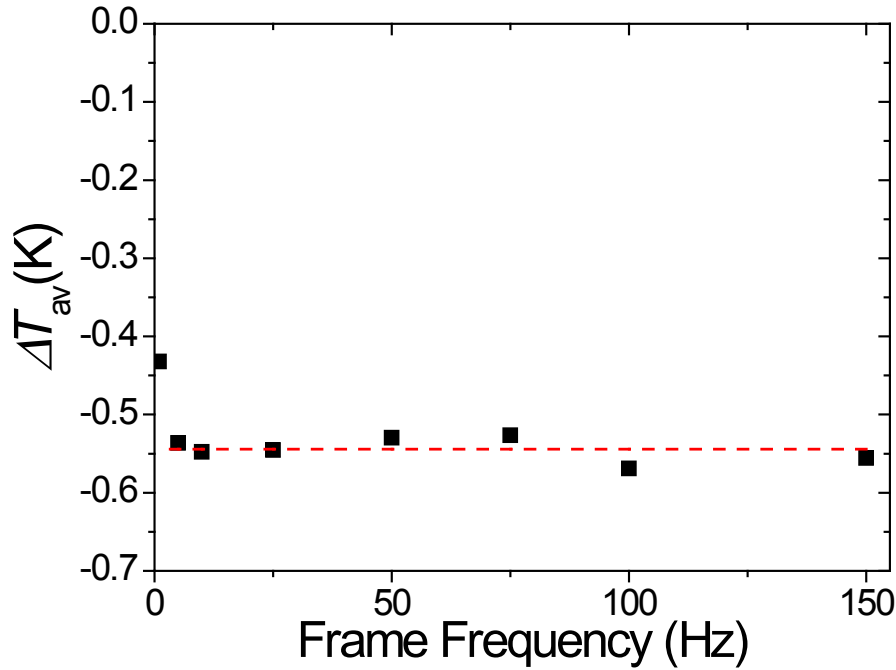


Figure 4.3: The average electrocaloric effect in MLC # 3 (polished side) obtained by averaging 9 different regions as a function of frame frequency of the IR camera when a voltage of 200 V is removed. Red dashed line is a guide for eye for the average value by 8 different data points ($\Delta T \equiv \Delta T_E$ in this Chapter).

scotch tape. 800-grit and 1200-grit abrasive papers are sequentially used to polish the top surface of MLCs. After that, ethanol is employed to wash and clean the MLCs. The IR camera with black-body calibration by the provider is deliberately set to focus on the side parallel to the electrode plates as shown in Fig. 4.1. In this regard, there is one top ceramic layer which is electrocaloric inactive.

4.3 SPATIALLY RESOLVED IMAGING OF ELECTROCALORIC EFFECT IN MULTILAYER CAPACITORS #1

Fig. 4.4(a) depicts the typical thermal images in MLC #1 (polished) with no applied voltage. In order to locally display electrocaloric properties in MLC #1, 15 different regions are selected with regions A_i ($i=1-9$) away from the terminals [Fig. 4.4(a)] and B_j ($j=1-6$) close to the terminals

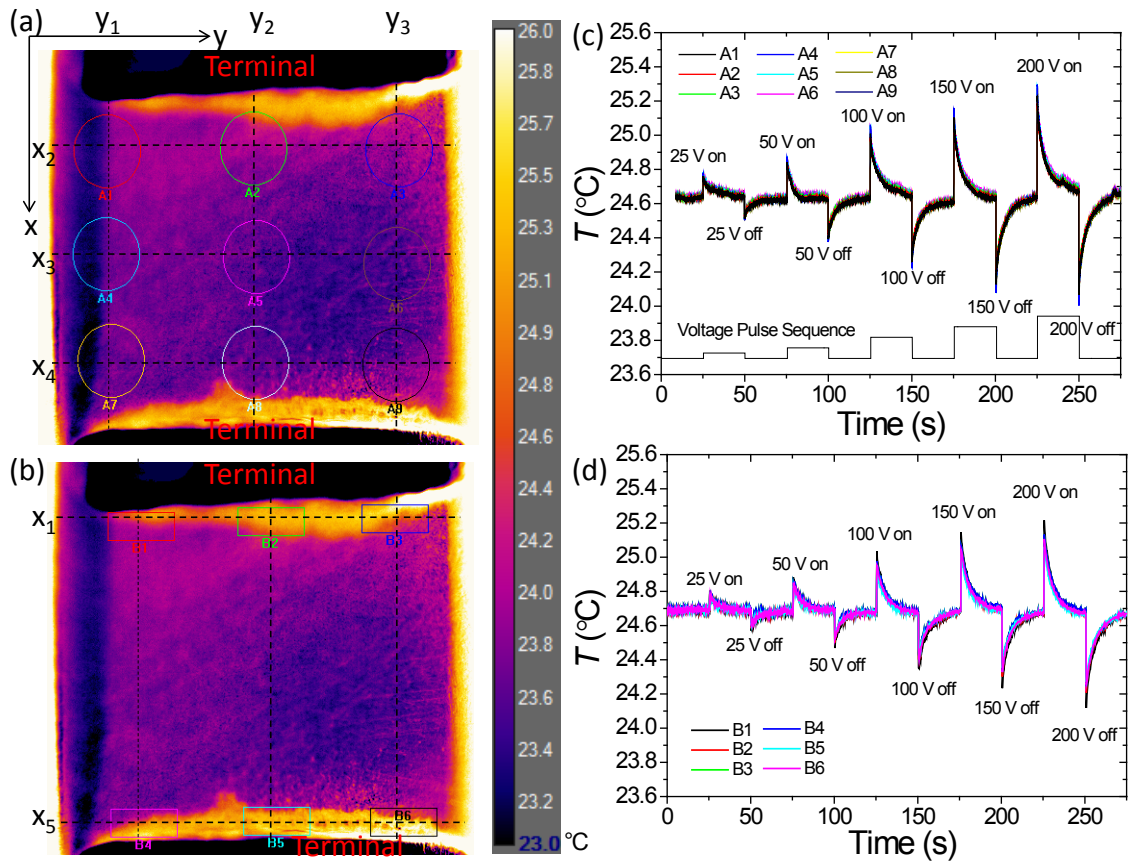


Figure 4.4: Thermal image of top surface of MLC #1 (polished) at room temperature with no applied voltage, where the $\sim 470 \mu\text{m}$ -diameter regions numbered A1-A9 and regions numbered B1-B6 ($\sim 520 \mu\text{m} \times \sim 200 \mu\text{m}$) are specifically marked, respectively in (a) and (b). Recorded temperatures (c) and (d) corresponding to different regions in (a) and (b) as a function of real time while the voltage pulse is applied/removed as schematically shown in the inset in (c).

Table 4.1: Emissivity ε_s of various regions for different multilayer capacitors under zero voltage.

| Region | ε_s (MLC #1 polished) | ε_s (MLC #2 unpolished) | ε_s (MLC #3 unpolished) | ε_s (MLC #3 polished) |
|---------|-----------------------------------|-------------------------------------|-------------------------------------|-----------------------------------|
| A1 | 0.752 | 0.830 | 0.882 | 0.850 |
| A2 | 0.863 | 0.948 | 0.910 | 0.898 |
| A3 | 0.839 | 0.860 | 0.827 | 0.880 |
| A4 | 0.839 | 0.775 | 0.857 | 0.790 |
| A5 | 0.750 | 0.920 | 0.830 | 0.780 |
| A6 | 0.743 | 0.995 | 0.780 | 0.787 |
| A7 | 0.720 | 0.730 | 0.880 | 0.790 |
| A8 | 0.740 | 0.878 | 0.968 | 0.790 |
| A9 | 0.770 | 0.952 | 0.900 | 0.830 |
| A10 | — | 0.875 | — | — |
| A11(B1) | 0.788 | 0.910 | — | — |
| A12(B2) | 0.947 | 1.000 | — | — |
| A13(B3) | 0.940 | 0.975 | — | — |
| A14(B4) | 0.880 | 0.950 | — | — |
| A15(B5) | 0.980 | 1.000 | — | — |
| A16(B6) | 1.000 | 0.833 | — | — |

[Fig. 4.4(b)]. The area is about 50-90 times as large as that selected on the terminals in the previous work [217], which is far above the spatial resolution ($\sim 6.5 \mu\text{m} \times 6.5 \mu\text{m}$) of the IR camera. In order to ensure that the sample as a whole should always show the same temperature without any applied voltages, we manually adjust the emissivity of different regions to overcome the spatial distribution of temperature profile (see Table. 4.1). As a result, the temperature of different regions can now reach a fixed temperature which is the same as that measured by the thermocouple (also see an example in MLC #2 as shown later). By doing this, the electrocaloric temperature change can be deduced by the variation of emissivity during application or removal of external fields. The change in emissivity then represents the real temperature change, which is managed by the software thanks to the provider's calibration. Typical electrocaloric responses in these 15 regions are shown in Figs. 4.4(c) and 4.4(d). It can be seen that the magnitude of $|\Delta T|$ near the terminals (Bj) in Fig. 4.4(d) is smaller than those which are not close to the terminals (Ai) in Fig. 4.4(c). This is in line with previous results reporting a decrease (~ 0.2 K) in the temperature change on moving from the MLCs as a whole to the terminals [217]. In addition, the contribution of Joule heating due to leakage current can be negligible since the IR signal returns to the baseline temperature after applying/removing the voltage [see Figs. 4.4(c) and 4.4(d)], in agreement with previous work.[12] As will be shown later, it does not even compromise under numerous cycles of high fields of about 180 kV/cm.

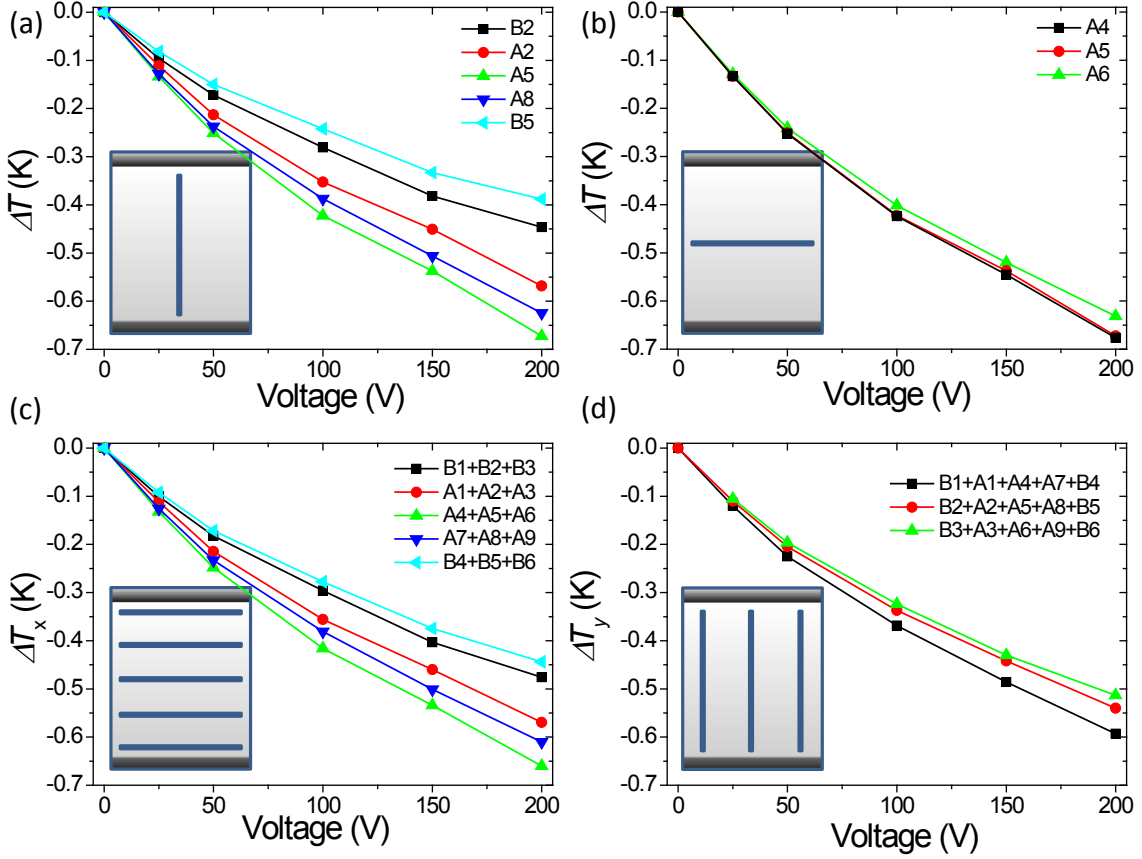


Figure 4.5: The electrocaloric temperature change ΔT induced by removing the external voltage as a function of voltage (0-200 V): (a) y_2 -regions (B2, A2, A5, A8, B5), and (b) x_3 -regions (A4, A5, A6). (c) Average temperature change ΔT_x for the regions (i.e., A1, A2 and A3) with the same x (i.e., x_1) values and (d) ΔT_y for the regions with similar y values. The inset cartoons depict the corresponding locations of selected regions.

Figs. 4.5(a) and 4.5(c) show typical results on spatial determination of electrocaloric peak values under different voltages. In this work, we present the electrocaloric effect in terms of the maximum temperature drop when applied voltage is removed in one cycle (data correspond to application of voltage can be found in Fig. 4.6). Interestingly, the non-uniformity of electrocaloric effect is directly evidenced with a significant distribution: the closer to the central regions (A4, A5 and A6), and the larger the magnitude of $|\Delta T|$ will be. The largest variation is 0.285 K between regions A4 (only very slightly larger than A5) and B5 when a voltage of 200 V is removed, which exceeds all previous results on electrocaloric anisotropy/gradient (~ 0.20 - 0.25 K) [217, 229, 230]. This temperature variation corresponds to 51% of the total electrocaloric effect (0.57 K) averaged over 15 different regions (A1-9 and B1-6).

The temperature change after activating the electrocaloric effect is not the same throughout one given MLC. Remarkably inhomogeneous distribution along x direction (perpendicular to the terminal) is observed to be more significant than that in y direction (along the terminal).

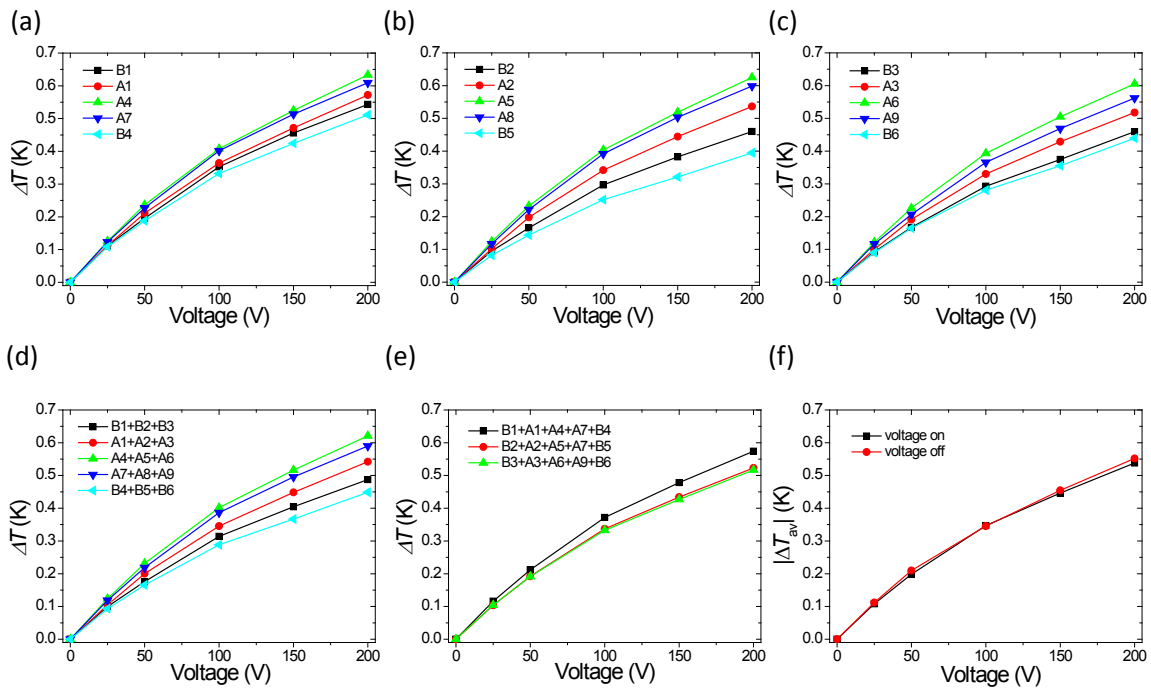


Figure 4.6: (a)-(c): Electrocaloric effect in regions A1-A9 and B1-B6 when the voltage is applied in one cycle; Average temperature change by several specific regions along y direction (d) and x direction (e). The total average temperature when the voltage is on and off (f).

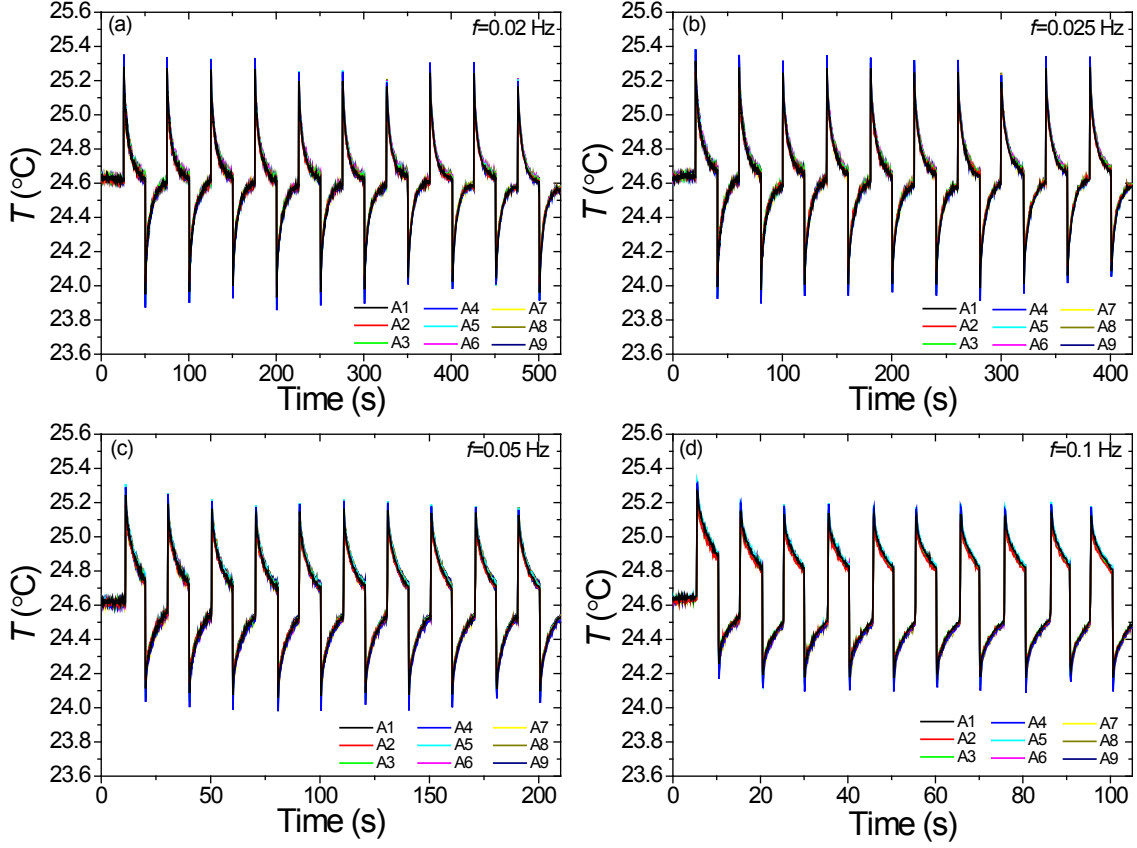


Figure 4.7: Recorded temperatures corresponding to different regions A1-A9 as a function of real time while the voltage pulse is applied/removed by ten successive voltage cycles between 0 and 200 V under various frequency in MLC #1: (a) $f=0.02$ Hz, (b) $f=0.025$ Hz, (c) $f=0.05$ Hz and (d) $f=0.1$ Hz.

For instance, it is shown in Fig. 4.5(c) that the largest difference between $|\Delta T_{x_3}|$ and $|\Delta T_{x_5}|$ is about 0.216 K, which is nearly three times as large as that (0.08 K) between $|\Delta T_{y_1}|$ and $|\Delta T_{y_3}|$ as shown in Fig. 4.5(d). The existence of $|\Delta T|$ gradient provides direct evidence of heat transfer between the central region of MLCs which is insulated and the region with the terminals which is not insulated (see sketch in Fig. 4.2). Therefore, our results explicitly indicate that the electrocaloric heat (negative here) is mainly drawn from the terminals towards the ceramic regions when the voltage is removed (Fig. 4.2, bottom panel). In the case of application of voltage, the heat (positive) transfer is inverted (see Fig. 4.2).

Besides, we carried out measurements under cyclic variation of applied voltage and also under different voltage frequency f as shown in Fig. 4.7. An illustrative example of recorded electrocaloric effect upon 10 successive voltage cycles between 0 and 200 V is summarized in Fig. 4.8. Reproducibility is confirmed in every region notably for high frequency pulses (see Figs. 4.9 and 4.10). This is due to the fact that the impact arising from the thermal surroundings can be minimized by high frequency pulses. For instance, the fluctuation in ΔT defined

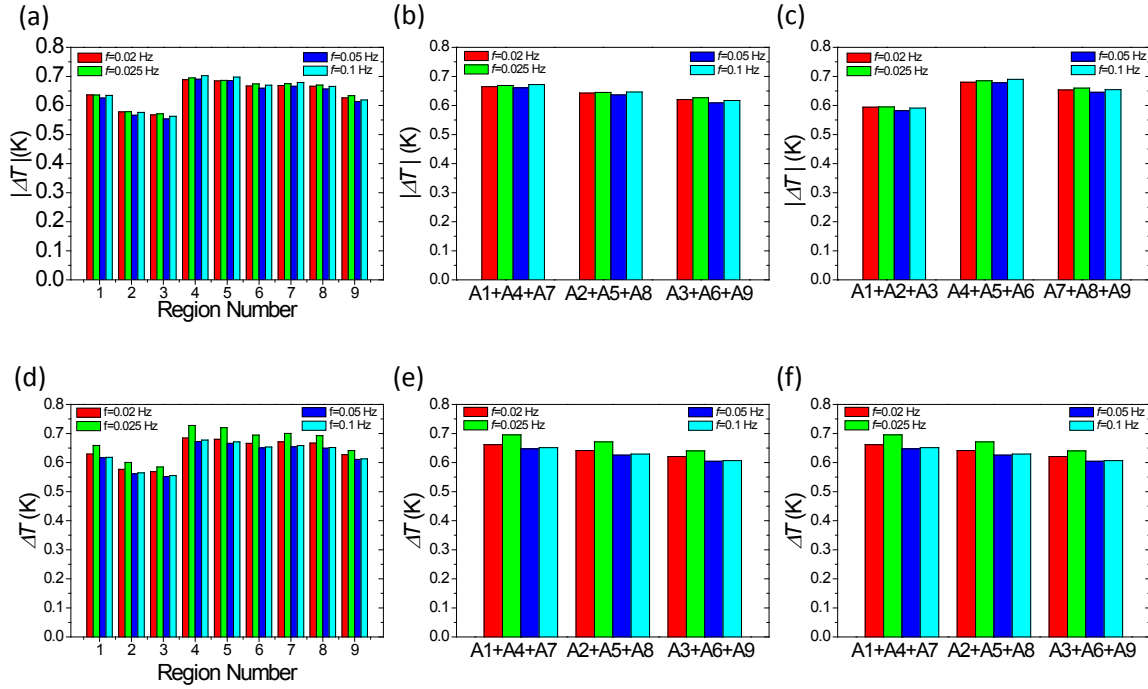


Figure 4.8: The local electrocaloric properties averaged by ten successive voltage cycles between 0 and 200 V under various frequency in MLC #1: (a) A1-A9; (b) y_{1-3} - regions [(A1, A4, A7), (A2, A5, A8) and (A3, A6, A9)] and (c) x_{2-4} -regions [(A1, A2, A3), (A4, A5, A6) and (A7, A8, A9)], when a voltage of 200 V is removed in one cycle. (d)-(f) correspond to the counterpart results when a voltage of 200 V is applied. It can be seen that systematic smaller cycle and frequency dependence is observed in (a)-(c) compared to that in (d)-(f). Note that using the data in (a)-(c) to present does not change the main results. Moreover, it may be more reasonable to employ the temperature drop to describe electrocaloric effect as it is directly related to cooling.

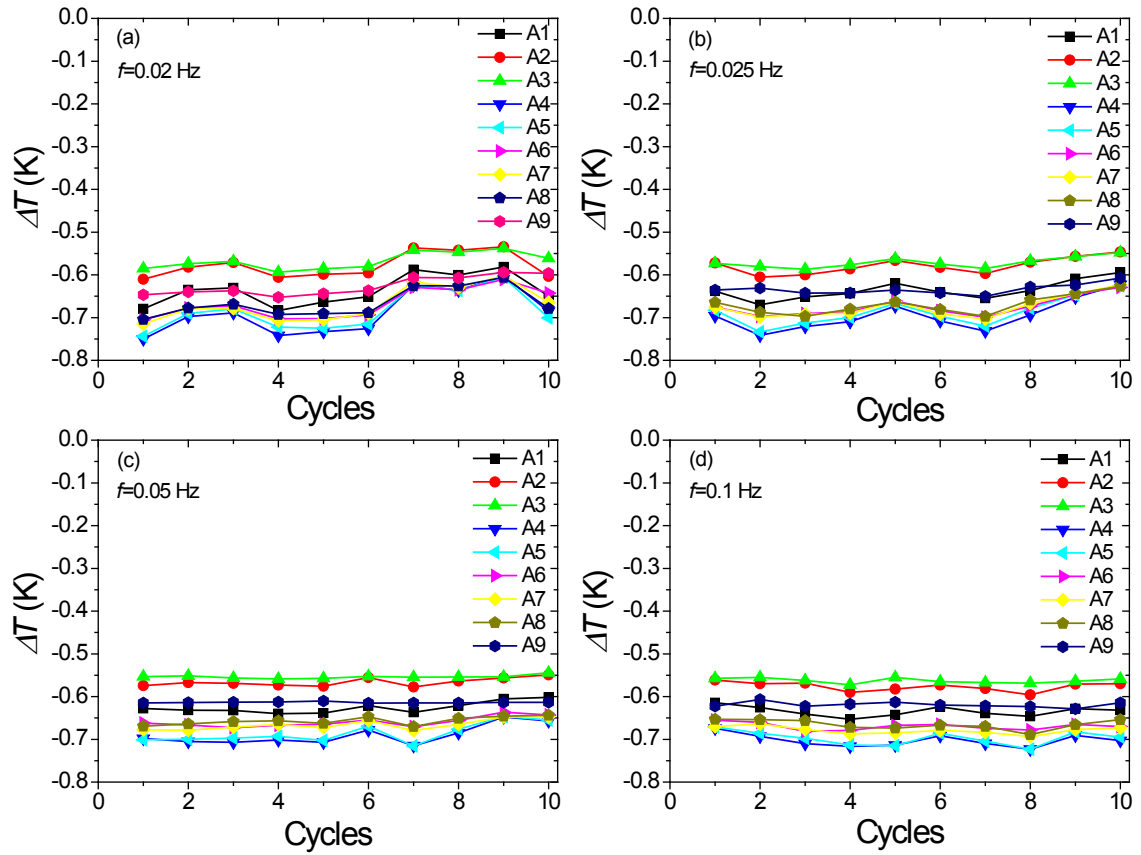


Figure 4.9: Electrocaloric effect in regions A1-A9 as a function of cycle number under different frequencies. Statistic results on the electrocaloric response during 10 successive voltage cycles (a)-(d) are shown in Table. 4.2.

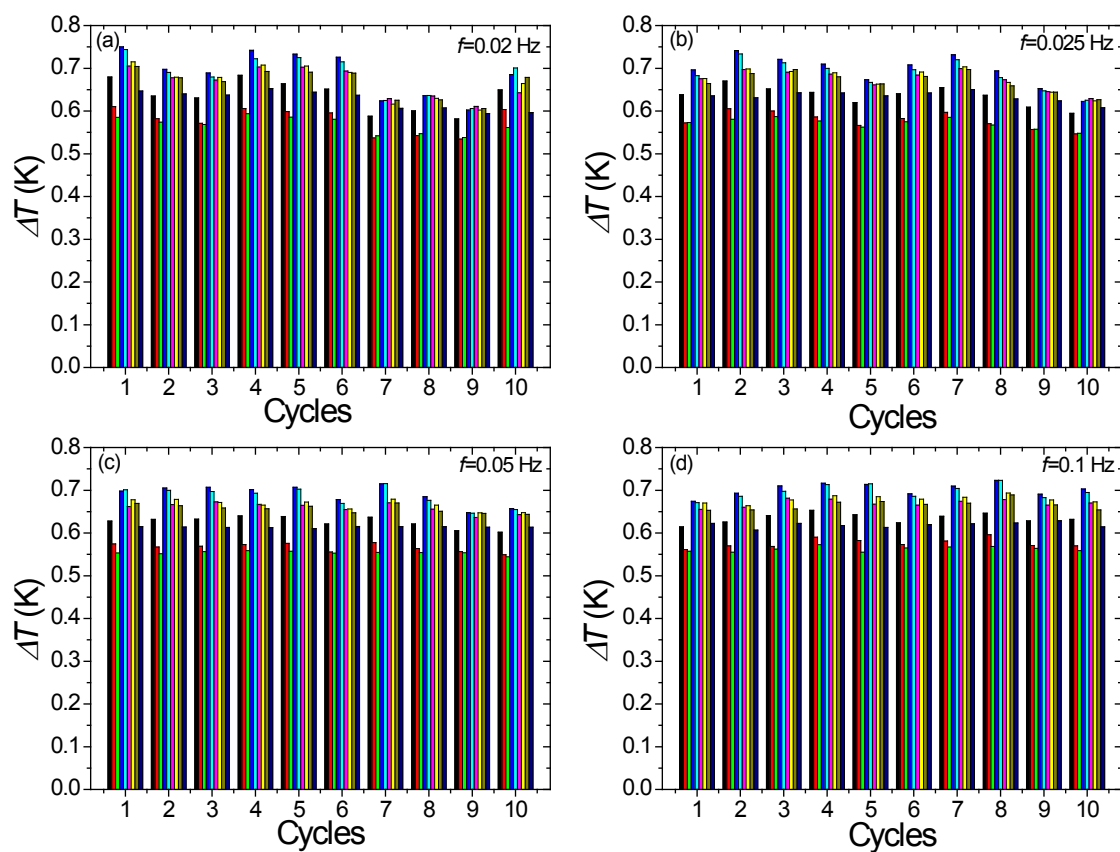


Figure 4.10: Distribution of electrocaloric effect in regions A1-A9 as a function of cycle number under different frequencies.

Table 4.2: Statistic results on the electrocaloric effect (ECE) during 10 successive voltage cycles in MLC #1.

| Region | ECE | $f=0.02$ Hz | $f=0.025$ Hz | $f=0.05$ Hz | $f=0.1$ Hz |
|--------|-------------------|-------------|--------------|-------------|------------|
| A1 | $\Delta\bar{T}$ | -0.636 | -0.636 | -0.626 | -0.635 |
| A1 | $+\delta T_{max}$ | 0.055 | 0.041 | 0.024 | 0.020 |
| A1 | $-\delta T_{max}$ | -0.047 | -0.034 | -0.014 | -0.018 |
| A2 | $\Delta\bar{T}$ | -0.578 | -0.578 | -0.566 | -0.576 |
| A2 | $+\delta T_{max}$ | 0.044 | 0.032 | 0.017 | 0.015 |
| A2 | $-\delta T_{max}$ | -0.028 | -0.027 | -0.012 | -0.019 |
| A3 | $\Delta\bar{T}$ | -0.568 | -0.571 | -0.554 | -0.563 |
| A3 | $+\delta T_{max}$ | 0.030 | 0.023 | 0.010 | 0.008 |
| A3 | $-\delta T_{max}$ | -0.026 | -0.016 | -0.005 | -0.010 |
| A4 | $\Delta\bar{T}$ | -0.688 | -0.695 | -0.690 | -0.703 |
| A4 | $+\delta T_{max}$ | 0.086 | 0.073 | 0.043 | 0.029 |
| A4 | $-\delta T_{max}$ | -0.062 | -0.046 | -0.025 | -0.021 |
| A5 | $\Delta\bar{T}$ | -0.684 | -0.686 | -0.686 | -0.697 |
| A5 | $+\delta T_{max}$ | 0.079 | 0.061 | 0.039 | 0.026 |
| A5 | $-\delta T_{max}$ | -0.060 | -0.047 | -0.030 | -0.026 |
| A6 | $\Delta\bar{T}$ | -0.667 | -0.674 | -0.659 | -0.670 |
| A6 | $+\delta T_{max}$ | 0.057 | 0.045 | 0.023 | 0.014 |
| A6 | $-\delta T_{max}$ | -0.038 | -0.025 | -0.014 | -0.012 |
| A7 | $\Delta\bar{T}$ | -0.669 | -0.675 | -0.666 | -0.679 |
| A7 | $+\delta T_{max}$ | 0.067 | 0.051 | 0.019 | 0.015 |
| A7 | $-\delta T_{max}$ | -0.046 | -0.028 | -0.013 | -0.015 |
| A8 | $\Delta\bar{T}$ | -0.666 | -0.670 | -0.657 | -0.665 |
| A8 | $+\delta T_{max}$ | 0.060 | 0.043 | 0.013 | 0.012 |
| A8 | $-\delta T_{max}$ | -0.038 | -0.027 | -0.013 | -0.023 |
| A9 | $\Delta\bar{T}$ | -0.626 | -0.634 | -0.614 | -0.619 |
| A9 | $+\delta T_{max}$ | 0.032 | 0.026 | 0.003 | 0.012 |
| A9 | $-\delta T_{max}$ | -0.026 | -0.016 | -0.002 | -0.010 |

as δT_{max} is found to decrease (the magnitude) from ± 0.030 K at $f=0.02$ Hz to ± 0.010 K at $f=0.1$ Hz for the region A3 with the average $\Delta\bar{T}$ slightly increasing from -0.568 K to -0.563 K (see Table. 4.2) and this change (5 mK) is far below the camera resolution of 25 mK. Moreover, almost all δT_{max} at $f=0.1$ Hz are smaller than the resolution of IR camera, and the spatial distribution of electrocaloric effect aforementioned at $f=0.02$ Hz can be well reproduced in the case of $f=0.1$ Hz. This strongly supports the reliability of our data, and the results shown in Figs. 4.4-4.6 can therefore represent the electrocaloric properties of MLC #1. In addition, previous work carried out direct measurement on MLCs using a thermocouple and reported three distinct types of electrocaloric response depending on frequency [234]. At a high frequency ($\gg 1$ Hz), it was shown that MLCs become hotter due to limited thermal conductivity of MLCs, which cannot afford such high frequency of heat transfer. Typical electrocaloric response like here can only be observed under relatively low frequency (i.e. 0.017 Hz) [234]. However, the frequency dependence of electrocaloric effect in the intermediate range (i.e. from 0.017 Hz to 1 Hz) was not reported in this previous study. This frequency range is actually located within the operational window as suggested in Ref. [234] and thus its frequency dependence is of importance for design of electrocaloric devices. Also recalling the controversial frequency dependence of electrocaloric effect in P(VDF-TrFE-CFE) terpolymer by IR imaging [212, 213], the temperature change in MLCs is found to be independent of voltage frequency in the range of 0.02-0.1Hz (see Figs. 4.7-4.10). Moreover, our findings indicate that IR camera is a powerful tool to spatially map the dynamic performances of electrocaloric prototypes such as field waveform [234], pulse duration [234, 352], frequency [212, 213, 227, 233, 234, 352] and electrocaloric fatigue under cyclic operating. These unexplored data can provide extremely valuable information for design of electrocaloric prototypes in the further studies.

4.4 SPATIALLY RESOLVED IMAGING OF ELECTROCALORIC EFFECT IN MULTILAYER CAPACITORS #2

Fig. 4.11 shows the zero-voltage thermal image of MLCs #2 which is free from any treatment of polishing. As mentioned above, the temperature profile along the MLCs is not homogenous with a significant spatial distribution, which can be seen more clearly in Fig. 4.12(a). This false outcome is due to the foregoing problem of emissivity of the rough surface of MLCs. In this regard, the measured temperature change may not necessarily represent the intrinsic electrocaloric properties especially for the case that electrocaloric response is relative weak like MLCs here. In order to deduce the real electrocaloric temperature change, we firstly adjusted the emissivity of selected regions to ensure that the temperature of different regions is the same as the ambient temperature before the electrocaloric effect is triggered (see Table. 4.2). After that, we can eventually measure the electrocaloric temperature change as shown in Figs. 4.12(b)-(d) and deduce the spatial electrocaloric response as a function of voltage as shown in Fig. 4.13. Similar to the case of MLC #1, we can also move the measured regions towards the terminals (Fig. 4.14), and the summary on the electrocaloric response which are shown in Figs. 4.14-4.16. The key feature here is that similar variation (0.20 K) in MLC #2 (unpolished) is found with a change of 34% of the total electrocaloric effect (0.58 K) as shown in Fig. 4.15.

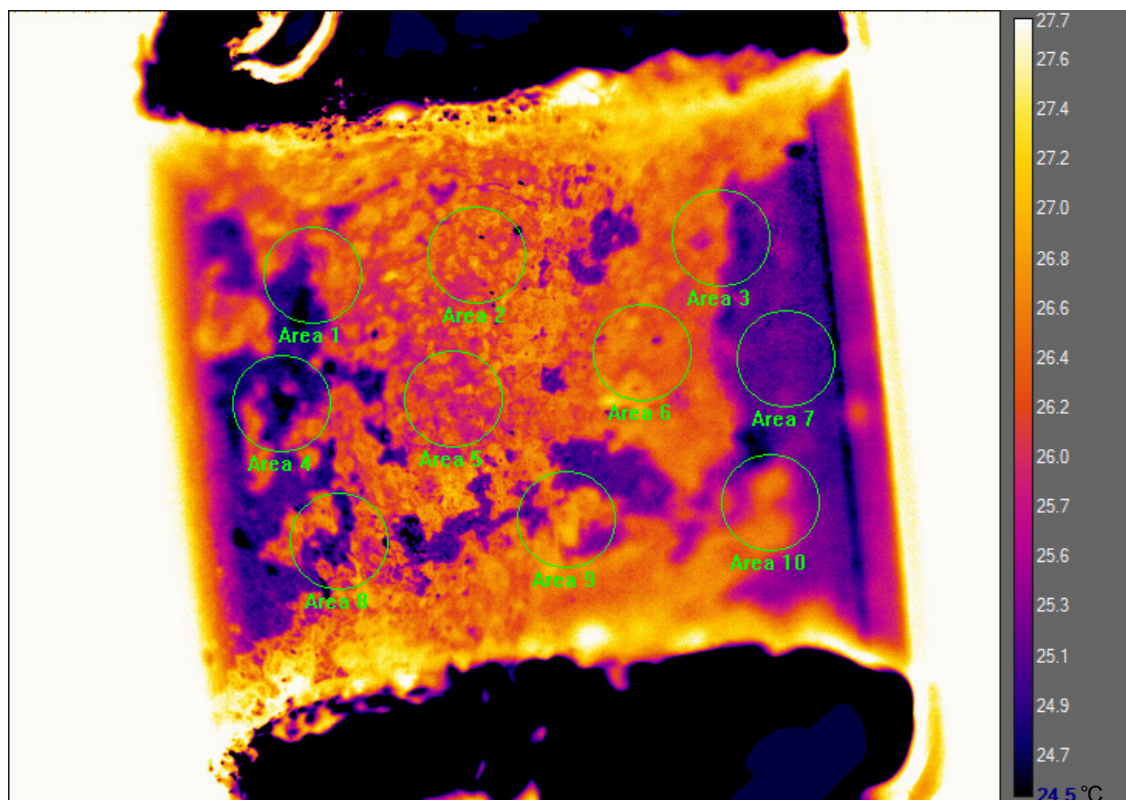


Figure 4.11: Thermal image of top surface of MLC #2 (unpolished) under no voltage at room temperature, and regions A1-A10 are specifically indicated.

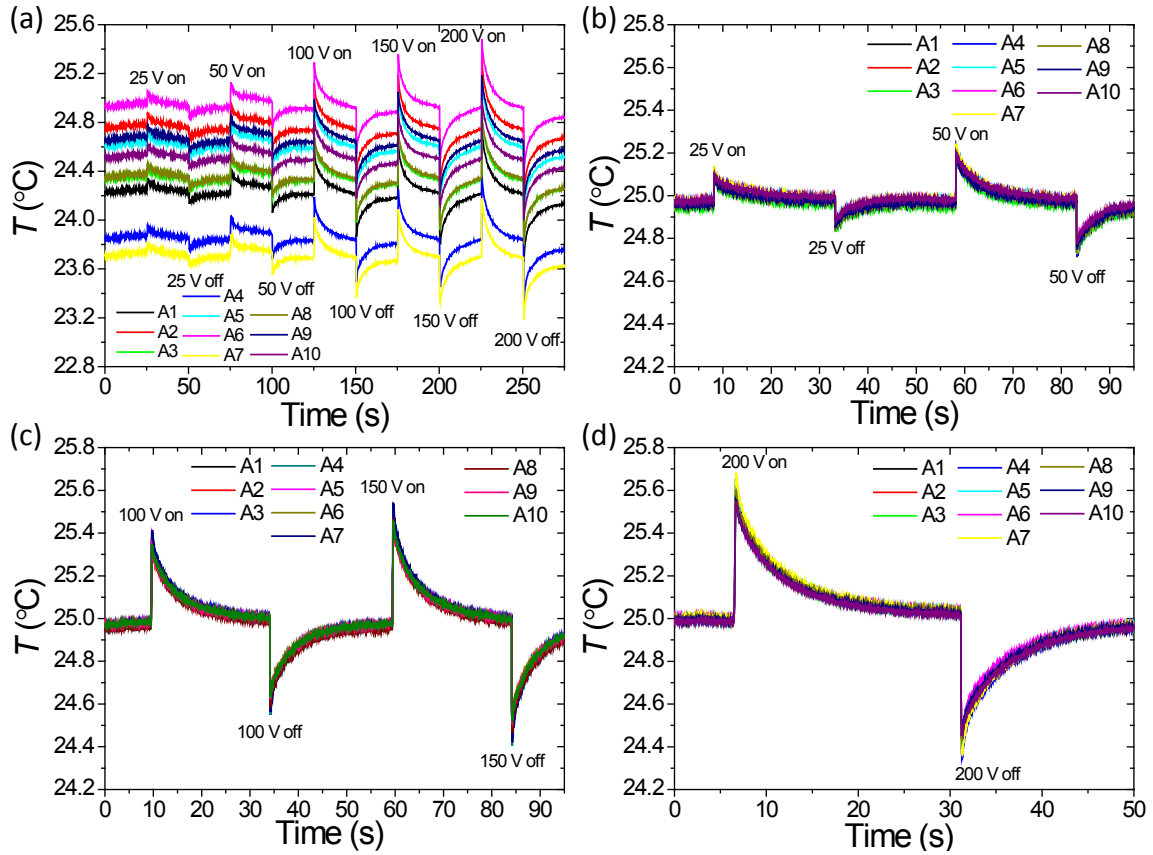


Figure 4.12: (a) Thermal recording on applying and removing a voltage of 25-200V at the times indicated, where the emissivity is set to be 1 across the whole MLCs. Fictitious spatial variations in temperature can be seen due to the surface roughness; (b)-(d) are the results obtained by using the mode of infra-red camera by fixing the temperature of MLC to a finite temperature. This can be achieved by adjusting the emissivity in different regions until they are all at the same real temperature (see Table. 4.2).

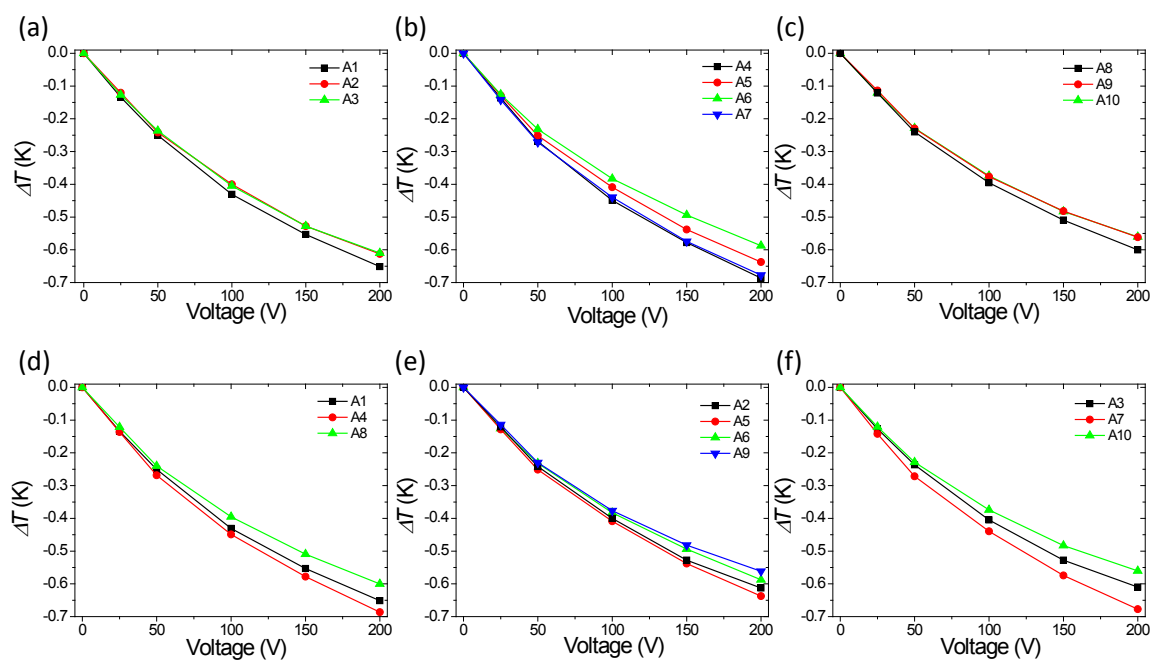


Figure 4.13: Summary on electrocaloric effect in regions A1-A10 obtained from Figs. 4.12(b)-(d).

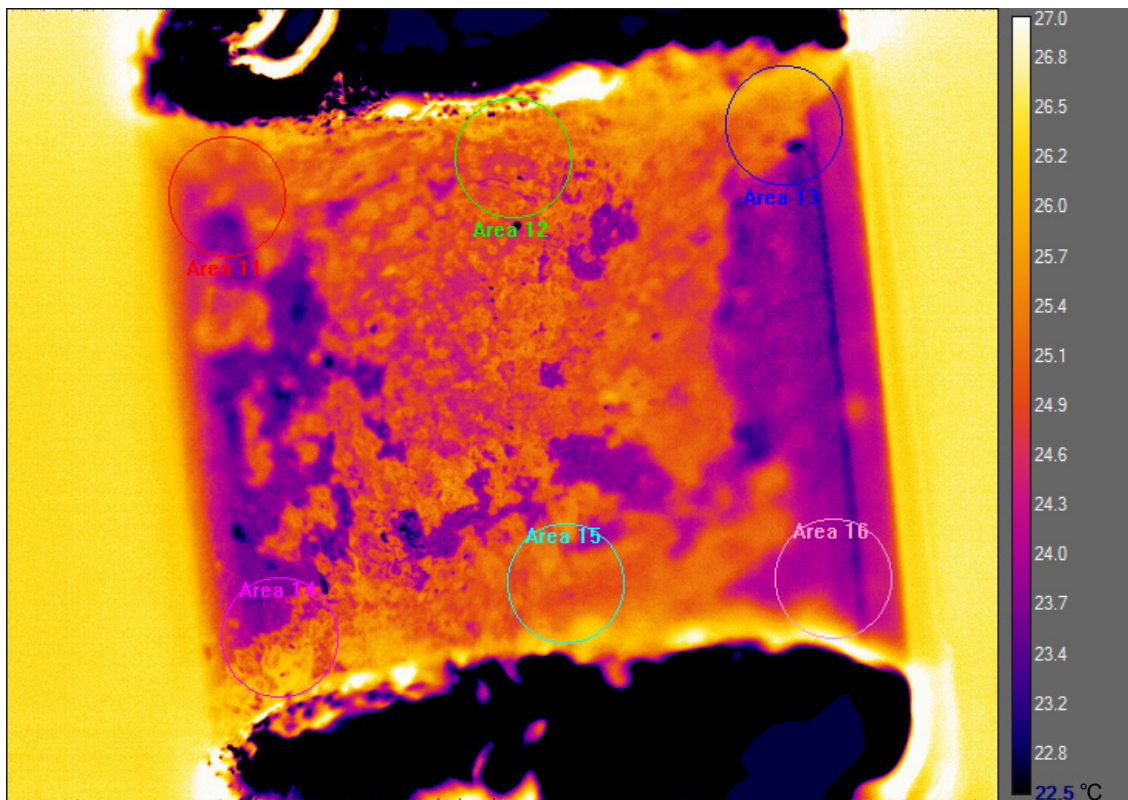


Figure 4.14: Thermal image of top surface of MLC #2 (unpolished) at room temperature, and regions A11-A16 are indicated.

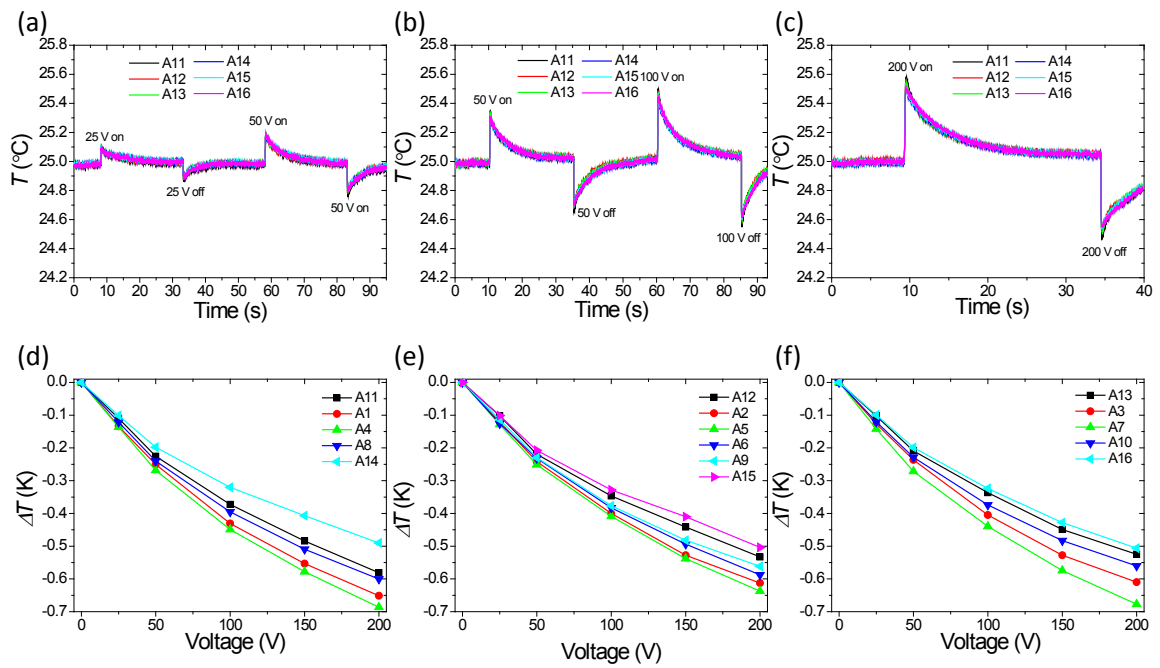


Figure 4.15: (a)-(c) Recorded temperatures corresponding to different regions in Fig. 4.14 as a function of real time while the voltage pulse is applied/removed. (d)-(f): The electrocaloric temperature change ΔT as a function of voltage (0-200 V) in selected regions in MLC #2 (unpolished).

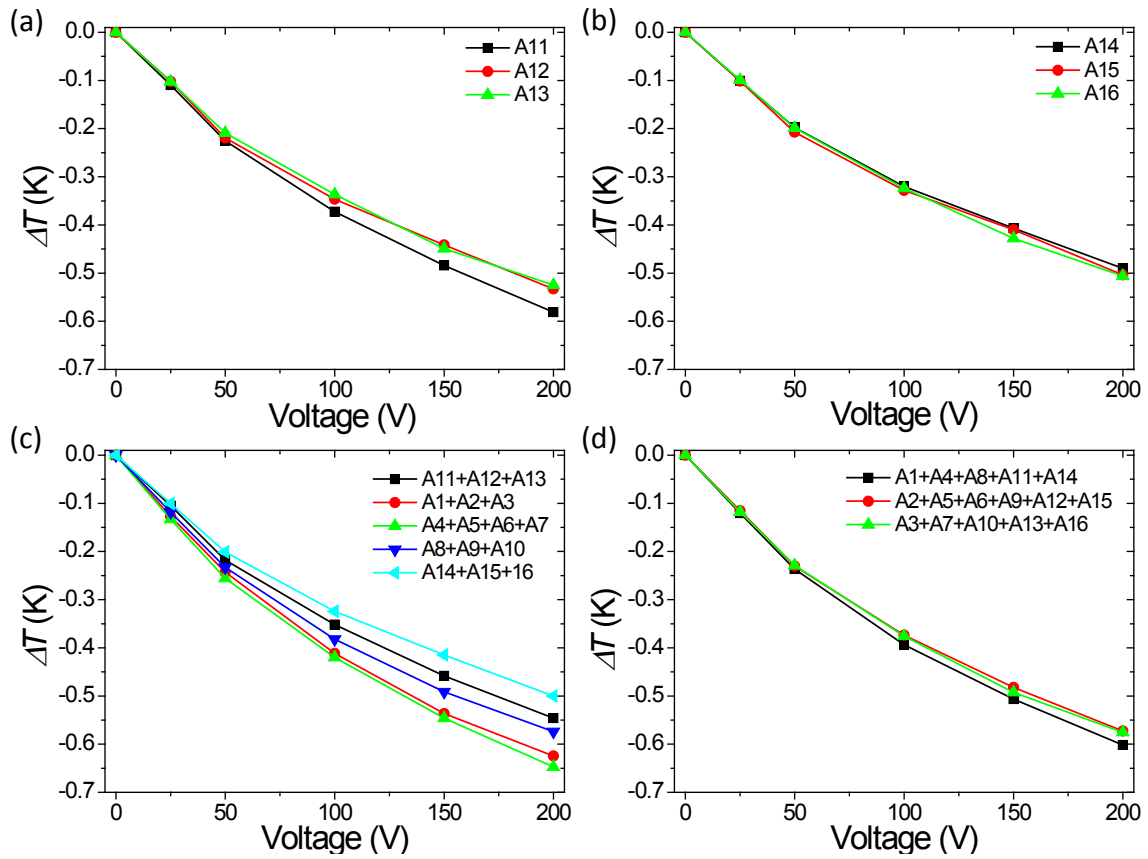


Figure 4.16: (a) and (b) Electrocaloric effect in regions A11-A16 obtained from Figs. 4.15(a)-(c). Average temperature change by several specific regions along y direction (c) and x direction (d).

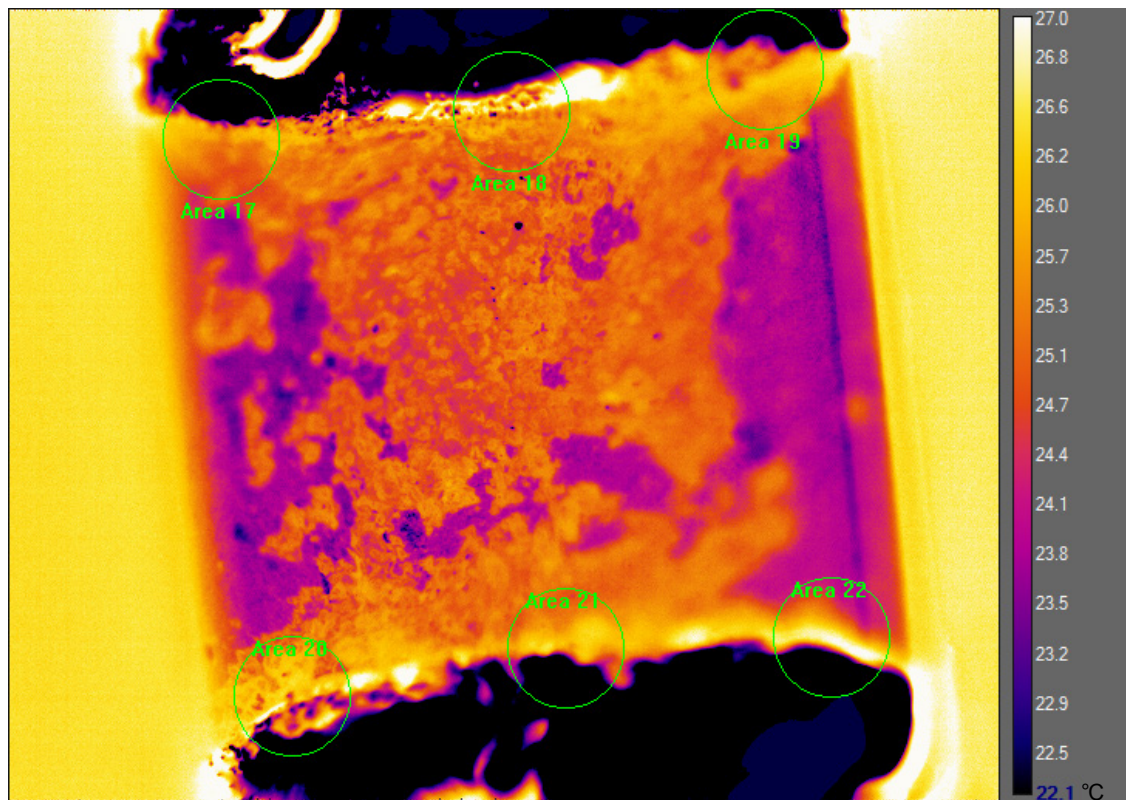


Figure 4.17: Thermal image of top surface of MLC #2 (unpolished) at room temperature, and regions A17-A22 are specifically indicated.

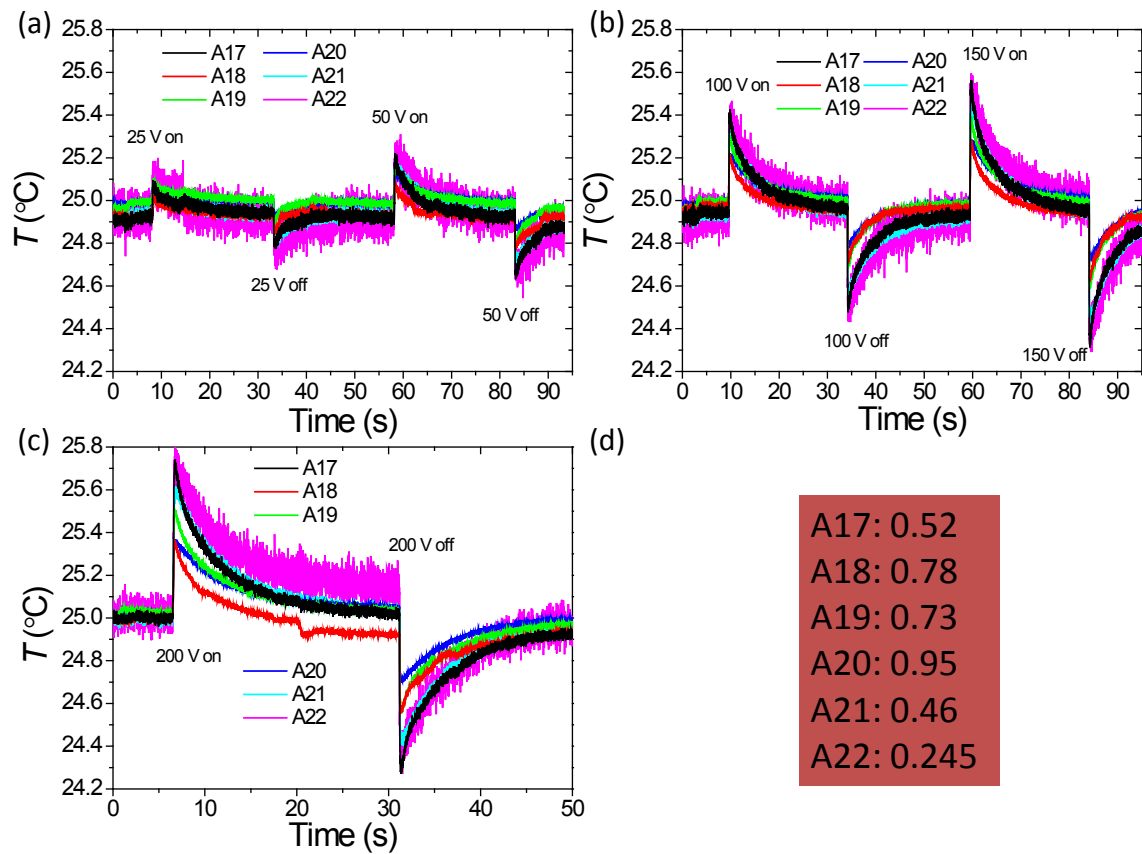


Figure 4.18: (a)-(c) Recorded temperatures corresponding to different regions in Fig. 4.17 as a function of real time while the voltage pulse is applied/removed. (d): the corresponding emissivity after its adjustment from Fig. 4.17.

Another interesting feature is that a very large fluctuation of signal is found when the focusing regions move more close to the tin coating (Figs. 4.17 and 4.18). This is due to the fact that the surface of tin coating is rather rough (the adjusted emissivity changes significantly from region to region), which makes it difficult to achieve a fixed temperature by adjusting the emissivity in different regions. This can be improved by polishing the tin coating as we have observed that the fluctuation aforementioned disappeared as long as the surface is flat (not shown here).

4.5 SPATIALLY RESOLVED IMAGING OF ELECTROCALORIC EFFECT IN MULTILAYER CAPACITORS #3

Following the strategies presented in MLCs #1 and #2, we now simply provide the experimental results on MLC #3. For comparison, the results from the unpolished side of MLC #3 are shown in Figs. 4.19-4.22 while the results deduced from polished sides are shown in Figs. 4.23 and 4.24. Once again, it is found that a remarkably spatial distribution of electrocaloric response exists regardless of unpolished or polished sides of MLC #3, which is consistent with previous results on MLC #1 and #2. In addition, it is shown that both sides have exactly the same spatial electrocaloric profile, which will be shown later in next Section.

4.6 ELECTROCALORIC HEAT FLUX IN MULTILAYER CAPACITORS

In order to gain further insight into the electrocaloric heat conducted between the MLCs and the terminals, the average temperature change ΔT_{av} , the largest average difference in x direction ΔT_{xmax} and y direction ΔT_{ymax} are plotted in Figs. 4.25(a)-(c), respectively. It is shown that all MLC samples display a significantly larger variation of electrocaloric effect in x direction than in y direction [$|\Delta T_{xmax}| \gg |\Delta T_{ymax}|$] as shown in Figs. 4.25(b) and 4.25(c)]. In other words, the closer to the terminals, and the smaller magnitude of temperature change is observed. This is due to the large thermal mass of the terminals [217] which are electrocaloric inactive and lead to massively diluted electrocaloric response as we observed in this work. Moreover, heat flux mainly follows the path towards the terminals and only dissipates weakly in direction vertical to this path (see Fig. 4.2). Since the terminals are directly responsible for heat transfer between the MLCs and heat/cold sink in the prototype [119, 121, 126, 233], geometrical optimization is highly desired. For instance, according to a finite element analysis, optimizing the length of active ceramic layers can shorten the path of electrocaloric heat transfer, which is accompanied by a significant increase in the cooling power and operating frequency [232]. In this regard, our findings imply that IR camera is emerging as an ideal technique to precisely image the dynamics of electrocaloric heat flow in MLCs. For instance, the existence of ΔT gradient not only indicates the main direction of heat flux (Fig. 4.2) but also implies the heat flux is not homogeneous i.e. weak heat flux exists in the direction of along the terminals (y direction) due to the temperature gradient ΔT_{ymax} . This also demands further studies to directly quantify this inhomogeneous heat flux by solving the heat equations as will be shown later.

Although polishing of top layer can make the surface emissivity more uniform (see comparison

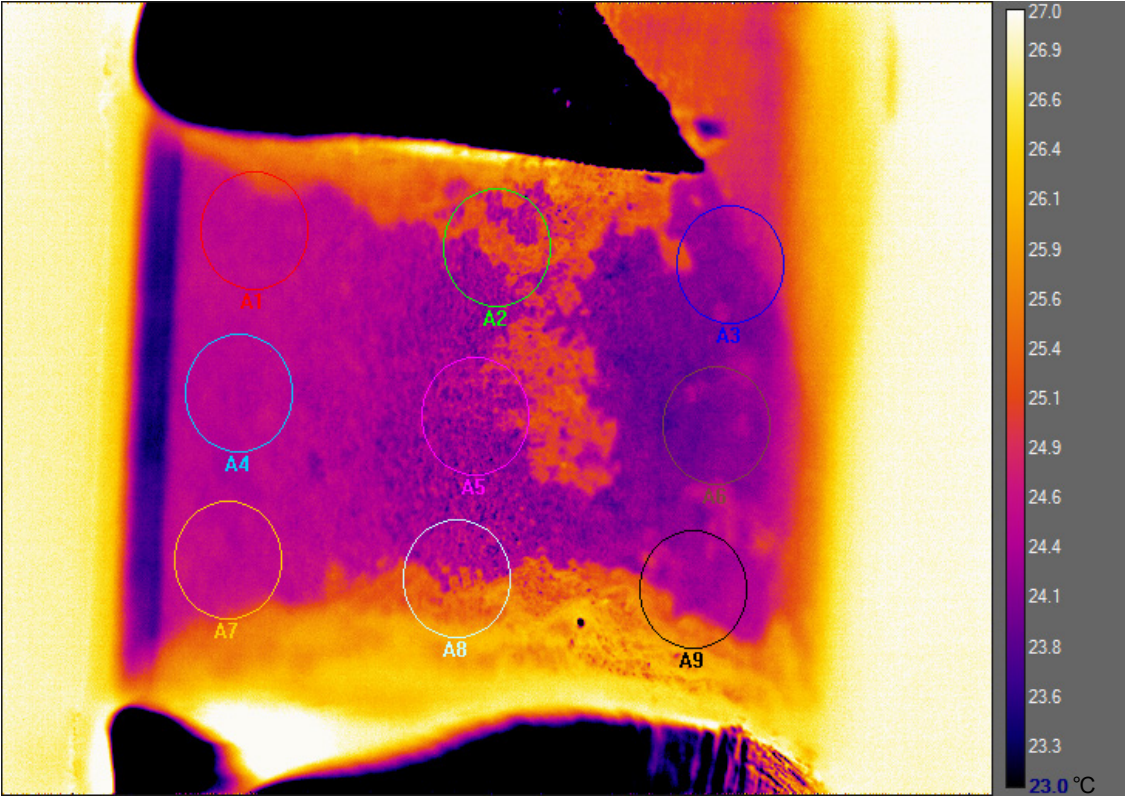


Figure 4.19: Thermal image of top surface of MLC #3 (unpolished side) at room temperature, and regions A1-A9 are specifically indicated.

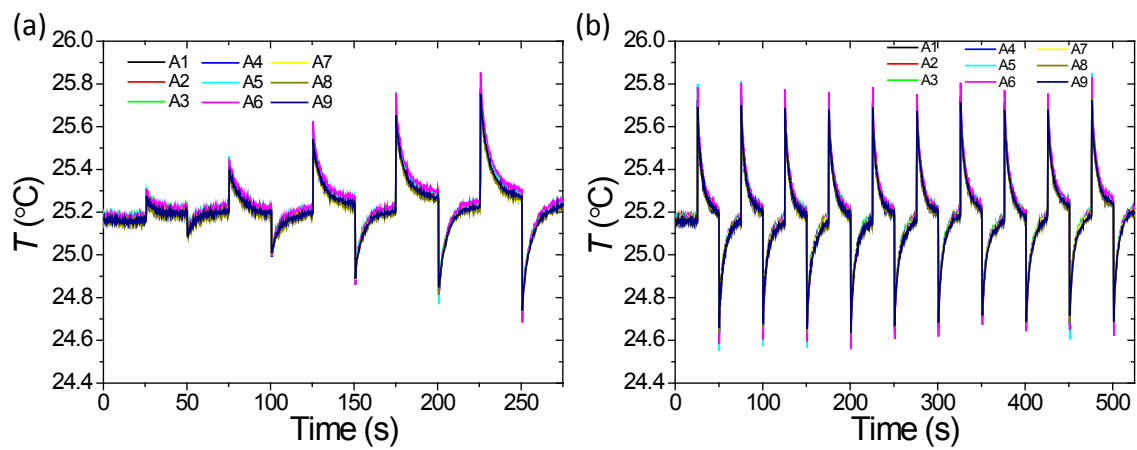


Figure 4.20: (a) Recorded temperatures corresponding to different regions in Fig. 4.19 as a function of real time while the voltage pulse is applied/removed. (b) the results obtained by 10 successive voltage cycles between 0 and 200 V.

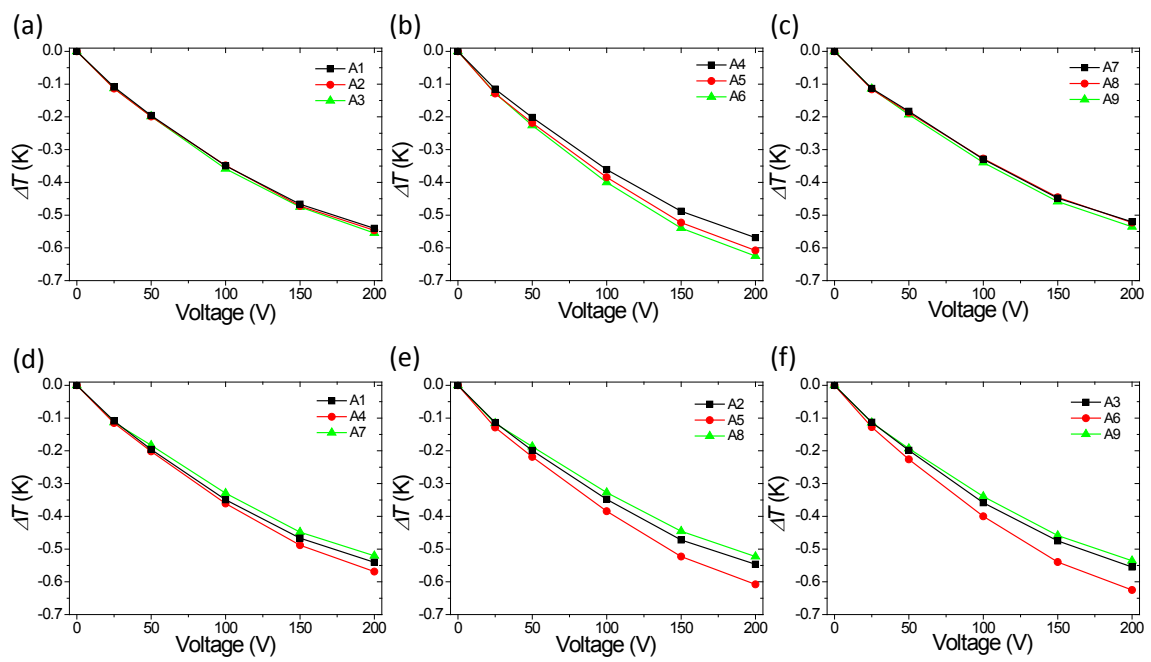


Figure 4.21: Electrocaloric effect in regions A1-A9 obtained from Fig. 4.20.

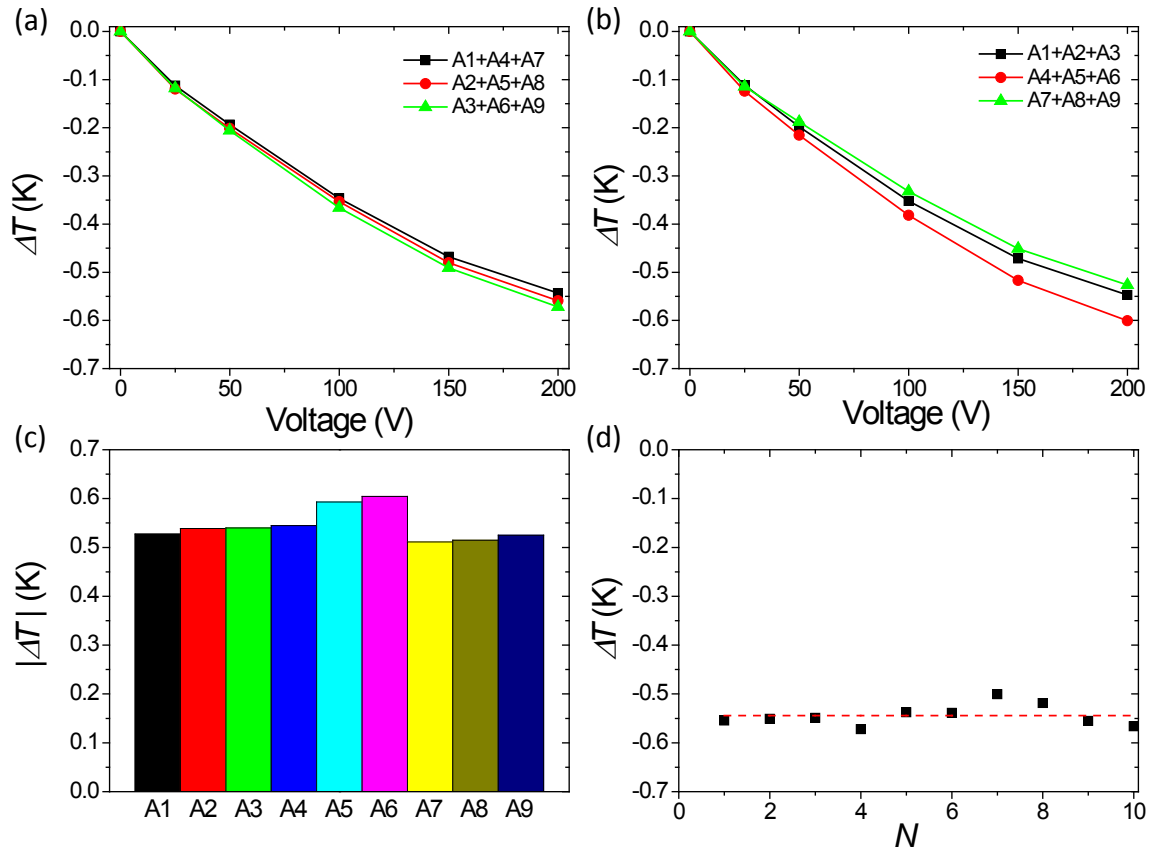


Figure 4.22: Average temperature change by several specific regions along y direction (a) and x direction (b). Distribution of electrocaloric effect in different regions when a voltage of 200 V is removed (c). The results are obtained by averaging 10 successive data points. The average electrocaloric effect obtained by averaging 9 different regions as a function of cycle number N (d). Red dashed line is a guide for eye for the average value by ten successive data points.

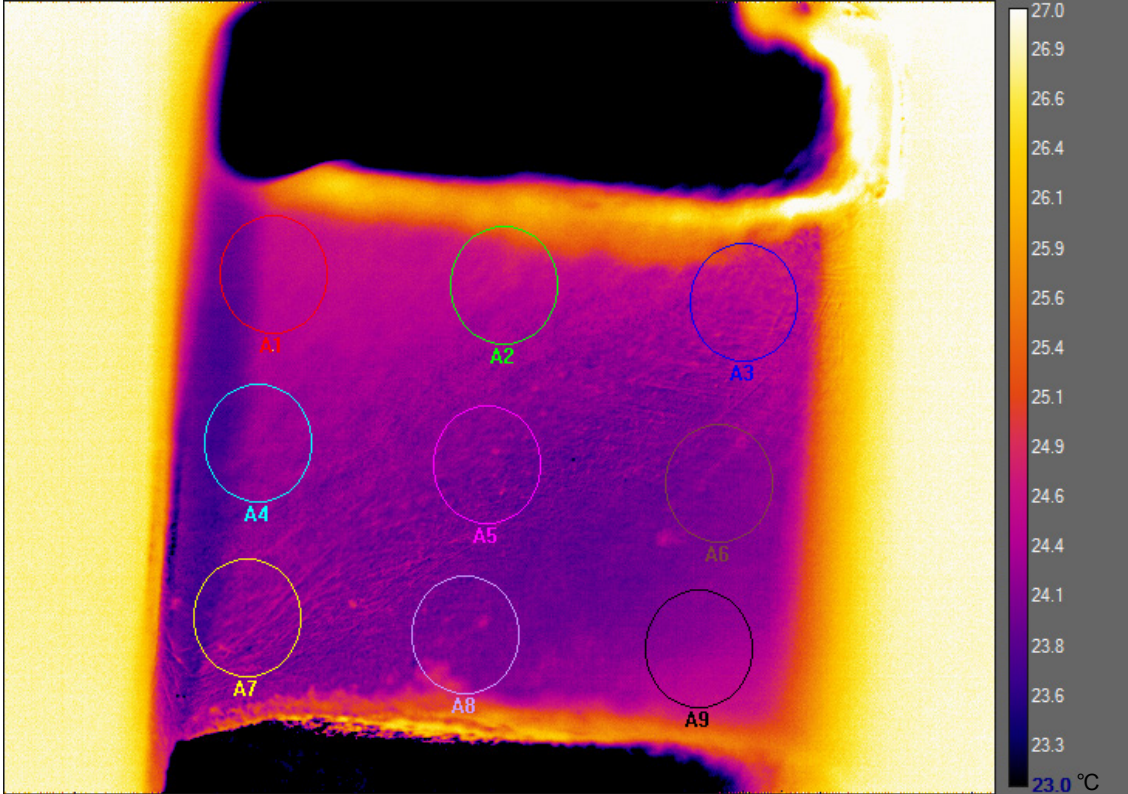


Figure 4.23: Thermal image of top surface of MLC #3 (polished side) at room temperature, and regions A1-A9 are specifically indicated.

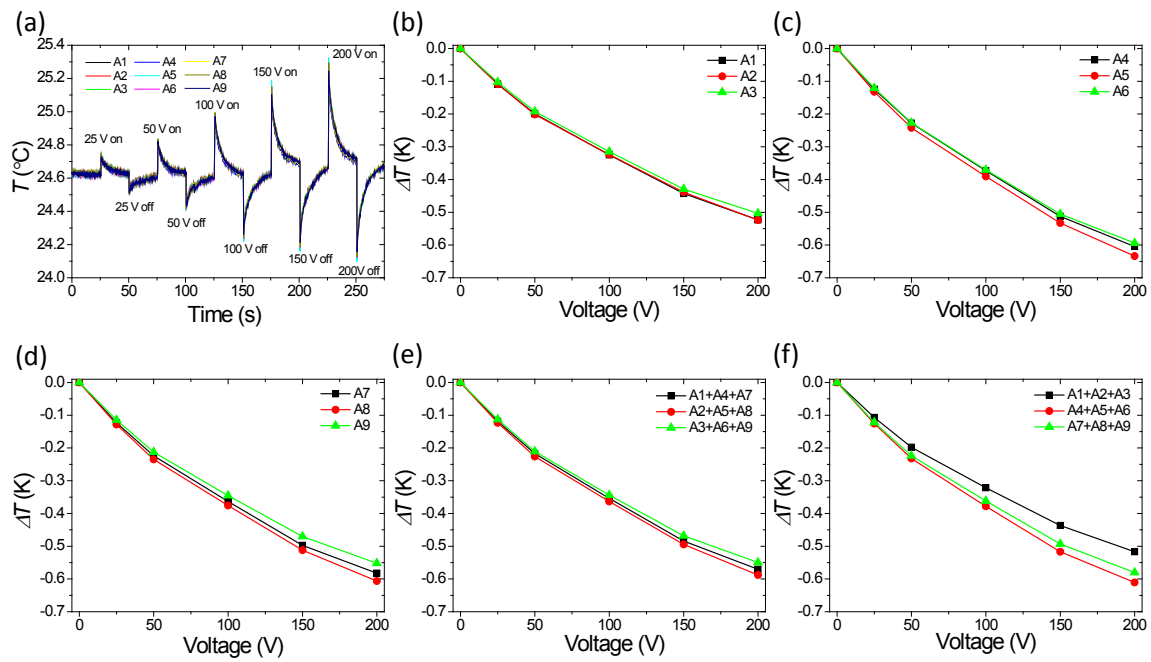


Figure 4.24: (a) Recorded temperatures corresponding to different regions in Fig. 4.23 as a function of real time while the voltage pulse is applied/removed. (b)-(d) Electrocaloric effect in regions A1- A9 obtained from (a). Average temperature change by several specific regions along y direction (e) and x direction (f).

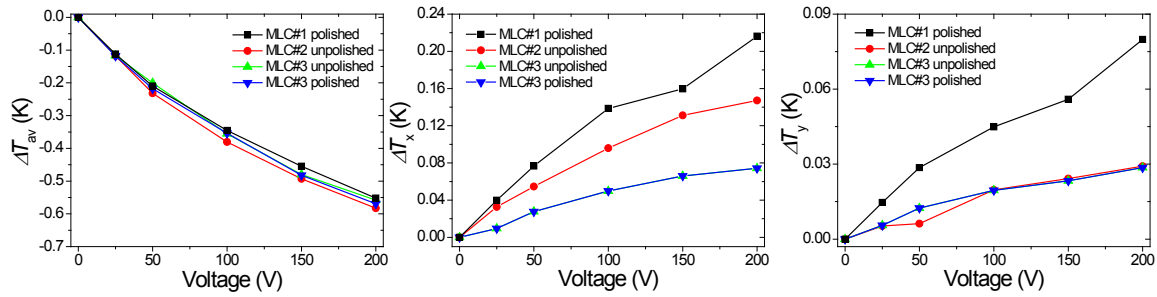


Figure 4.25: (a) The average temperature change ΔT_{av} obtained by averaging all the measured regions as a function of applied voltage; (e) ΔT_{xmax} indicates the largest difference in ΔT_x along x direction while (f) ΔT_{ymax} indicates the largest difference in ΔT_y along y direction.

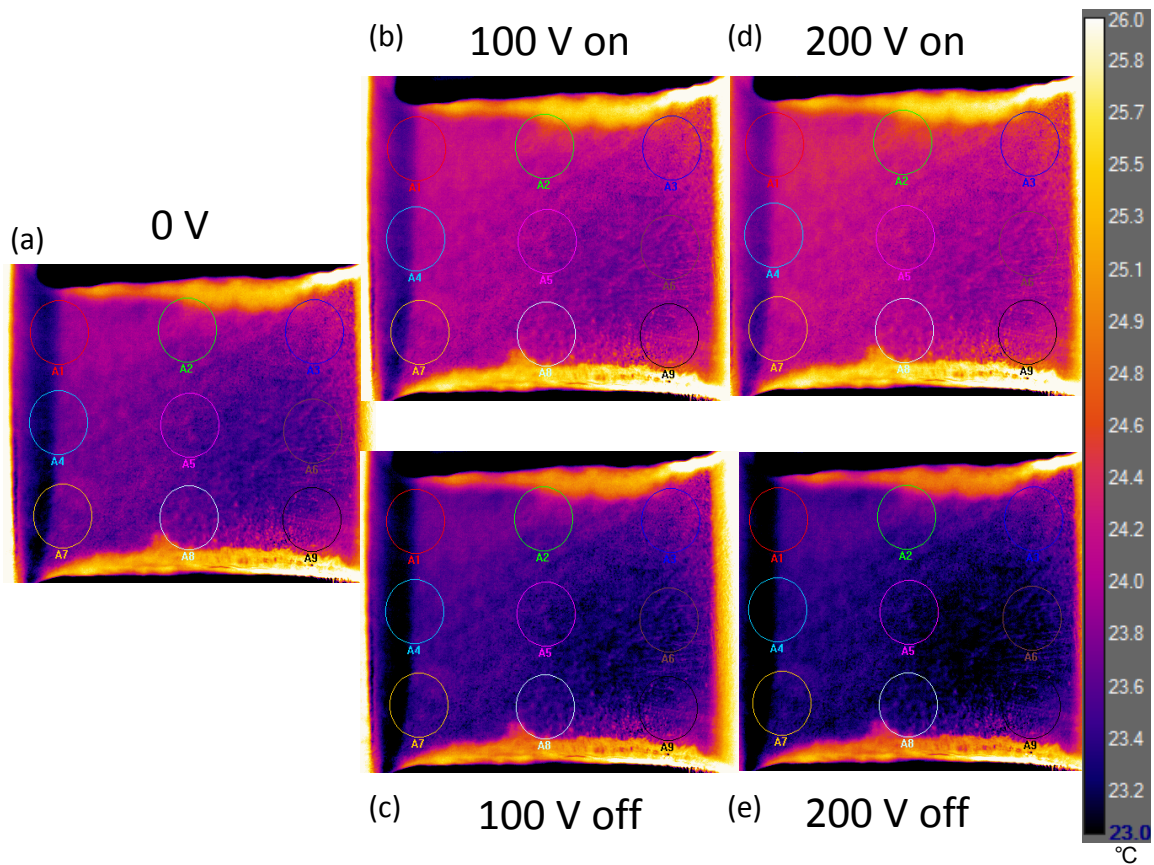


Figure 4.26: (Typical thermal image of top surface in MLC #1 at different times in a cycle: (a) $t=0$ s (voltage=0 V), (b) $t=125$ s (Voltage=100 V applied), (c) $t=150$ s (Voltage=100 V removed), (d) $t=225$ s (Voltage=200 V applied), and (e) $t=250$ s (Voltage=200 V removed).

of thermal images in two sides of MLC #3 in Figs. 4.19 and 4.23), no systematic dependence of electrocaloric effect on the treatment of polishing is found. For instance, electrocaloric properties are found to be exactly the same between the polished side and unpolished side in MLC #3 [see Figs. 4.25(b) and 4.25(c)]. Interestingly, given that ΔT_{av} is nearly the same for MLC #1 (polished) and MLC #2 (unpolished), both ΔT_{xmax} and ΔT_{ymax} shows remarkable different values when the same voltage is withdrawn [see Figs. 4.25(b) and 4.25(c)]. Moreover, the largest temperature change along the y direction is changing subtly either located at the side (i.e. $|\Delta T_{y1}|$ is the largest in MLC #1 and MLC #2) or central position (i.e. $|\Delta T_{y2}|$ in MLC #3). It provides direct experimental evidence demonstrating that heat flow behavior is actually more complex than either simple assumption in theoretical simulations [232] or general expectation from common knowledge about thermal conduction. This may be because: increased microstructural inhomogeneity or defects in MLCs resulting in a more inhomogeneous electrocaloric response in the direction along the terminal; The metallic Ni inner electrodes which conduct electrocaloric heat between the ceramic layers and the terminals inhomogeneously; inhomogeneous polishing of the inactive thin layer will decrease its thickness in an inhomogeneous manner leading to the inhomogeneous distribution of the heat ejected/absorbed by active electrocaloric MLCs; and because inhomogeneous capability of heat delivering of the inactive top layer due to its microstructural inhomogeneity. This underlines the need to pursue more studies such as measuring the side without inactive layer. Nevertheless, provided that this layer is over 200 times thinner than the active electrocaloric MLCs, its contribution to the electrocaloric heat transfer is unlikely to dominate since the same results are observed in MLC #3 regardless of polishing of the inactive layer. Figs. 4.25(b) and 4.25(c) again provide direct experimental evidence to confirm that the electrocaloric heat is mainly transferred in a path along interdigitated Ni inner electrodes away from (towards) the terminals (x direction) and it is weakly dissipated in the direction along the terminals (y direction) in a complex manner. Also note that we cannot simply use the temporal electrocaloric thermal images (Fig. 4.26) to directly reproduce the heat flux as schematically shown in Fig. 4.2 due to the foregoing problem of emissivity under no voltage or/and inhomogeneous polishing of top layer. In this case, the temporal profile also may provide a false thermal image when the electrocaloric effect is triggered. Our preliminary result implies that more careful polishing of top surface is highly desired in further works.

Finally, in order to gain deeper insights into dynamic behavior of the electrocaloric heat flux, we concentrate on the temporal evaluation of ΔT distribution as shown in Fig. 4.27. A significant reduction (over 50%) of ΔT is observed within 2 s in y_2 -regions after the voltage is removed at 250 s in MLC #1 (polished) [Fig. 4.27(a)]. The difference in ΔT close to the central regions (A2,A5,A8) becomes trivial after 255 s (5 s after the voltage is removed). However, a noticeable difference (>25 mK) in δT between the central ceramic regions and those close to the metallic terminals still exists [see comparison between regions B5 and A5 or regions B2 and A5 as shown in Fig. 4.27(a)]. Moreover, the magnitude of ΔT gradient along x direction is the largest corresponding to the time when the voltage is removed [see Fig. 4.27(b)] or applied [see Fig. 4.28(b)] and it then decays exponentially-like with time towards zero [see Figs. 4.27(a) and 4.28(a)]. The counterpart in y-direction firstly shows a small gradient of about 0.0449 K and becomes even smaller with a nearly constant value of about 0.017 K [the inset of Fig. 4.28(b)]. The typical temporal data again confirm our foregoing analysis on the direction of electrocaloric heat flux

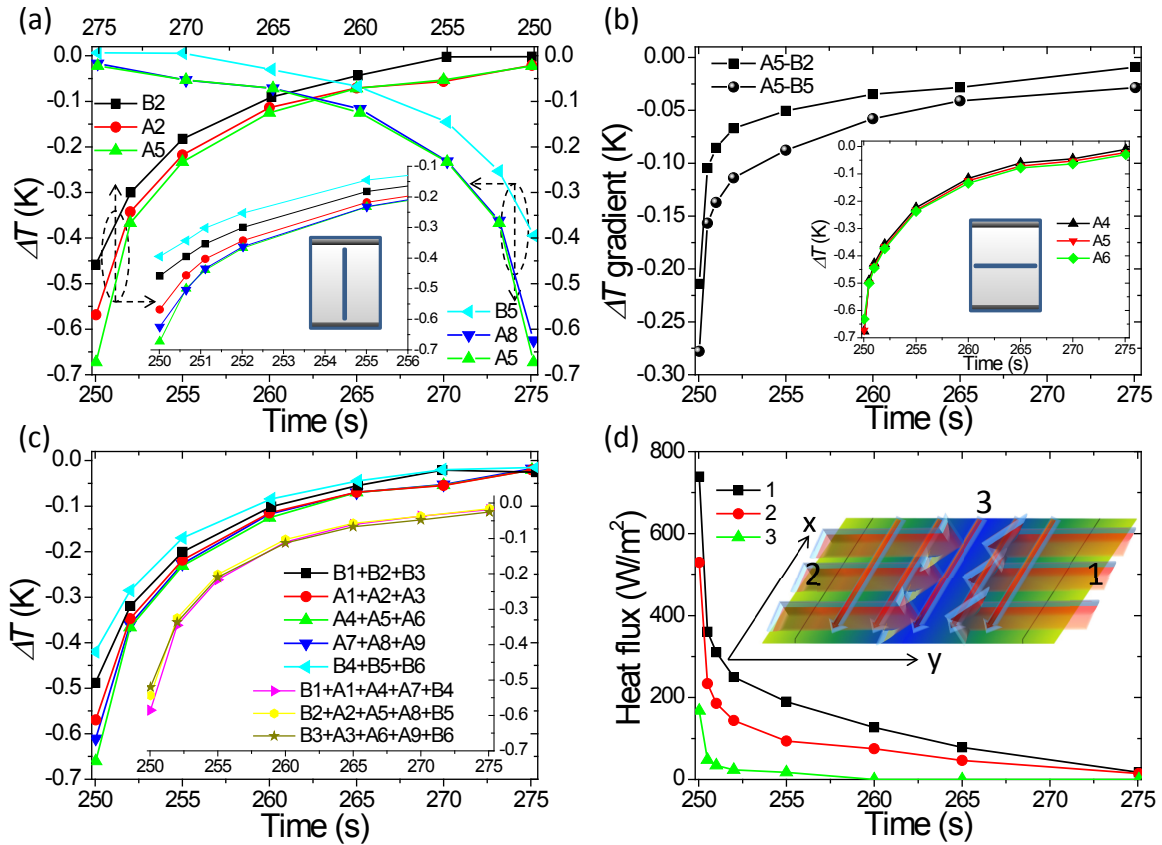


Figure 4.27: (a) Temporal ΔT in y_2 -regions (B2, A2, A5, A8, B5) after the voltage is removed at 250 s and the inset is an enlarged view of (a) specifically in time range of [250-256 s]. The dashed line and arrows act as a guide for axes of coordinates; (b) Temporal ΔT gradient between region A5 and B2 (B5) after the voltage is removed at 250 s and the temporal ΔT in x_3 -regions (A4, A5, A6) in the inset; The inset cartoons depict the corresponding locations of selected regions. Average temperature change (c) ΔT_x and (inset) ΔT_y as a function of real measurement time; (d) Heat flux 1, 2, and 3 along x and y directions corresponding to removal of 200 V as a function of real time. Accordingly, the inset corresponds to a schematic of heat flux 1, 2, and 3 in MLC #1 (polished) after 200 V is removed.

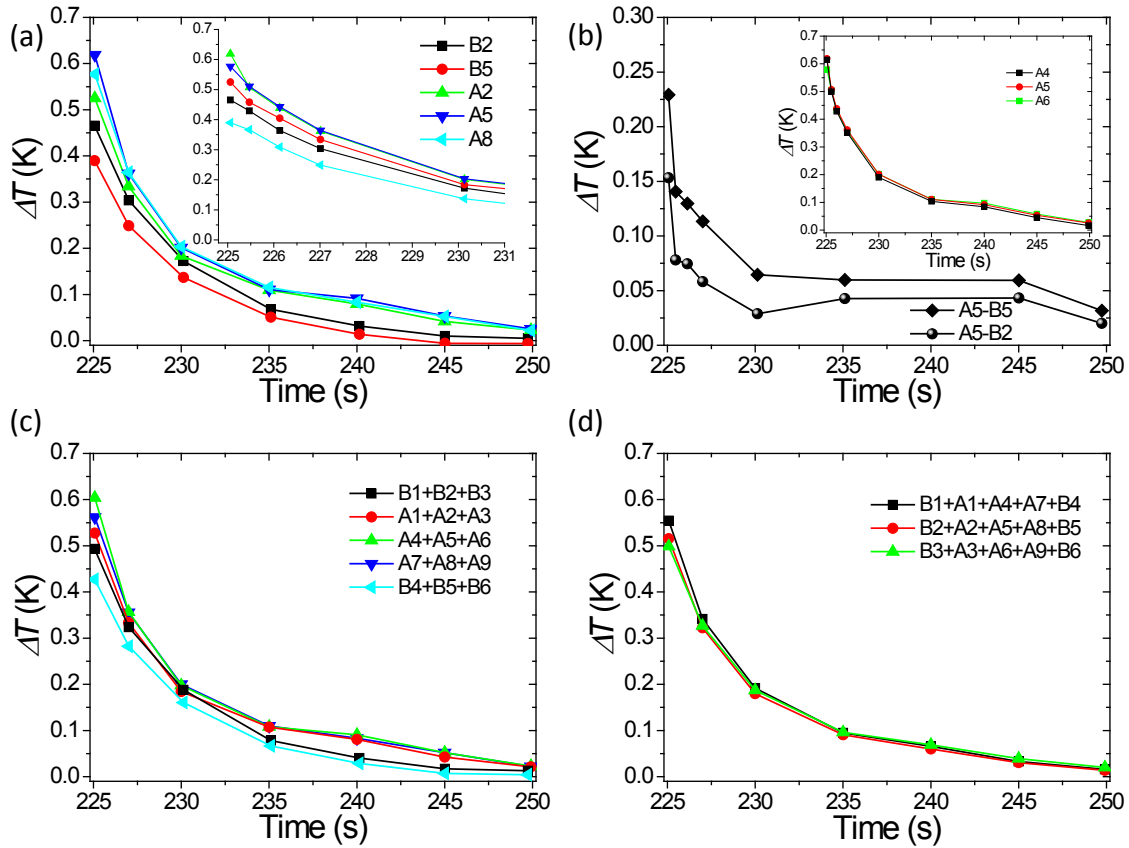


Figure 4.28: (a) Temporal ΔT in y_2 -regions (B2, A2, A5, A8, B5) after the voltage is applied at 225 s and the inset is an enlarged view of (a) specifically in time range of [225-231s]; (b) Temporal ΔT gradient in between region A5 and B2 (B5) after the voltage is applied at 225 s; the inset depicts the temporal ΔT in x_3 -regions (A4, A5, A6); Average temperature change (c) ΔT_x and (d) ΔT_y as a function of real measurement time.

at peak position and our proposed sketch in Fig. 4.2. More importantly, our study provides a practical route to extract thermal time constant τ for heat flow between central ceramic layers and metallic terminal, which is one of the key parameters to obtain the cooling power ($\propto 1/\tau$) according to recent finite element modelling [232]. We estimate this τ constant of about 1 s based on our results in Fig. 4.28(b), which is significantly larger than those (0.01-0.2 s) used in theoretical simulations [232] and the one (0.17 s) calculated by lumped thermal model [231] (as shown later). The larger measured τ is likely attributed to the enhancement in the total thermal resistance and the large thermal mass of BaTiO₃ might play an important role in affecting the thermal resistance and thus the relaxation time. In addition, a summary on the locally average ΔT along MLCs [see Figs. 4.27(c) and 4.27(d)] well reproduces the foregoing results in Figs. 4.27(a) and 4.27(b), which supports that the typical results in y_2 -regions and x_3 -regions can represent the behavior of the whole MLC #1.

In a lumped equivalent thermal circuit taking into account heat capacity and thermal conductivity of BaTiO₃ and Ni electrodes [231], the heat flux follow an exponential decrease $\dot{Q} = Q_{max} \exp(-t/R_{total}C_{total})$, where $Q_{max} = \Delta T_{Gra}/R_{total}$ is the initial electrocaloric heat flux at $t=0$ s, $R_{total} = R_{TH}^{Ni}/n$ is the total thermal resistance in series where $R_{TH}^{Ni} = L/2/\kappa_{Ni}A_{Ni}$ is a thermal resistance of single Ni electrode (L effective length, cross-sectional area A_{Ni}) and n is the number of total electrocaloric layers (150 in our case) and C_{total} is total thermal capacitance where $n/C_{total} = (1/C_{THNi} + 1/2C_{TH}^{EC})$. $C_{TH}^{Ni} = 66 \mu\text{J/K}$ [231] and $C_{TH}^{EC} = \rho_{EC}c_{EC}(v_{EC}) = 111.5 \mu\text{J/K}$ are the thermal capacitance of Ni and electrocaloric layer (BaTiO₃), respectively, where $\rho_{CE} = 5840 \text{ kg/m}^3$ and $v_{EC} = 8.8 \times 10^{-11} \text{ m}^3$ are the mass density and volume of BaTiO₃ layer. $\tau = R_{total}C_{total}$ is the thermal relaxation time.

Following this model, we firstly calculate the thermal relaxation time. Specifically, C_{total} is calculated as $7639.4 \mu\text{J/K}$ while $R_{total} = 22.7 \text{ K/W}$, and the thermal relaxation time $\tau = R_{total}C_{total}$ is about 0.17 s which is smaller than our measured value of 1 s [see Fig. 4.28(b)]. We attributed this difference to the enhanced thermal resistance R_{total} due to all experimental complications since C_{total} is unlikely changed due to the fact that both Ni and BaTiO₃ have nearly the same heat capacity. Using the experimental value of τ obtained in Fig. 4.28(b), we can thus calculate the total thermal resistance R_{total} as $R_{total} = \tau/C_{total} = 130 \text{ K/W}$, which is significantly larger than the theoretical value of $R_{total} = 22.7 \text{ K/W}$. The large thermal mass of BaTiO₃ might play an important role whose effect is only included in the thermal capacitance C_{total} through the relation $n/C_{total} = (1/C_{THNi} + 1/2C_{TH}^{EC})$ rather than thermal resistance R_{total} which is only related to the Ni electrode in this model as $R_{total} = R_{TH}^{Ni}/n$. Moreover, we then calculate the initial Q_{max} ($Q_{max} = \Delta T_{Gra}/R_{total}$) as 1.85 mW, 1.32 mW and 0.5 mW by using $R_{total} = 130 \text{ K/W}$ and $\Delta T_{Gra} = 0.240 \text{ K}$, 0.172 K and 0.0655 K for heat flux 1, 2, and 3 which are experimentally extracted from Fig. 4.28(c) which is smaller than the theoretical value of 0.74 K used in Ref. [231]. The average $Q_{av} = Q_{max}/20$ is 0.0925 mW, 0.066 mW and 0.025 mW for heat flux 1, 2, and 3. As a result, the cooling power of heat flux 1, 2 and 3 thus correspond to 0.037 kW/m^2 , 0.0265 kW/m^2 , and 0.0084 kW/m^2 , respectively.

Indeed, IR camera with spatially resolved temperature gradient is probably the only technique which can be used to directly determine the electrocaloric heat flux. The dynamic heat flux behaviour in MLC #1 is summarized in Fig. 4.28(d), which is obtained through a lumped thermal model (as shown above) by taking into account the experimental complications. It

is found in Fig. 4.28(d) that remarkable heat flux 1, 2, and 3 exist only within ~ 5 s and it decays dramatically from 738.9 W/m^2 , 529.3 W/m^2 , and 168.0 W/m^2 after removing the external voltage. Although the magnitude of heat flux 3 in x-direction is over twice smaller than those in y-direction, this noticeable heat dissipation should be avoided or reduced as much as possible for practical cooling applications [the inset of Fig. 4.28(d)]. Theoretical simulations also predicted substantial cooling power as a main promise of MLCs for cooling applications [231, 232]. Interestingly, this important parameter can be also obtained according to our dynamic heat flux through simple calculations as shown above. Specifically, the average cooling power for heat flux 1, 2, and 3 are 0.037 kW/m^2 , 0.0265 kW/m^2 , and 0.0084 kW/m^2 , respectively. These values are still smaller than recent theoretical predictions of $\sim 0.8\text{-}2.5 \text{ kW/m}^2$ in BaTiO_3 -based MLCs with Ni electrodes [231, 232]. The difference between heat flux 1 and 2 arises from the different thermal mass due to the different amount of tin deposition. It is known that cooling power of MLCs (being $\propto 1/\tau$) is limited by the thermal relaxation time [232]. Our findings here indicate that fast heat exchange cannot be simply realized using our current geometry of devices (our measured τ is larger than theoretical expectations), which may therefore prevent reaching a larger cooling power. As a result, a strong evacuation of the heat imposed on the terminals and/or further geometric optimization and/or good thermal transfer adhesive attached to MLCs are very desired in future works. Therefore, the temporal measurement combining the spatial type may open a route to extract the value of heat flow as function of position and time since the amount of heat displaced for a given duration can be readily obtained as highlighted here. In terms of design of prototype devices, our preliminary findings reveal the essential role of the metallic terminals for extracting electrocaloric heat. For information, we provide further sketches of electrocaloric heat flux in MLCs and Brayton-like refrigeration using MLCs, which are shown in Figs. 4.29 and 4.30, respectively.

Heat flux can be also estimated by Fourier's Law. In order to evaluate the heat flux results [Fig. 4.28(d)] obtained through lumped thermal model, we carry out heat flux calculations using Fourier's Law $\dot{Q} = -\kappa_{eff}\Delta T_{Gra}/l$, where κ_{eff} is the effective thermal conductivity combining contributions from ceramic layer and inner electrodes, l is the heat transfer length and ΔT_{Gra} is the temperature gradient obtained from Fig. 4.28(c). We note that we simplify the case that the heat flux of interest is laterally restricted with in-plane panel (x,y) while heat flux between different electrocaloric layers is not considered in this work. Each element has two materials: one is BaTiO_3 ceramic layer mainly generates the electrocaloric heat while the other one is inner Ni electrode which is mainly responsible to conduct this heat towards the terminals. But here we deliberately regard that BaTiO_3 layer and Ni electrode as a whole system and do not consider their electrocaloric heat transfer in the initial stage. In other words, we only make estimation of the amount of heat flow after that Ni and BaTiO_3 reach the same temperature. In this case, the total thermal conductivity of each element is calculated by BaTiO_3 layer $\kappa_{BTO} = 2.6 \text{ W/K m}$ and Ni ($\kappa_{Ni} = 4 \text{ W/K m}$) such that $1/(1/2.6+1/4)=2.53 \text{ W/K m}$. By doing this calculation, there may be one remaining Ni electrode either on the top/bottom whose contribution can be ignored. This is simply because we have already considered 150 electrodes and this end effect cannot affect the main results here. Moreover, since the specific heat of Ni (429 J/K kg) and BaTiO_3 (434 J/K kg) is nearly the same, its contributions to heat flux is trivial and the determining factor here is the thermal conductivity of BaTiO_3 . For information,

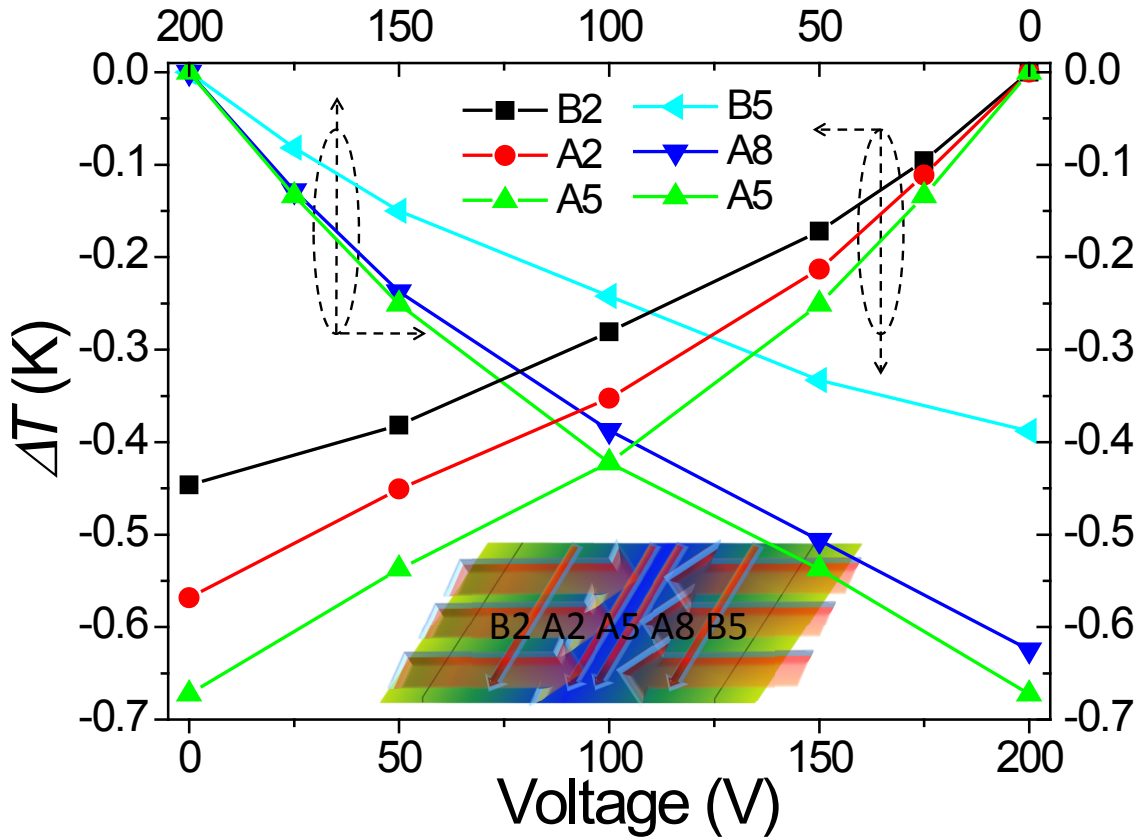


Figure 4.29: Spatial distribution of electrocaloric response and heat flux when the voltage is removed (adiabatic depolarization).

our experimental data also already takes into account both the thermal conductivity and specific heat in terms of thermal relaxation time as shown in Fig. 4.28(b). The average temperature gradient we used is extracted from Fig. 4.28(c). As expected, it is also found that remarkable heat flux 1, 2, and 3 exist only within 5 s and it decays significantly from 607 W/m^2 , 435 W/m^2 , and 132 W/m^2 after removing the external voltage. These values are smaller than those (738.9 W/m^2 , 529.3 W/m^2 , and 168.0 W/m^2) obtained from lumped thermal model due to foregoing underestimations. Specifically, the average cooling power for heat flux 1, 2, and 3 are 0.030 kW/m^2 , 0.022 kW/m^2 , and 0.0066 kW/m^2 , respectively. These values are also slightly smaller than those (0.037 kW/m^2 , 0.0265 kW/m^2 , and 0.0084 kW/m^2) obtained from lumped thermal model. We note that the estimations shown above may not necessarily meet the real conditions of electrocaloric heat flux due to the assumption that BaTiO_3 and Ni have the same temperature after the electrocaloric effect is triggered. Moreover, here we only consider the finite temperature gradient between the BaTiO_3 and Ni as a whole and the terminals which drives the heat flux. Nevertheless, such estimations give rise to very similar values of the heat flux and cooling power, which may support that our findings in Fig. 4.28(d) are reasonable.

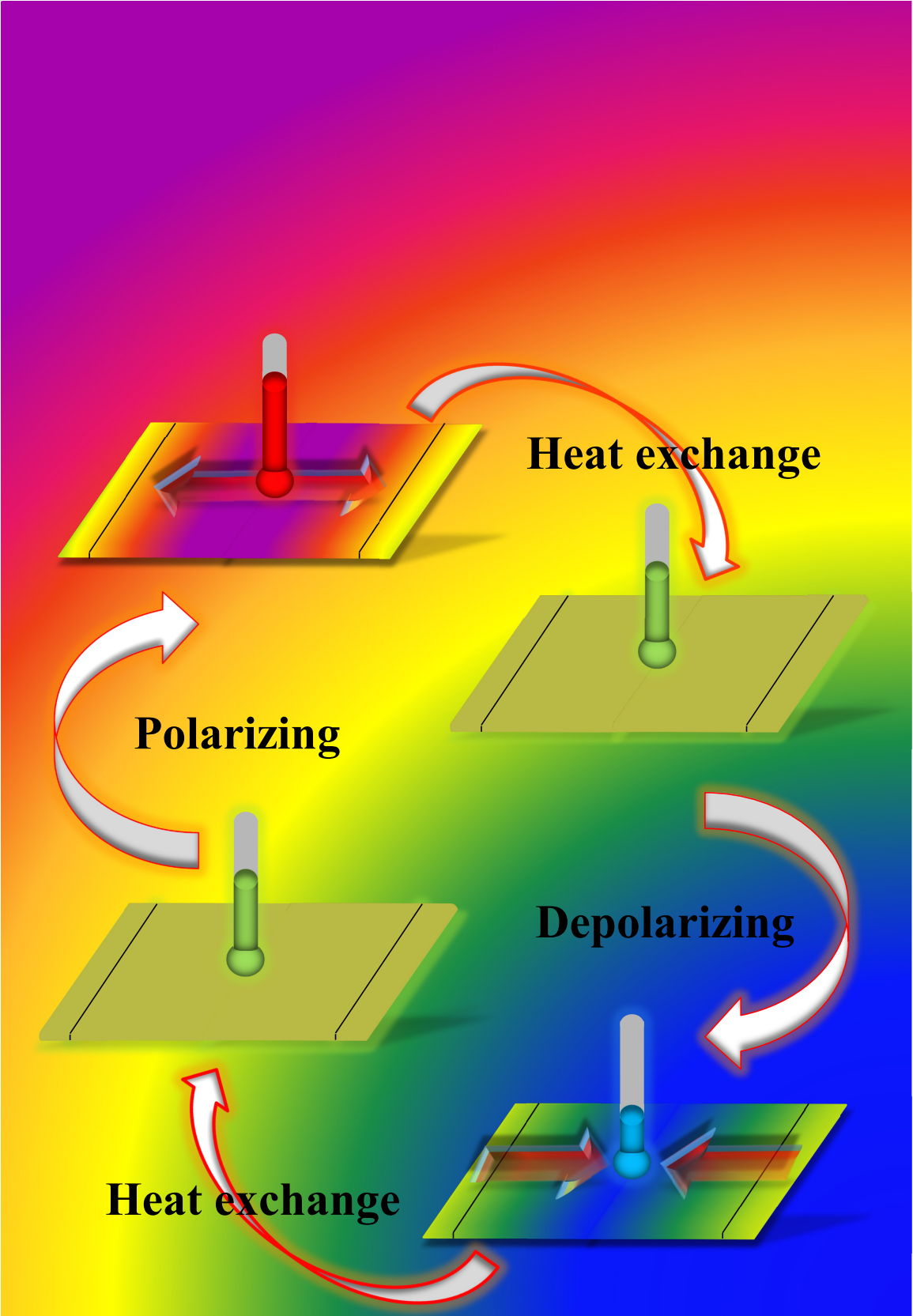


Figure 4.30: A sketch of Brayton-like electrocaloric refrigeration cycle using MLCs.

Obviously, electrocaloric performances of MLCs such as the magnitude of electrocaloric effect, thermal conductivity need to be further optimized to design an efficient prototype for practical applications. For instance, it was reported that MLCs with thinner electrocaloric layer thickness (around 1 μm) can permit high temperature change up to 7.2 K under an ultrahigh electric field of 800 kV/cm at 60 °C [209, 210]. Substitution of the BaTiO₃-based ceramics by inorganic relaxors [206], polymers [119], antiferroelectric [51], multiferroic [353] or composite materials [52, 214, 216, 334] would be desired. Mechanical stress [49, 50, 64, 165] and pressure [209, 210] may also be useful to tune the electrocaloric properties. Geometrical optimization [232] may be useful to improve the cooling powers of devices taking into account Joule heating associated with leakage and the thermal coupling of the device to the environment [127, 235]. Further evidence of the cooling efficiency [354, 355] and coefficient of performance (*COP*) [117] is also desired in future studies. IR camera can be a very powerful tool to testify all these possible optimizations.

4.7 SUMMARY

In summary, we have reported direct IR measurements on the uniformity and quality of electrocaloric effect in MLCs as a function of the amplitude and frequency of voltage pulses at room temperature. Our experimental findings not only evidence the large variation in electrocaloric response across the MLCs for the first time, but also demonstrate the advance of IR imaging in precisely probing the electrocaloric heat flux and the local electrocaloric performances. Our results highlight the promise of IR imaging in correlating the electrocaloric effect and heat flux with structural degrees of freedom and invite future direct measurements by this sensitive technique.

- CHAPTER 5 -

ELASTOCALORIC EFFECT IN FERROELECTRICS

In this chapter, we present our theoretical results on elastocaloric effect in ferroelectric thin films (Section 5.1 and Section 5.2) and single crystals (Section 5.3). Together with recent predictions derived from first-principles calculations [19, 49], our findings calculated by phenomenological approaches provides straightforward and simple physical guideline to experimental measurements.

5.1 ELASTOCALORIC EFFECT IN ULTRATHIN FERROELECTRIC FILMS NEAR ROOM TEMPERATURE

In this Section 5.1, we will show our results on elastocaloric effect in environmentally friendly ultrathin BTO capacitors. These capacitors can exhibit a giant stress-induced elastocaloric effect without hysteresis loss or Joule heating. By combining this novel elastocaloric effect with the intrinsic electrocaloric effect, an ideal refrigeration cycle with high performance (temperature change over 10 K with a wide working-temperature window of 60 K) at room temperature is proposed for future cooling applications.

5.1.1 Thermodynamical model

We considered a multilayer of ultrathin BTO capacitors grown on thick (001) STO cubic substrates as shown in Fig. 5.1. To simplify, we focused our study on a unique monolayer capacitor. Each ultrathin capacitor is made of a short-circuited (001) single-domain BTO film of thickness h sandwiched between two identical SRO electrodes. We restricted ourselves to the case of a uniform local loading σ_3 applied along the z direction, whereas the shear stresses σ_4 and σ_5 were neglected [321]. The uniform stress applied onto the top surface of ultrathin capacitors therefore rules out the flexoelectric effect caused by strain gradients [322]. According to the phase diagram of epitaxial BTO films subjected to a uniaxial stress [321], only the transition from the paraelectric phase ($P_x=P_y=P_z=0$) to the ferroelectric tetragonal phase ($P_x=P_y=0, P=P_z\neq 0$) is allowed

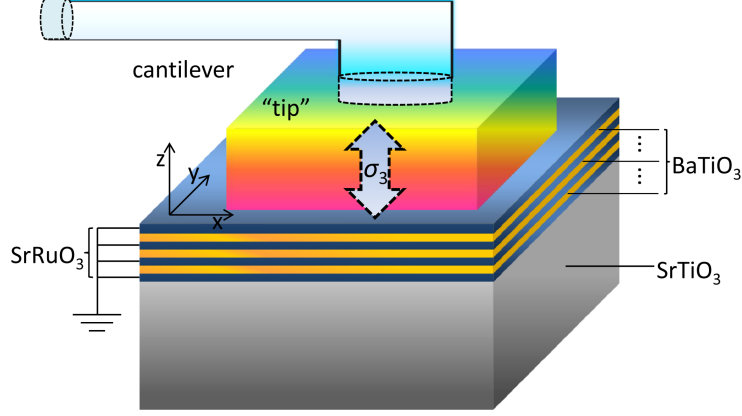


Figure 5.1: Schematic of a uniform loading σ_3 applied onto the ultrathin epitaxial SRO/BTO/SRO multilayer capacitors grown on a STO substrate.

near room temperature and is considered in this work. By taking into account the mechanical and electrical boundary conditions, we developed a multiscale thermodynamic model [271] that combines first-principles calculations and phenomenological theory (see Section 3.1.1.2). This model was already successfully used to explain size effects [200, 271] (see Section 3.1.1) and predict the giant electrocaloric effect [47, 201] (see Section 3.1.2 and Section 3.1.3) in ultrathin BTO-based capacitors. Most importantly, we checked that the unloaded thermal expansion coefficient α_0^E and Poisson's ratio ν at room temperature are in good agreement with recent theoretical and experimental results [356–358] (see Section 5.1.2), which further supports the validity of our approach.

The modified free energy per unit surface of the ferroelectric film can be expressed as:

$$\begin{aligned}
 F &= h\Phi + \Phi_S = \left[\frac{1}{2}\alpha_1^*P^2 + \frac{1}{4}\alpha_{11}^*P^4 + \frac{1}{6}\alpha_{111}P^6 + \frac{1}{8}\alpha_{1111}P^8 \right. \\
 &\quad \left. - \frac{1}{2}\vec{E}_{dep} \cdot \vec{P} + \frac{(u_m - S_{12}\sigma_3)^2}{S_{11} + S_{12}} - \frac{1}{2}S_{11}\sigma_3^2 \right] h + \eta P^2,
 \end{aligned} \tag{5.1}$$

where

$$\alpha_1^* = \alpha_1 - \frac{4Q_{12}}{S_{11} + S_{12}}u_m - 2\left(Q_{11} - \frac{2Q_{12}S_{12}}{S_{11} + S_{12}}\right)\sigma_3, \tag{5.2}$$

$$\alpha_{11}^* = \alpha_{11} + \frac{4Q_{12}^2}{S_{11} + S_{12}} \tag{5.3}$$

are the renormalized Landau coefficients. α_{ijkl} are the dielectric stiffness coefficients at constant stress, and only α_1 is temperature dependent through the Curie-Weiss law $\alpha_1 = (T - T_0)/\varepsilon_0 C$,

with T_0 and C being the Curie-Weiss temperature and constant, respectively. η is the quadratic coefficient of the surface energy Φ_S expansion for ferroelectric/electrode interfaces. S_{mn} and Q_{mn} are the elastic compliances and the electrostrictive coefficients of the films, respectively. u_m , which is the misfit strain caused by the lattice mismatch (u_0) and the substrate deformations (Δu_m), can be written as: [321]

$$\begin{aligned} u_m &= u_0 + \Delta u_m = (a_s - a_0)/a_s + A\sigma_3, \\ A &= s_{12} + (s_{11} - 2s_{12})(s_{11} + s_{12})/s_{11}, \end{aligned} \quad (5.4)$$

where a_s is the substrate effective lattice constant, and a_0 is the equivalent cubic cell constant of the free standing film. s_{mn} are the elastic compliances of cubic substrate. \vec{E}_{dep} is the depolarizing field which can be determined from the short-circuit condition:

$$\vec{E}_{dep} = -\frac{2\lambda}{h\varepsilon_0 + 2\lambda\varepsilon_b}\vec{P}, \quad (5.5)$$

where ε_b is the background dielectric constant, and ε_0 is the permittivity of free space. λ is the effective screening length of the BTO/SRO interface.

The equilibrium strain u_3 and polarization P_0 can be derived from the condition of thermodynamic equilibrium: $\frac{1}{h}\partial F/\partial\sigma_3 = -u_3$, $\frac{1}{h}\partial F/\partial P = 0$. u_3 can be obtained as follows

$$\begin{aligned} u_3 &= \left[S_{11} - \frac{2(A - S_{12})^2}{S_{11} + S_{12}} \right] \sigma_3 - \frac{2(A - S_{12})}{S_{11} + S_{12}} u_0 \\ &\quad - \frac{1}{2} \left(\frac{4AQ_{12}}{S_{11} + S_{12}} - 2Q_{11} + \frac{4S_{12}Q_{12}}{S_{11} + S_{12}} \right) P_0^2. \end{aligned} \quad (5.6)$$

For the case of asymmetric ferroelectric/electrode interfaces, the built-in electric field and surface effects can be incorporated [200, 271].

The elastocaloric change in temperature ΔT_{σ_3} upon application of a stress field in adiabatic conditions can be determined by Eq. (1.25) such that:

$$\Delta T_{\sigma_3} = - \int_0^{\sigma_3} \frac{T}{C_{\sigma_3}} \left(\frac{\partial u_3}{\partial T} \right)_{\sigma_3, E} d\sigma_3, \quad (5.7)$$

where the Maxwell relation $(\frac{\partial S}{\partial\sigma_3})_{E, T} = (\frac{\partial u_3}{\partial T})_{\sigma_3, E} = \alpha^E$ is used. S is the entropy and C_{σ_3} is the heat capacity under constant stress σ_3 . α^E is the coefficient for thermal expansion which is the same as that $(\frac{\partial S}{\partial\sigma_3})_{E, T}$ for the piezocaloric effect. All the parameters we used are the same as previous sections.

We note that the Landau potential coefficients α_{ijkl} used here are obtained at zero pressure/stress [283] (see Table. 3.1). However, to accurately describe the pressure/stress dependence of ferroelectric transition, one has to consider carefully that some Landau coefficients may be pressure/stress dependent [359, 360]. Fortunately, when solving the particular transition from paraelectric phase to ferroelectric tetragonal phase, the respective results calculated by pressure/stress dependent [359, 360] and independent Landau coefficients [283] are exactly the same and are both in good agreement with experimental data [361] as long as the magnitude of pressure/stress is below 6.5 GPa [360]. Therefore, our approach based on the zero pressure/stress

Landau coefficients is valid in this particular case. Further studies should take into account the pressure/stress-dependent Landau coefficients and quantum saturation of the order parameter at low temperatures [359, 360]. The approach in describing the elastocaloric and electrocaloric effects used in this work is a well-known indirect method [15, 46, 61, 84, 123, 306] mainly based on Maxwell relationships. Indeed, there is still debate on the validity of this method. While the indirect method may not necessarily yield reliable basis for electrocaloric response in the so-called relaxor ferroelectrics [149, 150, 163], it is demonstrated to be appropriate in case of normal ferroelectrics [48, 84, 100, 177, 317]. Even for the normal ferroelectrics, one should also be careful using the Maxwell relations near first order phase transition because as we mentioned above, such kind of transition is not thermodynamically reversible, while the Maxwell relations are derived from reversible thermodynamic process. Nevertheless, in our case the second order phase transition is ideally reversible which supports our approach in addition to previously emphasized agreements with the experimental results.

In addition, only a homogeneously uniaxial stress is considered in this study. Indeed, strain inhomogeneity in a loaded film especially near the edge of tip/film interface exists and this effect becomes increasingly more significant as the film thickness decreases to only a few nanometers [322]. In this case, our work represents a necessary first step in the development of the general nonlinear theory to describe elastocaloric effect in ultrathin films. Further works should be done including the effect of flexoelectricity in the future.

5.1.2 Thermal expansion coefficient and Poisson's ratio

Figure 5.2(a) displays the theoretical results of thermal expansion coefficient α^E at different stress fields for different film thicknesses. We note that α^E calculated here is the thermal expansion along z direction while the contribution of in-plane thermal expansion has been already included in the misfit strain u_m . To be specific, for epitaxial films, thermal strain arising from the small difference in the thermal expansion coefficients of BTO film and STO substrate as the film is cooled from deposition temperature to room temperature, is already included in u_m in the unloaded condition (u_0) is defined as the difference in the lattice parameters of the film and the substrate. Since the contribution of thermal strain is very small in this case [309], in addition to the relatively small temperature change (60 K), u_0 and therefore u_m in loaded cases can remain almost constant versus temperature. It can be seen that compared with that under the unloaded condition ($\sigma_3 = 0$ GPa), α^E experiences a much more drastic reduction with increasing the strength of compressive stress compared with the enhancement induced by increasing the tensile stress. Such large changes in α^E indicate that large elastocaloric (piezocaloric) effects can be achieved, which further supports our data obtained in Fig. 5.3(c). Moreover, the reduction of α^E becomes particularly sharp near the critical stress field σ_{3c} .

The interest here is that we may make direct comparison with experimental results of the thermal expansion coefficient α_0^E at zero stress field. Figure 5.2(b) shows that $|\alpha_0^E|$ decreases monotonically as the film thickness increases with a plateau above 3.6 nm. While we are not aware of any experimental studies of thermal expansion coefficient of ultrathin BTO films, our computational findings can be qualitatively compared to the experimental data in BTO ceramics and powder. The thickness-dependent α_0^E as shown in Fig. 5.2(b) is due to the structure change

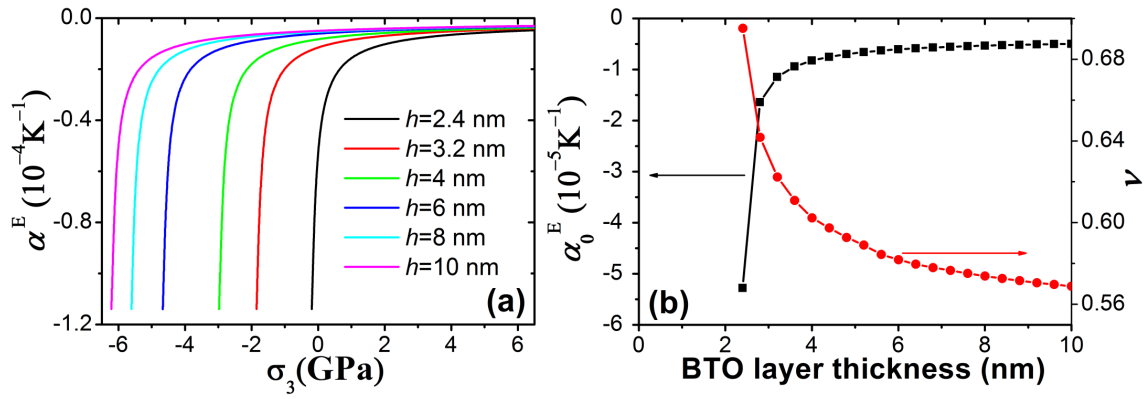


Figure 5.2: (a) The stress-dependent thermal expansion coefficient α^E for different film thicknesses at room temperature; The thickness-dependent thermal expansion coefficient α_0^E and the Poisson coefficient ν in the unloaded case ($\sigma_3 = 0$ GPa) at room temperature.

from tetragonal phase to cubic phase, which is in line with the experimental results. To be more specific, for $h = 10$ nm, the $|\alpha_0^E|$ value is about $4.98 \times 10^{-6} \text{ K}^{-1}$ which is in good agreement with $6.07 \times 10^{-6} \text{ K}^{-1}$ (Ref. [356]) and $7.55 \times 10^{-6} \text{ K}^{-1}$ (Ref. [357]) values obtained from experimental tetragonal BTO results. For the film thickness close to the critical thickness (2.4 nm) below which, e.g., 2 nm, ferroelectricity disappears at room temperature, $|\alpha_0^E|$ is significantly enhanced with its largest value about $5.29 \times 10^{-5} \text{ K}^{-1}$, which is more than one order of magnitude higher than that with $h = 10$ nm. For the thickness close to 2.4 nm, e.g., 2.8 nm, $|\alpha_0^E|$ is about $16.4 \times 10^{-6} \text{ K}^{-1}$ which is in the same range with the results obtained in cubic BTO structure, e.g., $12.88 \times 10^{-6} \text{ K}^{-1}$ (Ref. [356]) and $11.4 \times 10^{-6} \text{ K}^{-1}$ (Ref. [357]). This finding implies that size effect plays an important role in tuning the anisotropy of the thermal expansion between the out-of-plane and in-plane in ultrathin BTO films.

In addition, the Poisson's ratio defined as $\nu = -\frac{u_0}{u_3}$ in the unloaded case displays a monotonic rise with h decreasing, whereas the increase in ν becomes more dramatic for the BTO film thickness being close to the critical thickness (2.4 nm) [see Fig. 5.2(b)]. The approximated value of ν obtained far from the phase transition point ($h = 10$ nm) is 0.57, which is larger than experimental values developed in BTO single crystal (cubic) ~ 0.385 (Ref. [362]) and ceramics ~ 0.39 (Ref. [363]). However, it is smaller than the value of 0.65 predicted by first-principle calculations [358] in BTO thin films [We find that ν is 0.64 for $h = 2.8$ nm.].

5.1.3 Elastocaloric effect in ferroelectric ultrathin films

We first selected the BTO film at the desired thickness and temperature, and then we adiabatically applied a stress field σ_3 with a magnitude that continuously increased from 0 to 6.5 GPa for a tensile stress or decreased from 0 GPa to -6.5 GPa for a compressive stress. The stress was varied starting from 0 by incremental steps so that the system was always considered in quasistatic conditions. The maximum value of σ_3 used here was well below the local stress threshold (ca. 20 GPa) for irreversible plastic damage of the BTO surface [323]. For practical applications, we set the initial temperature at room temperature (300 K).

Figures. 5.3(a)-5.3(c) summarize the results of stress-dependent equilibrium polarization P_0 , strain u_3 , and adiabatic temperature change ΔT_{σ_3} , respectively. We evaluate the critical thickness $h_c \approx 2.4$ nm for $\sigma_3 = 0$ GPa, which is in good agreement with the value obtained from Raman spectroscopy [309]. Figure. 5.3(a) shows that there are two kinds of critical stress fields σ_{3c} at which the polarization either continuously disappears under application of compressive stress or continuously appears under tensile stress, depending on whether the initial unloaded BTO layer at room temperature is in its ferroelectric phase, i.e., for thickness larger than h_c or in its paraelectric phase, i.e., below h_c . The value of σ_{3c} decreases as that of h increases, which means that relatively thick BTO films can sustain their polarization within a much wider stress range. Here, the first-order-like stress-induced ferroelectric phase transition which was reported in bulk $\text{Ba}_{0.5}\text{Sr}_{0.5}\text{TiO}_3$ [19] was not found. Actually, the nature of the phase transition is transformed from first-order ($\alpha_{11}^* < 0$) to second-order-type ($\alpha_{11}^* > 0$) by the mechanical boundary conditions [see Eq. (5.3)]. The large change of polarization in response to applied stress, as shown in Fig. 5.3(a), is essentially due to the extreme sensitivity of the out-of-plane polarization to the in-plane misfit strain in BTO thin films [324, 364]. The strain sensitivity of polarization in

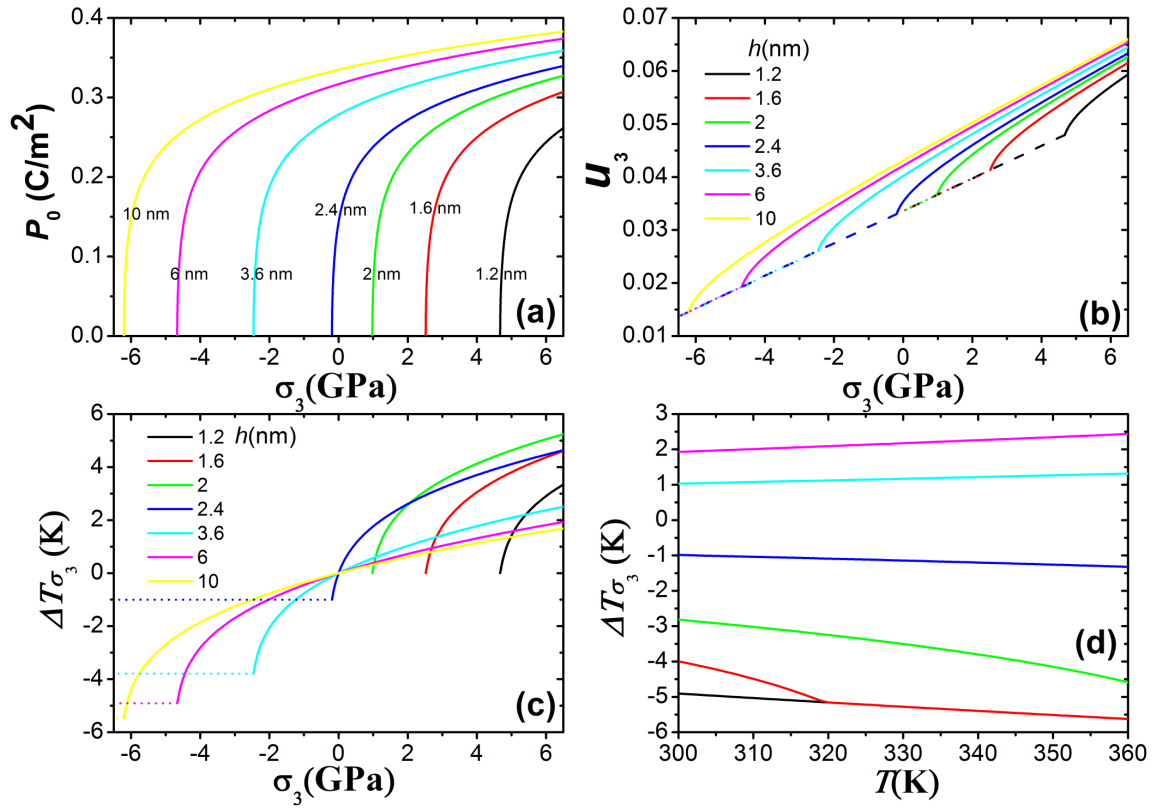


Figure 5.3: The dependence of (a) polarization P_0 , (b) strain u_3 , and (c) adiabatic temperature change ΔT_{σ_3} on the applied stress σ_3 with different BTO barrier thicknesses at room temperature; (d) dependence of ΔT_{σ_3} on the sample temperature T ($h=6$ nm). The different curves correspond to different stress values: from top to bottom the curves correspond to 6.5, 3, -2, -4, -4.5, and -5 GPa.

BTO films is much larger than that in PTO films [364]. As a result, the elastocaloric effect in PTO films is expected to be smaller under the same mechanical stimulus, which suggests that ecofriendly compound BTO is a better choice for higher elastocaloric performances than PTO.

Figure 5.3(b) shows the variation in strain u_3 at different applied stress fields. Surprisingly, the strain change Δu_3 induced by the uniform stress can be very large, much larger than those in other ferroelectrics such as $\text{Ba}_{0.5}\text{Sr}_{0.5}\text{TiO}_3$ alloys [19] and bulk PTO [49](see Table. 5.1). The equilibrium strain u_3 , according to Eq. (5.6) in Section 5.1.1, is composed of three parts: the direct stress-induced contribution which depends linearly on the applied stress and results in the large strain change as shown in Fig. 5.3(b); constant elastic strains (about 0.0336) to match the in-plane lattice parameters of the film to the substrate as well as the clamping effect of the substrate; and self-strains of the phase transition due to the coupling between strain and electrical polarization which contribute to the elastocaloric effect due to its temperature dependence.

The discontinuous strain change associated with the large latent heat at the first-order phase-transition point, i.e., ferromagnetic [59], martensitic [61–63, 86, 365], and ferroelastic/ferroelectric transition [19, 49], is the main origin of the giant elastocaloric effect when a material is subjected to an external mechanical stimulus. Shape-memory alloys are regarded as the most promising commercial materials due to their excellent ductility and broad elastocaloric temperature range [18]. However, as the size of current ferroelastic martensites shrinks towards the nanoscale, numerous problems and instability issues arise, including fatigue, microcracking, hysteresis, and so on [20]. Recently, reversible strains up to 14% driven by changes in temperature or electric field were observed in ferroelectric BiFeO_3 thin film [366], which demonstrated that an excellent superelasticity can be also realized in ferroelectric thin films. According to our calculations, a strain change of over 3.3% can be achieved by an ultrahigh stress of 6.5 GPa in BTO ultrathin films at room temperature. This large strain change may be considered as super-elasticity, which is over three times larger than those reported in superelastic BTO single crystal either (0.75%) induced by a low electric field of 2 kV/cm (Ref. [367]) or (0.85%) by a modest stress field of 15 MPa (Ref. [368]). The aforementioned large strain change Δu_3 [Fig. 5.3(b)] during the application of external stress indicates that a giant elastocaloric effect may also be obtained in ultrathin BTO capacitors. Moreover, this effect may therefore open a route to expand the elastocaloric family from the macroscopic to the nanoscale. The mechanism of elastocaloric effect here purely stems from the continuous changes of the strain, which is completely different from that in shape-memory alloys [61–63, 86, 365], and that in ferroelectric bulk [19, 49].

The existence of a giant elastocaloric effect in such capacitors is revealed in Fig. 5.3(c). The largest value of ΔT_{σ_3} found at 300 K is 5.5 K for $h = 10$ nm and $\sigma_3 = -6.5$ GPa, which is much larger than any electrocaloric temperature change reported in bulk BTO and relatively thick BTO films at room temperature [48, 209, 306]. The entropy change is moderate at about 8 J/K kg. Such findings clearly indicate that applied stress may be an effective tool for cooling/heating applications especially in ferroelectric ultrathin films. In addition, tensile stress can increase the sample temperature, while compressive stress tends to decrease it, which implies that both conventional (positive) and inverse (negative) elastocaloric effects can be achieved in our capacitors. This effect can be well understood in polarization versus stress curves shown in Fig. 5.3(a). The

Table 5.1: Comparison of elastocaloric properties of ultrathin BTO capacitors developed here with those in the literature.

| Material | T [K] | u_3 (no σ_3) | $\Delta\sigma_3$ [GPa] | Δu_3 [1] | $\Delta u_3/\Delta\sigma_3$ [1/GPa] | ΔT_{σ_3} [K] | $\Delta T_{\sigma_3}/\Delta\sigma_3$ [K/GPa] | Refs |
|--|------------|---------------------------|---------------------------|---------------------|--|------------------------------|---|------|
| Cu-Zn-Al | 300 | ~ 0.002 | 0.12 | 0.080 | 0.667 | 15 | 125 | [61] |
| Ba _{0.5} Sr _{0.5} TiO ₃ | 260 | ~ 0 | 1 | 0.012 | 0.012 | 9 | 9 | [19] |
| PTO | 700 | 0.004 | 1 | 0.011 | 0.011 | 20 | 20 | [49] |
| BTO (2.4 nm) | 300 | 0.0336 | 6.5 | 0.030 | 0.004 | 4.6 | 0.7 | Here |

sign of the elastocaloric effect can be effectively controlled by the direction of the applied stress field, which can be used to enhance elastocaloric efficiency by appropriately combining conventional and inverse elastocaloric effects for a given capacitor. Inverse elastocaloric effect can only take place when σ_{3c} is negative or for thicknesses $h \geq 2.4$ nm [see Fig. 5.3(c)]. Below the critical σ_{3c} value, there is no extra temperature change due to the disappearance of the ferroelectric phase, which is very similar to the elastocaloric effect predicted in bulk PTO [49]. Additionally, Figure. 5.3(c) shows that thinner films are more sensitive to tensile stress for obtaining a large temperature change, while thicker ones show larger sensitivity to compressive loading.

Comparison of ΔT_{σ_3} in ultrathin BTO capacitors with other typical elastocaloric materials is shown in Table. 5.1. The values of ΔT_{σ_3} and elastocaloric strength $\Delta T_{\sigma_3}/\Delta\sigma_3$ found in this study [4.6 K and 0.7 K/GPa ($h=2.4$ nm, $\Delta\sigma_3=6.5$ GPa)] are the smallest among the selected elastocaloric materials, which is in line with the second-order transition nature [88]. However, ultrathin BTO capacitors allow working at room temperature, which is therefore more favorable than bulk PTO with a higher operating temperature (ca. 700 K) [49]. Moreover, though Cu-Zn-Al alloys [61] and Ba_{0.5}Sr_{0.5}TiO₃ alloys [19] can also operate near room temperature, hysteresis losses associated with their first-order phase transitions are detrimental as irreversibilities related to hysteresis reduce the cooling efficiency of the material [8, 11, 18, 32]. For instance, a typical value of the hysteresis loss of Cu-Zn-Al alloys was reported to be about 0.6 MJ/m³ (Ref. [63]), which is comparable with their refrigeration capacity (2.5 MJ/m³ in Ref. [74] or 1.6 MJ/m³ in Ref. [63]). Moreover, even the energy dissipation can be reduced to be relatively small at the first few cooling cycles by using a second-order-like phase transition [63], e.g., 0.04 MJ/m³ (Ref. [63]); the total loss may still be extremely large as a cycle number of the order of 1×10^9 is required for cooling applications. In this sense, the second-order transition nature of ultrathin SRO/BTO/SRO capacitors may naturally solve this drawback (Table. 5.2). While more effort is thus made to address cyclic stability and fatigue in shape-memory alloys [62, 63, 86, 365], regarding the ferroelectric films, ultrathin BTO films have a remarkable fatigue endurance up to over 1×10^9 cycles of electric switching [369]. Therefore, our proposed elastocaloric system may be suitable for mechanical cyclic stability due to the strong coupling between polarization and strain in ferroelectrics. Additionally, no Joule heating accompanies the elastocaloric effect (Table. 5.2).

The important criteria for a stress-driven caloric device are paradoxically both hysteresis and

Table 5.2: Comparison of different caloric effects in selected materials.

| Material ^{a)} | ΔT [K] | (1) ^{b)} | (2) ^{c)} | (3) ^{d)} | (4) ^{e)} | (5) ^{f)} | (6) ^{g)} | Total |
|--|----------------|-------------------|-------------------|-------------------|-------------------|-------------------|-------------------|---------|
| Gd ^H | 20 | + | + | + | + | + | - | 5[88] |
| Gd ₅ Sr ₂ Ge ₂ ^H | 15 | + | - | - | + | + | + | 4[9] |
| MnAs _{1-x} Sb _x ^H | 13 | + | - | - | + | - | - | 2[30] |
| La(Fe _{0.89} Si _{0.11}) ₁₃ H _{1.3} ^H | 6.9 | + | - | - | + | + | + | 4[33] |
| PLZT ^{E, h)} | 40 | + | + | - | - | - | - | 2[15] |
| P(VDF-TrFE) _{68/32} ^E | 20 | + | - | - | - | + | - | 2[46] |
| Ba _{0.5} Sr _{0.5} TiO ₃ ^E | 12 | + | + | - | - | + | + | 4[177] |
| BaTiO ₃ ^E | 5.8 | + | + | + | - | + | + | 5[47] |
| Ni _{49.26} Mn _{36.08} In _{14.66} ^p | 4.5 | + | - | - | + | + | + | 4[69] |
| LaFe _{11.33} Co _{0.47} Si _{1.2} ^p | 2.2 | - | - | - | + | + | + | 3[71] |
| Gd ₅ Sr ₂ Ge ₂ ^p | 1.3 | + | - | - | + | + | + | 4[74] |
| Cu _{68.13} Zn _{15.74} Al _{16.13} ^σ | 15 | + | + | - | + | + | - | 4[61] |
| Ba _{0.5} Sr _{0.5} TiO ₃ ^σ | 9 | + | + | - | + | + | + | 5[19] |
| PbTiO ₃ ^σ | 20 | - | + | - | + | - | + | 3[49] |
| BaTiO ₃ ^σ | 5.5 | + | + | + | + | + | + | 6[Here] |

^{a)} *H*, *E*, *p* and σ indicate electrocaloric, magnetocaloric, barocaloric, and elastocaloric effects, respectively; ^{b)} (1) working temperature: near room temperature (+) or high/low temperature (-); ^{c)} (2) wide (+) or narrow (-) working temperature range; ^{d)} (3) without (+) or with (-) hysteresis loss; ^{e)} (4) without (+) or with (-) Joule heating; ^{f)} (5) ecofriendly (+) or not (-); ^{g)} (6) bicaloric cycles (+) or single caloric cycles (-); ^{h)} PLZT refers to (Pb_{0.86}La_{0.08})(Zr_{0.65}Ti_{0.35})O₃.

the lack of it: the material should lack thermal hysteresis (that is, its phase transition should be second-order) to minimize any latent heat. In that way the cooling cycle is optimized by running through the phase-transition temperature. However, ideally there should be strong stress-strain hysteresis to optimize the Carnot-like cooling cycle. Large hysteresis losses can be reduced significantly by doping [32], using multiresponse to different external stimuli [8, 11, 18], enhancing crystallographic compatibility between different phases [86], using a second-order-like phase transition [63], and so on. Moreover, the hysteretic losses may be completely eliminated by using a second-order phase transition as suggested herein. The second-order phase transition entails a smaller temperature even under a large stimulus, which is similar to the strategies of doping [32] and using a second-order-like transition [63].

Figure 5.3(d) shows elastocaloric temperature change ΔT_{σ_3} as a function of the initial temperature T (300-360 K) for $h = 6$ nm. The results for other film thicknesses can be found in Fig. 5.4. It can be clearly seen that ΔT_{σ_3} is non-sensitive to initial temperature (from 300 to 360 K) for different BTO thicknesses, which implies an extremely wide window of operational temperatures in ultrathin SRO/BTO/SRO capacitors. It is found that the largest value of ΔT_{σ_3} under tensile stress is about 6.1 K at 360 K for $h = 2$ nm in Fig. 5.4(b) while the smallest ΔT_{σ_3} under compressive loading is about 6.4 K at 360 K for $h = 10$ nm in Fig. 5.4(d). As the compressive stress decreases to below σ_{3c} , there is no additional change in ΔT_{σ_3} at different temperatures.

5.1.4 Ideal refrigeration cycle

Therefore, as well as their potential as non-volatile memories, [244, 322, 324] ultrathin ferroelectric films also demonstrate exciting perspectives for cooling applications. By taking all the aforementioned features we can propose an ideal refrigeration by pressure cycling as illustrated in Fig. 5.5. The cycle begins (step 1 or initial) by applying (increasing) a tensile stress field $\sigma_3 > 0$ GPa adiabatically, which is followed by a heat transfer to an external source at which σ_3 is kept constant (step 2). At step 3, the tensile σ_3 is removed (decreased) adiabatically, which results in a drop of the temperature due to the positive elastocaloric effect. Then a compressive stress field $\sigma_3 < 0$ GPa is adiabatically applied (by increasing the strength) that produces an additional drop of the temperature due to the negative elastocaloric effect (step 4), which is followed by a heat exchange with the external source under constant $\sigma_3 (\leq \sigma_{3c})$ (step 5). After step 4, a total change in temperature of about 6.8 K can be achieved ($h = 6$ nm). The cycle closes by means of adiabatic removal (decrease of the strength) of the compressive σ_3 , which results in the increase of the temperature due to the negative elastocaloric effect (step 6). During the elastocaloric refrigeration cycle, the electrocaloric effect can also be added, especially after step 5: the polarization is zero under the stress $\sigma_3 \leq \sigma_{3c}$ [see Fig. 5.3(a)], therefore even adiabatic application of a modest electric field can polarize the ultrathin film and induce a giant electrocaloric effect (see Fig. 5.6). Moreover, compared with the unloaded case, a significantly enhanced electrocaloric effect can be achieved in ultrathin BTO capacitors under compressive stress [166] (or see Section 3.1.4).

Figure 5.6 displays the proposed electrocaloric effect which can be added after step 5 in the elastocaloric refrigeration cycle shown in Fig. 5.5. Detailed calculations and analyses can be found in Section 3.1.4. In particular, here we choose a 6-nm-thick BTO film as an example,

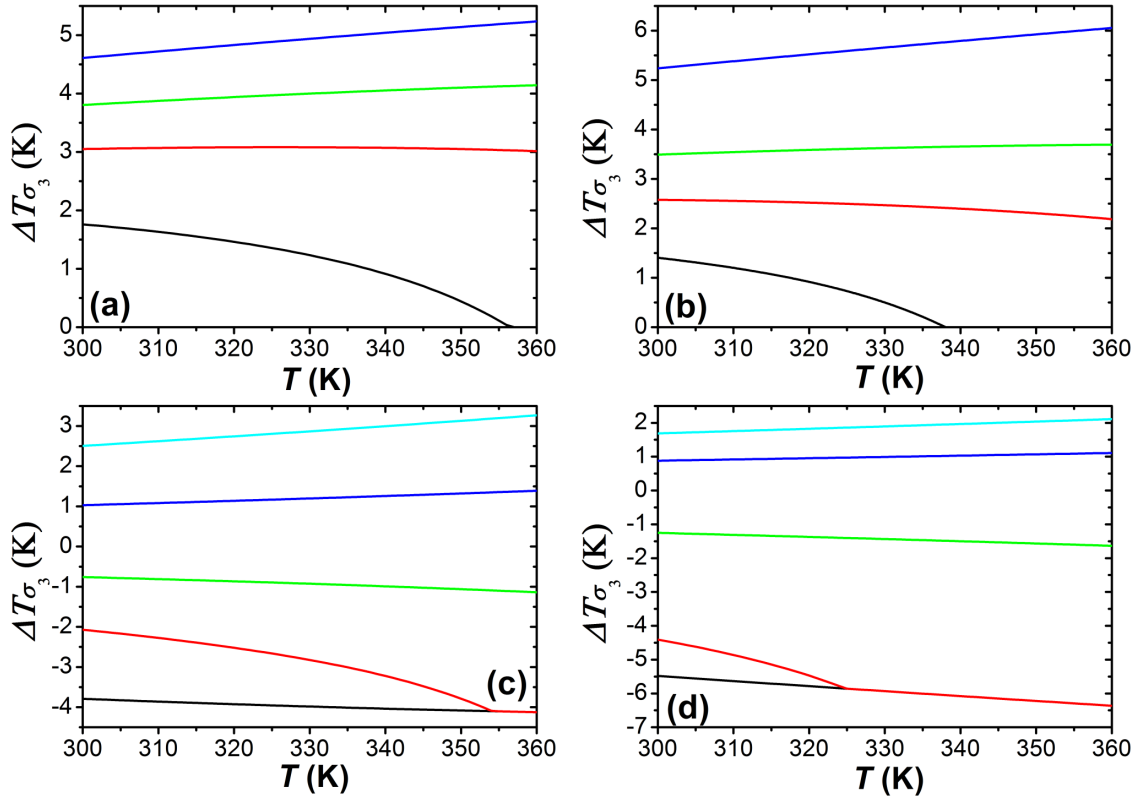


Figure 5.4: The dependence of the elastocaloric change in temperature ΔT_{σ_3} on the initial temperature T of the ultrathin epitaxial SRO/BTO/SRO capacitors with different BTO film thicknesses: (a) $h = 1.6$ nm; (b) $h = 2$ nm; (c) $h = 3.6$ nm and (d) $h = 10$ nm, respectively. Different curves correspond to different stress fields applied: from top to bottom the curves correspond to 6.5, 5, 4 and 3 GPa in (a); 6.5, 3, 2 and 1.3 GPa in (b); 6.5, 2, -1, -2, and -2.5 GPa in (c); 6.5, 3, -3, -6 and -6.5 GPa in (d). The stress is varied progressively being always in quasi-static conditions.

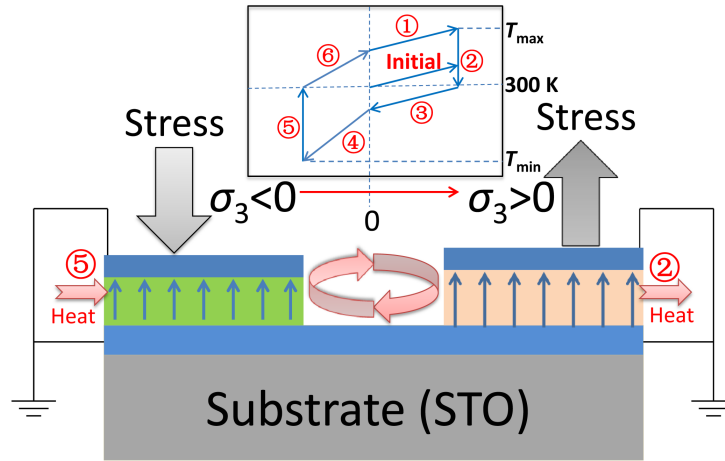


Figure 5.5: Ideal refrigeration cycle that uses both conventional (positive) and inverse (negative) elasto-caloric effects.

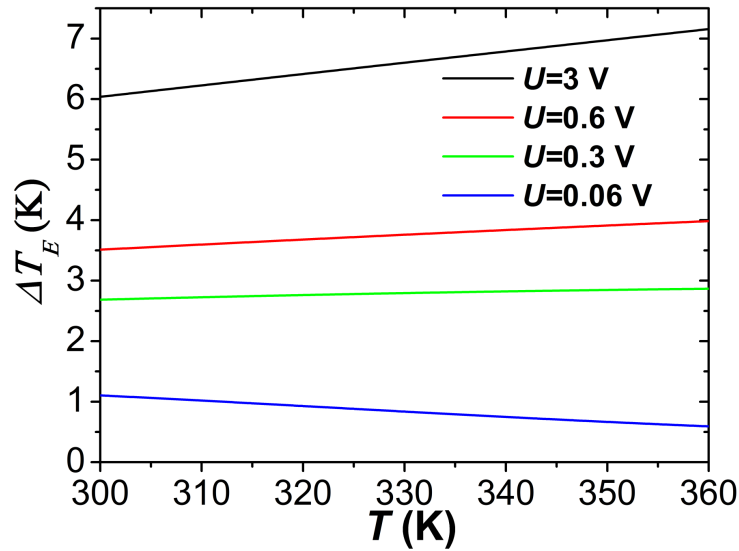


Figure 5.6: The adiabatic electrocaloric temperature ΔT_E in response to the external applied voltages $U = \Delta E h$ as a function of working temperature T for ultrathin epitaxial SRO/BTO/SRO capacitors ($h = 6$ nm) under a compressive stress of -5 GPa.

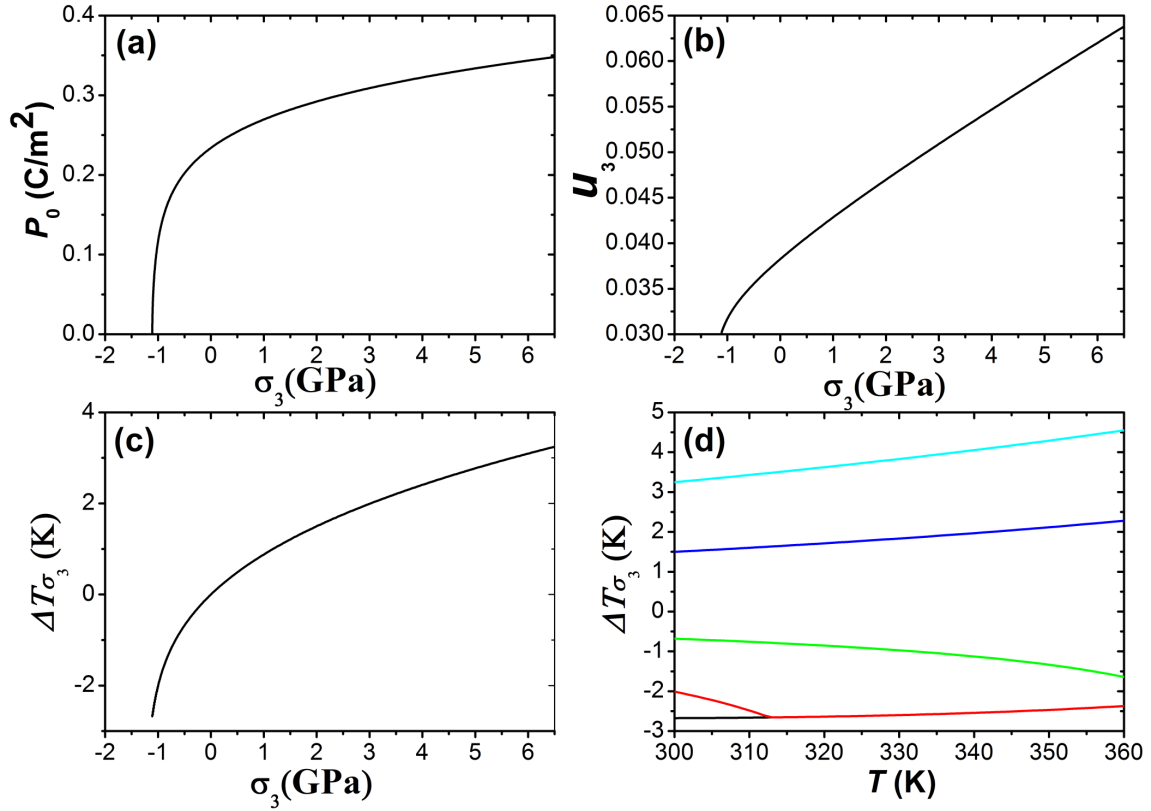


Figure 5.7: The dependence of (a) polarization P_0 , (b) strain u_3 , and (c) adiabatic temperature change ΔT_{σ_3} on the applied stress σ_3 in ultrathin epitaxial SRO/BTO/SRO capacitors ($h = 2.8$ nm); The dependence of the elastocaloric temperature change on the initial temperature T of the ultrathin epitaxial SRO/BTO/SRO capacitors ($h = 2.8$ nm). Different curves correspond to different stress fields applied: from top to bottom the curves correspond to 6.5, 2, -0.5, -1 and -1.5 GPa in (d). The stress is varied progressively being always in quasi-static conditions.

and the corresponding critical stress field σ_{3c} at room temperature is about -5 GPa according to Fig. 5.3. Joule heating can be negligible because the experimental resistance variations caused by fatigue were not observed even after many writing cycles in ultrathin BTO films [247]. After step 5, the polarization becomes zero ($\sigma_3 \leq \sigma_{3c}$), and therefore even a modest electric field can polarize the material again and should result in a remarkable electrocaloric effect. As expected, it is found that the adiabatical electrocaloric temperature ΔT_E can reach more than 6 K under a typical writing voltage of 3 V at room temperature, which is significantly enhanced compared with the unloaded films (2.6 K) under the same conditions [47]. Just like the elastocaloric counterpart, it is shown that the giant electrocaloric effect exists in a wide range of temperatures which is in line with our previous results under the unloaded conditions [47]. Together with the foregoing combination of both positive and negative elastocaloric responses (6.8 K, $h=6$ nm), the total temperature change of about 12.8 K can be achieved which is indeed in the range of temperature changes for other giant caloric effects as shown in Table. 5.2. Therefore, the total refrigerant efficiency can be further improved by including an additional electrocaloric effect and we believe that the proposed mechanism of bicaloric cycles by adequately combining electrocaloric and elastocaloric effects in the same material could lead to new routes for achieving room temperature solid-state refrigeration.

As a result, the total temperature change can be then further enhanced to reach a value of about 12.8 K or even more, which is indeed in the range of temperature changes for other giant caloric effects as shown in Table. 5.2. In addition, our study reveals that appropriate combinations of induced-phase transitions by stress and electric fields can be used to overcome the strict upper bounds in polar dielectrics [49]. Even for relatively weaker applied stresses, a large $\Delta T_{\sigma_3} \approx 2.7$ K can be still achieved by selecting useful film thickness (see Fig. 5.7). In order to illustrate the relatively large elastocaloric responses which can be achieved even under small stress fields, we select three different BTO thicknesses whereas the critical stress field σ_{3c} is near to 0 GPa. It is found that ΔT_{σ_3} can still reach a relatively large value of about -2.7 K for $h = 2.8$ nm and $\sigma_3 = -1.5$ GPa [see Fig. 5.7(c)]. Our proposed refrigeration cycle that combines both electrocaloric and elastocaloric effects in one material is different from those reported by Ponomareva and Lisenkov [19, 49].

5.1.5 Comments on elastocaloric effect

The aim of the present work is to theoretically demonstrate the giant elastocaloric effect in ferroelectric thin films for the first time. Generally, only a small force would be required to drive the elastocaloric effect in thin films, just as its electrocaloric counterpart is reported in thin films in which only a small voltage is required [15]. The relevant figure of merit for practical applications depends on the external force applied rather than the stress field generated [8, 18], which supports our assertion that our proposed multicaloric cycle in Fig. 5.5 is promising for designing real cooling devices in the future. We recognize that the findings in this study require further consideration, for instance, the schematic shown in Fig. 5.1 likely needs some technical issues addressing, such as to avoid the thermal leak between the “tip”/substrate and ferroelectric films [15]. An appreciable piezocaloric effect is still anticipated taking into account the contributions of flexoelectricity since two external stimuli (a uniform stress and strain gradient-

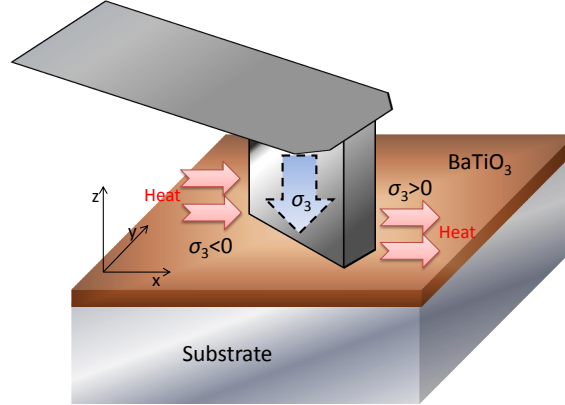


Figure 5.8: Schematic of a uniform loading σ_3 applied onto the ultrathin epitaxial SRO/BTO/SRO capacitor grown on a compressive substrate.

induced flexoelectricity) can both remarkably tune the magnitude of polarization in ferroelectric ultrathin films [321, 322]. While further discussions of any practical engineering of elastocaloric devices are far beyond the scope of this study, we suggest that experiments should first be made in the future to confirm our predictions.

5.2 INFLUENCE OF EPITAXIAL STRAIN ON ELASTOCALORIC EFFECT IN FERROELECTRIC THIN FILMS

We have predicted ferroelastic ferroelectric thin films can hold remarkable elastocaloric properties in previous Section 5.1 comparable with ferroelastic martensites [61–63, 86, 365], which further expands the elastocaloric family. Indeed, issues of latent heat, size effect, fatigue in ferroelastic elastocalorics have attracted more attention [7]. For instance, it was reported that the hysteresis loss can be lowered in Fe-Pd single crystal exhibiting a second-order like martensitic transition [63]. In addition, as the size of current shape-memory alloys shrinks towards the nano-scale, numerous problems and instabilities arise, including fatigue, micro-cracking and oxidation [20]. In this regard, ferroelectric thin films may have potential advantages [366]. Moreover, changing the mechanical boundary conditions by varying the epitaxial misfit strain can remarkably affect the phase transition, which may be helpful to tune the elastocaloric properties of ferroelectric thin films [123, 306, 324, 370, 371]. This is of great interest and importance to design the elastocaloric cooling devices in the future and therefore motivates us to study the elastocaloric effect in ferroelectric thin films under the influence of epitaxial strain.

We consider (001) BTO films epitaxially grown on several compressive substrates, namely

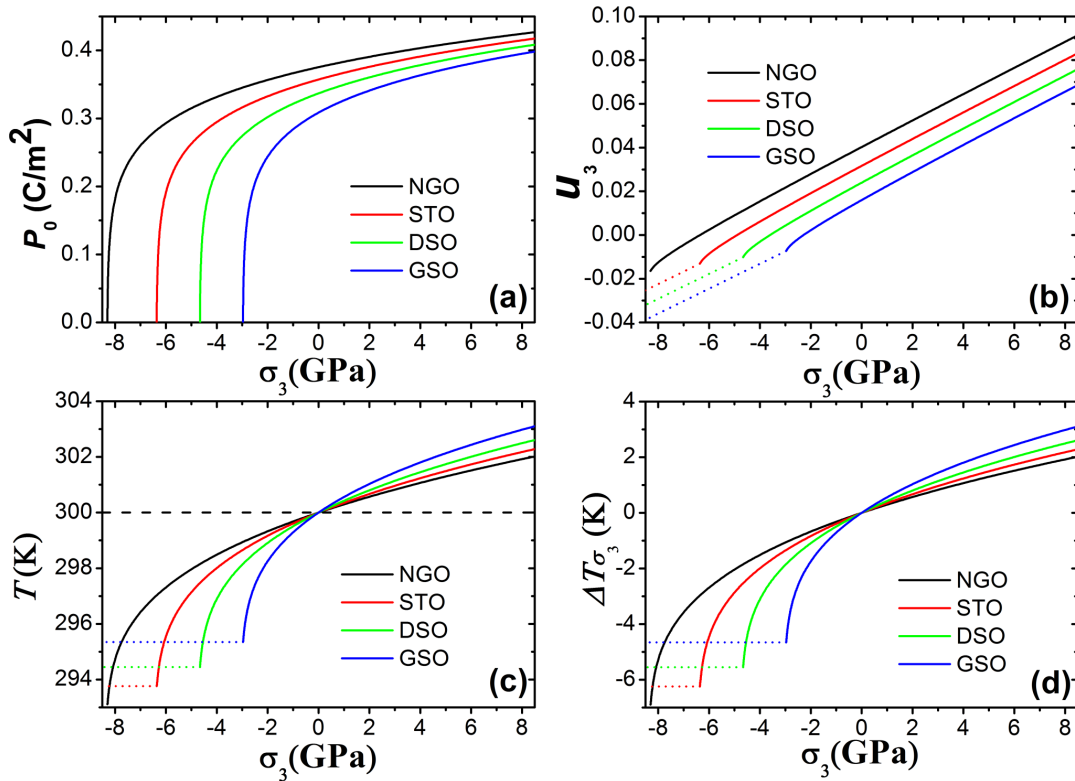


Figure 5.9: The dependence of (a) polarization P_0 , (b) strain u_3 , (c) sample temperature T and (d) adiabatic temperature change ΔT_{σ_3} on stress σ_3 in epitaxial BTO thin films grown on different compressive substrates at room temperature. The dashed line in (c) indicates the initial temperature which is set as room temperature (300 K).

GdScO₃ (GSO), DyScO₃ (DSO), STO, and NdGaO₃ (NGO), having various in-plane misfit strains u_m ranging from -1% for GSO [324] to -3.2% for NGO [244] owing to mismatch in lattice parameters between the films and the underlying substrates. We restrict ourselves to the case of a uniform local loading σ_3 applied along the z direction (perpendicular to the film surface) with the shear stresses σ_4 and σ_5 and the flexoelectric effect being ingored as schematized in Fig. 5.8. Compressive substrates are chosen since we only consider the polarization and strain change along the direction z (out-of plane) conjugate to the direction of the external stress according to the “misfit strain-stress” phase diagrams [321]. Therefore, the transition from the paraelectric phase ($P_x=P_y=P_z=0$) to ferroelectric tetragonal phase ($P_x=P_y=0, P=P_z \neq 0$) is favored to occur near room temperature [321]. In order to ensure that the effect of misfit strain on the elastocaloric response is clearly seen from our thermodynamical calculations, we simplify by neglecting the the depolarizing field and the substrate deformations (see Section 5.1.1).

From the viewpoint of practical applications, it is of interest to set the initial temperature T at room temperature (300 K). Figures. 5.9(a)-5.9(d) summarize the stress-dependent equilibrium

polarization P_0 , strain u_3 and adiabatic temperature change ΔT_{σ_3} , respectively. It is shown in Fig. 5.9(a) that there exists a critical stress field σ_{3c} at which P_0 continuously disappears, which is essentially attributed to the second-order phase transition ($\alpha_{11}^* > 0$) modified by the mechanical boundary conditions [321]. As the misfit-strain $|u_m|$ increases, $|\sigma_{3c}|$ increases remarkably from 2.97 GPa for GSO to 8.30 GPa for NGO, which indicates that polarization in BTO thin films grown on NGO substrate is more difficult to suppress by a uniaxial stress than the other substrates. And the total polarization change induced by different σ_{3c} increases considerably as $|u_m|$ increases.

Figure 5.9(b) shows that a large strain change can be achieved, which is in line with our previous result [51]. For instance, for the film on GSO substrate, the strain change is about 1.6% under a compressive stress of -3 GPa, which is approximately two times as large as those reported in superelastic BTO single crystal either (0.75%) induced by a low electric field of 2 kV/cm (Ref. [368]) or (0.85%) by a modest stress field of 15 MPa (Ref. [367]).

As expected, the noticeable elastocaloric effect is depicted in Figs. 5.9(c) and 5.9(d). It appears that the elastocaloric response of BTO thin films is maximized when the stress reaches σ_{3c} . After that, no additional change in ΔT_{σ_3} is observed due to the disappearance of the polarization [see Fig. 5.9(a), Eqs. (5.6) and (5.7)]. $|\Delta T_{\sigma_3}|$ increases as $|u_m|$ increases and reaches its largest value of 6.9 K at 8.30 GPa (on NGO substrate). Note that 6.9 K is indeed in the range of temperature changes for other elastocaloric systems reported in the literature [18, 19, 49, 59, 61–63, 85, 86, 365]. Moreover, due to the second-order nature of the phase transition, it is expected that the hysteresis loss and irreversibilities associated with first-order phase transition vanish, which is of importance to enhance refrigerant efficiency [7, 18, 51]. In addition, the system can operate in a wide temperature window for all compressive substrates we investigated [see, e.g. the 60 K window considered in Figs. 5.10(a)-5.10(d)], which is very desired for cooling applications. Therefore, here we demonstrate that ferroelectric thin films may be good candidates for elastocaloric cooling, which also can potentially expand the elastocaloric family from macroscopic scale to nanoscale [51].

The foregoing findings are summarized in Fig. 5.11. It is shown that the critical driving stress $|\sigma_{3c}|$ decreases significantly from 8.30 GPa for NGO to 2.97 GPa for GSO as misfit-strain $|u_m|$ decreases, which can provide an effective approach to lower the driving stress. However, the elastocaloric peak $\Delta T_{\sigma_3}(max)$ also experiences a considerable decrease from 6.9 K to 4.6 K during that change in $|u_m|$. Note that the relevant figure of merit for real devices depends on the external force rather than the applied stress. Though a much higher driving stress is required here, which is orders-of-magnitude larger than those reported in other typical elastocaloric materials [18, 19, 49, 61–63, 86, 365], only an extremely small force is needed for ferroelectric thin films. Figure 5.11 clearly shows that the elastocaloric response of ferroelectric thin films can be remarkably tuned by changing the substrates. Interestingly, if the substrate could be electrically active, designing hybrid elastocaloric/electrocaloric devices controlled by an electric field rather than a mechanical stress can be considered in the future.

Note that we assume that thermal expansion coefficients in the paraelectric phase plays a negligible contribution to the corresponding entropy change. Indeed, this nominal thermal expansion coefficient behavior is directly supported by recent theoretical and experimental results in various materials. For instance, a direct approach based on first-principles calculations does show

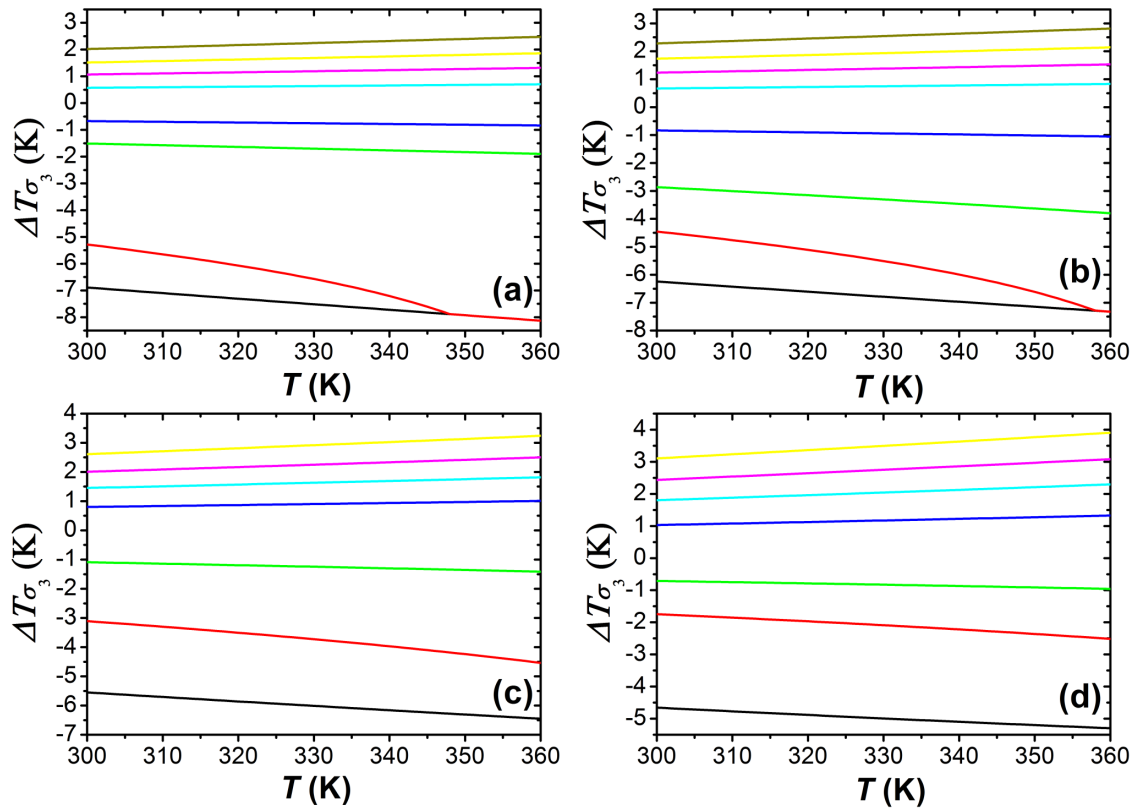


Figure 5.10: Dependence of ΔT_{σ_3} on T of epitaxial BTO thin films grown on (a) NGO, (b) STO (c) DGO and (d) GSO substrates. The different curves correspond to different stress values: from top to bottom the curves correspond to (a) 8.5, 6, 4, 2, -2, -4, -8 and -8.5 GPa; (b) 8.5, 6, 4, 2, -2, -5, -6 and -6.5 GPa; (c) 8.5, 6, 4, 2, -2, -4 and -5 GPa; (d) 8.5, 6, 4, 2, -1, -2 and -3 GPa.

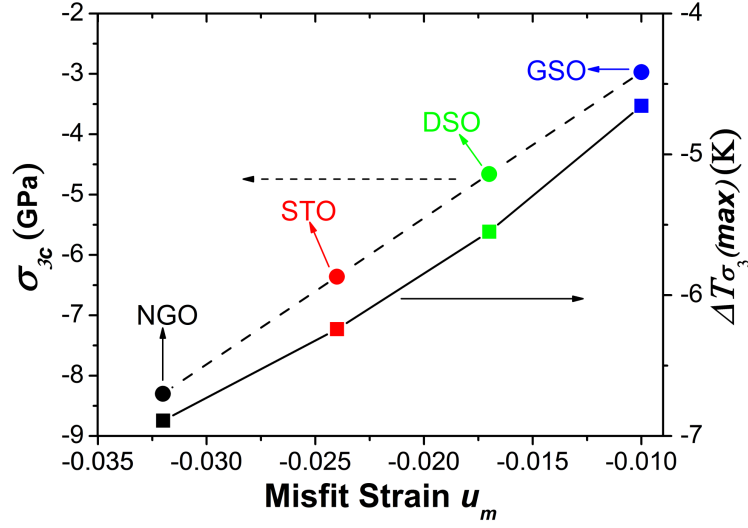


Figure 5.11: The critical driving stress σ_{3c} and corresponding maximum elastocaloric response $\Delta T_{\sigma_3}(\max)$ in epitaxial BTO thin films grown on different compressive substrates at room temperature.

that the elastocaloric response in pto above the phase transition temperature is nearly zero while it only emerges through by the appearance of the polarization induced by a large enough tensile stress (see Fig. 2 in Ref. [49] for more details). Immediately, one can see that the thermal expansion coefficients are negligible in the paraelectric phase according to Eqs. (5.6) and (5.7). This behavior is also confirmed by a recent thermodynamic model showing that both the conventional elastocaloric response [64] and inverse barocaloric effect [76] in BTO single crystals disappear in the paraelectric phase. On the other hand, it was reported in both ferroelectric PTO [75] and ferromagnetic La-Fe-Co-Si [71] that the appreciable barocaloric effect can be only experimentally observed in vicinity of the phase transition temperature. Indeed, both the elastocaloric and barocaloric response strongly depend on the relationship of thermal expansion coefficient versus temperature. Since the thermal expansion coefficient peaks at the phase transition and the thermal expansion coefficient versus temperature curves are almost flat in the paraelectric phase, the corresponding intrinsic entropy change in paraelectric phase cannot be comparable with that near the phase transition [71, 75]. Therefore, it is rational to ignore the contribution from that above the phase transition. In this regard, the corresponding thermal expansion coefficient can therefore be set to be extremely small or zero in the paraelectric phase. Most importantly, we found that the thermal expansion coefficients experienced a dramatic change by one order of magnitude for a stress reaching the critical stress [50], which strongly supports that our foregoing treatment is reasonable.

The thermal expansion coefficients we calculated here may be called as anomalous ones while the normal contributions are presumably set to be negligible (i.e., zero in our case) compared to anomalous parts. The normal thermal expansion coefficient can be added by introducing

the thermo-electric and the thermo-elastic couplings into the free energy. It was reported that such modification allows to describe the evolution of polarization with temperature in the different polar phases in a slightly more accurate manner [372]. This treatment may also result in non-zero thermal expansion coefficient (normal thermal expansion coefficient) in both ferroelectric and paraelectric phases. However, it is expected that the thermal expansion coefficients in the paraelectric phase resulting from this modification should be almost flat or only weakly dependent on temperature, as evidenced by existing experiments [71, 75]. Obviously, the corresponding contribution to the entropy change induced by a stress field or a hydrostatic pressure in the paraelectric phase is still significantly smaller than that at the phase transition. Note that the anomalous part we concentrated on is much larger than the ordinary linear thermal expansion above the phase transition temperature as demonstrated recently by experiments in $(\text{CH}_3\text{NHCH}_2\text{COOH})_3\text{CaCl}_2$ [373]. More importantly, it was shown by Lashley *et al.* that the thermal expansion behavior does not satisfy Landau theory. Instead, it satisfies the defect-driven theory of Levanyuk and Sigov [374]. Therefore, it is trivial to introduce such a risky term into free energy, not to mention that our results are already well supported by recent experimental and theoretical works. Let us consider now the electrocaloric response which can be added to the elastocaloric one as proposed in the prior section (see Section 5.1.4). In particular, the electrocaloric properties of BTO thin films have been intensively investigated [47, 50, 123, 166, 201, 208, 209, 231, 306, 375]. Interestingly, it was reported that applying a uniaxial compressive stress could enhance and widen the electrocaloric response considerably in ultrathin BTO films due to tuning of the depolarization field [166]. It is also reported that the electrocaloric peak under tensile stresses moves towards higher temperatures with its magnitude slightly enhanced in BTO single crystals [64]. For the case under hydrostatic pressure, a slight reduction of the electrocaloric peak with increasing pressure is found in BTO single crystals [76].

For the unloaded case, it can be seen that as $|u_m|$ decreases, the electrocaloric response increases considerably, which agrees well with the previous study [123]. Because the ferroelectricity in BTO thin films grown on NGO substrate is already larger than those grown on other substrates [244], in this case it is more difficult to achieve a larger polarization change under the same electric field. Indeed, mechanical stress may find use in tuning the electrocaloric effect. Stress may modify the height, the width and the position of the peak in ΔT_E in ferroelectric thin films, according to Section 3.1.4.

Here, we may consider the critical case as follows and we find that stress can act as a way to significantly enhance the electrocaloric effect, which is shown in Figs. 5.12(a)-5.12(d). For instance, it is shown in Fig. 5.12(a) that ΔT_E in the compressive loaded state ($\sigma_3 \leq \sigma_{3c}$) is about 4.23 K ($E=1000$ kV/cm) at 300 K which is over 6 times larger than that (0.55 K) in the unloaded case at 300 K under the same E (NGO substrate). Note that the polarization is close to zero when the stress is in proximity of σ_{3c} . Therefore, even a modest electric field can readily polarize the film and produce a remarkably enhanced electrocaloric response. As a result, it can be seen from Figs. 5.12(a)-5.12(d) that a several fold enhancement in the electrocaloric effect can be achieved. This behavior is observed within the temperature range of interest and for all substrates we considered [see Figs. 5.12(a)-5.12(d)]. Therefore, our findings in this work may also open a route for cooling applications by combining the enhanced electrocaloric effect mediated by mechanical stress and elastocaloric effect in a single material [50, 166]. Note that a very

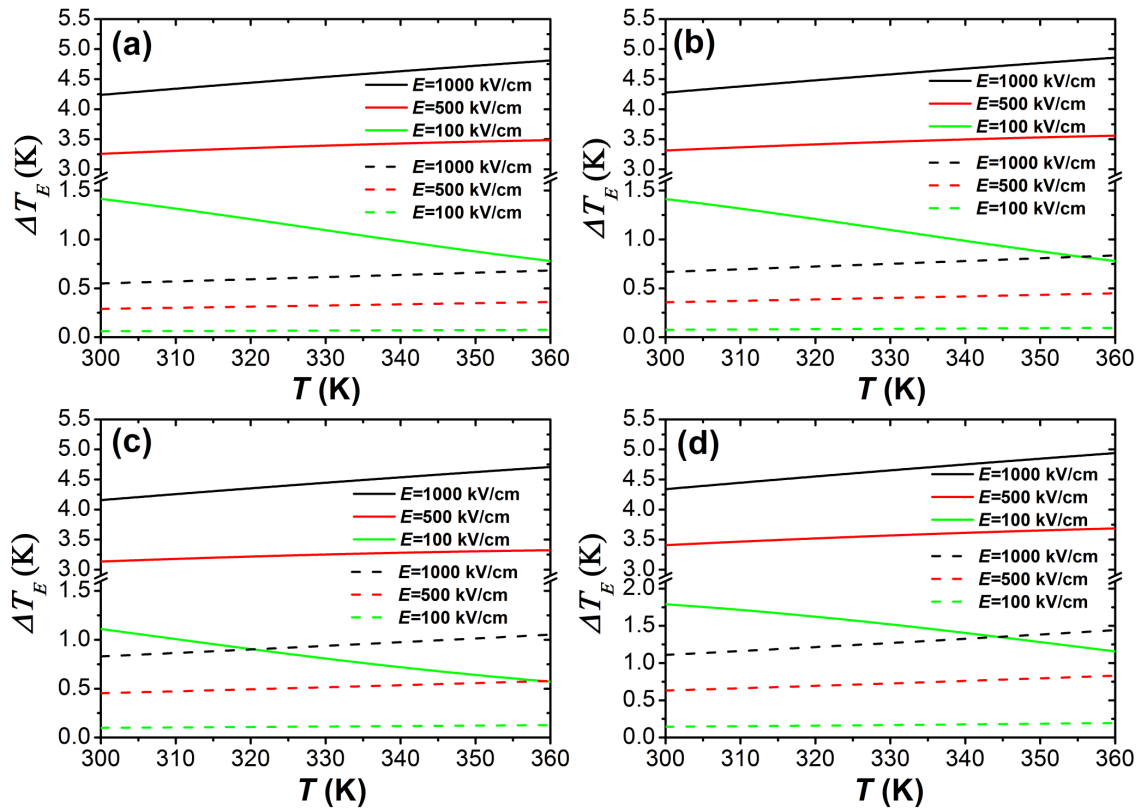


Figure 5.12: Electrocaloric effect in epitaxial BTO thin films under different compressive loadings (solid line): (a) on a NGO substrate ($\sigma_3 = -8.5$ GPa), (b) on a STO substrate ($\sigma_3 = -6.5$ GPa), (c) on a DGO substrate ($\sigma_3 = -5$ GPa) and on a GSO substrate ($\sigma_3 = -3$ GPa), respectively. The dash line refers to the electrocaloric effect in the unloaded state.

recent study reported that secondary contribution from the piezoelectric strain and associated elastocaloric effect in $\text{PbZr}_{1-x}\text{Ti}_x\text{O}_3$ thin films may reduce the overall electrocaloric entropy change [205]. This secondary effect is expected to play a negligible role in our case since fully strained BTO thin films considered here show extremely small piezoelectric response [244].

5.3 GIANT ELASTOCALORIC STRENGTH IN BaTiO_3 IN SINGLE CRYSTALS

5.3.1 Brief introduction

During the last two decades, great efforts have been made to develop solid-state cooling refrigeration mainly due to concern about the environmental impact and energy efficiency limit of the vapor-cycle cooling technologies [8, 18, 84, 108, 112]. As a result, there has been rapid progress in research on caloric (including magnetocaloric, electrocaloric, elastocaloric, and barocaloric) effects [8, 18, 84, 108, 112]. In recent years, growing attention has also been focused on searching multicaloric materials [10, 49, 376] or designing hybrid caloric structures [36] since enhanced caloric responses, refrigerant efficiency, and capacity can be achieved in these materials [18].

In this context, ferroelectrics are naturally multicaloric materials since the total entropy may change significantly near the structural phase transition induced by the multistimuli (electric field, stress, pressure and magnetic field if the magnetoelectric coupling exists). Therefore, it motivates increasing amount of experimental and theoretical studies to investigate the electrocaloric, elastocaloric and barocaloric effects, which may be of great significance and future impact [8]. For instance, intensive studies are focused on BTO single crystal [48, 164, 319], which are classical ferroelectric materials. Due to the sharp first-order phase transition, a giant electrocaloric strength defined as $|\Delta T_E|/\Delta E$ has been demonstrated by several groups with its ever reported largest value of 0.48 K cm/kV under an electric field change ΔE of 10 kV/cm in BTO single crystals [319]. However, the magnitude of electrocaloric temperature change $|\Delta T_E|$ is modest (~ 1 K reported in Refs. [48, 164, 319]), which directly limits further practical applications, not to mention the large voltage required in the experiments. Since the transition temperature (~ 400 K) is well above room temperature [48, 164, 319], it is of interest to lower the working temperature approaching room temperature. In addition, barocaloric effect in BTO single crystals was demonstrated near room temperature recently which can be comparable with its electrocaloric response [76]. Additionally, it was reported that a hydrostatic pressure can be used to shift the barocaloric peak to room temperature [76]. Note that the study on the elastocaloric effect in BTO single crystals near the sharp first-order phase transition which may show novel and interesting properties is still lacking.

It was reported that the multicaloric effects can be induced either by applications of either single stimulus [10, 376] or several stimuli simultaneously [49]. Due to the strong couplings between different degrees of freedom, i.e., magnetoelectric [10, 376] and ferroelastic couplings [49], the multicaloric effect can exceed any single caloric effect. On the other hand, one may consider combining several stimuli in a “step-by-step” manner according to previous study. For instance, in the case of BTO single crystals the stress applied first (elastocaloric effect) may change

the phase transition temperature before the withdrawal of this stimulus, which may act as an effective tool to tune the later caloric (i.e., electrocaloric) effect [100, 166]. It therefore motivates the present study on the elastocaloric and stress-mediated electrocaloric effects in ferroelectric BTO single crystals. Indeed, although the study on the elastocaloric effect in ferroelectrics has attracted much more attention, it is still at the early stage compared with the shape memory alloys [61–63, 86, 365]. Recently, the remarkable elastocaloric effect in both ferroelectric bulk [19, 49] and thin film [50] is predicted using first-principles calculations and the phenomenological approach, respectively, which can even compete with that reported in shape memory alloys [61–63, 86, 365]. It is of specific interest to revisit the elastocaloric response of BTO single crystals using phenomenological calculations since this approach is easy to understand and simple to achieve without using costly large-scale computing. In addition, it can describe the ferroelectric behavior accurately especially near the phase transition.

5.3.2 Landau theory of elastocaloric effect

An applied stress field σ_3 (all tensors appear in Voigt notation) can reversibly change the temperature of an elastocaloric material under adiabatic conditions, and the temperature change ΔT_{σ_3} is usually maximized near phase transitions [19, 49, 50, 61–63, 86, 365]. Note that σ_3 here is a uniaxial stress applied along the polar axis of ferroelectric and denoted as σ_3 for short in the following parts. In order to obtain ΔT_{σ_3} , one may consider using the indirect method via the Maxwell relation in Eq. (1.25) or Eq. (5.7). The validity of the indirect method is still under debate especially in the field of the electrocaloric effect. [8, 100, 163, 177, 204, 231] Indeed, the Maxwell relations are applicable only for thermodynamically reversible equilibrium and ergodic systems. However, the first-order phase transition is always associated with thermodynamically irreversible hysteretic loss. As a result, Eq. (5.7) can give only an approximation of ΔT_{σ_3} provided that the irreversible contribution is relatively small [61, 104]. Interestingly, first-principle calculations have demonstrated that ΔT_{σ_3} calculated based on Eq. (5.7) fails to reproduce the direct measurement results in bulk ferroelectric PTO [49]. However, ΔT_{σ_3} can be derived through the use of Landau-type theory irrespective of the order nature of phase transition. In this case, we argue that the elastocaloric effect in BTO single crystals may be evaluated in terms of polarization change rather than strain change near the first-order phase transition, as expected in proper ferroelectrics for which the strain variation results from the polarization change [49]. Such treatment is directly supported by first-principles calculations showing that indeed the elastocaloric effect in PTO nearly vanishes to zero in the paraelectric phase due to the disappearance of polarization [49]. Additional experimental evidence signals that the barocaloric effect in PTO is noticeable only near the pressure-free Curie temperature [75].

To allow direct comparison with recent first-principles studies [19, 49], we concentrate on the condition of a uniaxial tensile stress $\sigma_3 > 0$ applied along the [001] direction of BTO. Moreover, we focus on the transition from the cubic phase to the tetragonal one, which is widely studied in electrocaloric BTO samples in the form of single crystals, thin films and ceramics [47, 48, 76, 123, 125, 164, 166, 201, 209, 319]. Taking into account of the foregoing mechanical boundary

conditions, the Gibbs free energy can be expressed as [360]

$$G = \alpha_{68}P^2 + \alpha_{11}P^4 + \alpha_{111}P^6 + \alpha_{1111}P^8 - \frac{1}{2}S_{11}\sigma_3^2 - Q_{11}\sigma_3P^2, \quad (5.8)$$

where S_{11} is the elastic compliance and Q_{11} is the electrostrictive coefficient. α_1 , α_{11} , α_{111} , and α_{1111} are the dielectric stiffness coefficients at constant stress, and only α_1 is temperature dependent. The higher-order electrostrictive coupling between stress and polarization has been included in the stress-dependent Landau potential coefficients α_{11} and α_{111} [360].

In the following part, we use a phenomenological Landau-type model which was initially proposed to describe the electrocaloric effect in relaxor ferroelectric and BTO single crystals [163, 164]. The theoretical predictions of this model were found to agree well with the experimental results [163, 164]. In addition, this model was recently developed to describe the barocaloric effect in BTO single crystals [76]. It assumes that the total entropy S can be divided into two parts namely the dipolar contribution S_{dip} and the lattice contribution S_{latt} as follows [163]:

$$S = S_{latt} + S_{dip}, \quad (5.9)$$

where S_{dip} is due to the entropy contribution of the dipolar degrees of freedom and is thus a function of the dielectric polarization $P(E, T)$, which depends on E at a given T . S_{latt} is an electric field independent lattice contribution. Another assumption is that the dipolar free energy can be written in the standard Landau form [163]. For the elastocaloric effect here, both assumptions can be satisfied. To be more specific, this model may be developed by replacing the electric stimulus by stress σ_3 , making it applicable to our case. Following the strategy developed by Pirc *et al.* [163, 164], we can then obtain a self-consistent equation to derive $\Delta T_{\sigma_3} = T_2 - T_1$ such that

$$T_2 = T_1 \exp\left\{\frac{a_1}{2C_{latt}}[P_0^2(\sigma, T) - P_0^2(0, T)]\right\}, \quad (5.10)$$

where $a_1 \equiv d\alpha_1/dT$ and C_{latt} is the lattice contribution to the total heat capacity. P_0 is the equilibrium polarization obtained from the equilibrium condition $\partial G/\partial P = 0$. $C_{latt}(T)$ and mass density ρ are taken from the experimental data reported in Ref. [164]. When solving the particular transition from paraelectric phase to ferroelectric tetragonal phase, the respective results calculated by pressure/stress dependent [360] and independent Landau coefficients [283] are exactly the same and are both in good agreement with experimental data as long as the magnitude of pressure/stress is below 6.5 GPa [360]. As a result, the Landau potential coefficients used here are obtained at zero pressure/stress. Further studies should take into account the pressure/stress-dependent Landau coefficients and quantum saturation of the order parameter (especially at low temperatures) [360].

5.3.3 Elastocaloric effect in BaTiO_3 single crystals

Figure. 5.13(a) summarizes the equilibrium polarization P_0 under different σ_3 as a function of T . It is shown that the Curie temperature $T_c(\sigma_3)$ increases with increasing stress. Specifically,

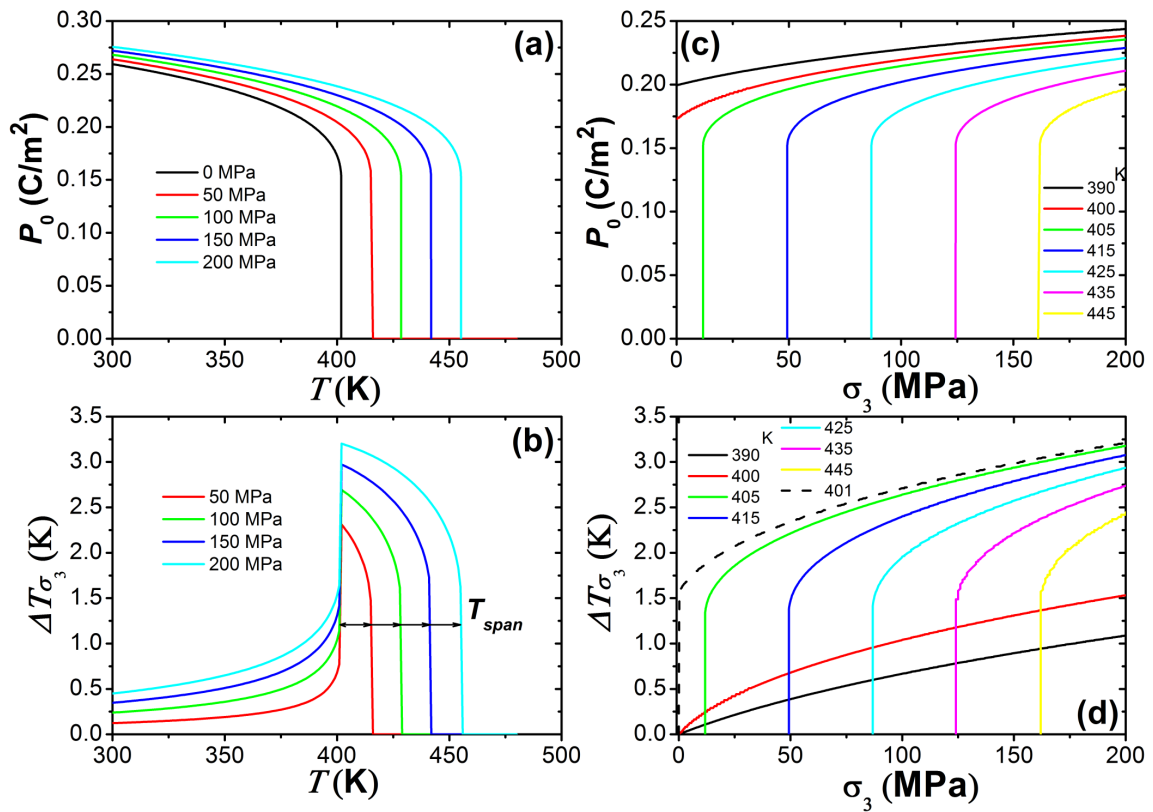


Figure 5.13: The polarization P_0 and (b) adiabatic temperature change ΔT_{σ_3} under different σ_3 as a function of ambient temperature T . The dependence of (c) P_0 and (d) ΔT_{σ_3} on σ_3 at different T .

Table 5.3: Comparison of elastocaloric properties of BTO single crystals developed in this work with those in the literature.

| Material | $T_c(0)$ [K] | T_{span} [K] | σ_3 [MPa] | $ \Delta T_{\sigma_3} $ [K] | $\Delta T_{\sigma_3}/\sigma_3$ [K/MPa] | $ \Delta S_{\sigma_3} $ [J/kg K] | $ R $ [J/kg] | Refs |
|--|-----------------|-------------------|---------------------|--------------------------------|---|-------------------------------------|-----------------|------|
| NiTi | 242 | – | 600 | 17 | 0.023 | – | – | [62] |
| FePd | 230 | 50 | 100 | 2 | 0.020 | – | – | [63] |
| TiNiCu | 318 | – | 330 | 6 | 0.018 | – | – | [86] |
| CuZnAl | 234 | 130 | 275 | 6 | 0.022 | 17.9 | 107 | [61] |
| $\text{Ba}_{0.5}\text{Sr}_{0.5}\text{TiO}_3$ | 250 | 50 | 1000 | 9 | 0.009 | ~ 16 | 144 | [19] |
| PTO | 750 | ~ 30 | 1000 | 20 | 0.020 | ~ 9.6 | 192 | [49] |
| BTO | 401 | 50 | 200 | 3.2 | 0.016 | ~ 3.2 | 10.2 | Here |

$T_c(\sigma_3)$ increases from 401 K at 0 MPa to 455 K at 200 MPa. As a result, P_0 is consistently enhanced especially at temperatures above the stress-free Curie temperature $T_c(0) \approx 401$ K.

The elastocaloric behavior of BTO single crystals is revealed in Fig. 5.13(b). It can be seen that ΔT_{σ_3} peaks at $T_c(0)$, which is consistent with the predictions by first-principles calculations [19, 49]. Just above $T_c(0)$, ΔT_{σ_3} drops sharply due to the dramatic reduction of polarization change $[P(\sigma_3, T) - P(0, T)]$ as shown in Fig. 5.13(a). Finally, ΔT_{σ_3} vanishes due to the disappearance of polarization, which again agrees with the results obtained by first-principles calculations [49]. Our finding is also in line with the barocaloric effect reported in PTO in which the maximum barocaloric response was observed at the pressure-free Curie temperature of PTO [75]. The largest ΔT_{σ_3} found here is about 3.2 K at 200 MPa, while ΔT_{σ_3} can reach 2.3 K at 50 MPa. ΔT_{σ_3} at 200 MPa found here (3.2 K) is smaller than that (6 K) in PTO [49] but is larger than that (~ 1 K) in $\text{Ba}_{0.5}\text{Sr}_{0.5}\text{TiO}_3$ [19] under the same stress condition. In addition, it is shown that as σ_3 increases, the working temperature window T_{span} increases considerably from ~ 15 K at 50 MPa to ~ 50 K at 200 MPa [see Fig 5.13(b)]. In addition, the elastocaloric strength defined as $\alpha = |\Delta T_{\sigma_3}/\sigma_3|$ in BTO (0.016 K/MPa) is already in the range of the previous results obtained from CuZnAl shape memory alloys and other ferroelectric bulk materials though the entropy change ΔS_{σ_3} (3.2 J/kg K) and refrigerant capacity $R \simeq |\Delta S_{\sigma_3} \Delta T_{\sigma_3}|$ (Ref. [86]) are relatively low (see Table 5.3).

The stress-dependent P_0 and ΔT_{σ_3} under different T are shown in Figs. 5.13(c) and 5.13(d). It turns out that P_0 increases as σ_3 increases. It can be seen in Fig. 5.13(c) that above $T_c(0)$ there exists a critical stress field σ_{3c} at which P_0 jumps to roughly 0.15 C/m^2 due to the stress-induced first-order phase transition. As T increases, larger stresses are needed to induce the discontinuous transition. Consequently, σ_{3c} increases significantly from ~ 12 MPa at 405 K to ~ 161 MPa at 445 K. Below $T_c(0)$, the polarization jump does not occur as BTO is already in its ferroelectric phase. In addition, it is found that the closer to $T_c(0)$, the larger the change of polarization will be. Accordingly, the elastocaloric response in Fig. 5.13(d) shows that ΔT_{σ_3} increases as σ_3 increases irrespective of T . Moreover, Fig. 5.13(d) clearly indicates that the largest ΔT_{σ_3} occurs at $T_c(0)$, which is consistent with the findings in Fig. 5.13(b). In addition, the elastocaloric

effect predicted here has the potential to compete with the measured electrocaloric counterpart (~ 1 K in Refs. [48, 164, 319]) depending on the maximum value of mechanical stress applied in the practical situation. This result clearly demonstrates that applied stress may be an effective tool to directly induce the large caloric response for cooling/heating applications especially in ferroelectrics [19, 49, 50].

Obviously, in real situations, the high stress used in theoretical calculations warrants further consideration. For instance, for compressive stress ($\sigma_3 < 0$), single crystal BTO usually bears an upper bound $|\sigma_3|$ of less than 30 MPa, while a polycrystalline sample can hold an order of magnitude higher stress (i.e., ~ 300 MPa) [368, 377]. As a result, the elastocaloric effect observed by experiment should be significantly smaller than the predicted one produced by the ultrahigh stress [19, 49]. In order to achieve large elastocaloric responses, it may be helpful to reconsider the critical elastocaloric behavior near $T_c(0)$. It should be noted that all the elastocaloric data shown in Table 5.3 are accomplished by full transition of samples and bounded by $\Delta T_{\sigma_3} = \frac{T}{C_{\sigma_3}} \Delta S_{\sigma_3}$. In our case, a high stress of 200 MPa can be used for the full transition [see Figs. 5.13(c) and 5.13(d)]. At low stresses, the elastocaloric strength $\alpha_{elasto} = |\Delta T_{\sigma_3}/\sigma_3|$ is controlled by the slope in the $\sigma_3 - T$ phase diagram (Clausius-Clapeyron relation) and the sharpness of the transition as shown later. Detailed discussion about this issue in the magnetocaloric effect can be found elsewhere [378]. In addition, only a single domain model is considered in the phenomenological theory here and first-principles calculations [19, 49], which just gives the static or quasistatic solutions. In the practical conditions, it will be of interest to include other domain structures, i.e., 90° domain switching [368] in future studies. In this regard, stress relaxation taking place in the region of deformation related to twin boundary motions [379, 380] should also be taken into account.

The elastocaloric properties especially at the temperatures approaching $T_c(0)$ are depicted in Figs. 5.14(a) and 5.14(b). It can be seen that the critical driving stress σ_{3c} drops remarkably from ~ 30 MPa at 410 K to ~ 0.5 MPa at 402 K. Interestingly, the corresponding elastocaloric temperature change $\Delta T_{\sigma_{3c}}$ remains nearly unchanged from 1.32 K at 30 MPa to 1.29 K at 0.5 MPa, which is still comparable with its electrocaloric counterpart in BTO single crystals [48, 164, 319]. This finding is of importance since the driving stress can be tuned to be much smaller as long as T is close to $T_c(0)$. Note that here the transition has just been opened by the critical stress field σ_{3c} and the corresponding temperature change $|\Delta T_{\sigma_{3c}}|$ of about 1.3 K is caused directly by the discontinuous polarization jump near the transition point [see Figs. 5.13(a) and 5.13(c)]. In this case, the elastocaloric strength has to be redefined as $\alpha_c = |\Delta T_{\sigma_{3c}}/\sigma_{3c}|$ as we concentrated on elastocaloric response under a low stress. It is shown in Fig. 5.14(b) that as T decreases towards $T_c(0)$, the elastocaloric strength defined as α_c first increases slowly from 0.043 K/MPa at 410 K to 0.16 K/MPa at 404 K and then experiences a steep jump to 2.32 K/MPa at 402 K. Note that α_c experiences a sharp drop as T [starting from $T_c(0)$] decreases further (not shown here), which indicates that $\alpha_c \propto 1/|T - T_c(0)|$ is also maximized at $T_c(0)$. This phenomenon is very similar with the behavior of the electrocaloric strength near $T_c(0)$ [48, 125, 164, 319]. Note that the giant elastocaloric strength of 2.32 K/MPa found here is two orders of magnitude higher than that (0.016 K/MPa) under full transition induced by a large stress (see Table 5.3). However, just like its electrocaloric counterpart [48, 125, 164, 319], the giant elastocaloric strength benefits from the sharp first-order phase transition but in turn

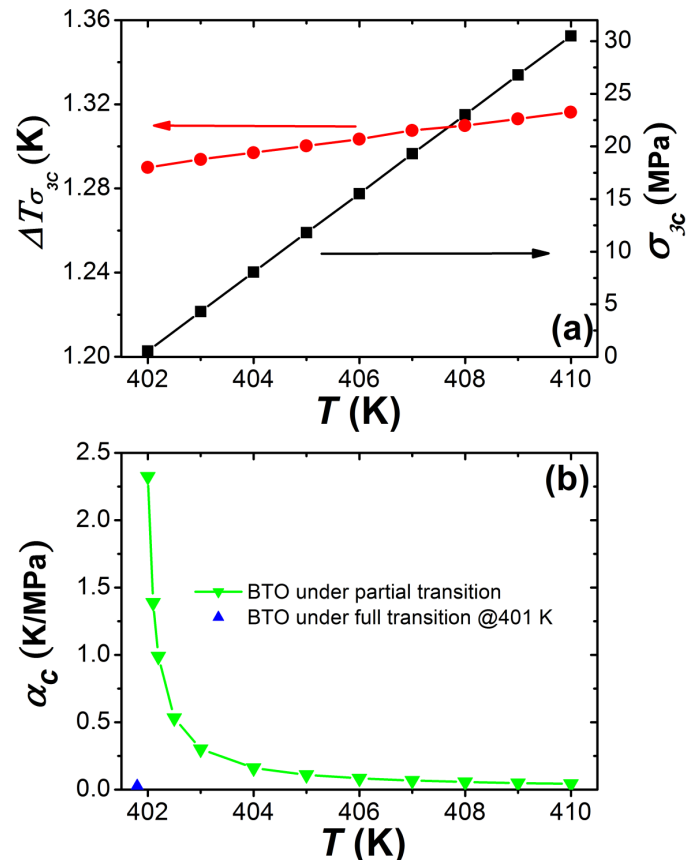


Figure 5.14: (a) The critical driving stress σ_{3c} and corresponding elastocaloric response $\Delta T_{\sigma_{3c}}$ as a function of T ; (b): the critical elastocaloric strength α_c as a function of T [402-410 K]. The result obtained in BTO under full transition at 401 K is also added.

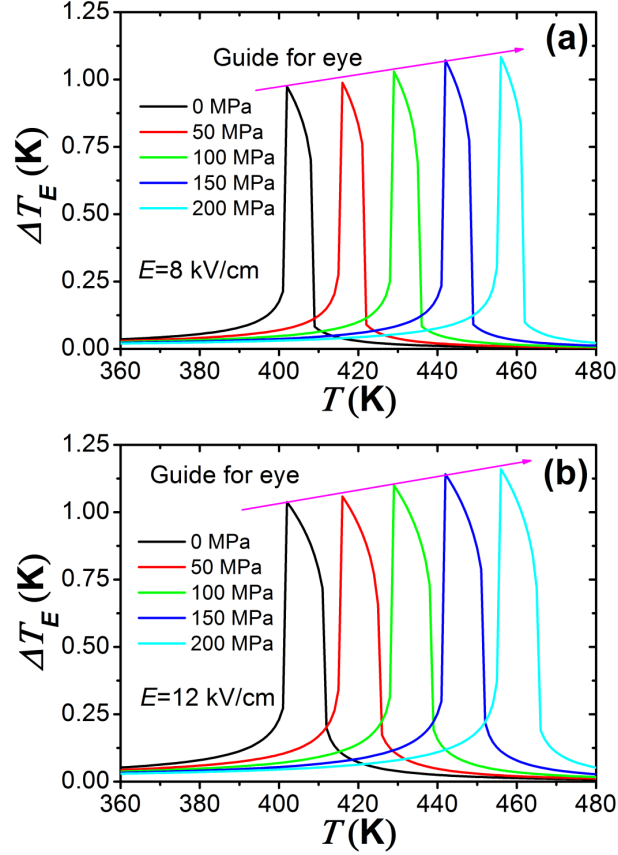


Figure 5.15: Electrocaloric effect under different mechanical conditions.

suffers by the strong temperature dependence of ΔT_{σ_3} near $T_c(0)$. As a consequence, the narrow T_{span} (<9 K) limits the potential cooling applications of BTO in elastocaloric and electrocaloric devices. From this regard, martensite shape-memory alloys show better performance.

5.3.4 Stress-mediated electrocaloric effect in BaTiO_3 single crystals

Understanding the stress-mediated electrocaloric effect in BTO single crystals is of particular interest as it may give a handle in tuning the electrocaloric effect. For instance, it was reported that applying compressive stresses on BTO ultrathin films can lead to the enhancement of the electrocaloric response due to the tuning of the depolarizing field [166]. In our work, we used the foregoing model [163, 164] to study the effect of tensile stress on the electrocaloric effect in BTO single crystal, which is shown in Fig. 5.15. It can be seen that the largest electrocaloric temperature changes ΔT_E induced by two typical electric fields of 8 kV/cm and 12 kV/cm at 0 MPa are 0.97 K and 1.03 K, respectively. These results are consistent with the direct measurement data, i.e., 0.80 K and 0.90 K (Ref. [48]) or 1.10 K and 1.20 K (Ref. [164]), respectively. On the contrary, the calculated values here differ from those obtained by an

indirect approach where the ΔT_E peak value is about 4.8 K ($E=10$ kV/cm) [319]. In addition, it is shown that the peak of ΔT_E moves remarkably towards higher temperatures, which is essentially attributed to the shift of $T_c(\sigma_3)$ [Fig. 5.13(a)]. Moreover, the magnitude of the ΔT_E peak increases slightly from 0.97 K at 0 MPa to 1.08 K at 200 MPa.

The stress-mediated electrocaloric behavior described above can be understood qualitatively as follows. ΔT_E can be estimated using $\Delta T_E \cong - \int_0^E \frac{T}{C_E} (\frac{\partial P^0}{\partial T})_{E,\sigma_3} dE$, where C_E is the volumetric heat capacity under constant E . In our case, the term $|\frac{\partial P^0}{\partial T}|_{E,\sigma_3}$, which is the pyroelectric coefficient, is slightly reduced when a tensile stress is applied. Note that a higher $|\frac{\partial P^0}{\partial T}|_{E,\sigma_3}$ does not necessarily guarantee a larger magnitude of the electrocaloric effect [123, 177], because the ambient temperature, heat capacity and electric field change also contribute to the above integration. In BTO single crystals, it is found that the enhancement in the term of $\frac{T}{C_E}|_{E,\sigma_3,T}$ is dominant over compensating the reduction stemming from the term $|\frac{\partial P^0}{\partial T}|_{E,\sigma_3}$. As a result, a slight increase in ΔT_E is observed as σ_3 increases.

5.4 CONCLUSIONS

In summary, we show that ecofriendly ultrathin BTO capacitors can exhibit giant stress-induced elastocaloric effect without hysteresis losses or Joule heating. Taking advantage of both conventional and inverse elastocaloric effect in combination with the large electrocaloric effect, we suggest an ideal refrigeration cycle with high performances at room temperature (temperature change over 10 K with a wide operational-temperature window of 60 K). We believe that our findings open the route towards improved and novel solid-state refrigeration which should be useful and very efficient in nanoelectronic devices.

Using a thermodynamic model we have studied the elastocaloric effect and stress-mediated electrocaloric effect in BTO thin films grown on different compressive substrates. Our results reveal that epitaxial strain can significantly tune the elastocaloric peak and the critical driving stress. It is shown that a several fold enhancement of the electrocaloric effect can be achieved for stress approaching to the critical value. Our preliminary findings suggest a potential route to design hybrid elastocaloric/electrocaloric devices controlled by a modest electric field and combine the elastocaloric effect and stress-mediated-and-enhanced electrocaloric effect in the same material.

Using a thermodynamic model, we demonstrate that a giant elastocaloric strength of 2.32 K/MPa can be achieved near zero-field Curie temperature in BTO single crystals. The giant elastocaloric strength found here benefits from the sharp first-order phase transition but in counterpart the elastocaloric response suffers from the strong temperature dependence. It is found that the tensile stress can shift the electrocaloric peak to higher temperatures and simultaneously increase the magnitude of the electrocaloric peak slightly. Our findings clearly show that the elastocaloric effect in BTO single crystals has great potential to compete with its electrocaloric counterpart depending on the stress applied in practice. Hopefully, our study will stimulate further experimental and theoretical investigations on the elastocaloric effect and stress-mediated electrocaloric effects especially in ferroelectrics. In particular, the elastocaloric effect under compressive stresses taking into account ferroelastic domain switching [368] is highly

desirable.

- CHAPTER 6 -

BAROCALORIC EFFECT IN FERROELECTRICS

In this Chapter, we firstly describe the barocaloric effect in BTO single crystals using Landau theory in Section 6.1. And then we make discussions about the effect of hydrostatic pressure on the electrocaloric effect in BTO single crystals in Section 6.2. Finally, it is the conclusion part (Section 6.3) in this Chapter.

6.1 BAROCALORIC EFFECT IN BaTiO_3 SINGLE CRYSTALS

Applying a hydrostatic pressure can reversibly change the temperature (entropy) of a barocaloric material under adiabatic (isothermal) conditions, which is similar to the conventional vapor-cycle refrigeration [67, 381]. Although research in solid-state barocaloric effect is still at its early stage, it is receiving considerable interest as barocaloric refrigeration is thought to be one of potential alternatives to the current cooling technologies [18, 73]. During the last nearly 20 years, appreciable barocaloric effects have been successively reported in various ferroic materials [18, 67–69, 71–75, 77, 78, 381–394]. For instance, an adiabatic temperature change ΔT_p of about 4.5 K and isothermal entropy change ΔS_p of 24.4 J/kg K were observed in Ni-Mn-In magnetocaloric alloys under a hydrostatic pressure of 0.26 GPa [69]. In Ni-Mn-In alloys, the entropy (temperature) decreases (increases) with pressure, which indicates that the barocaloric effect is conventional. Interestingly, an inverse barocaloric effect (i.e., temperature decreases when the pressure is applied) can be also observed as reported in La-Fe-Co-Si alloys [71].

Note that room-temperature barocalorics are still rare since most reported materials undergo a phase transition at T_c (transition temperature) either below or above room temperature [18, 67–69, 71–75, 77, 78, 381–394]. Moreover, the strong temperature dependence of barocaloric response near the first-order phase transition results in a narrow operational temperature window T_{span} (see Table. 6.1), which is a limiting factor for practical cooling applications. Using a thermodynamic approach [163], in this section we report a giant barocaloric effect ($\Delta T_p > 3$ K) in BTO single crystal near room temperature, in which a wide temperature span about 50 K can be achieved. Moreover, we find that the electrocaloric peak decreases slightly with increasing the

Table 6.1: Comparison of barocaloric properties of BTO single crystal developed here with those in the literature.

| Materials | T_{span} [K] | $ \Delta T_p $ [K] | p [GPa] | $ \Delta T_p /p$ [K/GPa] | R [J/kg] | Reference |
|---|-------------------|-----------------------|--------------|-----------------------------|---------------|-----------|
| CeSb | 14-17 | 2.0 | 0.52 | 3.8 | ~ 38.0 | [68] |
| EuNi(Si _{0.15} Ge _{0.85}) ₂ | 50-65 | 0.5 | 0.48 | 1.0 | ~ 15.6 | [68] |
| Rb ₂ KMoO ₃ F ₃ | 200-220 | 16.0 | 0.50 | 32.0 | ~ 480.0 | [388] |
| La-Fe-Co-Si | 230-245 | ~ 2.2 | 0.21 | 10.5 | 18.9 | [71] |
| Gd ₅ Si ₂ Ge ₂ | 267-273 | 1.2 | 0.20 | 6.0 | 13.2 | [74] |
| Ni-Mn-In | 291-295 | ~ 4.5 | 0.26 | 17.3 | 109.8 | [69] |
| La _{0.7} Pb _{0.3} MnO ₃ | 339-345 | 1.1 | 0.40 | 2.8 | 1.9 | [391] |
| PTO | 758-766 | 2.2 | 0.03 | 73.3 | 6.6 | [75] |
| BTO | 305-353 | 3.0 | 2.00 | 1.5 | ~ 11.8 | this work |

hydrostatic pressure, which is in contrast to the behavior predicted in relaxor ferroelectrics [99] and LiNbO₃ [100].

In order to calculate ΔT_p , one may use the indirect method in virtue of the Maxwell relation $(\frac{\partial S}{\partial p})_{E,T} = -(\frac{\partial V}{\partial T})_{p,E}$ following Eq. (1.24):

$$\Delta T_p = \int_0^p \frac{T}{C_p} (\frac{\partial V}{\partial T})_{p,E} dp, \quad (6.1)$$

where V is the volume and E is the electric field. C_p is the volumic heat capacity under constant hydrostatic pressure p . Eq. (6.1) suggests that a remarkable barocaloric effect can be observed in materials for which the volume depends strongly on the temperature. Note that the Maxwell relations are valid only for thermodynamically reversible equilibrium and ergodic systems. As a result, Eq. (6.1) may need to be modified by taking into account the irreversible contributions or the discontinuous change of the volume. Otherwise, Eq. (6.1) can give only an approximation of ΔT_p provided that the hysteresis loss is small. On the other hand, one may use Landau-type theory to derive ΔT_p . The discontinuous volume change at the first-order phase transition ($T_c \sim 401$ K) is the result of the polarization jump in BTO (a proper ferroelectric) due to the strong coupling between the lattice and spontaneous polarization [395]. Consequently, we may evaluate the barocaloric effect in terms of the polarization change. Such treatment can readily explain why appreciable barocaloric effect was observed only near the phase transition not in paraelectric phase in PTO [75]. Another experimental evidence shows that the change in the thermal expansion coefficient of BTO is only significant near T_c (Ref. [357]), which implies that ΔT_p derived from Eq. (6.1) is negligible in the paraelectric phase. Indeed, our forementioned treatment is directly supported by recent first-principles simulations of the elastocaloric effect in PTO showing that elastocaloric response nearly vanishes above T_c due to the disappearance of polarization [49]. Moreover, it is useful to consider the polarization, rather than the volume, as the order parameter to determine ΔT_p or ΔS_p using the Landau-type theory.

Under a hydrostatic pressure p , the Gibbs free energy can be written as [360]

$$G = f_0 - \left(\frac{3}{2}S_{11} + 3S_{12}\right)p^2 + p(Q_{11} + 2Q_{12})(P_1^2 + P_2^2 + P_3^2), \quad (6.2)$$

where S_{mn} are the elastic compliances and Q_{mn} are the electrostrictive coefficients. f_0 , which is the Landau-Devonshire potential expanded as a eighth-order polynomial of the spontaneous polarization components $P_i (i=1,2,3)$, can be expressed as

$$\begin{aligned} f_0 = & \alpha_1(P_1^2 + P_2^2 + P_3^2) + \alpha_{11}(P_1^4 + P_2^4 + P_3^4) + \alpha_{12}(P_1^2P_2^2 + P_1^2P_3^2 \\ & + P_2^2P_3^2) + \alpha_{123}P_1^2P_2^2P_3^2 + \alpha_{111}(P_1^6 + P_2^6 + P_3^6) + \alpha_{112}[P_1^2(P_2^4 \\ & + P_3^4) + P_2^2(P_1^4 + P_3^4) + P_3^2(P_1^4 + P_2^4)] + \alpha_{1111}(P_1^8 + P_2^8 + P_3^8) \\ & + \alpha_{1122}(P_1^4P_2^4 + P_1^4P_3^4 + P_2^4P_3^4) + \alpha_{1112}[P_1^6(P_2^2 + P_3^2) + P_2^6(P_1^2 \\ & + P_3^2) + P_3^6(P_1^2 + P_2^2)] + \alpha_{1123}(P_1^4P_2^2P_3^2 + P_1^2P_2^4P_3^2 + P_1^2P_2^2P_3^4), \end{aligned} \quad (6.3)$$

where α_{ijkl} are the dielectric stiffness coefficients at constant stress, and only α_1 is temperature dependent. In particular, we focus on the transition from the cubic phase ($P_1=P_2=P_3=0$) to tetragonal phase ($P_1=P_2=0, P = P_3 \neq 0$) here. In this case, there is no need to include the higher-order electrostrictive coupling between stress and polarization [283, 360].

Recently, Pirc *et al.* proposed a model to describe the electrocaloric effect in normal ferroelectrics and relaxors [125, 163, 164]. Without the use of Maxwell relation, they found that their theoretical results agree well with the direct measurements. Interestingly, their model can be developed by replacing the stimulus of the electric field by the hydrostatic pressure, which is thus also applicable to our case. The crucial assumption in this model is that the total entropy can be written as the sum of a lattice part S_{latt} plus a dipolar part S_{dip} : [163]

$$S = S_{latt} + S_{dip}, \quad (6.4)$$

where S_{dip} is due to the entropy contribution of the dipolar degrees of freedom and is thus a function of the dielectric polarization $P_i(p, T)$, which depends on the hydrostatic pressure at a give temperature. S_{latt} is a pressure independent lattice contribution. In addition, the dipolar free energy can be written in the standard Landau form. Following the strategy by Pirc *et al.* [163, 164], we can then obtain a self-consistent equation to derive $\Delta T_p = T_2 - T_1$ as follow:

$$T_2 = T_1 \exp\left\{\frac{a_1}{2C_{latt}}[P_0^2(p, T) - P_0^2(0, T)]\right\}, \quad (6.5)$$

where $a_1 \equiv d\alpha_1/dT$ and C_{latt} is the lattice contribution to the total heat capacity.

Figure. 6.1(a) summarizes the pressure-dependent equilibrium polarization P_0 in BTO single crystal under different initial temperatures T . Here the equilibrium condition $\partial G/\partial P = 0$ has been applied. It is shown that the polarization decreases with pressure and the critical pressure p_c , at which the polarization discontinuously decreases to zero, decreases significantly from 2.41 GPa at 285 K to 0.86 GPa at 360 K. The first-order nature of the phase transition is conserved for the investigated pressure range. In addition, P_0 under different finite hydrostatic pressures as a function of ambient temperature T is shown in Fig. 6.1(b). It is found that the

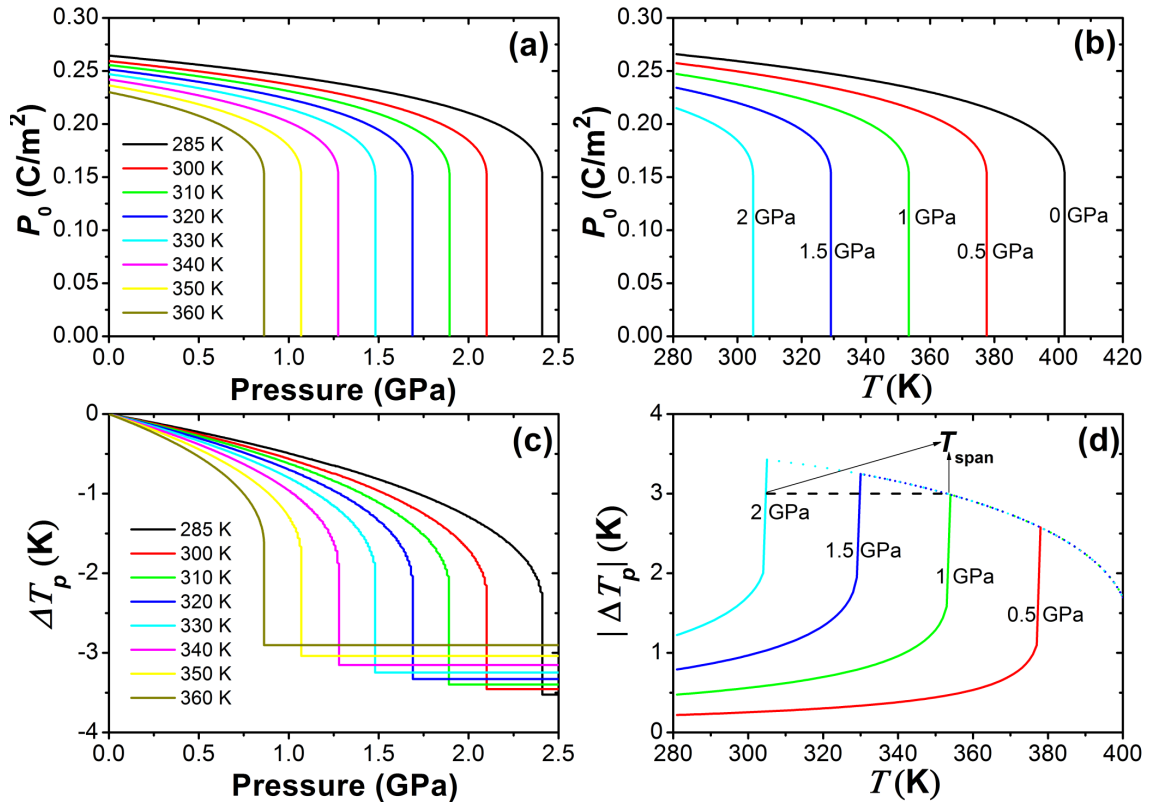


Figure 6.1: The dependence of (a) polarization P_0 and (c) adiabatic temperature change ΔT_p on hydrostatic pressure p at different initial temperatures T in BTO single crystal; (b): P_0 under different finite hydrostatic pressures as a function of ambient temperature T ; (d): Dependence of $|\Delta T_p|$ on the initial temperature T of BTO single crystal, where the temperature range T_{span} is also plotted.

ferroelectric transition temperature decreases with increasing pressure. To be more specific, the Curie temperature moves from 401 K at zero pressure towards room temperature at about 2 GPa as the hydrostatic pressure increases. These results agree well with the previous publication [360].

The existence of negative barocaloric effect in BTO single crystal is revealed in Fig. 6.1(c). At each given temperature, it is shown that $|\Delta T_p|$ increases with pressure, reaching its maximum near the first-order transition temperature as indicated in Fig. 6.1(a). Above T_c , $|\Delta T_p|$ is unchanged due to the disappearance of the spontaneous polarization, which is similar with the elastocaloric response reported in PTO [49]. As the initial temperature increases, the largest $|\Delta T_p|$ value decreases from 3.5 K at 285 K to 2.9 K at 360 K. This is due to the reduction of polarization mismatch $[P(p, T) - P(0, T)]$ as T increases as shown in Fig. 6.1(a). Due to the shift of transition temperature induced by the pressure, Fig. 6.1(c) shows that the giant barocaloric effect can be achieved close to room temperature. For instance, the largest $|\Delta T_p|$ value at 300 K is 3.46 K under a hydrostatic pressure of 2.1 GPa, which is roughly three times as large as the maximum electrocaloric temperature change of about 1 K measured by a direct approach in BTO single crystal [48, 125, 164]. In addition, $|\Delta T_p|$ is indeed in the range of temperature changes for other barocaloric effects as shown in Table. 6.1. The most important feature found here is that BTO can be operational at room temperature compared with other barocaloric materials (see Table. 6.1). Nevertheless, the driving pressure is much higher than those used in other barocaloric materials resulting in a modest value of $|\Delta T_p|/p$ (see Table. 6.1). In order to lower the high pressure, one may increase the initial temperature according to Fig. 6.1(c). Unfortunately, the foregoing advantage (working near room temperature) is lost using this technique. Alternately, it may be useful to consider $\text{Ba}_x\text{Sr}_{1-x}\text{TiO}_3$ solid solutions, in which an introduction of Sr into BTO can lower the transition temperature [19, 177]. Therefore, it is expected that the barocaloric effect in $\text{Ba}_x\text{Sr}_{1-x}\text{TiO}_3$ can remain large and operational near room temperature in which a significantly lower driving pressure is needed near its relatively “high” T_c .

Figure. 6.1(d) shows the barocaloric temperature change $|\Delta T_p|$ as a function of the initial temperature T [281–400 K] with different pressures applied. The most interesting feature found here is that there are very small variations in $|\Delta T_p|$ (<0.5 K), which suggests an extremely wide operational temperature window [305–353 K]. Note that the first-order phase transition usually results in a sharp caloric response in the vicinity of the transition point, which is not desired for cooling applications. In our case, such behavior is exactly observed prior to T_c . Above T_c , the driving pressure p_c needed to suppress the polarization decreases [see Fig. 6.1(b)]. For instance, p_c at 300 K is 2.1 GPa while p_c is about 1.5 GPa at 330 K. In other words, the identical hydrostatic pressure (i.e., 2 GPa) at a relatively low temperature (300 K) is actually above the critical pressure (1.5 GPa) at higher temperatures (330 K). Therefore the sharp phase transition is already over and there is no additional change in $|\Delta T_p|$. As T increases, the pressure-induced-polarization change becomes smaller, which finally results in the findings in Fig. 6.1(d) that $|\Delta T_p| > 3$ K can span a wide temperature range of about 50 K. Note that the spanning temperature T_{span} can be further expanded over 50 K by increasing pressure [see Fig. 6.1(c)]. Note that the finding here is similar with the elastocaloric effect reported in PTO, in which a wide working temperature window is also obtained by application of a tensile stress field [49]. In addition, Table. 6.1 also compares the refrigerant capacity $R \simeq |\Delta S_p||\Delta T_p|$ obtained in this work with

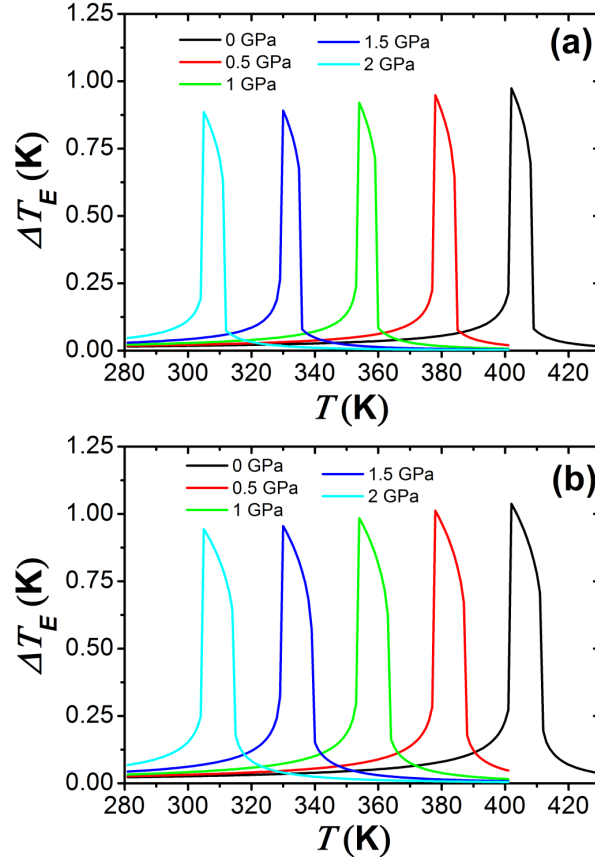


Figure 6.2: Electrocaloric temperature change ΔT_E in response to adiabatic application of an external electric field E under different hydrostatic pressure states as a function of temperature T in BTO single crystal: (a) $E=8$ kV/cm and (b) $E=12$ kV/cm, respectively.

those reported in the literature. It is shown that the refrigerant capacity obtained in BTO single crystal is about 11.8 J/kg, which is comparable to the other typical barocaloric materials.

6.2 PRESSURE-MEDIATED ELECTROCALORIC EFFECT IN BaTiO_3 SINGLE CRYSTALS

Electrocaloric effect has been intensively investigated in various BTO samples including single crystal and thin films [47, 48, 76, 123, 125, 164, 166, 201, 209, 319]. Note that BTO single crystal is not suitable for near room-temperature refrigeration as the Curie temperature ($T_c \sim 401$ K) is well above room temperature [48, 125, 164, 283, 319, 360, 395]. There is no experimental report on the effect of pressure on the electrocaloric property in BTO single crystal. While understanding the pressure-mediated electrocaloric effect in BTO single crystal is of special interest, as it may provide a solution to tune the electrocaloric effect. For example, it was

reported that pressure can result in a several fold enhancement of the electrocaloric peak in relaxors at 0.5 GPa [99]. In addition, application of uniaxial stress was reported to enhance the electrocaloric effect in ultrathin BTO films [166]. In our study, we used the foregoing model [125, 163, 164] to calculate ΔT_E in BTO single crystal under different hydrostatic pressures, which is depicted in Figs. 6.2(a) and 6.2(b).

It is shown that the electrocaloric peaks under typical electric fields of 8 kV/cm and 12 kV/cm at 0 GPa in Figs. 6.2(a) and 6.2(b) are 0.97 K and 1.03 K, respectively. These calculated values agree well with those obtained by direct measurements, e.g., 0.80 K and 0.90 K (Ref. [48]) or 1.10 K and 1.20 K (Ref. [164]). However, our results differ from the data obtained by an indirect approach in which the peak value of ΔT_E at 10 kV/cm was reported to be about 4.8 K [319]. Moreover, our results show that application of a hydrostatic pressure can remarkably move the electrocaloric peak toward room temperature due to the shift of the transition temperature induced by pressure [see Fig. 6.1(b)], which is in line with the behaviors reported in relaxor ferroelectrics [99] and LiNbO₃ [100]. However, the magnitude of the electrocaloric peak decreases slightly with pressure, which is in contrast to those reported in relaxor ferroelectrics [99] and LiNbO₃ [100]. This can be understood qualitatively as follows. ΔT_E can be estimated: $\Delta T_E \cong - \int_0^E \frac{T}{C_E} (\frac{\partial P^0}{\partial T})_{E,p} dE$, where C_E is the heat capacity under a constant electric field. In our case, the term $|\frac{\partial P^0}{\partial T}|_{E,p}$, which is the pyroelectric coefficient, is slightly enhanced when hydrostatic pressure is applied. This result is in line with the behavior of LiNbO₃ [100]. Note that $|\frac{\partial P^0}{\partial T}|_{E,p}$ does not necessarily ensure the magnitude of the electrocaloric effect [123, 177, 306], since the temperature, heat capacity and electric field change also contribute to the above integration. In BTO single crystal, it is found that the reduction in the term $\frac{T}{C_E}|_{E,p,T}$ is dominant, which compensates the enhancement coming from the term $|\frac{\partial P^0}{\partial T}|_{E,p}$. As a result, a slight decrease in ΔT_E with pressure is observed.

6.3 SUMMARY

In summary, we have studied the barocaloric effect and pressure-mediated electrocaloric effect in BTO single crystal using a thermodynamic model. It is demonstrated that a giant barocaloric effect ($|\Delta T_p| > 3$ K) with a wide temperature span about 50 K can be achieved in BTO single crystal near room temperature. In addition, tuning of the electrocaloric effect by the hydrostatic pressure in BTO single crystal mainly has two outcomes: a significant shift of electrocaloric peak towards room temperature and a slight reduction of the electrocaloric effect. Our preliminary results reveal a potential route to combine the pressure-induced barocaloric effect and pressure-mediated electrocaloric effect in the same material, which may give a handle to tune the electrocaloric effect and further enhance total refrigerant capacity and efficiency.

- CHAPTER 7 -

MULTICALORIC EFFECT IN FERH/BATIO₃ HETEROSTRUCTURE

In multiferroic materials and heterostructures [98], “multicaloric” effects [8, 10] can exploit multiple sources of entropy and be driven by either single stimulus [10] or multiple stimuli (applied/removed simultaneously or sequentially) [8]. While theoretical descriptions of multicaloric effects are now emerging [10, 49, 50, 105, 376], experiments are still limited to probing individual effects [65, 66, 396]. In particular, multiple-stimulus caloric cycles have yet to be realized, and their advantage over conventional cycles is not clear. In this chapter, we propose and realize a magnetic-electric multicaloric cycle in a multiferroic heterostructure, and use it to solve a real and longstanding problem, i.e., a large hysteresis that impeded reversibility in an otherwise promising magnetocaloric material FeRh (Section 7.1). Then we will present a purely electric-field driven refrigeration cycle which was overlooked in the literature (Section 7.2). Finally, it is the conclusion part (Section 7.3) in this Chapter. Note that the work done in this chapter is done in strong collaboration with Lee C. Phillips, Richard Mattana, Manuel Bibes, and Agnès Barthélémy from Oxitronics group of Thales lab at Palaiseau.

7.1 LARGE REVERSIBLE CALORIC EFFECT IN FERH THIN FILMS VIA A DUAL-STIMULUS MULTICALORIC CYCLE

Our heterostructure consists of a thin film of equiatomic FeRh alloy on a single-crystal BaTiO₃ (BTO) substrate. FeRh exhibits a giant negative magnetocaloric effect near room temperature [13], arising from an unusual first-order transition near 350 K between antiferromagnetic and ferromagnetic order, whose physical origin is still under debate. For instance, it was originally reported that the electronic entropy change drives this transition and therefore results in the giant magnetocaloric effect [13, 85, 397]. Recent x-ray photoemission [398] and Hall [399] measurements showed that the electronic structure changes significantly during the transition. However, the electronic contribution is regarded insufficient to depict the large entropy change at the transition. While recent specific heat data indicated that the electronic entropy part is small, the transition and thus magnetocaloric effect are dominated by magnetic fluctuations [400]. In addition, the origin of giant magnetocaloric effect was suggested to be from change of magnetic

Table 7.1: Comparison of different magnetocaloric effects in selected materials ($\mu_0 H=2$ T).

| Material | Year | T [K] | $ \Delta S/\mu_0 H $ [J/K kg T] | $ \Delta T/\mu_0 H $ [K/T] | Reference |
|--|------|------------|------------------------------------|-------------------------------|-----------|
| Fe ₄₉ Rh ₅₁ | 1990 | 308 | 10.0 | 6.5 | [13] |
| Gd ₅ Si ₂ Ge ₂ | 1997 | 280 | 7.0 | 3.7 | [9] |
| MnAs | 2001 | 317 | 15.5 | 2.4 | [30] |
| Ni _{52.6} Mn _{23.1} Ga _{24.3} | 2001 | 300 | 3.2 | 2.1 | [31] |
| MnFeP _{0.45} As _{0.55} | 2002 | 305 | 7.3 | 3.9 | [32] |
| LaFe _{11.57} Si _{1.43} H _{1.3} | 2003 | 291 | 12.0 | 3.5 | [33] |
| LaFe _{11.7} Si _{1.3} H _{1.1} | 2003 | 287 | 14.0 | 3.6 | [33] |
| Ni ₅₀ Mn ₃₇ Sn ₁₃ | 2005 | 299 | 2.4 | 1.6 | [34] |
| MnCoGeB _{0.02} | 2010 | 277 | 10.0 | 5.1 | [35] |
| Ni _{45.2} Mn _{36.7} In ₁₃ Co _{5.1} | 2012 | 317 | 9.0 | 3.1 | [11] |
| La _{0.7} Ca _{0.3} MnO ₃ | 2013 | 190 | 9.0 | 3.0 | [36] |
| Ni ₄₄ Mn _{36.7} In _{14.1} Co _{5.2} | 2014 | 300 | 8.0 | 3.0 | [12] |

state of Rh between antiferromagnetic phase and ferromagnetic phase [401]. Nevertheless, it is known that the phase transition in FeRh alloys can be induced by temperature [402], magnetic field [13, 85, 397], mechanical stress [59], hydrostatic pressure [78, 394, 402, 403], and laser [404]. As we have mentioned already in the Chapter 1, FeRh is quite special in caloric family. The giant magnetocaloric effect was discovered in FeRh [13] some years before the better-known result in Gd₅Si₂Ge₂ compounds [9], and its caloric parameters ~ 20 J/K kg and ~ 13 K (in 2 T field) [13] make FeRh a highly competitive magnetocaloric material even today (see Table. 7.1) [8, 14]. As the transition is accompanied by a unit cell volume expansion of about 1%, FeRh is also barocaloric [78, 394] and elastocaloric [59]. As long as the sharp first-order phase transition is triggered, a giant caloric effect with a large entropy change (~ 12 - 20 J/K kg) [13, 59, 78, 85, 394, 397, 401, 404] is achieved regardless of whatever stimulus is used. This makes this alloy very promising in cooling applications. However, the broad hysteresis often associated with the transition [9, 14, 85, 405] (and to a lesser extent the high cost of Rh) are key drawbacks for applications. The former results in a dramatic degradation of magnetocaloric effect versus refrigeration cycles as observed by recent direct measurements [394], which is in contrast to the nominal reproducible magnetocaloric effect results calculated either by DSC [78] or by magnetization-magnetic field curves [406]. The irreversibility of the magnetocaloric is associated with very broad or incomplete transitions, which arise in disordered thick films [407] and in very thin FeRh films [408, 409]. In particular, the irreversibility of the magnetocaloric effect is severe in very thin FeRh films due to an extremely broad or incomplete transition [408, 409]. While the irreversibility and hysteresis losses in other caloric materials with first-order magnetic transitions have been reduced by doping [83, 175], or introducing porosity [174], such reductions have remained elusive in the case of FeRh.

Previous works showed that FeRh/BTO heterostructures exhibit the largest magnetoelectric

coupling coefficient [103, 410], implying the existence of a large effective electrocaloric effect (technically an electric-field induced mechanocaloric effect [8], as will be discussed later) driven by a voltage applied across the BTO. Unfortunately, in our previous work [103] the electric field-induced transition was mostly irreversible. Here we achieve a large reversible magnetocaloric effect in FeRh/BTO structures via a dual-stimulus multicaloric cycle that employs both magnetic and electric fields. Although dual-stimulus cycles do not remove intrinsic losses as previously claimed [11], we show that those losses are not important enough to exclude practical applications, and we thus suggest a route to revive the potential of FeRh for magnetic cooling applications. We recall that there is still a controversy over whether magnetocaloric effect in FeRh is reversible [9, 78, 394, 405, 406, 411]. Most papers indicate that this effect is not reversible during the first application of magnetic field due to the sharp first-order phase transition. Our multicaloric cycle provides one possible solution to overcome this irreversibility including the first cycle and following cycles.

Our dual-stimulus multicaloric refrigeration cycle is schematized in Fig. 7.1. While a similar multicaloric cycle using pressure was discussed elsewhere [11], the full cycle was not performed experimentally. For the following proposal only, we suppose that all steps can be performed fast enough to avoid heat leakage from the FeRh thin film into the BTO substrate, aided e.g. by a thermal barrier layer that preserves strain coupling. Under these circumstances, we imagine the rapid changes to be “adiabatic” in principle. Initially, the FeRh thin film is in its antiferromagnetic phase and the BTO substrate has a mixed 90° *a/c* ferroelastic domain structure. The cycle begins (step 1) by applying (increasing) a magnetic field H adiabatically, favouring the FM phase of FeRh and causing the FeRh film to cool down. This is followed by absorbing heat from an external source keeping constant (step 2), due to the negative magnetocaloric effect [8, 13, 14, 78, 85, 394, 406]. At step 3, the electric field E is applied adiabatically to the BTO substrate resulting in more *c*-domains and thus favoring the antiferromagnetic phase of FeRh thin films [103, 410]. The magnetic field H is then removed (decreased) adiabatically causing the FeRh to heat up (step 4), followed by a heat ejection towards the external source (step 5). Finally, electric field E is removed (step 6). Our proposed refrigeration cycle differs from purely magnetic ones by the introduction of electric field in steps 3 and 6, whose effect on FeRh is in principle similar to that of a magnetic field [Fig. 7.1(b)], but which in practice does not stimulate the FeRh transition. The typical magnetocaloric effect in FeRh follows a path with a large virgin effect, followed by a smaller reversible trajectory [394, 406][path 1-2-3, Fig. 7.1(c)]. By selecting appropriate values of electric field E , we may apparently cancel the hysteresis and achieve repeatable “anhysteretic” magnetic loops [path 1-4, Fig. 7.1(c)], although the electric-field induced elastic strain applied in steps 3 and 6 converts an amount of mechanical work into heat that is similar to the magnetic work saved [Fig. 7.1(d)]. Instead, we achieve reversible changes that are considerably larger than those achievable in a single-stimulus cycle with either magnetic or electric field. We now present an experimental demonstration of a slow, isothermal analogue of the proposed cycle in FeRh/BTO.

We grew a ~40-nm thick epitaxial FeRh film at 630 °C by magnetron sputtering (at 903 K with a power of 45 W and in argon pressure of 0.860 Pa) from an equiatomic Fe₅₀Rh₅₀ target onto a 500- μ m thick single-crystal (001) BTO (SurfaceNet GmbH) substrate. The films were then annealed *in situ* at 1003 K for 90 min. The high film quality, including epitaxy, surface and

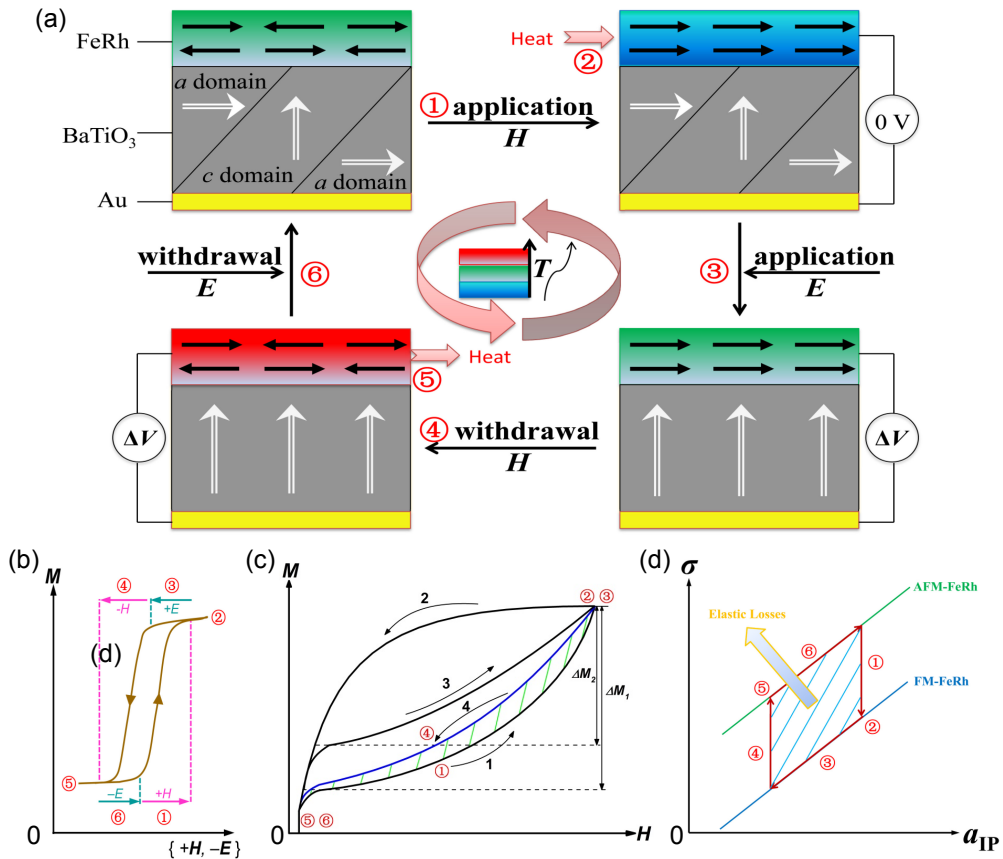


Figure 7.1: Multicaloric refrigeration cycle. (a) Schematic of a dual-stimulus multicaloric refrigeration cycle. (b) Schematic of the effect of electric and magnetic fields (E , H) on the magnetization M of FeRh. The electric field overcomes the hysteresis, but does not itself cause M to change. (c) Schematic of magnetic cycles, in the space of magnetization M versus magnetic field H . The blue curve denotes a path followed in the presence of the electric field. Black uncircled numbers refer to measurement paths described in the main text. (d) Schematic of elastic losses, in the space of biaxial thin film stress σ versus average in-plane lattice constant of FeRh a_{IP} . In (a-d) the red circled numbers 1-6 correspond to the steps described in the main text, and in (b-d) arrows indicate the sequence of proposed measurements.

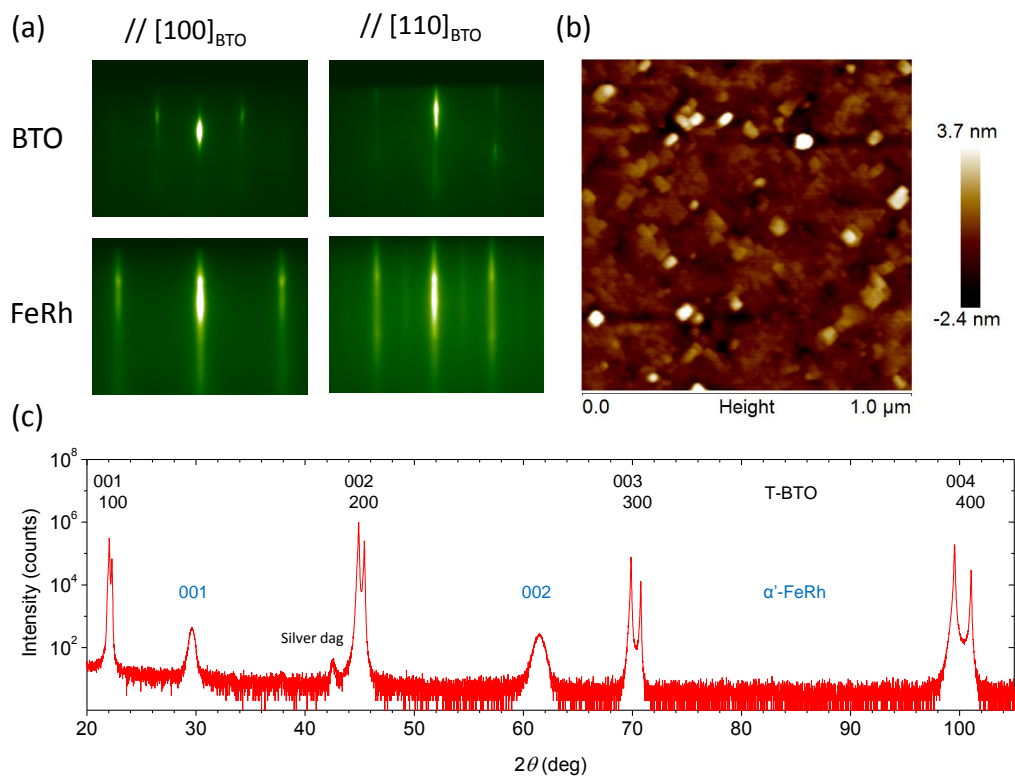


Figure 7.2: (a) Reflection high-energy electron diffraction images of the BTO substrate before growth and the FeRh after growth and annealing, at two azimuths along $[100]_{BTO}$ and $[110]_{BTO}$, respectively; (b) Surface morphology FeRh thin films characterized by tapping mode Atomic Force Microscope over over $1 \mu\text{m}^2 \times 1 \mu\text{m}^2$ images; (c) θ - 2θ scans of FeRh films grown BTO substrate at 300 K.

Fe/Rh order parameter, were confirmed by reflection high-energy electron diffraction images, Atomic Force Microscope images and X-ray diffraction scans in Fig. 7.2, respectively [103]. A 50-nm-thick Au layer was sputtered on the back side of the BTO as a bottom electrode, and voltages were applied across the thickness of the BTO substrate.

We use a film around twice as thick as in our previous work [103, 410] in order to avoid the particularly large hysteretic losses of very thin FeRh films [103, 408–410] which are due to grain size reduction [408] and substrate-induced strain [103]. Magnetization measurements were carried out in a Quantum Design superconducting quantum interference device (SQUID) magnetometer with a maximum accessible temperature of 400 K and the capability to apply magnetic field up to 5 T. Given that most experimental works on the caloric effect were characterized by isothermal entropy changes rather than direct measurement of adiabatic temperature changes^{1,11}, we use magnetization as a proxy for the progress of the first-order transition, because the fast heat exchange between thin films and substrates prevents us from carrying out direct thermal measurements [36].

Figure. 7.3 shows isothermal magnetization (M) versus magnetic field (H) curves measured on increasing and decreasing magnetic field at 385 K [Figs. 7.3(a)-7.3(c)] and 395 K [Figs. 7.3(d)-7.3(f)] immediately after heating from room temperature, either with no applied electric field [Figs. 2(a) and 7.3(d)], or magnetized and demagnetized under various moderate voltages ΔV close to the coercive voltage ($\pm \sim 50$ V) of the BTO [103, 410]: -10 V and 60 V [Figs. 7.3(b) and 7.3(e)], and 0 V and 100 V [Figs. 7.3(c) and 7.3(f)], where the voltage values are chosen to manipulate the fraction of BTO a - and c -domains, as explained previously [410]. We chose two temperatures within the broad FeRh transition to show that the shapes of the curves have no systematic temperature dependence, although absolute M values are higher at 395 K where ferromagnetic-FeRh is generally favoured. Similarly, in Figs 7.3(b) and 7.3(c) the BTO contained mostly c -domains throughout, resulting in generally lower M values. Our calculations consider only the region $\mu_0 H > 0.25$ T where the ferromagnetic phase is magnetically saturated, and thus the magnetization represents the amount of ferromagnetic phase present. We define the *reversible range* of FeRh magnetization ΔM as the range in M that is covered in both increasing and decreasing H sweeps [green bars, Figs. 7.3(a)-7.3(f)]. The irreversibility is apparent in Fig. 7.3(a) where we have included the results of a second magnetic field sweep, during which the magnetization remains rigidly within this reversible range.

Our main result is that optimized multicaloric cycles [Figs. 7.3(c) and 7.3(f)] yield larger reversible ΔM , and hence the reversible isothermal heat Q pumped during one magnetocaloric cycle [Fig. 7.3(g)] is also larger compared to either magnetic field alone [Figs. 7.3(a) and 7.3(d)] or electric field alone (Fig. 3 of Ref. [103]). Here we use $Q = T\rho V\Delta S_{max}(\Delta M/\Delta M_{max})$ where the FeRh film has mass density $\rho=9760$ kg cm⁻³, V is the film volume, and we use literature values $\Delta M_{max}=1190$ e.m.u./cm³ (Ref. [78]) and $\Delta S_{max}=17$ J/K kg (Ref. [400]) for the complete transition because the SQUID maximum temperature of 400 K prevents us from acquiring the full dataset to estimate ΔS_H via the Maxwell relation [412].

Interestingly, we also reduce the magnetic work (or magnetic hysteresis losses) W_{mag} , defined by the difference in area $\int M dH$ between curves with increasing and decreasing H , by up to 96% [Fig. 7.3(h)] because the voltage-induced strain effect arising from the BTO domain structure [103, 410] brings the FeRh close to the onset of transformation before each variation

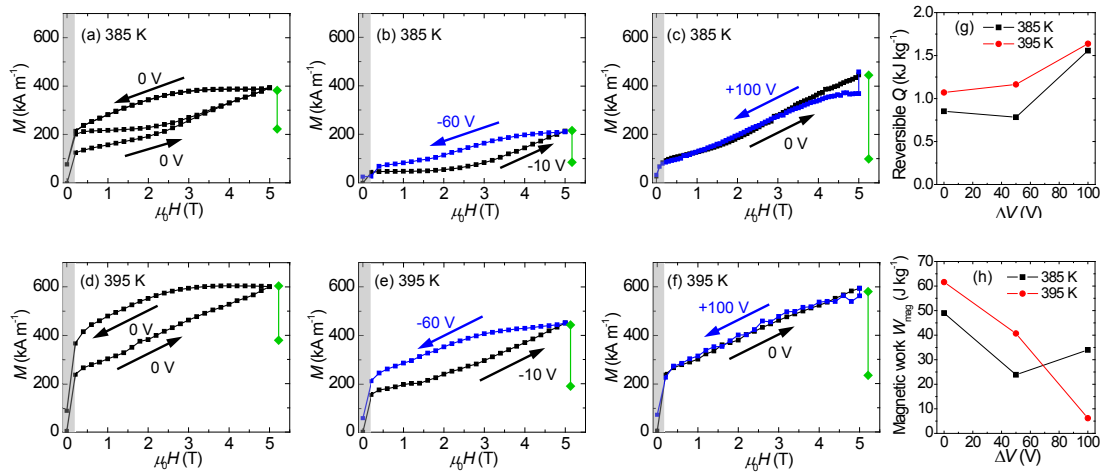


Figure 7.3: Isothermal magnetic measurements. (a-f) Experimental magnetization versus magnetic field curves during isothermal (a,d) magnetic, (b-c, e-f) magnetic-electric cycles at (a-c) 385 K and (d-f) 395 K. The grey shaded region ($\mu_0 H < 0.25$ T) is dominated by rearrangement of ferromagnetic domains. Diamond-headed green markers indicate the reversible magnetization change ΔM achieved in each cycle. (g) Reversible isothermal heat Q and (h) magnetic work done, vs. the change in voltage ΔV at $\mu_0 H = 5$ T.

Table 7.2: Comparison of isothermal heat $Q = |T\Delta S_H|$, hysteresis loss W and coefficient of performance $COP_{max} = Q/W$, between $Gd_5Ge_2Si_2$ alloys (before/after doping with Fe in Ref. [83]) and FeRh thin films.

| Material | H | Q | W | COP_{max} |
|--------------------------------|-----|---------|--------|-------------|
| | [T] | [kJ/kg] | [J/kg] | |
| $Gd_5Si_2Ge_2$ | 2 | 5.1 | 78.0 | 65.4 |
| $Gd_5Si_2Ge_{1.9}Fe_{0.1}$ | 2 | 2.135 | 3.9 | 555.5 |
| FeRh/BTO (without ΔV) | 5 | 1.64 | 61.6 | 26.9 |

of H . Such a reduction would be superior to previous work on hysteresis reduction in Ni-Mn-In-Co/Pb(Mg_{1/3}Nb_{2/3})O₃-PbTiO₃(PMN-PT) (Ref. [12]), but as we introduce work in the elastic cycle [Fig. 7.1(b)], we do not make this claim, and we use the term hysteresis losses to describe W_{mag} here. Comparing our work to Ref. [12], the epoxy bonding in Ni-Mn-In-Co/PMN-PT is much weaker than our epitaxial contact, and the resulting relatively weak magnetoelectric coupling may limit the reversibility of magnetocaloric effect for applications. The important mechanical work was also overlooked in the elastic cycle [12]. Therefore we emphasize the need for caution when analyzing multicaloric refrigeration cycles of the type we propose in Fig. 7.1.

To understand whether losses in our FeRh/BTO system would prohibit practical applications, in Table. 7.2 we compare it with undoped and doped $Gd_5Si_2Ge_2$ [83] in terms of the fundamental parameters of magnetocaloric cooling devices [8], i.e. the isothermal heat Q and the pumped heat/total work ratio Q/W , which constitutes an upper bound to the thermodynamic coefficient of performance (COP), COP_{max} , for refrigerators. Here we take Q for FeRh/BTO at 395 K and $\Delta V=100$ V, but we use $W=W_{mag}$ for the cycle at 395 K without voltage, because the total W should be approximately the same for all multicaloric cycles. While the value $COP_{max}=26.9$ for our highly lossy FeRh thin film is lower than for even undoped $Gd_5Si_2Ge_2$, this should not at all be the dominant inefficiency in the system. For example, in a non-isothermal refrigeration cycle with a hot reservoir at $T_h=395$ K and a temperature span ($T_h - T_c$)=8.5 K (Ref. [85]), the COP is bounded by the Carnot limit $COP_{Carnot} = T_c/(T_h - T_c)=45.5$; assuming $COP_{Carnot} = Q/W_{Carnot}$, our additional work W would lead to $COP = Q/(W + W_{Carnot})=16.8$ or 37% of the Carnot efficiency. These figures are competitive, and it is likely that the real COP would be dominated by other losses in the device, which in our case would include losses in the substrate ferroelectric cycle (which can themselves be reduced by optimization). We do not calculate the refrigerant capacity (Ref. [83]) here, as our data does not reveal the full temperature dependence of the entropy change.

Although here we report data only at 385 K and 395 K, an advantage of using FeRh thin films is that the large reversible caloric effects can be potentially achieved at any temperature within the ~ 100 K wide tetragonal phase field of BTO (including room temperature) because the FeRh transition temperature can be tuned over hundreds of kelvins and through room temperature by doping with other metallic elements [413]. This extreme tunability is in contrast with, for example, the La_{0.7}Ca_{0.3}MnO₃/BTO system (~ 6 K) where reversible magnetocaloric effect is

restricted to the vicinity of the rhombohedral-orthorhombic transition of BTO at around 200 K [8]. We note that the tuning of the metamagnetic phase transition temperature by electric field as we have already achieved in Refs. [103] and [410] is also ideal to achieve a large temperature span in an active magnetic regenerator [12]. Moreover, the tunability of our FeRh/BTO system is considerably greater than that in Ni-Mn-In-Co/PMN-PT (<10 K, Ref. [12]).

The fact that the transition from antiferromagnetic phase to ferromagnetic phase at 385 K is not fully achieved under 5 T [see Figs. 7.3(a)-7.3(b)], in line with previous results on ultrathin FeRh thin films [408, 409], suggests that even larger effects could be obtained by microstructural optimization, e.g. by nanopatterning to artificially introduce porosity. Also, as the strain states in FeRh are discrete i.e., related to either an *a*- or *c*-domain of BTO, it is difficult to access to a wider range of strain states in FeRh [103, 410]. In contrast, a continuous range of electro-strains can be achieved if FeRh thin films are grown on a relaxor substrate like PMN-PT, which would also fortuitously reduce the losses in the substrate (as in Ref. [12]).

7.2 GIANT ELECTRIC-FIELD INDUCED MECHANOCALORIC EFFECT IN HYBRID FERH/BATIO₃ HETEROSTRUCTURE

Indeed, an optimized device may also permit a purely electric-field driven refrigeration cycle consisting of steps 3 and 6 alone. To be specific, one ideal refrigeration cycle can be designed as schematized in Fig. 7.4. Initially, the FeRh thin film is in its ferromagnetic phase. The cycle begins (step 1) by applying an electric field on BTO substrate adiabatically, favoring the antiferromagnetic phase of FeRh thin films. As expected, it causes a heating of FeRh thin films due to a negative caloric effect and follows a heat exchange by ejecting heat from thin film to the load (step 2). At step 3, the electric field is removed adiabatically leading to a cooling of FeRh thin film by absorbing heat from a sink (step 4).

This overlooked electric-field induced mechanocaloric effect [8] may also open a new paradigm to potentially overcome the inevitable uneconomic investments on clumsy magnets in magnetic cooling. Unlike traditional magnetocalorics [8, 14], the entropy change is induced upon application of an electric field on BTO substrate rather than a magnetic field directly applied on FeRh (step 1) thanks to the magnetoelectric coupling. As the elastic hysteresis losses are not critical, the novel mechanocaloric effect subjected to the electric-field induced two-dimensional stress/strain (see Fig. 7.4) could be a low-cost approach for developing the next generation of solid state refrigeration.

We emphasize that our multicaloric effects rely on strain-mediated coupling [98] but not on any phase transition of BTO, and are thus exempt from the requirement that the magnetic and ferroelectric/piezoelectric layers should have similar phase transition temperatures [10, 376] suggested in a recent theoretical study [415]. In addition, a purely magnetic heat-pump scheme without any second stimulus was proposed theoretically in FeRh without experimental evidence [416] while our proposed multicaloric refrigeration cycle is realized by experimental support.

Tables. 7.3 and 7.4 together with Figs. 7.5(a)-7.5(d) show the promise of FeRh/BTO in the electric-field induced mechanocaloric effect by comparing its performance with a representative sample of competitive electrocaloric materials [46, 48, 150]. FeRh/BTO would perform compara-

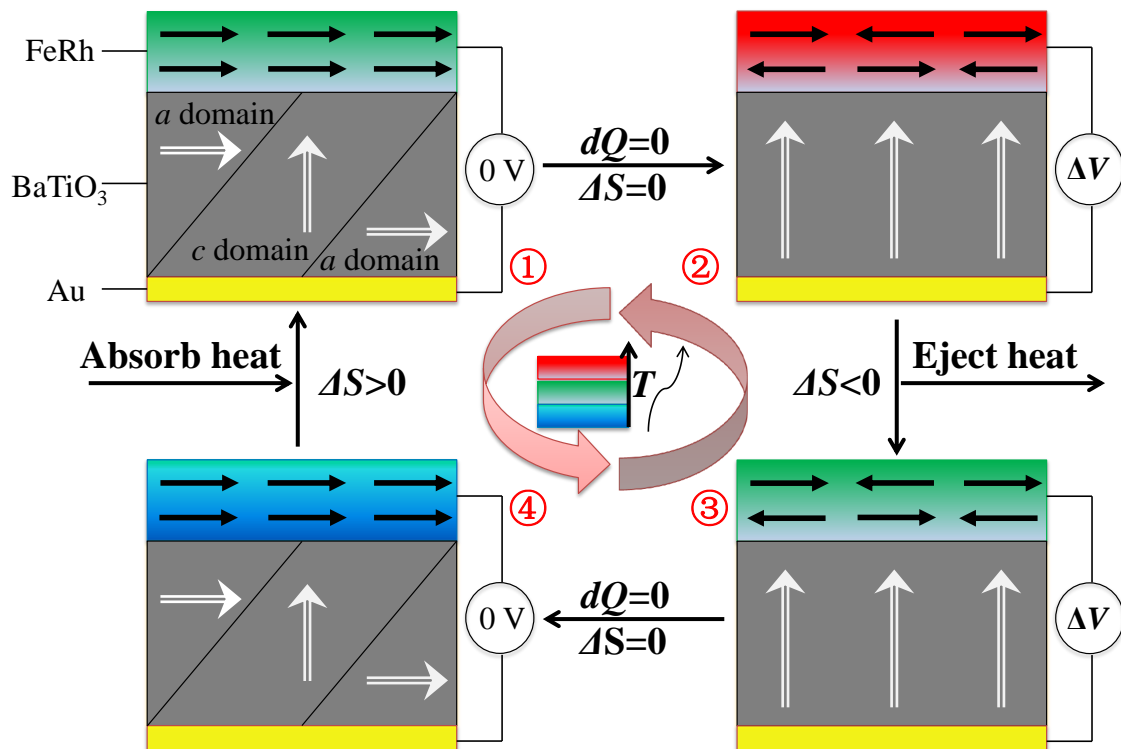


Figure 7.4: Schematic of an ideal electric-field induced mechanocaloric refrigeration cycle.

Table 7.3: Comparison of different electric-field induced caloric effects in selected materials (A).

| Material ^{a)} | T [K] | ΔE [kV/cm] | ΔS_E [J/K kg] | $ \Delta S_E/\Delta E $ [J cm/kV kg K] | Refs |
|--|------------|-----------------------|--------------------------|---|-------|
| BTO ^{SC} | 397 | 4 | 2.1 | 0.53 | [48] |
| BTO ^{SC} | 409 | 10 | 5.9 | 0.59 | [319] |
| Pb(Mg _{1/3} Nb _{2/3}) _{0.75} Ti _{0.25} O ₃ ^{SC} | 383 | 25 | 1.0 | 0.042 | [414] |
| Pb _{0.99} Nb _{0.02} (Zr _{0.75} Sn _{0.20} Ti _{0.05})O ₃ ^C | 434 | 30 | 4.3 | 0.14 | [44] |
| BaZr _{0.2} Ti _{0.8} O ₃ ^C | 312 | 145 | 8.0 | 0.055 | [150] |
| BaTi _{0.895} Sn _{0.105} O ₃ ^C | 301 | 20 | 0.83 | 0.042 | [161] |
| Terpolymer ^{b)} /BNNSs/BST67 ^{NC} | 303 | 2500 | 210 | 0.084 | [214] |
| Terpolymer ^{c)} /PMN-PTNC ^{NC} | 303 | 1800 | 133 | 0.074 | [52] |
| PbZr _{0.95} Ti _{0.05} O ₃ ^{TF} | 495 | 500 | 8.1 | 0.016 | [15] |
| (Pb _{0.97} La _{0.02})(Zr _{0.95} Ti _{0.05})O ₃ ^{TF} | 303 | 308 | -5.4 | 0.018 | [51] |
| P(VDF-TrFE) ^{TF} | 343 | 2000 | 55.4 | 0.028 | [46] |
| BTO ^{UTF} | 300 | 12500 | 8.4 | 0.00067 | [47] |
| LSMO/PMN-PT ^{HH} | 280 | 7 | -1.43 | 0.20 | [106] |
| FeRh/BTO ^{HH} | 385 | 2 | -7.8 | 3.9 | Here |

^{a)} *SC*, *C*, *NC*, *TF*, *UTF*, and *HH* indicate the material form of Single Crystal, Ceramic, Nanocomposite, Thin Film, Ultrathin Film, and Hybrid Heterostructure, respectively.

^{b)} Terpolymer refers to the relaxor ferroelectric P(VDF-TrFE-CFE) with a composition of 62.3/29.9/7.8 mol%, BNNSs refers to Boron nitride nanosheets (9 vol%) and BST67 refers to Ba_{0.67}Sr_{0.33}TiO₃.

^{c)} Terpolymer refers to P(VDF-TrFE-CFE) (59.4/33.4/7.2 mol%) and PMN-PT refers to 0.9PMN-0.1PT nanoparticles with the content of 37.5 wt%.

Table 7.4: Comparison of different electric-field induced caloric effects in selected materials (B).

| Material ^{a)} | T [K] | ΔE [kV/cm] | ΔT_E [K] | $ \Delta T_E/\Delta E $ [K cm/kV] | Refs |
|--|------------|-----------------------|---------------------|--------------------------------------|-------|
| BTO ^{SC} | 397 | 4 | 0.87 | 0.22 | [48] |
| BTO ^{SC} | 409 | 10 | 4.8 | 0.48 | [319] |
| Pb(Mg _{1/3} Nb _{2/3})0.75Ti _{0.25} O ₃ ^{SC} | 383 | 25 | 1.1 | 0.044 | [414] |
| Pb _{0.99} Nb _{0.02} (Zr _{0.75} Sn _{0.20} Ti _{0.05})O ₃ ^C | 434 | 30 | 2.5 | 0.083 | [44] |
| BaZr _{0.2} Ti _{0.8} O ₃ ^C | 312 | 145 | 4.5 | 0.031 | [150] |
| BaTi _{0.895} Sn _{0.105} O ₃ ^C | 301 | 20 | 0.61 | 0.0305 | [161] |
| Terpolymer ^{b)} /BNNSs/BST67 ^{NC} | 303 | 2500 | 50.5 | 0.0202 | [214] |
| Terpolymer ^{c)} /PMN-PT ^{NC} | 303 | 1800 | 31 | 0.0172 | [52] |
| PbZr _{0.95} Ti _{0.05} O ₃ ^{TF} | 495 | 500 | 12 | 0.024 | [15] |
| (Pb _{0.97} La _{0.02})(Zr _{0.95} Ti _{0.05})O ₃ ^{TF} | 303 | 308 | -5.0 | 0.016 | [51] |
| P(VDF-TrFE) ^{TF} | 343 | 2000 | 12 | 0.006 | [46] |
| BTO ^{UTF} | 300 | 12500 | 5.8 | 0.00046 | [47] |
| LSMO/PMN-PT ^{HH} | 280 | 7 | 0.61 | 0.087 | [106] |
| FeRh/BTO ^{HH} | 385 | 2 | -5.2 | 2.6 | Here |

^{a)} *SC*, *C*, *NC*, *TF*, *UTF*, and *HH* indicate the material form of Single Crystal, Ceramic, Nanocomposite, Thin Film, Ultrathin Film, and Hybrid Heterostructure, respectively.

^{b)} Terpolymer refers to the relaxor ferroelectric P(VDF-TrFE-CFE) with a composition of 62.3/29.9/7.8 mol%, BNNSs refers to Boron nitride nanosheets (9 vol%) and BST67 refers to Ba_{0.67}Sr_{0.33}TiO₃.

^{c)} Terpolymer refers to P(VDF-TrFE-CFE) (59.4/33.4/7.2 mol%) and PMN-PT refers to 0.9PMN-0.1PT nanoparticles with the content of 37.5 wt%.

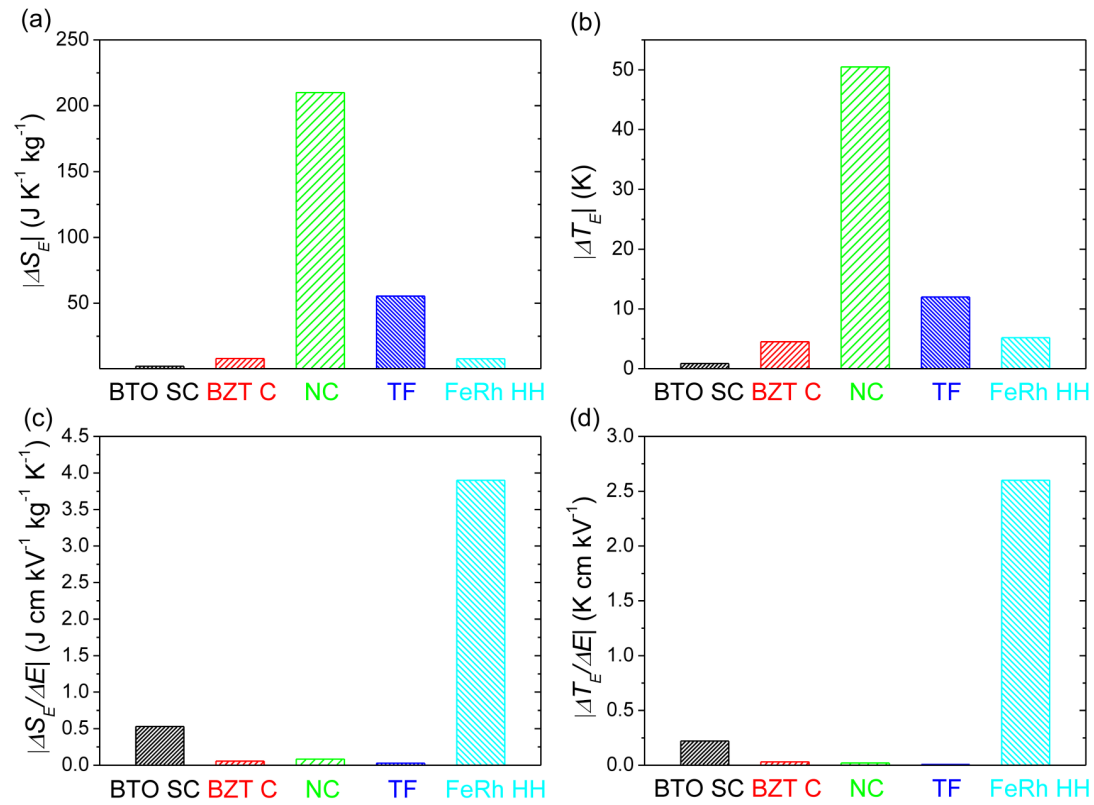


Figure 7.5: Comparison of different electric-field induced caloric effects in selected materials. Comparison of caloric effect [(a) $|\Delta S_E|$ and (b) $|\Delta T_E|$] and strength [(c) $|\Delta S_E/\Delta E|$ and (d) $|\Delta T_E/\Delta E|$] between FeRh/BaTiO₃ hybrid heterostructure (HH) and typical giant electrocaloric materials in the literature: BaTiO₃ single crystal (SC) (Ref. [48]), BaZr_{0.2}Ti_{0.8}O₃ (BZT) ceramic (C) (Ref. [150]), P(VDF-TrFE-CFE)/Boron nitride nanosheets/Ba_{0.67}Sr_{0.33}TiO₃ nanocomposite (NC) (Ref. [214]), and P(VDF-TrFE) thin film (TF) (Ref. [46]), respectively.

bly to all of these systems except for P(VDF-TrFE-CFE)/Boron nitride nanosheets/Ba_{0.67}Sr_{0.33}TiO₃ nanocomposite (NC) (Ref. [214]), which apparently outperforms all other systems. There are few mechanocaloric data available for FeRh, possibly due to concerns about irreversibility and the high price of Rh. Here we use elastocaloric parameters ($|\Delta S_E| \sim 7.8 \text{ J K}^{-1} \text{ kg}^{-1}$ and $|\Delta T_E| \sim 5.2 \text{ K}$, Ref. [59]) rather than larger barocaloric parameters (i.e., $|\Delta S_p| \sim 12.5 \text{ J K}^{-1} \text{ kg}^{-1}$, Ref. [78]) to deduce approximately the mechanocaloric effect. Interestingly, Figs. 7.5(a)-7.5(d) show that the caloric strengths $|\Delta S_E/\Delta E|$ ($3.9 \text{ J cm V}^{-1} \text{ K}^{-1} \text{ kg}^{-1}$) and $|\Delta T_E/\Delta E|$ (2.6 K cm/kV) under an electric field ΔE of $\sim 2 \text{ kV/cm}$ are at least one order of magnitude larger than previous best reports on electrocaloric effect in BTO single crystals [48] (SC), and nearly three orders of magnitude larger than those in P(VDF-TrFE) thin films [46] (TF). Our results also make a significant improvement on previous multiferroic heterostructures: $|\Delta S_E|$ is significantly larger than that ($1.43 \text{ J K}^{-1} \text{ kg}^{-1}$) in La_{0.7}Sr_{0.3}MnO₃/PMN-PT while $|\Delta S_E/\Delta E|$ is over one order of magnitude larger than that ($0.20 \text{ J cm V}^{-1} \text{ K}^{-1} \text{ kg}^{-1}$) in La_{0.7}Sr_{0.3}MnO₃/PMN-PT [106]. Obviously, electric-field-driven caloric effect strongly depends on the magnetoelectric coupling coefficient [10, 106]. As highlighted by recent first-principles calculations, the magnetoelectric coupling coefficient under adiabatic condition can be significantly enhanced compared to that under isothermal condition [107]. However, this important temperature mediated mechanism was overlooked in previous theoretical studies [10, 106]. By taking into account the thermally mediated mechanism, we modified the thermodynamic framework [10] by Vopson as follows (See Section 1.6 for more information):

$$\Delta S_E = \int_0^E \frac{\alpha_{iso}}{\chi} \left(\frac{\partial M}{\partial T} \right)_E dE. \quad (7.1)$$

$$\Delta T_E = -\mu_0 \int_0^E \frac{T}{C_E} \left[\frac{(\frac{\partial M}{\partial T})_E (\frac{\partial T}{\partial E})_S + \alpha_{iso}}{\chi} \left(\frac{\partial M}{\partial T} \right)_E \right] dE. \quad (7.2)$$

Eq. (7.1) derived from Gibbs free energy [10] is very similar to that derived from Helmholtz type [106] but with different signs. Moreover, Eq. (7.2) indicates that even though the isothermal magnetoelectric coupling coefficient $\alpha_{iso} = \mu_0 (\frac{\partial M}{\partial E})_T$ ($\Delta S_E = 0$) is zero, the adiabatic temperature change ΔT_E may not necessarily be zero due to the isentropic magnetoelectric coupling term $(\frac{\partial M}{\partial T})_E (\frac{\partial T}{\partial E})_S$ in the numerator of Eq. (7.2). Most importantly, the isentropic magnetoelectric coupling $(\frac{\partial M}{\partial T})_E (\frac{\partial T}{\partial E})_S$ does not necessarily need strong intrinsic couplings between magnetic and electric order parameters but requires that both magnetocaloric effect and electrocaloric effect alone should be large as possible [107].

Eqs. (7.1) and (7.2) have provided basic insights into achieve the largest multicaloric effect in multiferroics assuming that the temperature-mediated magnetoelectric coupling coexists with strain-mediated type. Obviously, in order to confidently determine the multicaloric effect, rigorous experimental measurements on the parameters in Eqs. (7.1) and (7.2) should be carried out especially near the ferroic phase transition rather than estimated by using any specific constant values as treated in previous studies [10, 106, 376, 415]. Obviously, other parameters including the layer thicknesses and heat capacities are important in the eventual design of a cooling system, so that their values in a composite multiferroic should be taken into account in order to determine the optimal design parameters [415].

In our FeRh/BTO heterostructures, the isothermal magnetoelectric coupling coefficient α_{iso} is the largest [103]; Magnetocaloric effect in FeRh is one of the most competitive (see Table. 7.1) [13, 59, 78, 85, 394, 397, 401, 404] while electrocaloric strength in BTO single crystals is giant [48]. As a result, the electric-field-driven caloric effect in FeRh/BTO could be significantly enhanced especially under adiabatic condition. Our results thus invite further investigations of isentropic caloric effect driven by electric field in hybrid heterostructures.

7.3 SUMMARY

In summary, our results here demonstrate that the historical irreversibility of magnetocaloric effect in FeRh discovered almost 26 years ago [13] can be solved by using an electric field. The dual-stimulus multicaloric cycle creates larger caloric effects, although the magnetic hysteresis losses are not destroyed but simply transferred to an elastic cycle. Since research in multicaloric materials has intensified recently [8], we believe that our work will stimulate more efforts in multiferroic systems [98] where strong mechanical coupling between ferroic order parameters may provide more diverse choices for the design of efficient solid-state refrigeration, including purely electric-field-driven systems. Finally, revisiting overlooked compounds like FeRh using hybrid heterostructures can also provide a new life for many magnetocaloric materials.

CONCLUSIONS AND PERSPECTIVES

8.1 CONCLUSIONS

Ten years old, the discovery of giant electrocaloric effect in ferroelectric materials showed that it is possible to employ this effect for substantial cooling applications. This last decade has been marked by increasing research interest especially in characterizing and measuring the electrocaloric effect using both so-called indirect and direct approaches. In this context, a comprehensive summary and careful reexamination of these approaches is very timely and of great importance to justify the assumptions used in different measurement techniques. The review in Chapter 2 is therefore dedicated to cover recent important and rapid advances from both the indirect and direct measurements and provides critical insights relevant for quantifying electrocaloric effect. We hope that our review will not only provide a useful background to fundamentally understand the electrocaloric effect and what we are really measuring, but also may act as a practical guide to exploit and develop electrocalorics towards design of suitable devices.

We have systematically studied the electrocaloric effect in ferroelectric ultrathin films (Section 3.1), antiferroelectric thin films (Section 3.2), ferroelectric ceramics (Section 3.3) and multilayer capacitors (Chapter 4). The key conclusions are summarized as follows:

The contribution of a built-in electric field to ferroelectric phase transition in asymmetric ferroelectric tunnel junctions is studied using a multiscale thermodynamic model. It is demonstrated in details that there exists a critical thickness at which an unusual ferroelectric-“polar non-ferroelectric” phase transition occurs in asymmetric ferroelectric tunnel junctions. In the “polar non-ferroelectric” phase, there is only one non-switchable polarization which is caused by the competition between the depolarizing field and the built-in field, and closure-like domains are proposed so as to form to minimize the system energy. The transition temperature is found to decrease monotonically as the ferroelectric barrier thickness is decreased and the reduction becomes more significant for the thinner ferroelectric layers. As a matter of fact, the built-in electric field not only results in smearing of phase transition but also forces the transition to take place at a reduced temperature. Such findings may impose a fundamental limit on the work

temperature and thus should be further taken into account in the future ferroelectric-tunnel-junction-type or ferroelectric-capacitor-type devices.

Electrocaloric effect in ultrathin symmetric SrRuO₃/BaTiO₃/SrRuO₃ capacitors is calculated by using a multiscale thermodynamic model. It is found that the electrocaloric coefficient vs working temperature is shifted to higher temperatures with increasing the BaTiO₃ layer thickness (above critical thickness). The electrocaloric effect above the critical thickness is much stronger than that below it. Furthermore, it is demonstrated that a giant electrocaloric effect (3.5 K under 0.24 V) in such capacitors (six BaTiO₃ unit cells) at 300 K can be achieved, which suggests that ultrathin ferroelectric capacitors may be promising candidates for room temperature solid-state refrigeration.

Room-temperature electrocaloric properties of Pt/BaTiO₃/SrRuO₃ ferroelectric tunnel junctions are studied by using a multiscale thermodynamic model. It is found that there is a divergence in the adiabatic temperature change ΔT_E for the two opposite polarization orientations. This difference under a typical writing voltage of 3 V can reach over 1 K as the barrier thickness decreases. Thanks to the ultrahigh external stimulus, a giant electrocaloric effect (1.53 kelvin per volt) with ΔT_E being over 4.5 K can be achieved at room temperature, which demonstrates the perspective of ferroelectric tunnel junctions as a promising solid-state refrigeration.

Using a phenomenological approach, we demonstrate that a giant mechanically-mediated electrocaloric effect can be obtained in ultrathin ferroelectric SrRuO₃/BaTiO₃/SrRuO₃ capacitors at room temperature. Our results show that the electrocaloric properties of such capacitors can be systematically tuned by applying an external stress. The depolarizing field, whose effect is usually ignored in the literature, is found to be detrimental to the electrocaloric response, especially for the thinner films. Moreover, a remarkable enhancement and broadening of the electrocaloric response can be achieved in relatively thick films under compressively loaded conditions compared with the unloaded case.

We reveal a giant negative electrocaloric effect with a significantly enhanced temperature of about -5 K under a moderate electric field of 415 kV/cm in Pb_{0.97}La_{0.02}(Zr_{0.95}Ti_{0.05})O₃ thin films. In contrast to the high working temperatures ($\sim 220^\circ\text{C}$) required for using the conventional electrocaloric effect in these films, the negative electrocaloric effect can be operated near room temperature. We demonstrate that both conventional and negative electrocaloric effect contribute to the caloric response near room temperature. We also make a systematic comparison with other typical electrocaloric materials in the literature stressing the potentialities of the system we studied. Although a solid theoretical model is still missing, our findings are qualitatively supported by recent theoretical study based on Kittel model. Moreover, we also propose a simple mechanism to understand the negative electrocaloric effect in antiferroelectrics. Our results show that antiferroelectric thin films may act as a new class of solid-state caloric materials with giant negative electrocaloric response near room temperature. Such findings make antiferroelectrics serious candidates in the field of solid-state coolers. We believe that the giant negative electrocaloric effect found here may open up a new paradigm for light, compact, reliable and high efficient refrigeration devices.

The electrocaloric effect in lead-free BaTi_{1-x}Sn_xO₃ (BTSn, x=0.08, 0.105, and 0.14) ferroelectric ceramics was studied by using an indirect method. It was found that the largest electrocaloric response could be achieved in BTSn with x=x_{QP}=0.105 near room temperature with an adi-

abatic temperature change ΔT_E of 0.61 K and an electrocaloric strength $\Delta T_E/\Delta E$ of 0.31 K mm/kV, under a modest electric field ΔE of 20 kV/cm, which is comparable with the best values reported in lead-free materials. These enhanced values are attributed to the multiphase (four phases) coexistence at $x=x_{QP}$ corresponding to the quasi-quadruple point composition.

Inhomogeneous electrocaloric temperature distributions in multilayer capacitors are directly imaged by infra-red camera. The largest variation of electrocaloric response across the multilayer capacitors is 0.285 K corresponding to 51% of the average temperature change. A sustained cooling power of 0.037 kW/m² is experimentally revealed and must be extracted from the terminals in any future device. Our results highlight the promise of infra-red imaging in correlating the electrocaloric effect with structural degrees of freedom and invite future direct measurements by this sensitive technique. From the point of Materials Science, our work provides direct imaging of spatial distribution of electrocaloric effect in multilayer capacitors, one of the most studied systems which were regarded as most promising electrocaloric prototype devices. Our work actually represents the first experimental study to carry out spatially-resolved measurement on electrocaloric effect using Infra-red camera with very comprehensive data and information. From the point of Engineering, our findings provide the first direct experimental evidence on the electrocaloric heat flux both temporally and spatially in a specific electrocaloric device for the first time. We note that understanding and control of the heat flow behavior in a caloric prototype is extremely valuable for optimizing devices. Its importance has been recognized in detail in Chapter 6 of a recent book (Ref. [6]) as well as international conferences. The measurement mode of Infra-red camera we developed here is not only useful for directly measuring the electrocaloric effect but also applicable to measure magnetocaloric and elastocaloric effects. Our findings open a route to obtain useful and unique data by using such a tool, and thus invite a broad “caloric” community for future investigations to be explored and challenged.

We have systematically studied the elastocaloric effect in ferroelectric ultrathin films (Section 5.1 and Section 5.2) and ferroelectric single crystals (Section 5.3). The key conclusions are summarized as follows:

We explore the elastocaloric response in ultrathin ferroelectric SrRuO₃/BaTiO₃/SrRuO₃ capacitors based on a developed thermodynamic model. Interestingly, while better known for their potential as non-volatile memories, we show that such capacitors reveal also exciting perspectives for cooling applications. Indeed, our calculations predict a giant room-temperature elastocaloric effect (also known as piezocaloric effect) in such ultrathin ferroelectric films. Comparison with other caloric effects demonstrates that the giant elastocaloric response found for the first time in this study can naturally overcome the drawbacks of potentially large hysteresis losses associated with first-order phase transitions, and further can limit Joule heating accompanying electrocalorics and is easier to induce than in magnetocaloric, barocaloric and other elastocaloric counterparts. Moreover, taking advantage of this unexpected large elastocaloric response in combination with the electrocaloric effect which is intrinsic to any ferroelectric, we propose an original concept of device allowing to circumvent the several current challenges in the literature. This new kind of solid-state refrigeration based on ultrathin ferroelectric capacitors with the above bicaloric (elasto- and electro-) effect is an overlooked and promising candidate for future nanodevice coolers.

We have studied the influence of epitaxial strain u_m on the elastocaloric properties of BaTiO₃

thin films. Using thermodynamic calculations, we show that there exists a critical compressive stress σ_{3c} at which the elastocaloric effect is maximized for any compressive misfit strain we investigate. Moreover, it is found that $|\sigma_{3c}|$ decreases significantly with decreasing $|u_m|$, which is accompanied by a reduction of the elastocaloric response. Interestingly, a several fold enhancement in the electrocaloric effect can be achieved for stress in proximity of σ_{3c} . The elastocaloric effect predicted here may find potential cooling applications by combining the stress-mediated electrocaloric effect or designing hybrid elastocaloric/electrocaloric devices in the future.

An applied stress field σ_3 can reversibly change the temperature of an elastocaloric material under adiabatic conditions, and the temperature change ΔT_{σ_3} is usually maximized near phase transitions. Using a thermodynamic approach, we demonstrate that an elastocaloric strength $\alpha = |\Delta T_{\sigma_3}|/|\sigma_3|$ of 0.016 K/MPa can be achieved benefiting from the full first-order phase transition in BaTiO₃ single crystals, which is comparable with typical elastocaloric materials reported in the literature. The elastocaloric temperature change is found to be giant (3.2 K) under a stress of 200 MPa with a temperature span of over 50 K, which can be significantly larger than its electrocaloric counterpart (~ 1 K). Moreover, it is found that the elastocaloric strength can be remarkably enhanced (2.32 K/MPa) as long as the phase transition is triggered even by a modest stress near the sharp first-order phase transition, which is two orders of magnitude larger than those accomplished by full transition. Therefore, even a low stress (< 30 MPa) can induce a modest elastocaloric effect (1.3 K) comparable with the electrocaloric counterpart, which is accompanied by a reduction of the working temperature span. In addition, it is found that the electrocaloric peak under tensile stresses moves towards higher temperatures with its magnitude slightly enhanced. Hopefully, our study will stimulate further investigations on elastocaloric and stress-mediated electrocaloric effects in ferroelectrics.

We have systematically studied the barocaloric effect in ferroelectric single crystals (Section 6.1 and Section 6.2). The key conclusions are summarized as follows:

Barocaloric effect in BaTiO₃ single crystals is studied by a thermodynamic phenomenological model. It is demonstrated that a giant barocaloric effect can be achieved near room temperature with an adiabatic temperature change of more than 3 K and a temperature span about 50 K. As expected, the electrocaloric peak can be shifted towards room temperature by pressure. However, a slight reduction of the electrocaloric peak is found in contrast to relaxor ferroelectrics and LiNbO₃. We believe that our findings could open a potential route by combining the barocaloric effect and pressure-mediated electrocaloric effect in BaTiO₃ single crystals for cooling devices.

We have systematically studied the magnetocaloric and multicaloric effects in FeRh/BaTiO₃ (Section 7.1 and Section 7.2). The key conclusions are summarized as follows:

Giant magnetocaloric materials are promising for solid-state refrigeration, as an alternative to hazardous gases used in conventional cooling devices. A giant magnetocaloric effect was discovered near room temperature in near-equiatom FeRh alloys some years before the benchmark study in Gd₅Si₂Ge₂ that launched the field. However, FeRh has attracted significantly less interest in cooling applications mainly due to irreversibility in magnetocaloric cycles associated with the large hysteresis of its first-order metamagnetic phase transition. Here we overcome the irreversibility via a dual-stimulus magnetic-electric refrigeration cycle in FeRh thin films via coupling to a ferroelectric BaTiO₃ substrate. This first experimental realization of a multicaloric cycle yields larger reversible caloric effects than either stimulus alone. While magnetic hysteretic

losses appear to be reduced by 96% in dual-stimulus loops we show that the losses are simply transferred into an elastic cycle, contrary to common belief. Nevertheless, we show that these losses do not necessarily prohibit integration of FeRh in practical refrigeration systems.

Our demonstration of a multicaloric refrigeration cycle suggests numerous novel designs for efficient solid-state cooling applications. For instance, an optimized device may permit a purely electric-field driven refrigeration cycle based on a novel electric-field induced mechanocaloric effect. This may open a new paradigm to potentially overcome the inevitable uneconomic investments on clumsy magnets in magnetic cooling. Unlike traditional magnetocalorics, the entropy change is induced upon application of an electric field on BaTiO₃ substrate other than a magnetic field directly applied on FeRh thanks to the magnetoelectric coupling. Moreover, the caloric strength can be enhanced by at least one order of magnitude compared to previous best reports on electrocaloric effect. As the elastic hysteresis losses are not critical, the electric-field induced mechanocaloric effect could be a low-cost approach for developing the next generation of solid state refrigeration.

8.2 PERSPECTIVES

We have mainly concentrated on the inorganic electrocalorics while there is no denying that polymeric materials such as copolymers of PVDF and trifluoroethylene are also very promising for developing electrocaloric prototype devices due to their large electrocaloric response, and flexible nature [5, 46, 84, 110, 112, 149, 203]. Based on current research stage in the field of electrocaloric effect, it is difficult to make a conclusion that which material is the better especially between inorganic ceramics and organic polymers [354]. In this regard, the compromise emerging as composite materials by combining these two compounds together may be promising. The concept of using nanocomposites was firstly proposed to obtain enhanced electrocaloric cooling [417]. Later on, a “colossal” electrocaloric effect was reported in nanocomposites [52, 214, 334] taking advantage of the significantly enhanced breakdown field due to the presence of the boron nitride nanosheets (BNNSs) [418] by Penn State University. The electrocaloric properties of nanocomposites even surpass those of the recently reported giant magnetocalorics [8], which demonstrates the interest and potential role of electrocaloric effect in next-generation refrigeration. For instance, composites combining relaxor terpolymer P(VDF-TrFE-CFE), Ba_{0.67}Sr_{0.33}TiO₃ ceramics and BNNSs shows a huge electrocaloric temperature change of over 50 K at room temperature under a ultrahigh electric field of 2500 kV/cm (Ref. [214]) while relaxor composites based on P(VDF-TrFE-CFE) and PMN-PT [52] are also demonstrated to be comparable to this performance (see Table. 2.1). It demands more efforts to reproduce their published results firstly and then optimize the electrocaloric properties of nanocomposites for design of devices. For instance, the contrast between the experimental results and theoretical upper bounds needs to be addressed in further studies. In this regard, the significantly enhanced breakdown field achieved in nanocomposites may play a dominate role [52, 214, 334]. Testifying the giant electrocaloric effect in other nanostructures such as nanoparticles [187, 191, 419], nanotubes [420] and nanowires [421] is highly desired since recent experimental results demonstrated that electrocaloric effect in polymer nanocomposites can be tailored by the morphology of the ferroelectric

nanofillers [334]. As a result, the idea of using nanowires for towards wearable cooling applications been achieved in highly bendable and stretchable $\text{Ba}_{0.67}\text{Sr}_{0.33}\text{TiO}_3$ nanowires arrays [422]. In this case, experimental results show that sizable electrocaloric response could remain in these highly flexible nanowire arrays under a safe voltage (<36 V), mechanical stretching (25%) up to 10000 cycles [422]. Interestingly, combining electrocalorics with magnetocalorics i.e. in the form of multiferroic heterostructure may be useful to organize a mutlicaloric cycle and design of giant electric-field driven caloric effect, which was demonstrated very recently in $\text{FeRh}/\text{BaTiO}_3$ heterostructure [353] (or see Section 7.1).

As we addressed several times in this thesis, great caution should be made when one tries to use indirect approach to evaluate the caloric properties. As an important lesson from magnetocaloric effect is the so-called “colossal” magnetocaloric effect was also reported in $\text{Mn}_{1-x}\text{Fe}_x\text{As}$ [423] in 2006 by *Nature Materials* a top journal in the field of material science. However, this “colossal” magnetocaloric effect was questioned by several groups. The so-called “colossal” magnetocaloric response were demonstrated spurious due to inadequate uses of the Maxwell relation during the coexistence of paramagnetic and ferromagnetic phases [424]. As a result, the realistic entropy change [424] was found to be one order of magnitude smaller than that reported in *Nature Materials* [423].

There is a yet unexploited commercial application for ferroelectrics near quantum critical points (i.e., for $T_C \rightarrow 0$ K). These include tris-sarcosine calcium bromide (TSSB), Ba-, Sr-, or Pb-hexaferrites ($\text{MFe}_{12}\text{O}_{19}$), and others. Readers should be aware that the electrocaloric and magnetocaloric effects are useful not just for near-room-temperature devices, but also for cryogenics (especially the later has been commercialized). There is a long history led by Lawless (Ref. [207] and others) of using ferroelectric anomalies in perovskite oxides as precision thermometers for T in the mK regime. Of course electrocalorics have an advantage in not requiring magnets. In the future a severe worldwide shortage of He is expected, with consequent increase in price, and we note that cryogen-free cryostats are already commercially available: e.g., Cambridge Cryogenics. www.cambridgecryogenics.com (The present author has no connection with this company). Their systems are fitted with coaxial wires to the mK temperature range and magnets ideal for ferroelectric and multiferroic measurements. Tuning parameters include temperature, magnetic field, electric field, field angle (computer controlled rotator), and pressure. Extension to multiferroic coolers is likely in the near future, with temperature ranges down to the mK regime. One interesting ferroelectric junction structure might be employed as low-temperature coolers as its transition temperature can be tuned in quite a wide range by film thickness [47]. On 16 Sept 2016 the US Navy is launching a mini-satellite with a ferroelectric memory for “cold airless space”. Further satellite applications are eminent in China.

In addition, since all present electrocalorics should generally work in the relatively small voltage regime, extension to very high fields may develop soon e.g. in multilayer capacitors. Oxide perovskites can withstand breakdown fields up to 1 or 2 GV/m (Ref. [311]). When very large fields are applied, reversible wrinkling can occur, adding additional entropy [425]. However, if fields are too high, irreversible folding occurs, for example the Hilfrich-Hursault lamellar instability in ferroelectric C^* smectic liquid crystals, or the Ramberg-Osgood instability in other materials [426, 427].

Careful examination should be made for electrocaloric properties of voltage-driven Mott tran-

sitions, such as NdNiO_3 . Here there is a significant entropy change with either voltage or temperature. Interestingly, a remarkable electrocaloric effect (about -3.8 K under a voltage change of 0-3V) was observed in bulk VO_2 due to electric-field induced metal-insulator phase transition [428]. Note that in such materials thermoelectric effect i.e. variation of temperature through the electrical current can also contribute to the caloric response.

We have discussed uniaxial stress for elastocaloric effects, but it is of interest to point out that rotational stress might also be useful. Similarly, toroidocaloric effect in ferrotoroidic materials was reported recently by a Landau free energy framework [429]. From a practical point of view it is trivial to apply a torque to a thin film, but for other geometries such as nanorods and nanotubes this might be feasible. One might consider applying torques to nanotubes to cool a fluid inside it. Applied torques are especially interesting for incommensurate ferroelectrics/-ferroelastics, because most incommensurate ferroelectrics have screw axes [430]. There is also a special interest in tetragonal structures such as Scheelites (AMO_4 , with $A=\text{Ba, Ca, Sr}$ and $M=\text{Mo or W}$). These structures have Laue type-II tetragonal symmetry, which means that they have nonzero (unusual) d_{16} piezoelectricity [431]. Application of some stresses can retain the tetragonal symmetry (e.g., C_{4h} to C_4 point group) but eliminate d_{16} , causing large hysteresis. In addition, hoop stress plays an unexpected role in the free energy for small devices such as nanotubes, etc [183], which may be considered in further analysis of the elastocaloric effect in ferroelectrics. In addition, only a homogeneously uniaxial stress is considered in this manuscript. Indeed, strain inhomogeneity in a loaded film especially near the edge of tip/film interface exists and this effect becomes increasingly more significant as the film thickness decreases to only a few nanometers [322]. In this case, our work represents a necessary first step in the development of the general nonlinear theory to describe elastocaloric effect in ultrathin films. Further works should be done including the effect of flexoelectricity in the future.

As addressed in Chapter 7, the mechanical work plays an important role in energy conversion. Moreover, the important role of magnetically, electrically and mechanically induced work in magnetocaloric, electrocaloric and mechanocaloric effects need to be exploited in further investigations, in order to obtain information on efficiency of caloric materials [355]. This is of importance especially for design of prototype cooling devices. Multicaloric effect also needs further experimental evidence. In particular, measurement of multicaloric effects under simultaneous multiple stimuli is highly desired. In addition to strong coupling between different order parameters, phase transition temperatures need to be close to each other [10, 376]. Moreover, the characteristic time constant of materials in response to different external stimuli is crucial since optimal caloric effect is expected when the constant is within the same scale. Challenges still exist to demonstrate that multicaloric effect can really work efficiently as least in the scientific laboratories. No experimental data are available in case of multicaloric effect under simultaneous multiple stimuli until this manuscript is completed. It may be easier to firstly to exploit the multicaloric effect by arranging different stimuli applied sequently, as we firstly proposed theoretically in ferroelectric ultrathin films and realized in hybrid $\text{FeRh}/\text{BaTiO}_3$ for the first time.

BIBLIOGRAPHY

- [1] J. U. Ahamed, R. Saidur, and H. H. Masjuki. *Renewable and Sustainable Energy Reviews*, 15:1593 600, 2011.
- [2] D. Coulomb. The IIR and environmental challenges facing the refrigeration sector. In: Poredos, A., Sarlah, A. (Eds.), *Proceedings of the Second International Conference on Magnetic Refrigeration at Room Temperature*, (April 11-13, 2007), Portoroz, Slovenia. International Institute of Refrigeration, Paris, pp. 3-5.
- [3] D. C. Wang, Y. H. Li, D. Li, Y. Z. Xia, and J. P. Zhang. *Renewable and Sustainable Energy Reviews*, 14:344 353, (2010).
- [4] A. M. Tishin and Y. I. Spichkin. *The magnetocaloric effect and its applications*, (CRC Press, September 1, 2003).
- [5] T. Correia, and Q. Zhang. *Electrocaloric Materials: New Generation of Cooler*, (Springer Verlag Berlin Heidelberg, London, UK, 2014).
- [6] A. Kitanovski, J. Tušek, U. Tomc, U. Plaznik, M. Ožbolt, and A. Poredoš. *Magnetocaloric energy conversion: from theory to applications*, (Springer International Publishing Switzerland, 2015).
- [7] S. Fähler, U. K. Rößer, O. Kastner, J. Eckert, G. Eggeler, H. Emmerich, P. Entel, S. Müller, E. Quandt, and K. Albe. *Adv. Mater.*, 4:10 19, (2012).
- [8] X. Moya, S. Kar-Narayan, and N. D. Mathur. *Nat. Mater.*, 13:439 450, (2014).
- [9] V. K. Pecharsky and K. A. Gschneidner, Jr. *Phys. Rev. Lett.*, 78:4494 4497, (1997).
- [10] M. M. Vopson. *Solid State Commun.*, 152:2067 2070, (2012).
- [11] J. Liu, T. Gottschall, K. P. Skokov, J. D. Moore, and O. Gutfleisch. *Nat. Mater.*, 11:620 626, (2012).
- [12] Y.-Y. Gong, D.-H. Wang, Q.-Q. Cao, E.-K. Liu, J. Liu, and Y.-W. Du. *Adv. Mater.*, 27:801 805, (2015).

-
- [13] S. A. Nikitin, G. Myalikgulyev, A. M. Tishin, M. P. Annaorazov, K. A. Asatryan, and A. L. Tyurin. *Physics Letters A*, 148:363 366, (1990).
- [14] V. Franco, J. S. Blázquez, B. Ingale, and A. Conde. *Annu. Rev. Mater. Res.*, 42:305 342, (2012).
- [15] A. S. Mischenko, Q. Zhang, J. F. Scott, R. W. Whatmore, and N. D. Mathur. *Science*, 311:1270 1271, (2006).
- [16] J. Peräntie, J. Hagberg, A. Uusimäki, and H. Jantunen. *Phys. Rev. B*, 82:134119, (2010).
- [17] Y. Bai, G.-P. Zheng, and S.-Q. Shi. *Mater. Res. Bull.*, 46:1866 1869, (2011).
- [18] L. Mañosa, A. Planes, and M. Acetb. *J. Mater. Chem. A*, 1:4925 4936, (2013).
- [19] S. Lisenkov and I. Ponomareva. *Phys. Rev. B*, 86:104103, (2012).
- [20] T. Waitz, K. Tsuchiya, T. Antretter, and F. D. Fischer. *MRS Bull*, 34:814 821, (2009).
- [21] G. A. Samara. *Ferroelectr.*, 2:277 289, (1971).
- [22] P. Weiss and A. Piccard. *J. Phys. (Paris)*, 7:103 109, (1917).
- [23] P. Debye. *Ann Phys (Leipzig)*, 386:1154 1160, (1926).
- [24] W. F. Giauque. *J. Am. Chem. Soc.*, 49:1864 1870, (1927).
- [25] W. F. Giauque and D. P. MacDougall. *Phys. Rev.*, 43:768, (1933).
- [26] G. Urbain, P. Weiss, and F. Trombe. *Comptes Rendus*, 200:2132 2134, (1935)
- [27] G. V. Brown. *J. Appl. Phys.*, 47:3673 3680, (1976).
- [28] J. A. Barclay and W. A. Steyert. Active magnetic regenerator. *US Patent 4.332.135 A* (1982)
- [29] Z. B. Guo, Y. W. Du, J. S. Zhu, H. Huang, W. P. Ding, and D. Feng. *Phys. Rev. Lett.*, 78:1142-1145, (1997).
- [30] H. Wada and Y. Tanabe. *Appl. Phys. Lett.*, 79:3302 3304, (2001).
- [31] F.-X. Hu, B.-G. Shen, J.-R. Sun, and G.-H. Wu. *Phys. Rev. B*, 64:132412, (2001).
- [32] O. Tegus, E. Brück, K. H. J. Buschow, and F. R. de Boer. *Nature(London)*, 415:150 152, (2002).
- [33] A. Fujita, S. Fujieda, Y. Hasegawa, and K. Fukamichi. *Phys. Rev. B*, 67:104416, (2003).
- [34] T. Krenke, E. Duman, M. Acet, E. F. Wassermann, X. Moya, L. Mañosa, and A. Planes. *Nat. Mater.*, 4:450 454, (2005).

- [35] N. T. Trung, L. Zhang, L. Caron, K. H. J. Buschow, and E. Brück. *Appl. Phys. Lett.*, 96:172504, (2010).
- [36] X. Moya, L. E. Hueso, F. Maccherozzi, A. I. Tovstolytkin, D. I. Podyalovskii, C. Ducati, L. C. Phillips, M. Ghidini, O. Hovorka, A. Berger, M. E. Vickers, E. Defay, S. S. Dhesi, and N. D. Mathur. *Nat. Mater.*, 12:52 58, (2013).
- [37] P. Kobeko and J. Kurtschatov. *Zeit. Phys.*, 66:192 205, (1930).
- [38] H. Granicher. *Helv. Phys. Acta*, 29:210 212, (1956).
- [39] E. Hegenbarth. *Cryogenics*, 1:242 243, (1961).
- [40] A. I. Karchevskii. *Sov. Phys. Sol. Stat.*, 3:2249 2254, (1962).
- [41] G. Wiseman and J. K. Kuebler. *Phys. Rev.* 131(5):2023-2027 (1963).
- [42] P. D. Thacher. *J. Appl. Phys.*, 39:1996 2002, (1968).
- [43] R. Radebaugh, W. N. Lawless, J. D. Siegwarth, and A. J. Morrow. *Cryogenics*, 19:187 208, (1979).
- [44] B. A. Tuttle and D. A. Payne. *Ferroelectr.*, 37:603 606, (1981).
- [45] L. Shebanovs, K. Borman, W. N. Lawless, and A. Kalvane. *Ferroelectr.*, 273:137 142, (2002)
- [46] B. Neese, B. J. Chu, S. G. Lu, Y. Wang, E. Furman, and Q. M. Zhang. *Science*, 321:821 823, (2008).
- [47] Y. Liu, X.-P. Peng, X. J. Lou, and H. Zhou. *Appl. Phys. Lett.*, 100:192902, (2012).
- [48] X. Moya, E. Stern-Taulats, S. Crossley, D. Gonzalez-Alonso, S. Kar-Narayan, A. Planes, L. Mañosa, and N. D. Mathur. *Adv. Mater.*, 25:1360 1365, (2013).
- [49] S. Lisenkov, B. K. Mani, C.-M. Chang, J. Almand, and I. Ponomareva. *Phys. Rev. B*, 87:224101, (2013).
- [50] Y. Liu, I. C. Infante, X. J. Lou, L. Bellaiche, J. F. Scott, and B. Dkhil. *Adv. Mater.*, 26:6132 6137, (2014).
- [51] W. P. Geng, Y. Liu, X. J. Meng, L. Bellaiche, J. F. Scott, B. Dkhil, and A. Q. Jiang. *Adv. Mater.*, 27:3165 3169, (2015).
- [52] Q. Li, G. Z. Zhang, X. S. Zhang, S. L. Jiang, Y. K. Ye, and Q. Wang. *Adv. Mater.*, 27:2236 2241, (2015).
- [53] J. Gough. *Mem. Lit. Phil. Soc. Manchester*, 1 (2nd Series):288 295, (1805).
- [54] W. Tomson. *Quart. J. Math.*, (April 1855).

- [55] J. P. Joule. *Phil. Trans.*, 149:91 131, (1859).
- [56] J. F. Nye. *Physical Properties of Crystals* (Clarendon Press, Oxford, 1957), Chap. X.
- [57] C. Rodriguez and L. C. Brown. *Metall. Trans. A*, 11:147 150, (1980).
- [58] K. Mukherjee, S. Sircar, and N. B. Dahotre. *Mater. Sci. Eng.*, 74:75 84, (1985).
- [59] S. A. Nikitin, G. Myalikgulyev, M. P. Annaorazov, A. L. Tyurin, R. W. Myndyev, and S. A. Akopyan. *Phys. Lett. A*, 171:234 236, (1992).
- [60] J. Quarini and A. Prince. *Proc. Instn. Mech. Engrs.*, 218:1175 1178, (2004).
- [61] E. Bonnot, R. Romero, L. Mañosa, E. Vives, and A. Planes. *Phys. Rev. Lett.*, 100:125901, (2008).
- [62] J. Cui, Y. M. Wu, J. Muehlbauer, Y. H. Hwang, R. Radermacher, S. Fackler, M. Wuttig, and I. Takeuchi. *Appl. Phys. Lett.*, 101:073904, (2012).
- [63] F. Xiao, T. Fukuda, and T. Kakeshita. *Appl. Phys. Lett.*, 102:161914, (2013).
- [64] Y. Liu, J. Wei, P.-E. Janolin, I. C. Infante, J. Kreisel, X. J. Lou, and B. Dkhil. *Phys. Rev. B*, 90:104107, (2014).
- [65] A. Chauhan, S. Patel, and R. Vaish. *Appl. Phys. Lett.*, 106:172901, (2015).
- [66] A. Chauhan, S. Patel, and R. Vaish. *Acta Mater.*, 89:384 395, (2015).
- [67] K. Alex Müller, F. Fauth, S. Fischer, M. Koch, A. Furrer, and P. Lacorre. *Appl. Phys. Lett.*, 73:1056 1058, (1998).
- [68] T. Strässle, A. Furrer, Z. Hossain, and Ch. Geibel. *Phys. Rev. B*, 67:054407, (2003).
- [69] L. Mañosa, D. Gonzalez-Alonso, A. Planes, E. Bonnot, M. Barrio, J.-L. Tamarit, S. Aksoy, and M. Acet, *Nat. Mater.*, 9:478 481, (2010).
- [70] R. Szymczak, R. Kolano, A. Kolano-Burian, J. Pietosa, and H. Szymczak. *J. Magn. Magn. Mater.*, 322:1589 1591, (2010).
- [71] L. Mañosa, D. Gonzalez-Alonso, A. Planes, M. Barrio, J.-L. Tamarit, I. S. Titov, M. Acet, A. Bhattacharyya, and S. Majumdar. *Nat. Commun.*, 2:595, (2011).
- [72] E. Mikhaleva, I. Flerov, V. S. Bondarev, M. V. Gorev, A. D. Vasilliev, and T. N. Davydova. *Phys. Solid State*, 53:478 484, (2011).
- [73] N. A. de Oliveira. *J. Appl. Phys.*, 109:053515, (2011).
- [74] S. Yuce, B. Emre, E. Stern-Taulats, A. Planes, L. Mañosa, M. Barrio, J. L. Tamariti, Y. Mudryk, K. A. Gschneidner, Jr., and V. K. Pecharsky. *Appl. Phys. Lett.*, 101:071906, (2012).

- [75] E. Mikhaleva, I. Flerov, M. Gorev, M. Molokeev, A. Cherepakhin, A. Kartashev, N. Mikhashenok, and K. Sablina. *Phys. Solid State*, 54:1832 1840, (2012).
- [76] Y. Liu, J. Wei, P.-E. Janolin, I. C. Infante, X. J. Lou, and B. Dkhil. *Appl. Phys. Lett.*, 104:162904, (2014).
- [77] D. Matsunami, A. Fujita, K. Takenaka, and M. Kano. *Nat. Mater.*, 14:73 78, (2014).
- [78] E. Stern-Taulats, A. Planes, P. Lloveras, M. Barrio, J.-L. Tamarit, S. Pramanick, S. Majumdar, C. Frontera, and L. Mañosa. *Phys. Rev. B*, 89:214105, (2014).
- [79] P. Lloveras, E. Stern-Taulats, M. Barrio, J.-Ll. Tamarit, S. Crossley, W. Li, V. Pomjakushin, A. Planes, Ll. Mañosa, N. D. Mathur, and X. Moya. *Nat. Commun.*, 6:8801, (2015).
- [80] S. Patel, A. Chauhan, R. Vaish, and P. Thomas. *Appl. Phys. Lett.*, 108:072903, (2016).
- [81] E. Warburg. *Ann. Phys.*, 249:141 164, (1881).
- [82] A. Smith. *Eur. Phys. J. H*, 38:507 517, (2013).
- [83] V. Provenzano, A. J. Shapiro, and R. D. Shull. *Nature(London)*, 429:853 857, (2004).
- [84] J. F. Scott. *Annu. Rev. Mater. Res.*, 41:229 240, (2011).
- [85] M. O. Annaorazov, S. A. Nikitin, A. L. Tyurin, K. A. Asatryan, and A. K. Dovletov. *J. Appl. Phys.*, 79:1689 1695, (1996).
- [86] C. Bechtold, C. Chluba, R. Lima de Miranda, and E. Quandt. *Appl. Phys. Lett.*, 101:091903, (2012).
- [87] M. Bibes. *Nat. Mater.*, 11:354 357, (2012).
- [88] S. Yu. Dan'kov, A. M. Tishin, V. K. Pecharsky, and K. A. Gschneidner, Jr. *Phys. Rev. B*, 57:3478 3490, (1998).
- [89] J. F. Scott. *Ferroelectric Memories*, (Springer, Berlin, 2000).
- [90] J. Valasek. *Phys. Rev.*, 15:537, (1920); 17:475 481, (1921).
- [91] H. B. Liu and B. Dkhil. *Zeitschrift für Kristallographie*, 226(2):163170, (February 2011).
- [92] L. E. Cross. *Ferroelectr.*, 76:241 267, (1987).
- [93] E. K. H. Salje. *Annu. Rev. Mater. Res.*, 42:265 283, (2012).
- [94] J.-C. Toledano. *Annals of Telecommunications*, 29:249 270, (1974).
- [95] H. P. Weber, B. C. Tofield, and P. F. Liao. *Phys. Rev. B*, 11:1152 1159, (1975).
- [96] G. Errandonea. *Phys. Rev. B*, 21:5221 5236, (1980).

- [97] D. L. Fox, J. F. Scott, and P. M. Bridenbaugh. *Solid State Commun.*, 18:111 113, (1976).
- [98] W. Eerenstein, N. D. Mathur, and J. F. Scott. *Nature(London)*, 442:759-765, (2006).
- [99] L. J. Dunne, M. Valant, A.-K. Axelsson, G. Manos, and N. McN Alford. *J. Phys. D: Appl. Phys.*, 44:375404, (2011).
- [100] M. C. Rose and R. E. Cohen. *Phys. Rev. Lett.*, 109:187604, (2012).
- [101] Y. Tokura, S. Seki, and N. Nagaosa. *Rep. Prog. Phys.*, 77:076501, (2014).
- [102] C. A. F. Vaz. *J. Phys.-Condens. Mat.*, 24:333201, (2012).
- [103] R. O. Cherifi, V. Ivanovskaya, L. C. Phillips, A. Zobelli, I. C. Infante, E. Jacquet, V. Garcia, S. Fusil, P. R. Briddon, N. Guiblin, A. Mougin, A. A. Ünal, F. Kronast, S. Valencia, B. Dkhil, A. Barthélémy, and M. Bibes. *Nat. Mater.*, 13:345 351, (2014).
- [104] L. Mañosa, A. Planes, E. Vives, E. Bonnot, and R. Romero. *Funct. Mater. Lett.*, 2:73 78, (2009).
- [105] A. Planes, A. Castan, and A. Saxena. *Phil. Mag.*, 94:1893 1908, (2014).
- [106] Ch. Binek and V. Burobina. *Appl. Phys. Lett.*, 102:031915, (2013).
- [107] C.-M. Chang, B. K. Mani, S. Lisenkov, and I. Ponomareva. *Phys. Rev. Lett.*, 114:177205, (2015).
- [108] K. A. Gschneidner. V. K. Jr. Pecharsky, and A. O. Tsokol. *Rep. Prog. Phys.*, 68:1479, (2005).
- [109] J. F. Scott. *Science*, 315:954 959, (2007).
- [110] S. -G. Lu and Q. M. Zhang. *Adv. Mater.*, 21:1983 1987, (2009).
- [111] M. Valant. *Prog. Mater. Sci.*, 57:980 1009, (2012).
- [112] X. Y. Li, S.-G. Lu, X.-Z. Chen, H. M. Gu, X.-S. Qian, and Q. M. Zhang. *J. Mater. Chem. C*, 1:23 37, (2013).
- [113] S. Pamir Alpay, J. Mantese, S. Trolier-McKinstry, Q. M. Zhang, and R. W. Whatmore. *MRS Bull.*, 39:1099 1111, (2014).
- [114] I. Takeuchi and K. Seman. *Phys. Today*, 68:48 54, (2015).
- [115] S. Crossley, N. D. Mathur, and X. Moya. *AIP Adv.*, 5:067153, (2015).
- [116] Z. Kutnjak, B. Rožič, and R. Pirc. Electrocaloric Effect: Theory, Measurements, and Applications. Wiley Encyclopedia of Electrical and Electronics Engineering. 1-19, (2015).
- [117] A. Kitanovski, U. Plaznik, U. Tomc, and A. Poredoš. *Int. J. Refrig.*, 57:288 198, (2015).

- [118] Y. B. Jia and Y. Sungtaek Ju. *Appl. Phys. Lett.*, 100:242901, (2012).
- [119] H. Gu, X. S. Qian, X. Li, B. Craven, W. Zhu, A. Cheng, S. C. Yao, and Q. M. Zhang. *Appl. Phys. Lett.*, 102:122904, (2013).
- [120] H. Gu, X. S. Qian, H. J. Ye, and Q. M. Zhang. *Appl. Phys. Lett.*, 105:162905, (2014).
- [121] R. I. Epstein and K. J. Malloy. *J. Appl. Phys.*, 106:064509, (2009).
- [122] X. Y. Li, H. M. Gu, X. S. Qian, and Q. M. Zhang, Thermal thermomechanical phenomena in electronic systems (ITherm), 13th IEEE Intersociety Conference, 934-937, May 30 (2012)-June 1 (2012).
- [123] G. Akcay, S. P. Alpay, J. G. A. Rossetti, and J. F. Scott. *J. Appl. Phys.*, 103:024104, (2008).
- [124] S. G. Lu, B. Rozic, Q. M. Zhang, Z. Kutnjak, and R. Pirc. *Appl Phys A*, 107:559 566, (2012).
- [125] N. Novak, R. Pirc, and Z. Kutnjak. *Phys. Rev. B*, 87:104102, (2013).
- [126] Y. B. Jia and Y. Sungtaek Ju. *Appl. Phys. Lett.*, 103:042903, (2013).
- [127] M. Quintero, P. Gaztañaga, and I. Irurzun. *Appl. Phys. Lett.*, 107:151901, (2015).
- [128] S. Crossley. Thesis: “Electrocaloric materials devices”, University of Cambridge, (2013).
- [129] J. S. Young. Thesis: “Indirect measurement of the electrocaloric effect”, University of Cambridge, (2011).
- [130] K. M. Rabe. Antiferroelectricity in oxides: a reexamination, in functional metal oxides: new science and novel applications (Eds: S. B. Ogale, T. V. Venkatesan, M. G. Blamire), Wiley-VCH, Weinheim, Germany, Ch7, (2014).
- [131] J. Parui and S. B. Krupanidhi. *Phys. Stat. Sol. (RRL)*, 2:230 232, (2008).
- [132] X. H. Hao, Z. X. Yue, J. B. Xu, S. L. An, and C.-W. Nan. *J. Appl. Phys.*, 110:064109, (2011).
- [133] B. Peng, H. Fan, and Q. Zhang. *Adv. Funct. Mater.*, 23:2987 2992, (2013).
- [134] X. J. Jiang, L. H. Luo, B. Y. Wang, W. P. Li, and H. B. Chen. *Ceram. Int.*, 40:2627 2634, (2014).
- [135] Y. Zhao, X. H. Hao, and Q. Zhang, *ACS Appl. Mater. Inter.* 6:11633 11639, (2014).
- [136] W. P. Cao, W. L. Li, D. Xu, Y. F. Hou, W. Wang, and W. D. Fei. *Ceram. Int.*, 40:9273 9278, (2014).
- [137] R. Pirc, B. Rožič, J. Koruza, B. Malič, and Z. Kutnjak. *Europhys. Lett.*, 107:17002, (2014).

- [138] R. Pirc, B. Rožič, J. Koruza, G. Cordoyiannis, B. Malič, and Z. Kutnjak, *J. Phys.: Condens. Matter* 27:455902, (2015).
- [139] F. Le Goupil, J. Bennett, A.-K. Axelsson, M. Valant, A. Berenov, A. J. Bell, T. P. Comyn, and N. McN Alford. *Appl. Phys. Lett.*, 107:172903, (2015).
- [140] K. A. Gschneidner, Jr., V. K. Pecharsky, E. Brück, H. G. M. Duijn, and E. M. Levin. *Phys. Rev. Lett.*, 85:4190, (2000).
- [141] T. Tohei, H. Wada, and T. Kanomata. *J. Appl. Phys.*, 94:1800 1802, (2003).
- [142] J. Shen, J.-L. Zhao, F.-X. Hu, J.-F. Wu, M.-Q. Gong, Y.-X. Li, J.-R. Sun, and B.-G. Shen. *J. Appl. Phys.*, 107:09A931, (2010).
- [143] A. Midya, S. N. Das, P. Mal, S. Pya, and V. Ganesan. *Phys. Rev. B*, 84:235127, (2011).
- [144] H. Zhang, Y. W. Li, E. K. Liu, Y. J. Ke, J. L. Jin, Y. Long, and B.-G. Shen. *Sci. Rep.*, 5:11929, (2015).
- [145] A. Maurya, A. Thamizhavel, P. Bonville, and S. K. Dharar. Xiv:1507.05743, (2015).
- [146] S. Lisenkov, B. K. Mani, E Glazkova, C. W. Miller, and I. Ponomareva. *Sci. Rep.*, 6:19590, (2016).
- [147] K. Nishimura, Y. Nakazawa, L. W. Li, and K. Mori. *Mater. Trans.*, 49:1753 1756, (2008).
- [148] A. R. Akbarzadeh, S. Prosandeev, Eric J. Walter, A. Al-Barakaty, and L. Bellaiche. *Phys. Rev. Lett.* 108:257601, (2012).
- [149] S. G. Lu, B. Rožič, Q. M. Zhang, Z. Kutnjak, R. Pirc, M. Lin, X. Li, and L. Gorny. *Appl. Phys. Lett.*, 97:202901, (2011).
- [150] X.-S. Qian, H.-J. Ye, Y.-T. Zhang, H. Gu, X. Li, C. A. Randall, and Q. M. Zhang. *Adv. Funct. Mater.*, 24:1300 1305, (2013).
- [151] M. Sanlialp, V. V. Shvartsman, M. Acosta, B. Dkhil, and D. C. Lupascu. *Appl. Phys. Lett.*, 106:062901, (2015).
- [152] B. Rožič, M. Kosec, H. Uršič, J. Holc, B. Malič, Q. M. Zhang, R. Blinc, R. Pirc, and Z. Kutnjak. *J. Appl. Phys.*, 110:064118, (2011).
- [153] J. Hagberg, A. Uusimäki, and H. Jantunen. *Appl. Phys. Lett.*, 92:132909, (2008).
- [154] L. J. Dunne, M. Valant, A.-K. Axelsson, G. Manos, and N. M. Alford. *J. Phys D: Appl Phys*, 44:375404, (2011).
- [155] M. Valant, L. J. Dunne, A.-K. Axelsson, N. M. Alford, G. Manos, J. Peräntie, J. Hagberg, H. Jantunen, and A. Dabkowski. *Phys. Rev. B* 81:214110, (2011).
- [156] J. Peräntie, J. Hagberg, A. Uusimäki, and H. Jantunen. *Phys. Rev. B*, 82:134119, (2010).

- [157] Y. P. Shi and A. K. Soh. *Acta Mater.*, 59:5574 5583, (2011).
- [158] R. Pirc, Z. Kutnjak, R. Blinc, and Q. M. Zhang. *Appl. Phys. Lett.*, 98:021909, (2011).
- [159] Z. K. Liu, X. Li, and Q. M. Zhang. *Appl. Phys. Lett.*, 101:082904, (2012).
- [160] Y. Bai, X. Han, and L. Qiao. *Appl. Phys. Lett.*, 102:252904, (2013).
- [161] Z. D. Luo, D.-W. Zhang, Y. Liu, D. Zhou, Y. G. Yao, C. Q. Liu, B. Dkhil, X. B. Ren, and X. J. Lou. *Appl. Phys. Lett.*, 105:102904, (2014).
- [162] X. J. Wang, F. Tian, C. Zhao, J. Wu, Y. Liu, B. Dkhil, M. Zhang, Z. Gao, and X. J. Lou. *Appl. Phys. Lett.*, 107:252905, (2015).
- [163] R. Pirc, Z. Kutnjak, R. Blinc, and Q. M. Zhang. *J. Appl. Phys.*, 110:074113, (2011).
- [164] N. Novak, R. Pirc, and Z. Kutnjak. *Europhys. Lett.*, 103:47001, (2013).
- [165] Y. Liu, J. Wei, X. J. Lou, L. Bellaiche, J. F. Scott, and B. Dkhil. *Appl. Phys. Lett.*, 106:032901, (2015).
- [166] Y. Liu, I. C. Infante, X. J. Lou, D. C. Lupascu, and B. Dkhil. *Appl. Phys. Lett.*, 104:012907, (2014).
- [167] S. Prosandeev, I. Ponomareva, and L. Bellaiche. *Phys. Rev. B*, 78:052103, (2008).
- [168] F. L. Goupil, A. Berenov, A.-K. Axelsson, and M. Valant. *J. Appl. Phys.*, 111:124109, (2012).
- [169] A. K. Axelsson, F. L. Goupil, L. J. Dunne, G. Manos, M. Valant, and N. M. Alford. *Appl. Phys. Lett.*, 102:102902, (2013).
- [170] J. Íñiguez, M. Stengel, S. Prosandeev, and L. Bellaiche. *Phys. Rev. B*, 90:220103(R), (2014).
- [171] M. Marathe, A. Grünebohm, T. Nishimatsu, P. Entel, and C. Ederer. *Phys. Rev. B*, 93:054110, (2016).
- [172] T. M. Correia, J. S. Young, R. W. Whatmore, J. F. Scott, N. D. Mathur, and Q. Zhang. *Appl. Phys. Lett.*, 95:182904, (2009).
- [173] V. Bassoa, C. P. Sasso, G. Bertotti, and M. LoBue. *Int. J. Refrig.*, 29:1358 1365, (2006).
- [174] J. Lyubina, R. Schäfer, N. Martin, L. Schultz, and O. Gutfleisch. *Adv. Mater.*, 22:3735 3739, (2010).
- [175] F. Guillou, G. Porcari, H. Yibole, N. Dijk, and E. Brück. *Adv. Mater.*, 26:2671 2675, (2014).
- [176] L. von Moos, K. K. Nielsen, K. Engelbrecht, and C. R. H. Bahl. *Int. J. Refrig.*, 37:303 306 (2014).

- [177] I. Ponomareva and S. Lisenkov. *Phys. Rev. Lett.*, 108:167604, (2012).
- [178] A. Kukreti, A. Kumar, and U. C. Naithani. *Indian J. Pure Ap. Phy.*, 47:43 48, (2009).
- [179] W. Reese. *Phys. Rev.*, 181:905 919, (1969).
- [180] Z. Kutnjak, J. Petzelt, and R. Blinc. *Nature (London)*, 441:956 959, (2006).
- [181] N. Novak, R. Pirc, M. Wencka, and Z. Kutnjak. *Phys. Rev. Lett.*, 109:037601, (2012).
- [182] M. Dawber, K. M. Rabe, and J. F. Scott. *Rev. Mod. Phys.*, 77:1083 1130, (2005).
- [183] S. E. Rowley, M. Hadjimichael, M. N. Ali, Y. C. Durmaz, J. C. Lashley, R. J. Cava, and J. F. Scott. *J. Phys.-Condens. Mat.*, 27:395901, (2015).
- [184] K. Ding, Y. Bai, X. Han, W. J. Zhang, and L. J. Qiao. *Key Engineering Materials*, 492:164 167, (2012).
- [185] S. Crossley, T. Usui, B. Nair, S. Kar-Narayan, X. Moya, S. Hirose, A. Ando, and N. D. Mathur. *Appl. Phys. Lett.*, 108:032902, (2016).
- [186] J. F. Wang, T. Q. Yang, K. Wei, and X. Yao. *Appl. Phys. Lett.*, 102:152907, (2013).
- [187] Y. K. Zeng, B. Li, J. B. Wang, X. L. Zhong, W. Wang, F. Wang, and Y. C. Zhou. *RSC Adv.*, 4:30211 30214, (2014).
- [188] B. Li, J. B. Wang, X. L. Zhong, F. Wang, Y. K. Zeng, and Y. C. Zhou. *Europhys. Lett.*, 102:47004 47008, (2013).
- [189] J. Wang, M. Liu, Y. J. Zhang, T. Shimada, S.-Q. Shi, and T. Kitamura. *J. Appl. Phys.*, 115:164102, (2014).
- [190] G. Catalan, J. Seidel, R. Ramesh, and J. F. Scott. *Rev. Mod. Phys.*, 84:119 156, (2012).
- [191] B. Li, J. B. Wang, X. L. Zhong, F. Wang, B. L. Liu, and Y. C. Zhou. *J. Nanopart. Res.*, 15:1427 1430, (2013).
- [192] J. Karthik and L. W. Martin. *Appl. Phys. Lett.*, 99:032904, (2011).
- [193] Y.-B. Ma, K. Albe, and B.-X. Xu. *Phys. Rev. B*, 91:184108, (2015).
- [194] J. A. Brug and W. P. Wolf. *J. Appl. Phys.*, 57:4685 4701 (1985);57:4695 4701, (1985).
- [195] R. Caballero-Flores, V. Franco, A. Conde, and L. F. Kiss. *J. Appl. Phys.*, 105:07A919, (2009).
- [196] C. R. H. Bahl and K. K. Nielsen. *J. Appl. Phys.*, 105:013916, (2009).
- [197] K. K. Nielsen, A. Smith, C. R. H. Bahl, and U. L. Olsen. *J. Appl. Phys.*, 112:094905, (2012).

- [198] C. Romero-Muñiz, J. J. Ipus, J. S. Blázquez, V. Franco, and A. Conde. *Appl. Phys. Lett.*, 104:252405, (2014).
- [199] J. Junquera and P. Ghosez. *Nature (London)*, 422:506 509, (2003).
- [200] Y. Liu, X. J. Lou, M. Bibes, and B. Dkhil. *Phys. Rev. B*, 88:024106, (2013).
- [201] Y. Liu, I. C. Infante, X. J. Lou, and B. Dkhil. *Appl. Phys. Lett.*, 104:082901, (2014).
- [202] E. Glazkova, C.-M. Chang, S. Lisenkov, B. K. Mani, and I. Ponomareva. *Phys. Rev. B*, 92:064101, (2015).
- [203] P. F. Liu, J. L. Wang, X. J. Meng, J. Yang, B. Dkhil, and J. H. Chu. *New J. Phys.*, 12:023035, (2010).
- [204] S. G. Lu, B. Rožič, Q. M. Zhang, Z. Kutnjak, X. Y. Li, E. Furman, L. J. Gorný, M. Lin, B. Mali, M. Koseč, R. Blinc, and R. Pirc. *Appl. Phys. Lett.*, 97:162904, (2010).
- [205] T. Tong, J. Karthik, R. V. K. Mangalam, L. W. Martin, and D. G. Cahill. *Phys. Rev. B*, 90:094116, (2014).
- [206] H.-J. Ye, X.-S. Qian, D.-Y. Jeong, S. J. Zhang, Y. Zhou, W.-Z. Shao, L. Zhen, and Q. M. Zhang. *Appl. Phys. Lett.*, 105:152908, (2014).
- [207] W. N. Lawless and C. F. Clark. *Phys. Rev. B*, 36:459 465, (1987).
- [208] S. Kar-Narayana and N. D. Mathur. *J. Phys. D: Appl. Phys.*, 43:032002, (2010).
- [209] Y. Bai, G. P. Zheng, and S. Q. Shi. *Appl. Phys. Lett.*, 96:192902, (2009).
- [210] Y. Bai, G.-P. Zheng, K. Ding, L. J. Qiao, S.-Q. Shi, and D. Guo. *J. Appl. Phys.*, 110:094103, (2011).
- [211] X. Y. Li, X.-S. Qian, S. G. Lu, J. P. Cheng, Z. Fang, and Q. M. Zhang. *Appl. Phys. Lett.*, 99:052907, (2011).
- [212] G. Sebald, L. Seveyrat, J.-F. Capsal, and P.-J. Cottinet. *Appl. Phys. Lett.*, 101:022907, (2012).
- [213] D. Guo, J. Gao, Y.-J. Yu, S. Santhanam, G. K. Fedder, A. J. H. McGaughey, and S. C. Yao. *Appl. Phys. Lett.*, 105:031906, (2014).
- [214] G. Z. Zhang, Q. Li, H. M. Gu, S. L. Jiang, K. Han, M. R. Gadinski, M. A. Haque, Q. M. Zhang, and Q. Wang. *Adv. Mater.*, 27:1450-1454, (2015).
- [215] Z. Y. Jiang, X. C. Zheng, and G. P. Zheng. *RSC Adv.* 5:61946 61954, (2015).
- [216] L. Yang, X. S. Qian, C. M. Koo, Y. Hou, T. Zhang, Y. Zhou, M. R. Lin, J.-H. Qiu, and Q. M. Zhang. *Nano Energy*, 22:461-467, (2016).

- [217] S. Kar-Narayan, S. Crossley, X. Moya, V. Kovacova, J. Abergel, A. Bontempi, N. Baier, E. Defay, and N. D. Mathur. *Appl. Phys. Lett.*, 102:032903 (2013).
- [218] B. Rožič, B. Malič, H. Uršič, J. Holc, M. Kosec, B. Neese, and Q. M. Zhang. *Ferroelectr.*, 405:26 31, (2010).
- [219] V. K. Pecharsky, and K. A. Gschneidner, Jr.. *J. Appl. Phys.*, 86:565 575, (1999).
- [220] V. K. Pecharsky, and K. A. Gschneidner, Jr.. *J. Appl. Phys.*, 86:6315 6321, (1999).
- [221] H. Yao, K. Ema, and C. W. Garl. *Rev. Sci. Instrum.*, 69:172 178, (1998).
- [222] B. Asbani, J.-L. Dellis, Y. Gagou, H. Kaddoussi, A. Lahmar, M. Amjoud, D. Mezzane, Z. Kutnjak, and M. El Marssi. *Europhys. Lett.*, 111:57008, (2015).
- [223] H. Kaddoussi, A. Lahmar, Y. Gagou, B. Asbani, J.-L. Dellis, G. Cordoyiannis, B. Allouche, H. Khemakhem, Z. Kutnjak, and M. El Marssi. *J. Alloy Compd*, 667:198 203, (2016).
- [224] D. V. Christensen, R. Bjørk, K. K. Nielsen, C. R. H. Bahl, A. Smith, and S. Clausen. *J. Appl. Phys.*, 108:063913, (2010).
- [225] E. Vives, S. Burrows, R. S. Edwards, S. Dixon, L. Manosa, A. Planes, and R. Romero. *Appl. Phys. Lett.*, 98:011902, (2011).
- [226] H. Ossmera, F. Lambrecht, M. Gültiga, C. Chlubab, E. Qutb, and M. Kohla. *Acta Mater.*, 81:9 20, (2014).
- [227] J. Tušek, K. Engelbrecht, L. P. Mikkelsen, and N. Pryds. *J. Appl. Phys.*, 117:124901, (2015).
- [228] D. Delpueyo, X. Balraud, and M. Grédiac. *Mater. Sci. Eng.: A*, 528:8249 8258, (2011).
- [229] F. L. Goupil, A. K. Axelsson, L. J. Dunne, M. Valant, G. Manos, T. Lukasiewicz, J. Dec, A. Berenov, and N. M. Alford. *Adv. Energy Mater.*, 4:1301688, (2014).
- [230] Y. Bai, D. Wei, and L.-J. Qiao. *Appl. Phys. Lett.*, 107:192904, (2015).
- [231] S. Kar-Narayana and N. D. Mathur. *Appl. Phys. Lett.*, 95:242903, (2009).
- [232] S. Crossley, J. R. McGinnigle, S. Kar-Narayan, and N. D. Mathur. *Appl. Phys. Lett.*, 104:082909, (2014).
- [233] Y. D. Wang, S. J. Smullin, M. J. Sheridan, Q. Wang, C. Eldershaw, and D. E. Schwartz. *Appl. Phys. Lett.*, 107:134103, (2015).
- [234] B. Kwon, I.-J. Roh, S.-H. Baek, S. K. Kim, J.-S. Kim, and C.-Y. Kang. *Appl. Phys. Lett.*, 104:213902, (2014).
- [235] M. Quintero, L. Ghivelder, F. Gomez-Marlasca, and F. Parisi. *Appl. Phys. Lett.*, 99:232908, (2011).

- [236] U. Tomc, J. Tušek, A. Kitanovski, and A. Poredoš. *Appl. Therm. Eng.*, 58:10 19, (2013).
- [237] A. Majumdar. *Annu. Rev. Mater. Sci.*, 29:505 585, (1999).
- [238] S. Gomès, A. Assy, and P.-O. Chapuis. *Phys. Status Solidi A*, 212:477 494, (2015).
- [239] E. Y. Tsymbal, A. Gruverman, V. Garcia, M. Bibes, and A. Barthélémy. *MRS Bull.*, 37:138 143, (2012).
- [240] H. Kohlstedt, N. A. Pertsev, J. Rodríguez Contreras, and R. Waser. *Phys. Rev. B*, 72:125341, (2005).
- [241] M. Y. Zhuravlev, R. F. Sabirianov, S. S. Jaswal, and E. Y. Tsymbal. *Phys. Rev. Lett.*, 94:246802, (2005).
- [242] V. Garcia and M. Bibes. *Nat. Commun.*, 5:4289, (2014).
- [243] J. P. Velev, C.-G. Duan, K. D. Belashchenko, S. S. Jaswal, and E. Y. Tsymbal. *Phys. Rev. Lett.*, 98:137201, (2007).
- [244] V. Garcia, S. Fusil, K. Bouzehouane, S. Enouz-Vedrenne, N. D. Mathur, A. Barthélémy, and M. Bibes. *Nature (London)*, 460:81 84, (2009).
- [245] A. Gruverman, D. Wu, H. Lu, Y. Wang, H. W. Jang, C. M. Folkman, M. Y. Zhuravlev, D. Felker, M. Rzechowski, C. B. Eom, and E. Y. Tsymbal. *Nano Lett.*, 9:3539 3543, (2009).
- [246] A. Crassous, V. Garcia, K. Bouzehouane, S. Fusil, A. H. G. Vlooswijk, G. Rispens, B. Noheda, M. Bibes, and A. Barthélémy. *Appl. Phys. Lett.*, 96:042901, (2010).
- [247] A. Chanthbouala, A. Crassous, V. Garcia, K. Bouzehouane, S. Fusil, X. Moya, J. Allibe, B. Dlubak, J. Grollier, S. Xavier, C. Deranlot, A. Moshar, R. Proksch, N. D. Mathur, M. Bibes, and A. Barthélémy. *Nat. Nanotechnol.*, 7:101 104, (2011).
- [248] D. I. Bilc, F. D. Novaes, J. Íñiguez, P. Ordejón, and P. Ghosez. *ACS Nano*, 6(2):1473 1478, (2012).
- [249] D. Pantel, H. D. Lu, S. Goetze, P. Werner, D. J. Kim, A. Gruverman, D. Hesse, and M. Alexe. *Appl. Phys. Lett.*, 100:232902, (2012).
- [250] A. Chanthbouala, V. Garcia, R. O. Cherifi, K. Bouzehouane, S. Fusil, X. Moya, S. Xavier, H. Yamada, C. Deranlot, N. D. Mathur, M. Bibes, A. Barthélémy, and J. Grollier. *Nat. Mater.*, 11:860 864, (2012).
- [251] M. Y. Zhuravlev, S. S. Jaswal, E. Y. Tsymbal, and R. F. Sabirianov. *Appl. Phys. Lett.*, 87:222114, (2005).
- [252] C.-G. Duan, S. S. Jaswal, and E. Y. Tsymbal. *Phys. Rev. Lett.*, 97:047201, (2006).
- [253] S. Sahoo, S. Polisetty, C.-G. Duan, S. S. Jaswal, E. Y. Tsymbal, and C. Binek. *Phys. Rev. B*, 76:092108, (2007).

- [254] C.-G. Duan, Julian P. Velev, R. F. Sabirianov, W. N. Mei, S. S. Jaswal, and E. Y. Tsymbal. *Appl. Phys. Lett.*, 92:122905, (2008).
- [255] M. K. Niranjana, J. D. Burton, J. P. Velev, S. S. Jaswal, and E. Y. Tsymbal. *Appl. Phys. Lett.*, 95:052501, (2009).
- [256] J. D. Burton and E. Y. Tsymbal. *Phys. Rev. B*, 80:174406, (2009).
- [257] J. P. Velev, C.-G. Duan, J. D. Burton, A. Smogunov, M. K. Niranjana, E. Tosatti, S. S. Jaswal, and E. Y. Tsymbal. *Nano Lett.*, 9:427 432, (2009).
- [258] M. Y. Zhuravlev, S. Maekawa, and E. Y. Tsymbal. *Phys. Rev. B*, 81:104419, (2010).
- [259] V. Garcia, M. Bibes, L. Bocher, S. Valencia, F. Kronast, A. Crassous, X. Moya, S. Enouz-Vedrenne, A. Gloter, D. Imhoff, C. Deranlot, N. D. Mathur, S. Fusil, K. Bouzheouane, and A. Barthélémy. *Science*, 327:1106 1110, (2010).
- [260] M. Hambe, A. Petraru, N. A. Pertsev, P. Munroe, V. Nagarajan, and H. Kohlstedt, *Adv. Funct. Mater.*, 20:2436 2441, (2010).
- [261] S. Valencia, A. Crassous, L. Bocher, V. Garcia, X. Moya, R. O. Cherifi, C. Deranlot, K. Bouzheouane, S. Fusil, A. Zobelli, A. Gloter, N. D. Mathur, A. Gaupp, R. Abrudan, F. Radu, A. Barthélémy, and M. Bibes. *Nat. Mater.*, 10:753 758, (2011).
- [262] H. L. Meyerheim, F. Klimenta, A. Ernst, K. Mohseni, S. Ostanin, M. Fechner, S. Parihar, I. V. Maznichenko, I. Mertig, and J. Kirschner. *Phys. Rev. Lett.*, 106:087203, (2011).
- [263] L. Bocher, A. Gloter, A. Crassous, V. Garcia, K. March, A. Zobelli, S. Valencia, S. Enouz-Vedrenne, X. Moya, N. D. Marthur, C. Deranlot, S. Fusil, K. Bouzheouane, M. Bibes, A. Barthélémy, C. Colliex, and O. Stáphan. *Nano Lett.*, 12:376 382, (2012).
- [264] J. M. López-Encarnación, J. D. Burton, Evgeny Y. Tsymbal, and J. P. Velev. *Nano Lett.*, 11:599 603, (2011).
- [265] D. Pantel, S. Goetze, D. Hesse, and M. Alexe. *Nat. Mater.*, 11:289 293, (2012).
- [266] X. Luo, B. Wang, and Y. Zheng. *ACS Nano*, 5(3):1649 1656, (2011).
- [267] H. Lu, D. J. Kim, C.-W. Bark, S. Ryu, C. B. Eom, E. Y. Tsymbal, and A. Gruverman. *Nano Lett.*, 12:6289 6292, (2012).
- [268] R. R. Mehta, B. D. Silverman, and J. T. Jacobs. *J. Appl. Phys.*, 44:3379 3385, (1973).
- [269] D. J. Kim, J. Y. Jo, Y. S. Kim, Y. J. Chang, J. S. Lee, J.-G. Yoon, T. K. Song, and T. W. Noh. *Phys. Rev. Lett.*, 95:237602, (2005).
- [270] N. A. Pertsev and H. Kohlstedt. *Phys. Rev. Lett.*, 98:257603, (2007).
- [271] G. Gerra, A. K. Tagantsev, and N. Setter. *Phys. Rev. Lett.*, 98:207601, (2007).

- [272] A. K. Tagantsev, G. Gerra, and N. Setter. *Phys. Rev. B*, 77:174111, (2008).
- [273] M. Stengel, D. Vanderbilt, and N. A. Spaldin. *Nat. Mater.*, 8:392–397, (2009).
- [274] Y. Zheng, W. J. Chen, C. H. Woo, and B. Wang. *J. Phys. D: Appl. Phys.*, 44:139501, (2011).
- [275] Y. Zheng, W. J. Chen, X. Luo, B. Wang, and C. H. Woo. *Acta Mater.*, 60:1857–1870, (2012).
- [276] M.-Q. Cai, Y. Zheng, P.-W. Ma, and C. H. Woo. *J. Appl. Phys.*, 109:024103, (2011).
- [277] M.-Q. Cai, Y. Du, and B.-Y. Huang. *Appl. Phys. Lett.*, 98:102907, (2011).
- [278] Y. Umeno, J. M. Albina, B. Meyer, and C. Elsässer. *Phys. Rev. B*, 80:205122, (2009).
- [279] X. H. Liu, Y. Wang, P. V. Lukashev, J. D. Burton, and E. Y. Tsymbal. *Phys. Rev. B*, 85:125407, (2012).
- [280] H. Lu, X. Liu, J. D. Burton, C.-W. Bark, Y. Wang, Y. Zhang, D. J. Kim, A. Stamm, P. Lukashev, D. A. Felker, C. M. Folkman, P. Gao, M. S. Rzechowski, X. Q. Pan, C.-B. Eom, E. Y. Tsymbal, and A. Gruverman. *Adv. Mater.*, 24:1209–1216, (2012).
- [281] J. G. Simmons. *Phys. Rev. Lett.*, 10:10–12, (1963).
- [282] A. M. Bratkovsky and A. P. Levanyuk. *Phys. Rev. Lett.*, 94:107601, (2005).
- [283] Y. L. Li, L. E. Cross, and L. Q. Chen. *J. Appl. Phys.*, 98:064101, (2005).
- [284] M. B. Okatan, A. L. Roytburd, J. V. Mantese, and S. P. Alpay. *J. Appl. Phys.*, 105:114106, (2009).
- [285] Y. Liu and X.-P. Peng. *Appl. Phys. Express*, 5:011501, (2012).
- [286] Y. Liu and X.-P. Peng. *Chinese Phys. Lett.*, 29:057701, (2012).
- [287] M. B. Okatan, I. B. Misirlioglu, and S. P. Alpay. *Phys. Rev. B*, 82:094115, (2010).
- [288] I. I. Naumov, L. Bellaiche, and H. X. Fu. *Nature (London)*, 432:737–740, (2004).
- [289] I. Naumov and A. M. Bratkovsky. *Phys. Rev. Lett.*, 101:107601, (2008).
- [290] I. Kornev, H. X. Fu, and L. Bellaiche. *Phys. Rev. Lett.*, 93:196104, (2004).
- [291] P. Aguado-Puente and J. Junquera. *Phys. Rev. Lett.*, 100:177601, (2008).
- [292] T. Shimada, S. Tomoda, and T. Kitamura. *Phys. Rev. B*, 81:144116, (2010).
- [293] C. T. Nelson, B. Winchester, Y. Zhang, S.-J. Kim, A. Melville, C. Adamo, C. M. Folkman, S.-H. Baek, C.-B. Eom, D. G. Schlom, L.-Q. Chen, and X. Q. Pan. *Nano Lett.*, 11:828–834, (2011).

- [294] C.-L. Jia, K. W. Urban, M. Alexe, D. Hesse, and I. Vrejoiu. *Science*, 331:1420 1423, (2011).
- [295] X. Y. Wang, Y. L. Wang, and R. J. Yang. *Appl. Phys. Lett.*, 95:142910, (2009).
- [296] Y. L. Wang, X. Y. Wang, Y. Liu, B. T. Liu, and G. S. Fu. *Phys. Lett. A*, 374:4915 4918, (2010).
- [297] J. Junquera and P. Ghosez. *J. Comput. Theor. Nanosci.*, 5:2071 2088, (2008).
- [298] A. M. Bratkovsky and A. P. Levanyuk. *J. Comp. Theor. Nanosci.*, 6:465 489, (2005).
- [299] X. J. Lou and J. Wang. *J. Phys.-Condens. Mat.*, 22:055901, (2010).
- [300] Y. S. Kim, J. Y. Jo, D. J. Kim, Y. J. Chang, J. H. Lee, T. W. Noh, T. K. Songa, J.-G. Yoon, J.-S. Chung, S. I. Baik, Y.-W. Kim, and C. U. Jung. *Appl. Phys. Lett.*, 88:072909, (2006).
- [301] H. Z. Jin and J. Zhu. *J. Appl. Phys.*, 92:4594 4598, (2002).
- [302] M. Stengel, P. Aguado-Puente, N. A. Spaldin, and J. Junquera. *Phys. Rev. B*, 83:235112, (2011).
- [303] F. Chen and A. Klein. *Phys. Rev. B*, 86:094105, (2012).
- [304] A. S. Mischenko, Q. Zhang, R. W. Whatmore, J. F. Scott, and N. D. Mathur. *Appl. Phys. Lett.*, 89:242912, (2006).
- [305] H. Chen, T. -L. Ren, X. -M. Wu, Y. Yang, and L. -T. Liu. *Appl. Phys. Lett.*, 94:182902, (2009).
- [306] G. Akcay, S. P. Alpay, J. V. Mantese, and J. G. A. Rossetti. *Appl. Phys. Lett.*, 90:252909, (2007).
- [307] J. H. Qiu and Q. Jiang. *Phys. Lett. A*, 372:7191 7195, (2008).
- [308] S. Lisenkov and I. Ponomareva. *Phys. Rev. B*, 80:140102(R), (2009).
- [309] D. A. Tenne, P. Turner, J. D. Schmidt, M. Biegalski, Y. L. Li, L. Q. Chen, A. Soukiassian, S. Trolrier-McKinstry, D. G. Schlom, X. X. Xi, D. D. Fong, P. H. Fuoss, J. A. Eastman, G. B. Stephenson, C. Thompson, and S. K. Streiffer. *Phys. Rev. Lett.*, 103:177601, (2009).
- [310] D. D. Fong, A. M. Kolpak, J. A. Eastman, S. K. Streiffer, P. H. Fuoss, G. B. Stephenson, C. Thompson, D. M. Kim, K. J. Choi, C. B. Eom, I. Grinberg, and A. M. Rappe. *Phys. Rev. Lett.*, 96:127601, (2006).
- [311] F. D. Morrison, P. Zubko, D. J. Jung, J. F. Scott, P. Baxter, M. M. Saad, R. M. Bowman, and J. M. Gregg. *Appl. Phys. Lett.*, 86:152903, (2005).
- [312] D. Pantel and M. Alexe. *Phys. Rev. B*, 82:134105, (2005).

- [313] P. Maksymovych, S. Jesse, P. Yu, R. Ramesh, A. P. Baddorf, and S. V. Kalinin. *Science*, 324:1421–1425, (2009).
- [314] S. G. Yuan, J. B. Wang, X. L. Zhong, F. Wang, B. Li, and Y. C. Zhou. *J. Mater. Chem. C*, 1:418–421, (2013).
- [315] Z. Wen, C. Li, D. Wu, A. D. Li, and N. B. Ming. *Nat. Mater.*, 12:617–621, (2012).
- [316] Y. W. Yin, J. D. Burton, Y.-M. Kim, A. Y. Borisevich, S. J. Pennycook, S. M. Yang, T. W. Noh, A. Gruverman, X. G. Li, E. Y. Tsymbal, and Q. Li. *Nat. Mater.*, 12:397–402, (2012).
- [317] S. G. Lu, B. Rožič, Q. M. Zhang, Z. Kutnjak, and B. Neese. *Appl. Phys. Lett.*, 98:122906, (2011).
- [318] W. J. Chen, Y. Zheng, X. Luo, B. Wang, and C. H. Woo. *J. Appl. Phys.*, 114:064105, (2013).
- [319] Y. Bai, X. Han, X.-C. Zheng, and L. J. Qiao. *Sci. Rep.*, 3:2895, (2013).
- [320] J. Muhonen, M. Meschke, and J. Pekola. *Rep. Prog. Phys.*, 75:046501, (2012).
- [321] A. Yu. Emelyanov, N. A. Pertsev, and A. L. Kholkin. *Phys. Rev. B*, 66:214108, (2002).
- [322] H. Lu, C.-W. Bark, D. Esque de los Ojos, J. Alcalá, C. B. Eom, G. Catalan, and A. Gruverman. *Science*, 336:59–61, (2012).
- [323] Y. Gaillard, A. Hurtado Macías, J. Muñoz-Saldaña, M. Anglada, and G. Trápaga. *J. Phys. D Appl. Phys.*, 42:085502, (2009).
- [324] K. J. Choi, M. Biegalski, Y. L. Li, A. Sharan, J. Schubert, R. Uecker, P. Reiche, Y. B. Chen, X. Q. Pan, V. Gopalan, L.-Q. Chen, D. G. Schlom, and C. B. Eom, *Science*, 306:1005–1009, (2004).
- [325] H. N. Lee, S. M. Nakhmanson, M. F. Chisholm, H. M. Christen, K. M. Rabe, and D. Vanderbilt. *Phys. Rev. Lett.*, 98:217602, (2007).
- [326] D. Saranya, A. R. Chaudhuri, J. Parui, and S. B. Krupanidhi. *Bull. Mater. Sci.*, 32:259, (2009).
- [327] X. H. Hao and J. W. Zhai. *Appl. Phys. Lett.*, 104:022902, (2014).
- [328] X.-C. Zheng, G.-P. Zheng, Z. Lin, and Z.-Y. Jiang. *Thin Solid Films*, 522:125–128, (2012).
- [329] W. P. Geng, X. J. Lou, J. H. Xu, F. P. Zhang, Y. Liu, B. Dkhil, X. B. Ren, M. Zhang, and H. L. He. *Ceram. Int.*, 41:109–114, (2015).
- [330] X. H. Dai and D. Viehland. *J. Appl. Phys.*, 76, 3701–3703, (1994).
- [331] Z. Xu, X. H. Dai, and D. Viehland. *Phys. Rev. B*, 51:6261–6271, (1995).

- [332] X. H. Hao, J. W. Zhai, L. B. Kong, and Z. K. Xu. *Prog. Mater. Sci.* 63:1 116, (2014).
- [333] S. G. Lu and Q. M. Zhang. *J. Adv. Dielectr.*, 2:1230011, (2012).
- [334] G. Z. Zhang, X. S. Zhang, T. N. Yang, Q. Li, L.-Q. Chen, S. L. Jiang, and Q. Wang. *ACS Nano*, 9:7164 7174, (2015).
- [335] X. J. Lou, and J. Wang. *Appl. Phys. Lett.*, 96:102906, (2010).
- [336] F. Le Goupil, A. K. Axelsson, M. Valant, T. Lukasiewicz, J. Dec, A. Berenov, and N. M. Alford. *Appl. Phys. Lett.*, 104:222911, (2014).
- [337] X. Q. Liu, T. T. Chen, M. S. Fu, Y. J. Wu, and X. M. Chen. *Ceram. Int.*, 40:11269 11276, (2014).
- [338] X. Q. Liu, T. T. Chen, Y. J. Wu, X. M. Chen, and M. Valant. *J. Am. Ceram. Soc.*, 96:1021 1023, (2013).
- [339] Y. Bai, X. Han, K. Ding, and L.-J. Qiao. *Appl. Phys. Lett.*, 103:162902, (2013).
- [340] W. Liu and X. Ren. *Phys. Rev. Lett.*, 103:257602, (2009).
- [341] Y. Yao, C. Zhou, D. Lv, D. Wang, H. Wu, Y. Yang, and X. Ren. *Europhys. Lett.*, 98:27008, (2012).
- [342] G. Singh, V. S. Tiwari, and P. K. Gupta. *Appl. Phys. Lett.*, 103:202903, (2013).
- [343] M. Noda, T. Nomura, D. Popovici, S. Murakami, and M. Okuyama. *Integr. Ferroelectr.*, 63:35 40, (2004).
- [344] R. Chukka, J. W. Cheah, Z. Chen, P. Yang, S. Shannigrahi, J. Wang, and L. Chen. *Appl. Phys. Lett.*, 98:242902, (2011).
- [345] M. L. Plumer, A. Caillé, and K. Hood. *Phys. Rev. B*, 39:4489 4499, (1989).
- [346] N. Pertsev, A. Tagantsev, and N. Setter. *Phys. Rev. B*, 61:R825, (2000).
- [347] I. A. Kornev, L. Bellaïche, P.-E. Janolin, B. Dkhil, and E. Suard. *Phys. Rev. Lett.*, 97:157601, (2006).
- [348] A. N. Morozovska, Y. Gu, V. V. Khist, M. D. Glinchuk, L.-Q. Chen, V. Gopalan, and E. A. Eliseev. *Phys. Rev. B*, 87:134102, (2013).
- [349] V. V. Shvartsman, W. Kleemann, J. Dec, Z. K. Xu, and S. G. Lu. *J. Appl. Phys.*, 99:124111, (2006).
- [350] W. Kleemann, S. Miga, Z. K. Xu, S. G. Lu, and J. Dec. *Appl. Phys. Lett.*, 104:182910, (2014).
- [351] B. Asbani1, J.-L. Dellis, A. Lahmar, M. Courty, M. Amjoud, Y. Gagou, K. Djellab, D. Mezzane, Z. Kutnjak, and M. El Marssi. *Appl. Phys. Lett.*, 106:042902, (2015).

- [352] R. Chukka, S. Vandrangi, S. Shannigrahi, and L. Chen. *Europhys. Lett.*, 103:47011 47014, (2013).
- [353] Y. Liu, L. C. Phillips, R. Mattana, M. Bibes, A. Barthélémy, and B. Dkhil. *Nat. Commun.*, in press, (2016). DOI: 10.1038/ncomms11614.
- [354] E. Defay, S. Crossley, S. Kar-Narayan, X. Moya, and N. D. Mathur. *Adv. Mater.*, 25:3337 3342, (2013).
- [355] X. Moya, E. Defay, V. Heine, and N. D. Mathur. *Nat. Phys.*, 11:202 205, (2015).
- [356] M. V. R. Rao and A. Umarji. *Bull. Mater. Sci.*, 20:1023 1028, (1997).
- [357] Y. He. *Thermochimica Acta*, 419:135 141, (2004).
- [358] J. B. Neaton, C.-L. Hsueh, K. M. Rabe, *MRS Proceedings*, 718, (2002); C. Ederer and N. A. Spaldin. *Phys. Rev. Lett.*, 95:257601, (2005).
- [359] S. A. Hayward and E. K. H. Salje. *J. Phys.-Condens. Mat.*, 14:L599 L604, (2002).
- [360] J. J. Wang, P. P. Wu, X. Q. Ma, and L. Q. Chen. *J. Appl. Phys.*, 108:114105, (2010).
- [361] T. Ishidate, S. Abe, H. Takahashi, and N. Môri. *Phys. Rev. Lett.*, 78:2397 2402, (1998).
- [362] E. J. Huibregtse, W. H. Bessey, and M. E. Drougard. *J. Appl. Phys.*, 30:899 905, (1959).
- [363] T. Karaki, K. Yan, T. Masatoshi, A. Masatoshi. *Jpn. J. Appl. Phys.*, 46:L97 L98, (2007).
- [364] N. A. Pertsev and B. Dkhil. *Appl. Phys. Lett.*, 93:122903, (2008).
- [365] L. Mañosa, S. Jarque-Farnos, E. Vives, and A. Planes. *Appl. Phys. Lett.*, 103:211904, (2013).
- [366] J. X. Zhang, X. X. Ke, G. Y. Gou, J. Seidel, B. Xiang, P. Yu, W.-I. Liang, A. M. Minor, Y.-H. Chu, G. Van Tendeloo, X. B. Ren, and R. Ramesh. *Nat. Commun.*, 4:2768, (2013).
- [367] X. B. Ren. *Nat. Mater.*, 3:91 94, (2004).
- [368] Y. W. Li, X. B. Ren, F. X. Li, H. S. Luo, and D. N. Fang. *Appl. Phys. Lett.*, 102:092905, (2013).
- [369] Y. S. Kim, J. Y. Jo, D. J. Kim, Y. J. Chang, J. H. Lee, T. W. Noh, T. K. Song, J.-G. Yoon, J.-S. Chung, S. I. Baik, Y.-W. Kim, and C. U. Jung. *Appl. Phys. Lett.*, 88:072909, (2006).
- [370] N. A. Pertsev, A. G. Zembilgotov, and A. K. Tagantsev. *Phys. Rev. Lett.*, 80:1988 1991, (1998).
- [371] S. P. Alpay, I. B. Misirlioglu, A. Sharma, and Z.-G. Ban. *J. Appl. Phys.*, 95:8118 8123, (2004).

- [372] R. Renoud, M. Ragheb, C. Borderon, and H. W. Gundel. Free energy of BaTiO₃ single crystal, Applications of Ferroelectric and Workshop on the Piezoresponse Force Microscopy (ISAF/PFM), 34-37, Prague (2013). DOI:10.1109/ISAF.2013.6748727.
- [373] J. C. Lashley, J. H. D. Munns, M. Echizen, M. N. Ali, S. E. Rowley, and J. F. Scott. *Adv. Mater.*, 26:3860 3866, (2014).
- [374] J. F. Scott. *Europhys. Lett.*, 104:36004, (2014).
- [375] X. Zhang, J. B. Wang, B. Li, X. L. Zhong, X. J. Lou, and Y. C. Zhou. *J. Appl. Phys.*, 109:126102, (2011).
- [376] M. M. Vopson. *J. Phys. D: Appl. Phys.*, 46:345304, (2013).
- [377] J. E. Daniels, G. Picht, S. Kimber, and K. G. Webbe. *Appl. Phys. Lett.*, 103:122902, (2013).
- [378] K. G. Sandeman. *Scripta Mater.*, 67:566, (2012).
- [379] V. C. S. Prasad and E.C. Subbarao. *Appl. Phys. Lett.*, 22:424 425, (1973).
- [380] V. C. S. Prasad. *Bull. Mater. Sci.*, 5:71 78, (1983).
- [381] T. Strässle and A. Furrer. *High Pressure Res.*, 17:325 334, (2000).
- [382] T. Strässle, A. Furrer, A. Dönni, and T. Komatsubara. *J. Appl. Phys.*, 91:8543, (2002).
- [383] N. A. de Oliveira. *Appl. Phys. Lett.*, 90:052501, (2007).
- [384] L. G. de Medeiros Jr, N. A. de Oliveira, and A. Troper. *J. Appl. Phys.*, 103:113909, (2008).
- [385] N. A. de Oliveira. *J. Phys.-Condens. Mat.*, 20:175209, (2008).
- [386] M. V. Gorev, E. V. Bogdanov, I. N. Flerov, V. N. Voronov, and N. M. Laptash. *Ferroelectrics*, 397:76 80, (2010).
- [387] M. V. Gorev, E. V. Bogdanov, I. N. Flerov, A. G. Kocharova, and N. M. Laptash. *Phys. Solid State*, 52:167 175, (2010).
- [388] E. I. Pogorel'tsev, E. V. Bogdanov, M. S. Molokeev, V. N. Voronov, L. I. Isaenko, S. A. Zhurkov, N. M. Laptash, M. V. Gorev, and I. N. Flerov, *Phys. Solid State*, 53:1202 1211, (2011).
- [389] E. A. Mikhaleva, I. N. Flerov, V. S. Bondarev, M. V. Gorev, A. D. Vasiliev, and T. N. Davydova. *Ferroelectr.*, 430:78 83, (2012).
- [390] J.-D. Zou. *Chin. Phys. B.*, 21:037503, (2012).
- [391] A. V. Kartashev, E. A. Mikhaleva, M. V. Gorev, E. V. Bogdanov, A. V. Cherepakhin, K. A. Sablina, N. V. Mikhashonok, I. N. Flerov, and N. V. Volkov. *J. Appl. Phys.*, 113:073901, (2013).

- [392] E. Mikhaleva, I. Flerov, A. Kartashev, M. Gorev, A. Cherepakhin, K. Sablina, N. Mikhashenok, N. Volkov, and A. Shabanov. *J. Mater. Res.*, 28:3322-3328, (2013).
- [393] N. A. de Oliveira, P. J. Ranke, and A. Troper. *Int. J. Refrig.*, 37:237-245, (2014).
- [394] E. Stern-Taulats, A. Gràcia-Condal, A. Planes, P. Lloveras, M. Barrio, J.-L. Tamarit, S. Pramanick, S. Majumdar, and L. Mañosa. *Appl. Phys. Lett.*, 107:152409, (2015).
- [395] H. F. Kaya and P. Vousdena. *Phil. Mag.*, 40:1019-1040, (1949).
- [396] J. K. Murthy and A. Venimadhav. *J. Phys. D: Appl. Phys.*, 47:445002, (2014).
- [397] M. P. Annaorazov, K. A. Asatryan, G. Myalikgulyev, S. A. Nikitin, A. M. Tishin, and A. L. Tyurin. *Cryogenics*, 32:867-872, (1992).
- [398] A. X. Gray, D. W. Cooke, P. Krüger, C. Bordel, A. M. Kaiser, S. Moyerman, E. E. Fullerton, S. Ueda, Y. Yamashita, A. Gloskovskii, C. M. Schneider, W. Drube, K. Kobayashi, F. Hellman, and C. S. Fadley. *Phys. Rev. Lett.*, 108:257208, (2012).
- [399] M. A. de Vries, M. Loving, A. P. Mihai, L. H. Lewis, D. Heiman, and C. H. Marrows. *New J. Phys.*, 15:013008, (2013).
- [400] D. W. Cooke, F. Hellman, C. Baldasseroni, C. Bordel, S. Moyerman, and E. E. Fullerton. *Phys. Rev. Lett.*, 109:255901, (2012).
- [401] T. J. Zhou, M. K. Cher, L. Shen, J. F. Hu, and Z. M. Yuan. *Phys. Lett. A*, 377:3052-3059, (2013).
- [402] A. I. Zakharov, A. M. Kadomtseva, R. Z. Levitin, E. G. Ponyatovskii. *Sov. Phys. JETP*, 19:1348-1353, (1964).
- [403] A. Heeger. *J. Appl. Phys.*, 41:4751-4752, (1970).
- [404] G. P. Ju, J. Hohlfield, B. Bergman, R. J. M. van de Veerdonk, O. N. Mryasov, J.-Y. Kim, X. W. Wu, D. Weller, and B. Koopmans. *Phys. Rev. Lett.*, 93:197403, (2004).
- [405] V. K. Pecharsky and K. A. Gschneidner, Jr. *Appl. Phys. Lett.*, 70:3299, (1997).
- [406] M. Manekar, and S. B. Roy. *J. Phys. D: Appl. Phys.*, 41:192004, (2008).
- [407] J. van Driel, R. Coehoorn, G. J. Strijkers, E. Brück, and F. R. de Boer. *J. Appl. Phys.*, 85:1026-1036, (1999).
- [408] I. Suzuki, T. Koike, M. Itoh, T. Taniyama, and T. Sato. *J. Appl. Phys.*, 105:07E501, (2009).
- [409] G. C. Han, J. J. Qiu, Q. J. Yap, P. Luo, D. E. Laughlin, J. G. Zhu, T. Kanbe, and T. Shige. *J. Appl. Phys.*, 113:17C107, (2013).

- [410] L. C. Phillips, R. O. Cherifi, V. Ivanovskaya, A. Zobelli, I. C. Infante, E. Jacquet, N. Guiblin, A. A. Ünal, F. Kronast, B. Dkhil, A. Barthélémy, M. Bibes, and S. Valencia. *Sci. Rep.*, 5:10026, (2015).
- [411] A. Chirkova, K. P. Skokovb, L. Schultza, N. V. Baranove, O. Gutfleischb, and T. G. Woodcock. *Acta Mater.*, 106:15-21, (2016).
- [412] L. Caron, Z. Q. Ou, T. T. Nguyen, D. T. Cam Thanh, O. Tegus, and E. Brüüick. *J. Magn. Magn. Mater.*, 321:3559-3566, (2009).
- [413] R. Barua, F. Jiménez-Villacorta, and L. H. Lewis. *J. Appl. Phys.*, 115:17A903, (2014).
- [414] G. Sebald, L. Seveyrat, D. Guyomar, L. Lebrun, B. Guiffard, and S. Pruvost. *J. Appl. Phys.*, 100:124112, (2006).
- [415] M. M. Vopson, D. Zhou, and G. Caruntu. *Appl. Phys. Lett.*, 107:182905, (2015).
- [416] M.P. Annaorazov, M. Ünal, S. A. Nikitin, A. L. Tyurin, and K. A. Asatryan. *J. Magn. Magn. Mater.* 251:61-73, (2002).
- [417] X.-Z. Chen, X. Y. Li, X. S. Qian, M. R. Lin, S. Wu, Q. D. Shen, and Q. M. Zhang. *Polymer*, 54:5299 5302, (2013).
- [418] Q. Li, L. Chen, M. R. Gadinski, S. Zhang, G. Zhang, H. Li, A. Haque, L. Q. Chen, T. Jackson, and Q. Wang. *Nature(London)*, 523:576 579, (2015).
- [419] H. H. Wu, J. Zhu, and T. Y. Zhang. *Phys. Chem. Chem. Phys.*, 17:23897 23908, (2015).
- [420] M. Liu and J. Wang. *Sci. Rep.*, 5:7728 (2015).
- [421] R. Herchig, C.-M. Chang, B. K. Mani, and I. Ponomareva. *Sci. Rep.*, 5:17294, (2015).
- [422] G. Zhang, X. Zhang, H. Huang, J. Wang, Q. Li, L. Q. Chen, and Q. Wang. *Adv. Mater.* DOI: 10.1002/adma.201506118 (2016).
- [423] A. de Campos, D. L. Rocco, A. Carvalho, G. Magnus, L. Caron, A. A. Coelho, S. Gama, L. M. D. Silva, F. C. G. Gandra, A. O. D. Santos, L. P. Cardoso, P. J. von Ranke, and N. A. de Oliveira. *Nat. Mater.*, 5:802 804, (2006).
- [424] M. Balli, D. Fruchart, D. Gignoux, and R. Zach. *Appl. Phys. Lett.*, 95:072509, (2009).
- [425] J. F. Scott. *J. Phys.-Condens. Mat.*, 27:492001, (2015).
- [426] M.-W. Moon, S. H. Lee, J.-Y. Sun, K. H. Oh, A. Vaziri, and J. W. Hutchinson. *Proc. US Nat. Acad. Sci.*, 104:1130 1133, (2005).
- [427] W. Ramberg W. R. Osgood, "Description of stress-strain curves by three parameters", Technical Note 902, National Advisory Board for Aeronautics, Washington, DC, (1943).
- [428] D. Matsunami and A. Fujita. *Appl. Phys. Lett.*,106:042901, (2015).

- [429] T. Castán, A. Planes, and A. Saxena. *Phys. Rev. B*, 85:144429, (2012).
- [430] V. Katkanant, P. J. Edwardson, J. R. Hardy, and L. L. Boyer. *Phys. Rev. Lett.*, 57:2033-2036, (1986); 57:2877, (1986).
- [431] J. F. Scott. *J. Phys.-Condens. Mat.*, 25:331001, (2013).

PUBLICATIONS

1. **Yang Liu***, James F. Scott, and Brahim Dkhil, “Direct and indirect measurements on electrocaloric effect: recent developments and perspectives.” *Applied Physics Review*, in press.
2. **Yang Liu***, James F. Scott, and Brahim Dkhil*, “Some strategies for improving caloric responses with ferroelectrics.” *APL Materials*, **2016**, *4*, 064109/1-9.
3. **Yang Liu***, Brahim Dkhil, and Emmanuel Defay, “Spatially resolved imaging of electrocaloric effect and the resultant heat flux in multilayer capacitors.” **2016**, submitted.
4. **Yang Liu*[†]**, Lee C. Phillips*[†], Richard Mattana, Manuel Bibes, Agnès Barthélémy, and Brahim Dkhil. “Large reversible caloric effect in FeRh thin films via a dual-stimulus multicaloric cycle.” *Nature Communications* **2016**, *7*, 11614/1-6. [†]Equally contributed authors
5. Xiangjian Wang, Fang Tian, Chunlin Zhao, Jiagang Wu, **Yang Liu***, Brahim Dkhil, Ming Zhang, Zhipeng Gao, and Xiaojie Lou*, “Giant electrocaloric effect in $\text{Ba}_{0.94}\text{Ca}_{0.06}\text{Ti}_{1-x}\text{Sn}_x\text{O}_3$ ceramics with tunable Curie temperature.” *Applied Physics Letters* **2015**, *107*, 252905/1-5.
6. Wenping Geng[†], **Yang Liu*[†]**, Xiangjian Meng, James F. Scott, Brahim Dkhil, and Anquan Jiang. “Giant inverse electrocaloric effect in antiferroelectric La-doped $\text{Pb}(\text{ZrTi})\text{O}_3$ thin films near room temperature.” *Advanced Materials* **2015**, *27*, 3165-3169. (selected as Frontispiece)
[†]Equally contributed authors
7. **Yang Liu***, Jie Wei, Xiaojie Lou, Laurent Bellaiche, James F. Scott, and Brahim Dkhil. “Influence of epitaxial strain on elastocaloric effect in ferroelectric thin films.” *Applied Physics Letters* **2015**, *106*, 032901/1-5.

-
8. **Yang Liu**, Jie Wei, Pierre-Eymeric Janolin, Ingrid C. Infante, Jens Kreisel, Xiaojie Lou, and Brahim Dkhil*. "Prediction of giant elastocaloric strength and stress-mediated electrocaloric effect in BaTiO₃ single crystal." *Physical Review B* **2014**, *90*, 104107/1-6.
 9. Zhengdong Luo, Dawei Zhang, **Yang Liu***, Di Zhou, Yonggang Yao, Chenqi Liu, Brahim Dkhil, Xiaobing Ren, and Xiaojie Lou*. "Enhanced electrocaloric effect in lead-free BaTi_{1-x}Sn_xO₃ ceramics near room temperature." *Applied Physics Letters* **2014**, *105*, 102904/1-5.
 10. **Yang Liu**, Ingrid C. Infante, Xiaojie Lou*, Laurent Bellaiche, James F. Scott, and Brahim Dkhil*. "Giant elastocaloric effect in perovskite ultrathin films at room temperature." *Advanced Materials* **2014**, *26*, 6132-6137.
 11. **Yang Liu**, Jie Wei, Pierre-Eymeric Janolin, Ingrid C. Infante, Xiaojie Lou*, and Brahim Dkhil*. "Giant room-temperature barocaloric effect and pressure-mediated electrocaloric effect in BaTiO₃ single crystal." *Applied Physics Letters* **2014**, *104*, 162904/1-5.
 12. **Yang Liu***, Ingrid C. Infante, Xiaojie Lou, and Brahim Dkhil*. "Giant electrocaloric effect in asymmetric ferroelectric tunnel junctions." *Applied Physics Letters* **2014**, *104*, 082901/1-5.
 13. **Yang Liu***, Ingrid C. Infante, Xiaojie Lou, Doru C. Lupascu, and Brahim Dkhil. "Giant mechanically-mediated electrocaloric effect in ultrathin ferroelectric capacitors at room temperature." *Applied Physics Letters* **2014**, *104*, 012907/1-5.
 14. **Yang Liu***, Xiaojie Lou, Manuel Bibes, and Brahim Dkhil. "Effect of a built-in electric field in asymmetric ferroelectric tunnel junctions." *Physical Review B* **2013**, *88*, 024106/1-8.
 15. Ran Su, Zhengdong Luo, Dawei Zhang, **Yang Liu**, Zhipeng Wang, Junning Li, Jihong Bian, Yanxi Li, Xinghao Hu, Jinghui Gao, and Yaodong Yang*. "High energy density performance of polymer nanocomposites induced by designed formation of BaTiO₃@sheet-like TiO₂ hybrid nanofillers" *The Journal of Physical Chemistry C* in press DOI: 10.1021/acs.jpcc.6b01853.
 16. Jie Wei*, **Yang Liu**, Xiaofei Bai, Chen Li, Yalong Liu, Zhuo Xu, Raphael Haumont, Ingrid C. Infante, and Brahim Dkhil, "Crystal structure, leakage conduction mechanism evolution and enhanced multiferroic properties in Y-doped BiFeO₃ ceramics." *Ceramics International* **2016**,

6, 48779-48787.

17. Bobo Tian, J. L. Wang*, S. Fusil, **Yang Liu**, X. L. Zhao, S. Sun, S. Shen, T. Lin, J. L. Sun, C. D. Duan*, M. Bibes, A. Barthélemy, B. Dkhil, V. Garcia*, X. J. Meng, and J. H. Chu, "Tunnel electroresistance through organic ferroelectrics." *Nature Communications* **2016**, *7*, 11502/1-6.
18. Xiaofei Bai, Jie Wei, Bobo Tian, **Yang Liu**, T. Reiss, N. Guiblin, P. Gemeiner, B. Dkhil, I. C. Infante, "Size effect on optical and photocatalytic properties in BiFeO₃ nanoparticles." *The Journal of Physical Chemistry C* **2016**, *120*, 3595-3601.
19. Yalong Liu, Jie Wei*, **Yang Liu**, Xiaofei Bai, Peng Shi, Shengchun Mao, Xueqian Zhang, Chen Li, and Brhaim Dkhil. "Phase transition, leakage conduction mechanism evolution and enhanced ferroelectric properties in multiferroic Mn-doped BiFeO₃ thin films." *Applied Surface Science* **2016**, *27*, 3095-3102.
20. Bobo Tian*, **Yang Liu**, Liufang Chen, Jianlu Wang, Shuo Sun, Hong Shen*, Jinglan Sun, Guoliang Yuan, Stéphane Fusil, Vincent Garcia, Brahim Dkhil*, Xiangjian Meng, and Junhao Chu. "Space-charge effect on electroresistance in metal-ferroelectric-metal capacitors." *Scientific Reports* **2015**, *5*, 18297/1-9.
21. Bobo Tian, Liufang Chen, **Yang Liu**, Xiaofei Bai, Jianlu Wang, Shuo Sun, Guoliang Yuan, Jinglan Sun, Brahim Dkhil*, Xiangjian Meng*, and Junhao Chu. "Homogenous ferroelectric switching in ultrathin film of polyvinylidene fluoride (PVDF) polymers." *Physical Review B rapid communications* **2015**, *92*, 060102(R)1-4.
22. Bolu Liu, Bobo Tian, Jinglan Sun*, **Yang Liu***, Jianlu Wang, Shuo Sun, Xiangjian Meng, and Junhao Chu. "Confinement effect on coercive field in relaxor ferroelectric terpolymer nanowires." *Applied Surface Science* **2015**, *355*, 473-476.
23. Wenping Geng, **Yang Liu**, Xiaojie Lou*, Fuping Zhang, Qida Liu, Brahim Dkhil, Ming Zhang, Xiaobing Ren, Hongliang He, and Anquan Jiang*. "Polarization fatigue in antiferroelectric (Pb,La)(Zr,Ti)O₃ thin films: the role of the effective strength of driving signal." *Ceramics*

International **2015**, *41*, S289-S295.

24. Bobo Tian, Xiaofei Bai, **Yang Liu**, P. Gemeiner, X. L. Zhao, B. L. Liu, Y. H. Zou, X. D. Wang, H. Huang, J. L. Wang*, Sh. Sun, J. L. Sun, B. Dkhil*, X. J. Meng, and J. H. Chu. “ β phase instability in Poly(vinylidene fluoride/trifluoroethylene) P(VDF-TrFE) thin films near β relaxation temperature.” *Applied Physics Letters* **2015**, *106*, 092902/1-4.

25. Wenping Geng, Xiaojie Lou*, Jianghong Xu, Fuping Zhang, **Yang Liu**, Brahim Dkhil, Xiaobing Ren, Ming Zhang, and Hongliang He. “Effective driving voltage on polarization fatigue in (Pb,La)(Zr,Ti)O₃ antiferroelectric thin films.” *Ceramics International* **2015**, *41*, 109-114.

26. Xiaojie Lou*, Hongjia Zhang, Zhengdong Luo, Fuping Zhang, **Yang Liu**, Qida Liu, Aiping Fang, Brahim Dkhil, Ming Zhang, Xiaobing Ren, and Hongliang He. “Effect of polarization fatigue on the Rayleigh coefficients of ferroelectric lead zirconate titanate thin films: experimental evidence and implications.” *Applied Physics Letters* **2014**, *105*, 102907/1-5.

27. Zhengdong Luo, Xiaojie Lou*, Fuping Zhang, **Yang Liu**, Dingding Chang, Chenqi Liu, Qida Liu, Brahim Dkhil, Ming Zhang, Xiaobing Ren, and Hongliang He. “Rayleigh-like nonlinear dielectric response and its evolution during electrical fatigue in (Pb,La)(Zr,Ti)O₃ antiferroelectric thin film.” *Applied Physics Letters* **2014**, *104*, 142904/1-5.